School of Physics and Astronomy

Modelling And Studying Gravitational Waves From Black-Hole-Binary Mergers

Chinmay Kalaghatgi

Submitted for the degree of Doctor of Philosophy
School of Physics and Astronomy
Cardiff University

October 2019

Supervisor : Prof. Mark Hannam and Prof. Vivien Raymond

External examiner: Prof. Ian W. Harry

Internal examiner: Prof. Patrick Sutton

Chair: Dr Snehasis Tripathy

Date of viva: 12th August 2019

कर्मण्येवाधिकारस्ते मा फलेषु कदाचन ।
मा कर्मफलहेतुर्भूर्मा ते सङ्गोऽस्त्वकर्मणि ।।

You have the right to perform your duty, but are not entitled to the fruits of the same.
Do not consider yourself as the cause of the results, nor be inattentive towards your duty.

Bhagwat Gita, Chapter 2, Verse 47.

Co-authored Papers

Parts of this thesis are results of collaborative work. Chinmay Kalaghatgi (CK) is either the lead author or contributed significantly to the work.

1. "Effects of waveform model systematics on the interpretation of GW150914" : Abbott, Benjamin P. and others [1].
CK performed the PE runs with the Cardiff-UIB NR waveforms and `IMRPhenomPv2` waveform.

2. "First Higher-Multipole Model of Gravitational Waves from Spinning and Coalescing Black-Hole Binaries" : Lionel London, Sebastian Khan, Edward Fauchon-Jones, Cecilo Garcia, Mark Hannam, Sascha Husa, Xisco Jimenez-Forteza, Chinmay Kalaghatgi, Frank Ohme and Francesco Pannarale [2].
CK performed the PE runs for the paper with `IMRPhenomHM` waveform.

3. "Effects of in-plane spin direction on final waveform" : Chinmay Kalaghatgi and Mark Hannam.
CK obtained the required NR simulation data and the analysis of the data. (*Writing*)

4. "Parameter estimation with aligned-spin multi-mode templates" : Chinmay Kalaghatgi, Mark Hannam and Vivien Raymond.
CK obtained the required PN-NR hybrids and performed the PE runs. (*Writing*)

Summary of thesis

The source parameters of the first direct detection (GW150914 [3]) of gravitational waves (GW) from a binary black hole (BBH) system were determined by using approximate models of the BBH coalescence, the errors on which could be driven by the noise (statistical errors) or the approximate nature of the model (systematic errors). To determine the systematic errors, a set of numerical relativity (NR) waveforms with similar parameters as of GW150914 were injected over a range of inclination and polarisation values and recovered with `IMRPhenomPv2`. The main result of this study was that the systematic errors induced due to waveform model inaccuracies were much smaller than corresponding statistical errors, and hence, the statistical errors dominate the systematic for the inferred parameters of GW150914.

For current precessing waveform models, the six dimensional spin space is mapped to a two dimensional space of effective spin parameters. We investigate the effects of changing the in-plane spin direction on the GW signal and determine whether these effects are strong enough to be measured by current ground based GW detectors. We also study the effect of disregarding the mode-asymmetry content present in the signals and attempt to answer whether mode-asymmetries need to be included in future waveform models.

GW signals, when decomposed in the spin weighted spherical harmonic basis, are made of its different modes (h_{lm}s), with the quadrupole mode being dominant. The waveform model `IMRPhenomHM` models a few of the sub-dominant modes with the quadrupole mode for aligned-spin binaries. We wanted to investigate the effects of using a multimode (`IMRPhenomHM`) and quadrupole only (`IMRPhenomD`) waveform model to recover source parameters from multimode signals (`IMRPhenomHM` signals) and real physical signals (NR waveform signals) across a range of physical parameters and inclination values.

Declaration of Authorship

- **Declaration:**
  This work has not previously been accepted in substance for any degree and is not concurrently submitted in candidature for any degree.
  Signed:
  _____

  Date:
  _____

- **Statement 1:**
  This thesis is being submitted in partial fulfillment of the requirements for the degree of Doctor of Philosophy (PhD).
  Signed:
  _____

  Date:
  _____

- **Statement 2:**
  This thesis is the result of my own independent work/investigation, except where otherwise stated. Other sources are acknowledged by explicit references.
  Signed:
  _____

  Date:
  _____

- **Statement 3:**
  I hereby give consent for my thesis, if accepted, to be available for photo- copying and for inter-library loan, and for the title and summary to be made available to outside organisations.
  Signed:
  _____

  Date:
  _____

Acknowledgements

I am thankful for the Horizon 2020 grant for the funding over the past four years.

First of all, I would like to thank my family, Mom, Dad and Di; who have always helped and supported me through thick and thin, and who were always present with a sympathetic ear or with sound advice. I dedicate this thesis to all my family, but especially to Aababa, Alkai, Nani, Aaba, Shailya Atya, Fufa and Baba; all who believed in me but could not be here now. There are innumerous others who helped me along this path, so thank you all!

My heartfelt thanks to my supervisors, Mark Hannam and Vivien Raymond; who have been patient enough to explain (sometimes multiple times!) every doubt or confusion I had during the course of the PhD. No student could've asked for better advisors. To all the gravitational physics group, I would like to extend my thanks for making these PhD years enjoyable and loads of fun! I will especially miss the conversations in 53 (....when we're supposed to be working). I would like to take this opportunity to extend my thank-you to Dr. K.G. Arun and Dr. P. Ajith, who got me interested in the field of Gravitational Wave physics and guided me through my masters.

I would like to thank Mr. Milind Toro, who took in an unmotivated 11 year old brat and got him interested in the world of maths and physics. Without you, I'd probably have been gone down a career path that I was supposed to take, and maybe not one that I'd have liked. I'd also like to thank all my teachers till now, without whom none of this would've been possible.

It is not easy for a person when staying in a new country and without all the friends I made here, it would have been much much harder. To Aris, Greg, Adam, Danny S., Danny M., Penny, Eli, Val, Max, Ruth, and Iain; (and the people of Brewskis and the Beast) I'd like to thank you all for making the past four years a blast!

To my friends of old; Suraj, Palash, Mandar, Nischay, Vivin, Susmit, Aarya, Apurva, Aishwarya, Omkar, Narendra, Ateen, Pritish, Abhishek, Karishma, Renu, Neeraj, Piyu Di, Shantanu and Siddhant. Without you all, life would be less colourful and boring. Also, Mandar-Aarya and Palash-Aditi; sorry for not being able to attend your wedding due to writing up the thesis.

Finally, Samruddhi, who has always supported me through my best and helped me through my worst. Neither I nor all who know me, have yet understood how you handle me. Thank you, and love you!

Contents

List of Figures

List of Tables

Abbreviations

LIGO	**L**aser **I**nterferometer **G**ravitational-wave **O**bservatory
LHO	**L**IGO **H**anford **O**bservatory
LLO	**L**IGO **L**ivingston **O**bservatory
aLIGO	**a**dvanced **LIGO**
GW	**G**ravitational **W**ave
BBH	**B**inary **B**lack **H**ole
CBC	**C**oalescing **C**ompact **B**inary
PE	**P**arameter **E**stimation

Chapter 1

Gravitational wave basics : Theory and Detection

1.1 Introduction

Albert Einstein's special theory of relativity (STR) in 1905 revolutionized the prevailing understanding of classical mechanics. The axiom of a constant speed of light (c) in all frames of reference and the conclusion that nothing can travel faster than c led to new physics like length contraction, time-dilation and the mass-energy equivalence. In Newtonian theory, the gravitational force is instantaneous, which violates the basic axiom of STR. Efforts to make gravity consistent with STR eventually led to the birth of General Theory of Relativity (GR) where gravity was understood as the effect of spacetime curvature due to the presence of massive objects. One of the early predictions from GR was the existence of gravitational waves, which are ripples in the fabric of spacetime.

The first indirect evidence of the existence of gravitational waves was observed from the orbital period decay of the Hulse-Taylor pulsar binary (PSR 1913+16) [see Fig: 1.1]. The binary loses its orbital energy by emission of GWs, which causes its orbital period to decrease. The observed data of the shift in periastron time matches with the general relativistic prediction of energy loss due to GW [5].

From the 1960s, efforts were underway towards direct detection of GW signals. After decades of effort that led to technological breakthroughs in multiple areas, the aLIGO [6] and aVIRGO [7] detectors reached the required sensitivity for GW detection. The first ever detection of gravitational waves, from a binary black-hole (BBH) system, was achieved by the LVC (LIGO-VIRGO Collaboration) on September 14, 2015 [3]. Since then, until the writing of this thesis (March 2019), a total of 11 confirmed GW events have been observed [8],

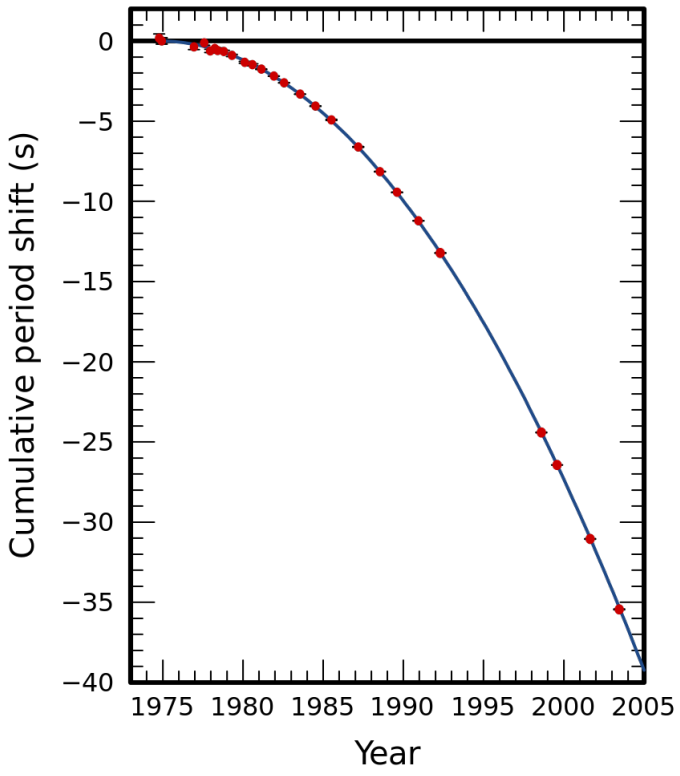

FIGURE 1.1: Cumulative shift in the periastron time of binary pulsar PSR 1913+16 with time. The dots are observed data points and the solid line is the general relativistic prediction. Image for representation purpose only from [4]

out of which 10 were BBH events and one was a binary neutron star coalescence (called GW170817) that was seen by both LIGO and VIRGO detectors. GW170817 was also followed up in the electromagnetic (EM) band and its associated γ-ray burst [9] was observed [10], [11]. This was the first observation of co-incident EM-GW signals from a binary neutron star. The event termed GW170814 [12] was the first three detector detection of a BBH GW signal.

From April of 2019, aLIGO and aVIRGO started their third observation run (O3) with improved detector sensitivity. aLIGO is expected to reach its design sensitivity by 2020, 2021 for aVIRGO. The Japanese cryogenic interferometer, KAGRA [13], [14], is expected to join the detector network by late 2019 or 2020, with the addition of LIGO-India [15], [16] in the detector network expected by 2024 [17]. The era of GW astronomy is just starting up and it would be very exciting to see what mysteries GW observations are going to throw at us and also hopefully provide information towards solving some currently known issues. The author would like to recommend any interested reader to [18] for more information on GW astronomy/astrophysics/cosmology.

This chapter will aim to provide a theoretical basis of gravitational waves in the linearized theory, a basic description of interferometer working, an introduction to aLIGO and end with a description of GW data analysis (searches and parameter estimation (PE)). The author will assume a basic understanding from the reader of General Relativity and will not spend much time on discussing GR. See [19], [20], [21] for a rigorous treatment of GR.

1.2 Gravitational waves

From GR, gravitational force is understood as a consequence of the curvature of spacetime due to mass-energy. Let $\mathcal{M}$ be the space-time manifold with a metric $(g_{\mu\nu})$ defined over $\mathcal{M}$. The metric $g_{\mu\nu}$ encapsulates the global properties of $\mathcal{M}$ (geodesics, singularities etc.). The proper distance $(\mathrm{d}s)$ between two points on the manifold is given as,

$$\mathrm{d}s^2 = g_{\mu\nu}\mathrm{d}x^\mu \mathrm{d}x^\nu, \tag{1.1}$$

where $(x^\mu = (x^0, x^1, x^2, x^3) = (t, x, y, z))$. All other important geometric quantities required to characterise the spacetime can then be computed from the metric and its first and second derivatives. General theory of relativity provides the relationship between the background spacetime metric $g_{\mu\nu}$ and energy-momentum tensor $T_{\mu\nu}$;

$$G_{\mu\nu} = \frac{8\pi G}{c^4} T_{\mu\nu}, \tag{1.2}$$

where $G_{\mu\nu} = R_{\mu\nu} - \frac{1}{2} g_{\mu\nu} R$ with $R_{\mu\nu}$ and R being the Ricci tensor and Ricci scalar respectively[1]. See Chapter 1 - 4 of [21] for a definition of the above quantities and their derivation from first principles.

Gravitational waves are ripples on the fabric of spacetime, or understood another way, a perturbation to *some* static background metric [2]:

$$g_{\mu\nu}^{full} = g_{\mu\nu}^{background} + h_{\mu\nu}. \tag{1.3}$$

1.2.1 Gravitational waves in Linearized theory

In the linearized theory of gravity, effects of dynamical perturbations to the static (generally flat) background metric $(g_{\mu\nu})$ are studied where the perturbations are much weaker in

[1] The cosmological constant is not considered in this discussion.

[2] For the next section (Linearized gravity) the background metric is assumed to be Minkowskian but in general, the background metric can be generic. In the limit of the length scale of metric variation $>>$ length scale of perturbation variation, the concepts of linearized theory can be applied locally.

strength than $g_{\mu\nu}$ [3]. As is standard, we will consider perturbations to the flat spacetime (Minkowskian) metric $(\eta_{\mu\nu})$ to demonstrate the important features of GW in this formalism.

Consider a small perturbation $(h_{\mu\nu})$ to the flat spacetime,

$$g_{\mu\nu} = \eta_{\mu\nu} + h_{\mu\nu}, \qquad |h_{\mu\nu}| << 1. \tag{1.4}$$

Using the form of metric from Eq: 1.4 in Eq: 1.2 and discarding any non-linear terms of $h_{\mu\nu}$ gives the Einsteins equations linear in $h_{\mu\nu}$($\partial_i \eta_{\mu\nu}$ being 0),

$$\Box\tilde{h}_{\mu\nu} + \eta_{\mu\nu}\partial^\rho\partial^\sigma\tilde{h}_{\rho\sigma} - \partial^\rho\partial_\nu\tilde{h}_{\mu\rho} - \partial^\rho\partial_\mu\tilde{h}_{\nu\rho} = \frac{-16\pi G}{c^4}T_{\mu\nu}, \tag{1.5}$$

where $\tilde{h}_{\mu\nu} = h_{\mu\nu} - \frac{1}{2}\eta_{\mu\nu}h$ with $\Box = \eta_{\mu\nu}\partial^\mu\partial^\nu$ being the 4D d'Alembertian in flat 4D space-time.

Linearized theory of gravity is gauge invariant under slowly varying diffeomorphisms, i.e. under a co-ordinate transformation of $x^{'\mu} \rightarrow x^\mu + \xi^\mu(x)$ where $\partial_\mu\xi^\nu(x) \sim |h|$. It can be proven that there always exists a function $\xi^\mu(x)$ (also called the *Lorentz gauge*) such that,

$$\partial^\nu\tilde{h}_{\mu\nu} = 0, \tag{1.6}$$

so that the last three terms of Eq: 1.5 vanish and it becomes a wave equation in 4D,

$$\Box\tilde{h}_{\mu\nu} = \frac{-16\pi G}{c^4}T_{\mu\nu}. \tag{1.7}$$

Eq: 1.7 gives the equation for gravitational wave generation from some source. For detection of gravitational waves and to study their effect on test-masses, it is instructive to study their vacuum behaviour, i.e., when $T_{\mu\nu} \sim 0$.

When $\Box\tilde{h}_{\mu\nu} = 0$, making another co-ordinate transformation of $x^{'\mu} \rightarrow x^\mu + \kappa^\mu(x)$ such that $\Box\kappa^\mu(x) = 0$ will conserve the Lorentz gauge and the wave equation. With this freedom, we can choose κ^0 such that trace of h vanishes ($\bar{h} = 0$) and κ^i so that $h^{0i} = 0$. The Lorentz gauge condition along with the choice of κ^i gives $\partial^0 h_{00} = 0$. This gauge choice is known as the transverse-traceless gauge. As h_{00} is constant, it will not affect the motion of masses and we need only consider the spatial components of the wave tensor. So, out of the ten free components of the wave tensor, four were restricted by the choice of Lorentz gauge and four more by the choice of transverse-traceless gauge, leaving two free components. These are called the plus and cross polarizations of a gravitational wave $(h_+, h_\times)$. Within

[3] The author would like to refer any interested reader to section 1.1 and 1.2 of [22] for a more detailed explanation of what follows here.

the transverse - traceless gauge, the wave solution for a gravitational wave travelling along $\hat{z}$ would be,

$$h_{ij}(t,z) = \begin{bmatrix} h_+ & h_\times & 0 \\ h_\times & -h_+ & 0 \\ 0 & 0 & 0 \end{bmatrix} \cos\left[\omega_{gw}(t - z/c)\right], \tag{1.8}$$

with ω_{gw} being the characteristic GW frequency. See Fig: 1.2 for an illustration of the effect of h_+ and $h_\times$ on a ring of test particles at $z = 0$.

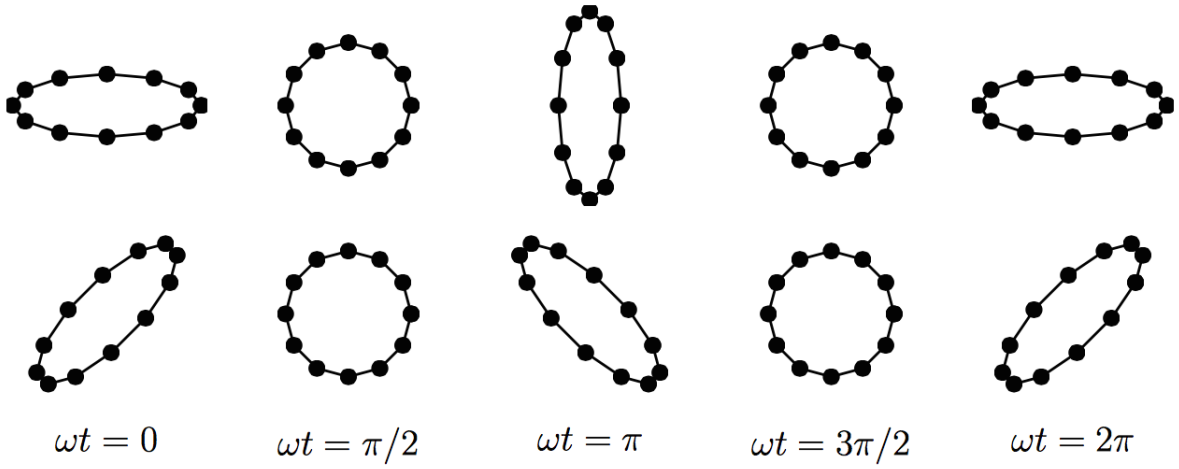

FIGURE 1.2: Effect of h_+ (top row) and $h_\times$ (bottom row) on a ring of freely falling test particles which lie in the x-y plane while the gravitational wave is propagating along $\hat{z}$ at different times.

1.2.2 Quadrupole generation of gravitational waves

Eq: 1.7 shows the connection between a mass distribution and the gravitational waves it would generate. This equation is a 4D wave equation and can be solved using the retarded Greens functions; which gives us,

$$\tilde{h}_{\mu\nu}(t,\vec{x}) = \frac{4G}{c^4} \int \mathrm{d}^3x' \frac{1}{|\vec{x} - \vec{x'}|} T_{\mu\nu}\left(t - \frac{|\vec{x} - \vec{x'}|}{c}, \vec{x'}\right). \tag{1.9}$$

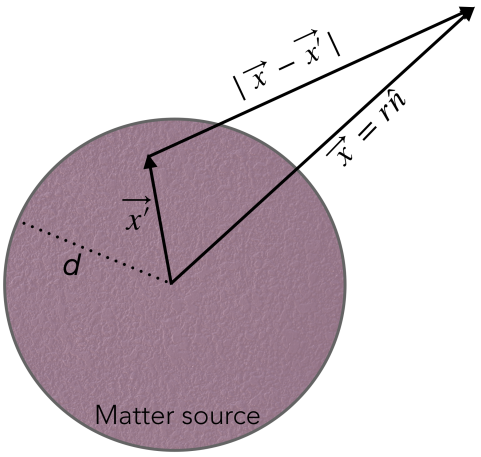

FIGURE 1.3: A representative situation of a matter source of size d generating gravitational waves at a point $r >> d$.

In the limit of $r >> d$ (See Fig: 1.3), the term $|\vec{x} - \vec{x'}| = r - \vec{x'}.\hat{n} + \mathcal{O}(d^2/r)$. In this limit, the Fourier transform of $T_{\mu\nu}$ would be,

$$T_{\mu\nu}(t - \frac{r}{c} + \frac{\vec{x'}.\hat{n}}{c}, \vec{x'}) = \int \frac{\mathrm{d}^4k}{(2\pi)^4} T_{\mu\nu}(\omega, \vec{k}) e^{-i\omega\left(t - r/c + \vec{x'}.\hat{n}/c\right) + i\vec{k}.\vec{x'}}. \tag{1.10}$$

Let ω_s be the characteristic GW frequency from which we can think of $\omega_s d \sim v_s$ as some characteristic velocity of the system generating the GWs. For all points $\vec{x'}$ within the source, $\omega\vec{x'}.\hat{n}/c \sim \omega_s d/c$. In limit of $v_s << c \implies \frac{\omega_s d}{c} << 1$, we have $\omega\vec{x'}.\hat{n}/c << 1$ and this term can then be used as a parameter around which we can Taylor expand the exponential term in Eq: 1.10, doing which gives us,

$$e^{-i\omega\left(t - r/c + \vec{x'}.\hat{n}/c\right)} = e^{-i\omega(t - r/c)} \left[1 - i\frac{\omega}{c} x'^i n^i - \frac{1}{2}\frac{\omega^2}{c^2} x'^i x'^j n^i n^j + \dots\right]. \tag{1.11}$$

Substituting Eq: 1.11 in Eq: 1.10 gives the low-velocity expansion of the stress-energy tensor,

$$T_{\mu\nu}(t - r/c. + \frac{\vec{x'}.\hat{n}}{c}, \vec{x'}) \simeq T_{\mu\nu}(t - r/c, \vec{x'}) + \frac{x'^i n^i}{c}\partial_t T_{\mu\nu} + \frac{1}{2c^2} x'^i x'^j n^i n^j \partial_t^2 T_{\mu\nu} \dots. \tag{1.12}$$

Defining the stress-energy tensor momenta as : $S^{ij}(t) = \int \mathrm{d}^3x T^{ij}(t, \vec{x})$, $S^{ij,k}(t) = \int \mathrm{d}^3x x^k T^{ij}(t, \vec{x})$ etc. Eq: 1.9 becomes,

$$\tilde{h}_{ij}^{TT}(t, \vec{x}) = \frac{1}{r}\frac{4G}{c^4} \Lambda_{ij,kl}^{TT}(\hat{n}) \left[S^{kl} + \frac{1}{c} n_m \dot{S}^{kl,m} + \dots\right], \tag{1.13}$$

where $\Lambda_{ij,kl}^{TT}(\hat{n})$ is the transverse-traceless projection tensor along $\hat{n}$. Let the mass density moment be $M^{ij} = \frac{1}{c^2}\int \mathrm{d}^3x T^{00}(t, \vec{x}) x^i x^j$. The momenta density ($T^{0i}$) moments can be defined in the same way. Applying the conservation of energy-momentum ($\partial_\mu T^{\mu 0} = 0$)

principle and conservation of angular-momentum of the source (symmetric behaviour of S^{ij}) to these moments gives a relation between the first stress-energy tensor moment with the quadrupole mass moment as,

$$S^{ij} = \frac{1}{2}\ddot{M}^{ij}. \tag{1.14}$$

The mass moment tensor, being symmetric, can be decomposed into its traceless part (which would contribute towards GW generation) and a scalar scaled by its trace. The traceless part is the Quadrupole moment (Q^{ij}),

$$Q^{ij} = M^{ij} - \frac{1}{3}\delta^{ij}M_{ll} = \int \mathrm{d}^3x\rho(t,\vec{x})(x^ix^j - \frac{1}{3}r^2\delta^{ij}). \tag{1.15}$$

Using the forms of Eq: 1.15 and Eq: 1.14 in Eq: 1.13 up to leading order, gives us the equation of generation of gravitational waves by a time varying quadrupole moment,

$$\tilde{h}^{TT}_{ij}(t,\vec{x}) = \frac{1}{r}\frac{2G}{c^4}\ddot{Q}^{TT}_{ij}(t - r/c). \tag{1.16}$$

In terms of these quadrupole mass moments, we can write the plus and cross polarisations of a gravitational wave travelling along $\hat{z}$ as,

$$h_+ = \frac{1}{r}\frac{G}{c^4}\left(\ddot{M}_{11} - \ddot{M}_{22}\right), \tag{1.17}$$

$$h_\times = \frac{1}{r}\frac{2G}{c^4}\ddot{M}_{12}. \tag{1.18}$$

In the linearized theory, all non-linear effects like gravitational wave radiation-reaction force, GW tails etc. are not considered. In Chapter 2, we will discuss the solving of Einsteins equations with the non-linearities included and the generation of resulting waveforms.

1.3 Detecting Gravitational waves

Efforts to detect gravitational wave signals have been ongoing since the late 1960s, starting with the Weber bar detector [23]. A gravitational wave with frequency close to the resonant frequency of the bar detector can cause length changes in the bar which can then be measured by piezoelectric sensors. Since then, there have been multiple other resonant bar detectors but none of them have yet been successful at detecting GWs from astrophysical systems [24].

Gravitational wave interferometric detectors have had tremendous success in GW observations over the past four years (from Sept. 2015). The first generation of interferometric detectors (iLIGO [25], eLIGO [26], VIRGO [27], GEO600 [25], TAMA300 [28]) which started

since 1990s, had a larger noise-floor than the current second generation detectors and did not observe any events. The basic idea behind interferometric gravitational wave detectors is to measure the differential length change (Δ**L**) between two test masses along both arms as a gravitational wave passes through. For most sources of astrophysical origin, like GWs from a distant coalescing BBH system, Δ**L** is very small.

In this section, we will start with how GWs change the length between two points, the behaviour of an interferometer in the presence of GWs, a description of aLIGO and end with a discussion of future GW detector networks.

1.3.1 Effect of GWs on test masses

Using the form of the metric perturbation given in the transverse-traceless gauge (see Eq: 1.8), the interval between two points ($\mathrm{d}s$) becomes,

$$\mathrm{d}s^2 = -c^2\mathrm{d}t^2 + [1 + h_+\cos(\omega_{gw}t)]\,\mathrm{d}x^2 + [1 - h_+\cos(\omega_{gw}t)]\,\mathrm{d}y^2 + 2h_\times\cos(\omega_{gw}t)\mathrm{d}x\mathrm{d}y + \mathrm{d}z^2, \tag{1.19}$$

where ω_{gw} is the gravitational wave frequency. Consider two masses along the x-axis at a proper distance of **L** from each other. A gravitational wave moving along $\hat{z}$ would modify the proper distance between the two masses (at a given time t),

$$\mathbf{L} \rightarrow \mathbf{L}\sqrt{(1 + h_+)} \sim \mathbf{L}(1 + \frac{1}{2}h_+). \tag{1.20}$$

Here, the square root term is Taylor expanded and terms of $\mathcal{O}(h^2)$ are discarded. Thus, a passing gravitational wave would cause a total length change Δ**L** between two test masses,

$$\Delta\mathbf{L} \propto h\mathbf{L}. \tag{1.21}$$

For a binary black hole source of 100$M_\odot$ at 100Mpc, $h \sim 10^{-21}$ and for an interferometer with arm length of $\mathcal{O}(10^3 m)$ (without Fabry-Perot cavities), $\Delta\mathbf{L} \simeq \mathcal{O}(10^{-18} m)$. This length change is very small, almost 1000 times smaller than the radius of a proton $\mathcal{O}(10^{-15} m)$ and due to the tiny change in length, one can expect that the noise would dominate interferometric measurements.

1.3.2 Operation of interferometer in presence of GWs

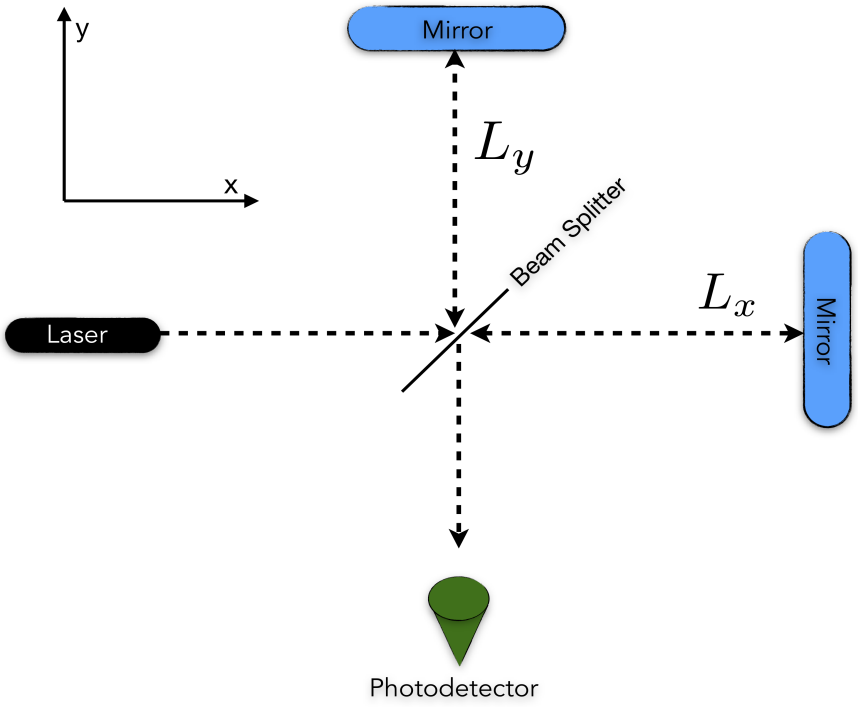

FIGURE 1.4: This figure shows the components of a basic interferometer. A beam of light emitted by the laser is split along the two perpendicular arms along $\hat{x}$ and $\hat{y}$ by the beam splitter. The final recombined electric field strength is measured by the photodetector.

A Michelson interferometer is able to accurately measure the differential length changes between its two arms. It does so by measuring the phase differences between the two beams of light that travel along the two arms caused by arm length changes from a GW. Fig: 1.4 illustrates the components of a generic interferometer. Let $E_0 e^{-i\omega_d t + i\vec{k}.\vec{x}}$ be the electric component of a light beam going along $\hat{x}$ (and a similar wave along $\hat{y}$), t_i be the time when the laser light leaves the beam-splitter and t_f be the time when the wave arrives back. If no gravitational waves are present, then it is straightforward to see that $t_f - t_i = \frac{2L_{x/y}}{c}$ $(\mathrm{d}s^2 = 0 \rightarrow c\mathrm{d}t = \mathrm{d}x)$ [4].

In presence of a gravitational wave (in the TT gauge) with only the plus polarization, $c\mathrm{d}t = \pm(1 + \frac{1}{2}h_+ \cos(\omega_{gw} t))$. After consistently choosing the sign for travel from (to) the beam splitter, we get,

$$t_f - t_0 = \frac{2L_x}{c} + \frac{1}{2}\int_{t_0}^{t_f} h(t')\mathrm{d}t' \sim \frac{2L_x}{c} + \frac{1}{2}\int_{t_0}^{t_0+\frac{2L_x}{c}} h_+ \cos(\omega_{gw} t)\mathrm{d}t'. \tag{1.22}$$

[4] This discussion closely follows the one in Sec: 9.1 of [22].

Solving the above integral gives us,

$$t_f - t_0 = \frac{2L_x}{c} + \frac{L_x}{c} h\left(t_0 + \frac{L_x}{c}\right) \frac{\sin(\omega_{gw} L_x/c)}{(\omega_{gw} L_x/c)}. \tag{1.23}$$

The time difference for travelling along $\hat{y}$ will be the same as above, but with a change in sign for the $h(t)$ term and with L_x replaced by L_y.

Let us consider the total electric field $(E_{tot}(t))$ at the beam-splitter at a given time t which would be a combination of the photons leaving the beam-splitter at time $t_0^{x/y}$ [5]. First, we need to invert t using Eq: 1.23 ,

$$t_0^x = t - \frac{2L_x}{c} - \frac{L_x}{c} h\left(t - \frac{L_x}{c}\right) \frac{\sin(\omega_{gw} L_x/c)}{(\omega_{gw} L_x/c)}, \tag{1.24}$$

with the opposite sign for the third term for t_0^y and with L_x replaced by L_y. Keeping the co-ordinate system fixed at the beam-splitter, gives us $E_{tot}(t)$,

$$E_{tot}(t) = E_x(t) + E_y(t) = \frac{1}{2} E_0 \left(e^{i\omega_d t_0^y} - e^{i\omega_d t_0^x}\right), \tag{1.25}$$

solving Eq: 1.25 using the relations given in Eq: 1.24 gives us,

$$E_{tot}(t) = -iE_0 e^{(-i\omega_d(t - L/c))} \sin(\phi_0 + \Delta\phi), \tag{1.26}$$

where $L = \frac{L_x + L_y}{2}$ and $\Delta\phi = \frac{\omega_d}{c} h_+ L_x \cos(\omega_{gw}(t - L_x/c)) \frac{\sin(\omega_{gw} L_x/c)}{(\omega_{gw} L/c)}$.

This change in the total electric field will be reflected at the total power output, which is measured. To sum up, the presence of a gravitational wave modifies the proper distance between the mirrors along the two arms of an interferometer which then affects the overall phase of the output electric field and is measured.

The analysis given above of the effect of GWs on interferometers is applicable when $L << \lambda$, where λ would be the characteristic wavelength of the GW. For cases where $L \sim \lambda$, the geodesic deviation equation between two points needs to be solved with a full GR consideration (for example: in the case of space based detectors where the arms are planned to be $\sim$ 1 million km long).

The plus and cross polarisations of a gravitational wave are defined in the source-frame. In general, the frame defined for the detector arms will not align with the source frame. So, the detector response to the gravitational wave polarisations would depend on the source sky-location (θ, ϕ) and an overall rotation between the polarisation and arm axes (ψ). The

[5] This calculation closely follows the one presented in Section:9.1.1 of [22]

response towards the plus (F_+) and cross polarisations ($F_\times$) are,

$$F_+(\alpha,\delta,\psi) = \frac{1}{2}(1+\cos^2\alpha)\cos(2\delta)\cos(2\psi) - \cos(\alpha)\sin(2\delta)\sin(2\psi), \tag{1.27}$$

$$F_\times(\alpha,\delta,\psi) = \frac{1}{2}(1+\cos^2\alpha)\cos(2\delta)\sin(2\psi) + \cos(\alpha)\sin(2\delta)\cos(2\psi), \tag{1.28}$$

with the total gravitational strain at the detector,

$$h_{resp}(t,\alpha,\delta,\psi) = F_+(\alpha,\delta,\psi)h_+(t) + F_\times(\alpha,\delta,\psi)h_\times(t). \tag{1.29}$$

See Sec:4.2.1 of [18] for a derivation of the response functions.

1.3.3 LIGO Detectors

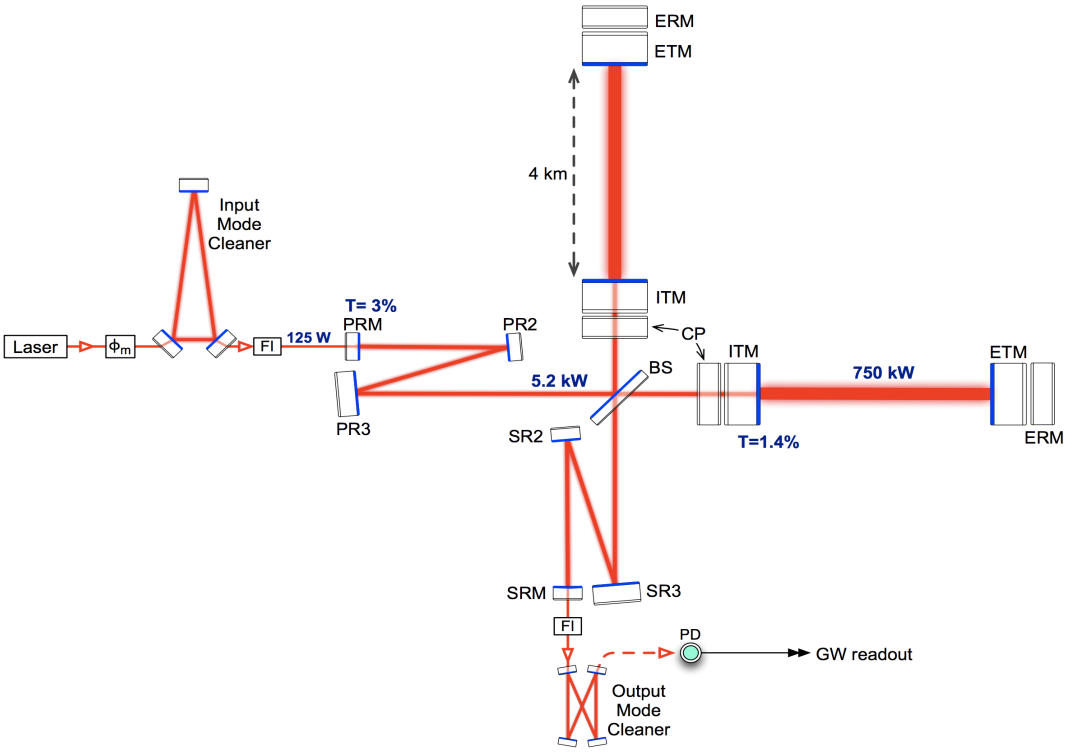

FIGURE 1.5: The above figure shows the design configuration of Advanced-LIGO [6]. A 1064nm Nd:YAG laser beam is cleaned through the mode cleaner and sent to the beam-splitter via a power recycling mirror (PRM) array to increase the input laser power. A resonant Fabry-Perot cavity is present between the two test masses (input-test mass (ITM) and end-test mass (ETM)) to increase the effective path length of the laser light and increase the overall detector output power. The output signal is sent via a signal recycling mirror(SRM) array to be cleaned before being read-out by the photodetector.

The LIGO detectors, commissioned in the 1990s [29], went through the Initial-LIGO [30], [31] and Enhanced-LIGO [32] phases and were searching for GW signals from 2002 to 2010, but none were found [33]–[36]. From then till 2015, the sensitivity of these detectors was

improved upon, with almost twice the distance reach for aLIGO as compared to iLIGO [17] and the first signal from a binary black hole was detected on the 14th of September 2015. See Fig: 1.5 for the aLIGO design.

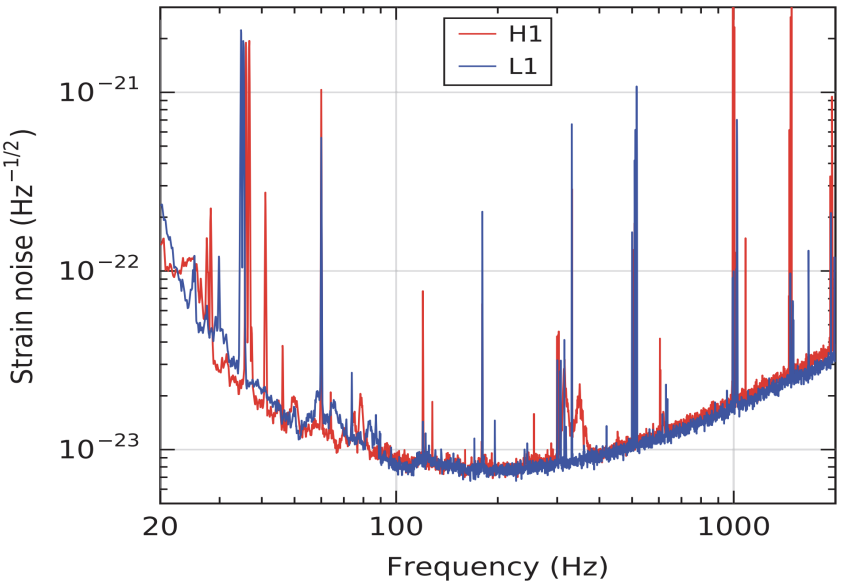

FIGURE 1.6: Power spectral density of the LIGO detectors at Hanford (H1) and Livingston (L1) during 14^{th} of September, 2015 when the first GW signal was observed [3].

The major challenge for LIGO was to reduce the noise contributions from various sources. At low frequencies, the seismic vibrations dominate while the quantum effects (photon shot noise) dominate at higher frequencies. The other sources of noise for LIGO include noise contributions from residual gas in the vacuum tubes, thermal brownian motion on the surface of test-mass mirrors, thermal motion of suspension strings etc. Various approaches have been used to reduce the noise from the different sources and the sensitivity of the aLIGO detectors has been improving. We will not go into much detail of noise contributions and techniques used to tackle them, but, the weak GW signal is buried within the noise at the output and various data analysis techniques are required to detect the presence of signals in the data and to measure the source parameters. See Fig: 1.6 for the sensitivity of the advanced LIGO detectors during the start of their observation run. Also, to improve detection range and to reduce statistical errors on measured parameters, constant work is ongoing to reduce noise (seismic suspensions, better mirror coatings, quantum squeezing of light etc.)

1.3.4 GW detector network

From 2015, aLIGO has gone through two science runs and gathered data and from the second half of 2017, Advanced Virgo joined the detector network which facilitated the first ever

three-detector detection of gravitational waves from a neutron star binary (GW170817) [9] and a binary black hole system (GW170814) [12]. As of early 2019, there are three detectors in the GW network, the two aLIGO detectors and the VIRGO detector. Another one in Japan, KAGRA [13], [14], should be ready soon and join observations by 2020. A LIGO detector has been planned to be built in India which should be online by 2025 [15], [16]. These ground based detectors have similar sensitivities and are called the second-generation detectors (initial/enhanced LIGO, inital-VIRGO, GEO600 being the first). The presence of a network of gravitational wave detectors will greatly improve the localization of sources and help to quickly search for electromagnetic counterparts (see Fig: 1.7 for locations of 2nd generation detector network).

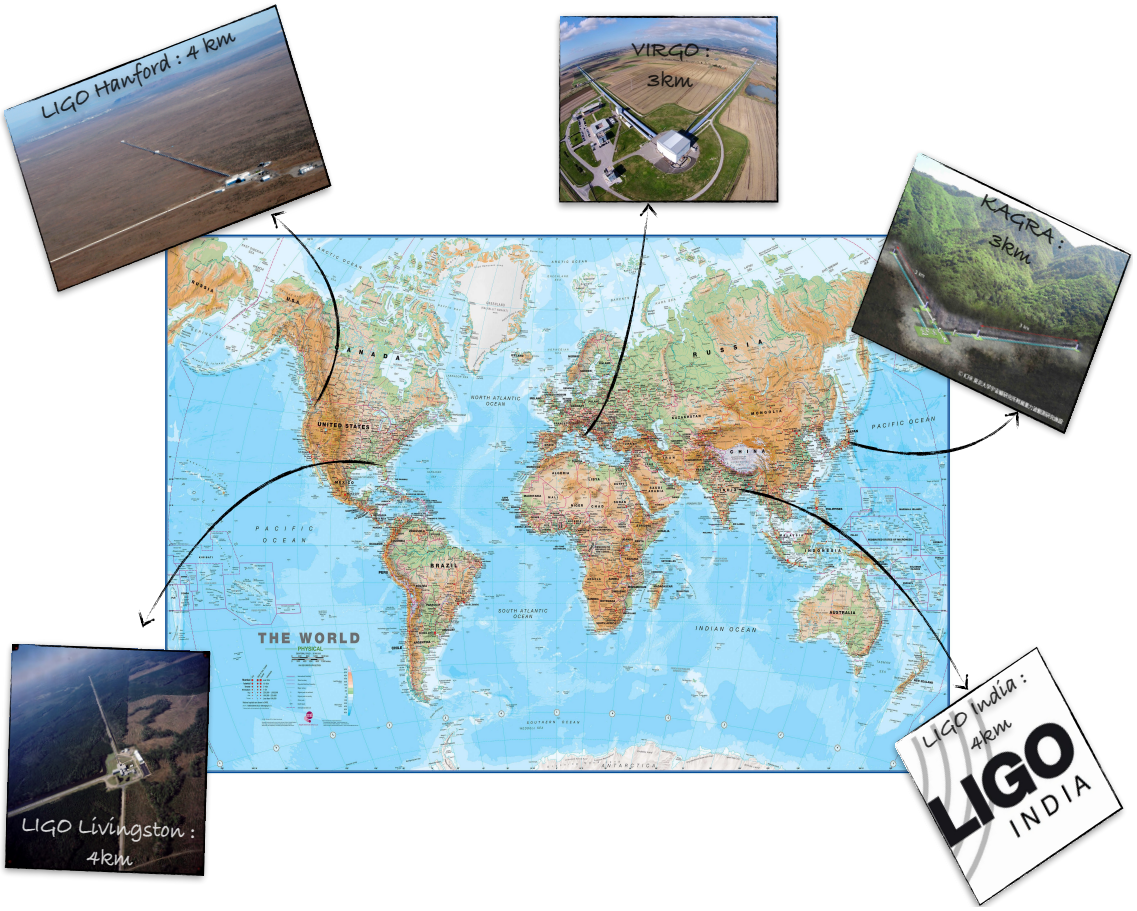

FIGURE 1.7: Locations of the current and planned gravitational wave detectors across the world. With increasing number of detectors, the source localization improves. The source can be constrained within a 9-12deg^2 with a five detector network as compared to the current 120-180deg^2 [17].

There are plans for "third-generation" detectors like the Cosmic explorer [37] and Einstein Telescope [38] which would greatly improve upon the current second-generation sensitivity thus allowing us to see farther out into the universe (see Fig: 1.8). These detectors are planned to have arms of $\sim \mathcal{O}$(10km) and with further improvements to reduce noise contributions, these third-generation detectors are expected to observe binary black hole

coalescence as far as z∼10 at SNRs ∼ 20. A space based antenna to detect GWs in the low frequency band (10^{-5}Hz to 1Hz), the Laser Interferometric Space Antenna (LISA) has also been planned [39] and is currently projected to be launched in the 2030s.

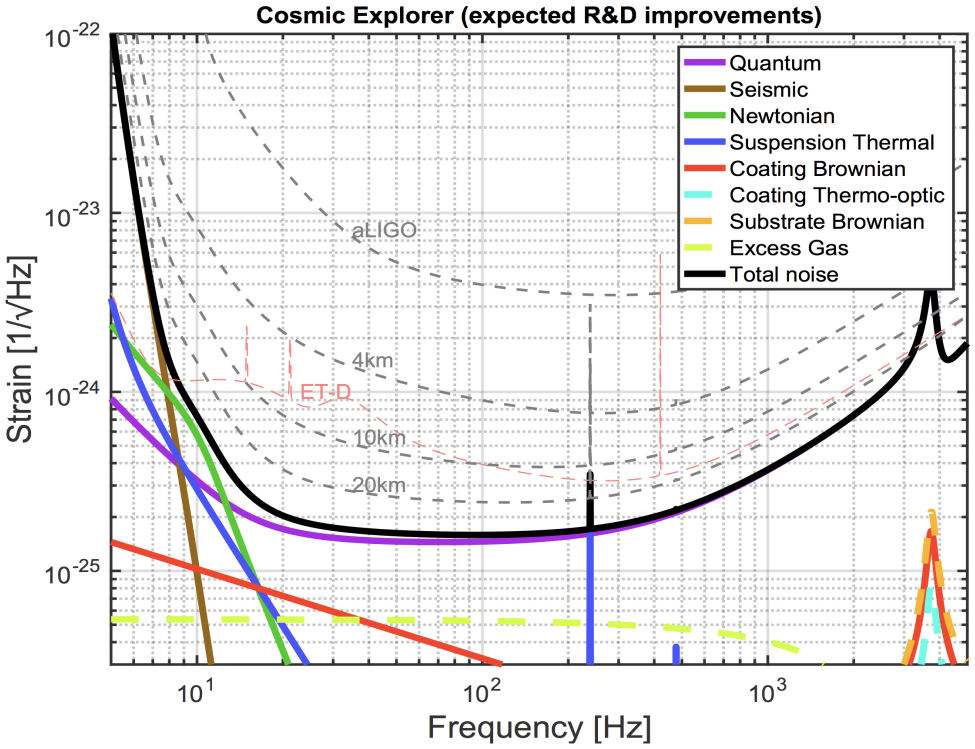

FIGURE 1.8: Expected sensitivity of Cosmic Explorer (CE) [37] with different arm lengths compared to aLIGO and Einstein Telescope (ET-D) sensitivity. This figure demonstrates the seismic noise wall at low frequencies and the quantum noise at high frequencies. The other noise sources contribute to the total noise in the intermediate frequencies. CE is planned to be about more than 10 times more sensitive aLIGO, thus greatly increasing the number of sources we could observe.

1.4 Analysing detector data

Any physical system with a time varying quadrupole moment can generate gravitational waves. Potential sources of GWs that could be observable by ground based detectors include, among others, i) Compact Binary Coalescence (CBCs) leading to short transient GW signals; ii) Deformed rotating neutron stars which act as a source of continuous GWs; iii) Core collapse supernovae leading to short burst signals; iv) GWs from cosmic strings that form one of the sources of the stochastic background. See Sec:3 of [18] and references within for description of the different sources.

In Section 1.3 we saw that the signal would be buried in the noise at the detector output. So various data analysis techniques are employed to search for gravitational wave events in the detector data and to measure the source parameters of a signal. There are different

methods of searching for GWs from CBCs in the detector data and LIGO data is analysed by the pyCBC search pipeline [40], gstLAL search pipeline ([41],[42]) and cWB (coherent wave-burst) search pipelines ([43], [44]). The author would like to refer the interested reader to [45]–[48] (and references therein) for the results of searching for non-CBC events during the second observation run of LIGO. As this thesis is concerned only about binary black hole signals, we will end the discussion for non BBH signals here.

Once the presence of a signal in detector data is confirmed, this data is cleaned and parameter estimation techniques based on Bayesian statistics are employed to measure the source parameters. The accuracy of these measurements depend largely on the detector noise, but systematic errors from model waveform inaccuracies can also affect measurements. This section will give a brief introduction to the techniques employed to search for signals, but the main focus will be on parameter estimation techniques. For further reading of the different search algorithms, the author would like to refer the interested reader to the references given above.

1.4.1 Searching for the signal

Let the output of the detector data ($d(t)$) be composed of a GW signal ($h(t)$) and the noise ($n(t)$),

$$d(t) = h(t) + n(t). \tag{1.30}$$

To check for the presence of a gravitational wave, one approach is to cross-correlate the detector data with a set of theoretical template waveforms and calculate the signal to noise ratio (SNR ρ) for each template. This set of template waveforms is called a *template-bank*. The SNR of the data with a template $h'(t)$ is given by,

$$\rho^2 = \frac{\left\langle \tilde{d}(f) \mid \tilde{h}'(f) \right\rangle}{\left\langle \tilde{h}'(f) \mid \tilde{h}'(f) \right\rangle}, \tag{1.31}$$

where $\tilde{d}(f), \tilde{h}'(f)$ are the Fourier transforms of $d(t)$ and $h'(t)$ respectively, i.e.,

$$\tilde{d}(f) = \int d(t) e^{-2\pi i f t} \mathrm{d}t, \tag{1.32}$$

and $\langle a(f)|b(f)\rangle$ is the noise-weighted inner product between two functions,

$$\langle a(f)|b(f)\rangle = \mathrm{Re}\left[\int_{-\infty}^{\infty} \frac{a(f)b^*(f) + a^*(f)b(f)}{S_n(f)}\right]. \tag{1.33}$$

$S_n(f)$ is the one-sided noise power spectral density (PSD) given by,

$$\langle n(f)n(f')\rangle = \frac{1}{2}S_n(f)\delta(f-f') \tag{1.34}$$

where the angular brackets denote an average over multiple noise realizations and $\delta(f-f')$ is the Dirac delta function. This process is also known as *match-filtering*.

During *match-filtering*, if the SNR for a template with a given set of intrinsic parameters and arrival time is higher than a pre-determined threshold then it might indicate the presence of a signal during that time and it is counted as a trigger. But, it is possible that the trigger could be due to the presence of non-stationary noise in the detector data, also called *glitches*. To determine the statistical significance of a trigger to be from a real signal and not a glitch, multiple other tests are done like co-incidence checks and signal consistency (χ^2) tests. The sensitivity of these searches largely depend on the template bank and the waveform model used to build the same. As parts of this thesis concentrate on parameter inference rather than signal detection, we will stop the discussion on signal searches here. For further details on search pipelines, the author would refer the interested reader to [40], [41],[42], [43], and [44] and references therein.

1.4.2 Measures of waveform accuracy

As mentioned in the previous section, the sensitivity of template banks towards detecting gravitational wave signals depends in-part on the accuracy of the waveform model at recreating the physical signals. The accuracy of a waveform model can be determined by its match value, its *faithfulness* and *effectualness*([49], [50]).

The normalized match between two waveforms, $h_a(f)$ and $h_b(f)$, is defined as the inner-product (see Eq: 1.33) between the normalized waveforms. If the two waveforms are exactly the same, then the match value would be 1.

$$\mathcal{M}(h_a(f),h_b(f)) = \frac{4}{|h_a(f)||h_b(f)|}\text{Re}\left[\int_0^\infty \frac{h_a(f)h_b^*(f)}{S_n(f)}\right] \tag{1.35}$$

The *faithfulness* of a template waveform is defined as the normalized match maximised over the extrinsic (time-phase of arrival) parameters keeping the intrinsic parameters the same. Hence, we can write the faithfulness as,

$$\mathcal{F}(h_a(f),h_b(f)) = \text{Max}_{t_c,\phi_c}[\mathcal{M}(h_a(f),h_b(f))] \tag{1.36}$$

The *effectualness* of a template waveform is defined as the normalized match maximised over the extrinsic and relevant intrinsic parameters. The extrinsic parameters are the distance (d_L), sky-position (α, δ), polarisation (ψ) and time (t_c) and phase of arrival (ϕ_c) with the binary masses (m_1, m_2) and their spin vectors ($\vec{S_1}, \vec{S_2}$) being the set of intrinsic parameters. If the vector of intrinsic parameters is given by $\vec{\lambda}$, the effectualness is,

$$\mathcal{E}(h_a(f), h_b(f)) = \mathrm{Max}_{t_c, \phi_c, \vec{\lambda}}[\mathcal{M}(h_a(f), h_b(f))] \tag{1.37}$$

The definition of the match as given in Eq: 1.35 is valid for non-spinning or aligned-spin systems. For precessing systems, the match computation is slightly more involved and will be discussed in more detail in Section 4.3.1.

1.4.3 Parameter Estimation basics

Let the detector output be given by **d**(t) and the noise of the detector be **n**(t). If a GW signal, **h**(t), is present, then the output **d**(t) = **h**(t) + **n**(t). Once we have a GW signal detection, the next step would be to infer the physical parameters of the source given a fixed waveform model (*parameter estimation*) or comparing the different waveform models to decide the most probable model given the detector data (*model selection*). Model selection is not used in this study and so details regarding the same will not be discussed here. I closely follow the PE treatment as given in [51] and would refer interested readers to the same (and references therein) for further reading.

Let $\mathcal{H}$ be a gravitational waveform model family described by the parameters $\boldsymbol{\theta}$ where $\boldsymbol{\theta}$ gives a N dimensional vector $\boldsymbol{\theta}$=($\theta^1, \theta^2, \ldots, \theta^N$) in the physical parameter space. Given the detector data and a model, we can calculate the *likelihood* $[p(\boldsymbol{d}|\boldsymbol{\theta}, \mathcal{H})]$ of observing the data **d** given a model $\mathcal{H}$ with parameters $\boldsymbol{\theta}$. The posterior probability over the physical parameters $\boldsymbol{\theta}$ $[p(\boldsymbol{\theta}|\boldsymbol{d}, \mathcal{H})]$ would then be proportional to the product of the likelihood with the *priors* defined over the said parameters $[p(\boldsymbol{\theta}|\mathcal{H})]$. The posterior probability is then given by,

$$p(\boldsymbol{\theta}|\boldsymbol{d}, \mathcal{H}) = \frac{p(\boldsymbol{d}|\boldsymbol{\theta}, \mathcal{H}) p(\boldsymbol{\theta}|\mathcal{H})}{p(\boldsymbol{d}|\mathcal{H})}, \tag{1.38}$$

where the *evidence* ($\mathcal{E}$), $p(\boldsymbol{d}|\mathcal{H})$, is the product of the prior and likelihood function integrated over the physical parameter space $\boldsymbol{\theta}$,

$$p(\boldsymbol{d}|\mathcal{H}) = \int_{\boldsymbol{\theta}} \mathrm{d}\theta_1 \mathrm{d}\theta_2 \ldots \mathrm{d}\theta_N p(\boldsymbol{\theta}|\mathcal{H}) p(\boldsymbol{d}|\boldsymbol{\theta}, \mathcal{H}). \tag{1.39}$$

Once we have the posterior probability density over $\boldsymbol{\theta}$, the posterior for one parameter eg: θ^1 can then be obtained by marginalizing over all other parameters,

$$p(\theta^1|\boldsymbol{d},\mathcal{H}) = \int \mathrm{d}\theta^2\mathrm{d}\theta^3..\mathrm{d}\theta^N p(\boldsymbol{\theta}|\boldsymbol{d},\mathcal{H}) \tag{1.40}$$

The posterior probability density is the likelihood weighted by the prior and the posteriors could be affected by the choice of prior used. The prior choice can be motivated by physical considerations (for eg: placing the upper limit on distance prior based on distance reach of the detector) or by the region of validity of a waveform model. Thus, the conclusions drawn about the source parameters depend on the information about the system prior to observations and data generated from the experiment. For example: For the case of black-hole binary coalescence with total mass M, if the frequency of innermost stable circular orbit, $f_{isco} \sim \frac{1}{M}$, is lower than the seismic cut-off frequency of LIGO f_{cut}, the signal will be completely buried in the noise. Let M_u be the mass at which $f_{isco}(M_u) = f_{cut}$. This information can then be used to place an upper limit bound on the total mass prior (M_u) for our analysis as LIGO will be insensitive to systems with masses higher than M_u. Priors on other parameters can be placed based on similar considerations. [6]

The Likelihood function provides a measure of how well the hypothesis $\mathcal{H}$ with parameters $\boldsymbol{\theta}$ match the data **d**. Assuming gaussian distributed detector noise, given the data **d**, the hypothesis $\mathcal{H}$ and parameter values $\boldsymbol{\theta}$, the likelihood is,

$$p(\boldsymbol{d}|\boldsymbol{\theta},\mathcal{H}) \propto e^{-\frac{\langle \boldsymbol{d}-h(\boldsymbol{\theta})|\boldsymbol{d}-h(\boldsymbol{\theta})\rangle}{2}}, \tag{1.41}$$

where $\langle \boldsymbol{d}-h(\boldsymbol{\theta})|\boldsymbol{d}-h(\boldsymbol{\theta})\rangle$ is the noise weighted inner product given in Eq: 1.33 and $S_n(f)$ is the power spectral density (PSD) of the detector which is the Fourier transform of the noise auto-correlation function (see Eq: 1.34).

Estimation of source parameters of the signal require computing the posterior density from the likelihood and prior, Eq: 1.38. The space of the waveform parameters is a continuous manifold with the prior and likelihood being smooth functions over the manifold. Generally, the parameter space has high dimensionality *($\sim$ 15 dimensional for precessing configurations)*(see Section 2.5) and, except for some simple special cases, the posteriors cannot be computed analytically. So we need numerical methods to get an estimate of the posterior distribution. One intuitive way would be to place a lattice over the parameter space and find the maximum likelihood areas, but given the high dimensionality of the manifold and computational constraints, such an approach is not feasible. So, we need other methods to either estimate the posterior distribution or the total evidence.

[6] The example given here is an illustrative example of how various considerations can be used to specify prior ranges, whereas for the actual PE codes, different priors are used.

The `LALInference` package [52], a part of the open LSC Algorithm Libary (`LALSuite`) [53], provides the necessary libraries to perform parameter estimation studies of the data given a waveform model. The parameter estimation codes employ two different methods to obtain the posterior.

1. **Nested Sampling:** The Nested Sampling algorithm, developed by Skilling [54], is a Monte Carlo method where the total evidence for the problem is obtained first and then the posterior distribution is calculated from the evidence. See Section 1.4.5 for further details.

2. **MCMC:** The Markov Chain Monte Carlo (MCMC) algorithm estimates the posterior by stochastically wandering through the parameter space, distributing samples proportional to the posterior density. See Section 1.4.4 for further details.

Once we have the posterior distribution, the statistical quantities like the mean, median etc can be calculated from it, but it is not always a certainty that the mean value reflects the true parameters of the system. A more interesting quantity is the *credible interval* (CI), which can be understood as the boundary of that region in the physical parameter space ($\mathcal{R}(\boldsymbol{\theta})$) that encompasses a given probability 'p' of the total posterior,

$$p = \int_{\mathcal{R}(\boldsymbol{\theta})} p(\boldsymbol{d}|\boldsymbol{\theta}, \mathcal{H}) \tag{1.42}$$

During parameter estimation of gravitational wave data, we generally compute the 90% credible intervals.

1.4.4 Markov Chain Monte Carlo Algorithm

The basic idea behind MCMC algorithm is to estimate the parameter posterior distribution by randomly sampling the parameter space and zeroing in on the target posterior. The MCMC algorithm for GW data analysis employs the Metropolis-Hastings algorithm [55] to generate new samples from existing ones via a proposal density function $\mathcal{Q}(\boldsymbol{\theta'}|\boldsymbol{\theta})$. The new sample proposal $\boldsymbol{\theta'}$ is accepted over the old one $\boldsymbol{\theta}$ with probability $r_s = min(1, \alpha)$ where,

$$\alpha = \frac{\mathcal{Q}(\boldsymbol{\theta}|\boldsymbol{\theta'})p(\boldsymbol{\theta'}|\boldsymbol{d}\mathcal{H})}{\mathcal{Q}(\boldsymbol{\theta'}|\boldsymbol{\theta})p(\boldsymbol{\theta}|\boldsymbol{d}\mathcal{H})}. \tag{1.43}$$

If accepted, $\boldsymbol{\theta'}$ is added to the chain or the process is repeated.

Typically, chains are started at random positions in the parameter space and they require some initial number of jumps before dependence of initial positions of the chain is lost. This

is called the *burn in* period and samples during the burn-in are discarded. Also, adjacent samples are generally correlated. For statistical analysis, uncorrelated samples are required and so, each chain is thinned by its auto-correlation time (ACT) τ which is given by,

$$\tau = 1 + 2\sum_{t} \hat{c}(t), \tag{1.44}$$

where t labels the iteration of the chain and $\hat{c}(t)$ is the Pearson correlation coefficient between the chain of samples and itself shifted by t samples. The chain is thinned by accepting every τ^{th} sample and the samples left after the burn-in and ACT thinning are called *effective samples*. The efficiency of this algorithm (acceptance rates & ACT) is largely governed by the jump proposal density function $\mathcal{Q}$. In `LALInference`, the MCMC algorithm uses various jump proposals tailored for the GW parameter estimation problem.

1.4.5 Nested Sampling

Nested Sampling is a computational algorithm developed by Skilling [54] in which the evidence $\mathcal{E}$ is computed first, from which the posterior distributions of the parameters are obtained. In this method, the multi-dimensional evidence integral, Eq: 1.39, is transformed into a one-dimensional integral over the *prior volume*. The prior mass, given by $\mathrm{X}(\lambda)$ such that $\mathrm{dX} = \mathrm{d}\boldsymbol{\theta} p(\boldsymbol{\theta}, \mathcal{H})$, is the fraction of total prior volume where the likelihood is greater than λ. Thus,

$$\mathrm{X}(\lambda) = \int_{p(\boldsymbol{d}|\boldsymbol{\theta},\mathcal{H})>\lambda} \mathrm{d}\boldsymbol{\theta} p(\boldsymbol{\theta}, \mathcal{H}). \tag{1.45}$$

Thus the evidence integral,

$$p(\boldsymbol{d}|\mathcal{H}) = \int \mathrm{d}\boldsymbol{\theta} p(\boldsymbol{\theta}|\mathcal{H}) p(\boldsymbol{d}|\boldsymbol{\theta}, \mathcal{H}) = \int_0^1 \mathcal{L}(\mathrm{X})\mathrm{dX}, \tag{1.46}$$

where $\mathcal{L}(\mathrm{X})$ is the inverse of Eq: 1.45 and is a decreasing function of X. The region in prior space with the highest likelihood value will be mostly concentrated near the real parameters whereas the full prior region will have an overall much lower likelihood.

As the prior is normalised, $\mathrm{X}(\lambda = 0)$ is the surface with the highest possible likelihood, $\mathcal{L}_{max}$, whereas $\mathrm{X}(\lambda = 1)$ is the surface enclosed by the minimum likelihood contour $\mathcal{L}_{min}$. In the presence of a signal, the evidence integral will be dominated by a small region of prior space where the likelihood is highest.

The basic idea behind nested sampling is to estimate the evidence integral by a selecting a set of random points and evolving those towards regions of higher likelihood (smaller prior mass) in the prior volume until a stopping criterion is reached. Consider a set of

monotonically decreasing prior masses $(\mathrm{X}_1, \mathrm{X}_2, \mathrm{X}_3, ..., \mathrm{X}_n)$ that are obtained at the end of sampling with corresponding likelihood values $(\mathcal{L}_1, \mathcal{L}_2, \mathcal{L}_3, ..., \mathcal{L}_n)$. Then the evidence integral is approximated by the trapezium rule as:

$$\mathcal{E} = \sum_i \frac{1}{2} \left(\mathrm{X}_{i-1} - \mathrm{X}_{i+1}\right) \mathcal{L}_i \tag{1.47}$$

The nested sampling algorithm works as follows. Initially, a set of N "live points" are randomly sampled from the prior distribution, each with its likelihood. Then, the sample with the lowest likelihood is removed to be replaced by a sample with a higher likelihood. The evidence integral is computed at each iteration. The process is stopped until a stopping criterion is reached. Defining the weight assigned to each sample as $w_i = \mathrm{X}_i - \mathrm{X}_{i-1}$, the stopping criterion is reached when $\mathcal{L}_{max} w_i / \mathcal{E}_i > e^{-5}$, where $\mathcal{L}_{max}$ is the highest likelihood found by the sampler yet and $\mathcal{E}_i$ is the current evidence estimate.

To summarise, the nested sampling algorithm goes through these 4 phases [56]:

1. Draw a sample of N live points from the prior $p(\boldsymbol{\theta})$. Thus the set of live points $\in (\boldsymbol{\theta}_1, \boldsymbol{\theta}_2, \boldsymbol{\theta}_3, ..., \boldsymbol{\theta}_N)$ and compute the associated likelihood values.
2. Set $\mathcal{E}_0 = 0$, i = 0, log$(w_0) = 0$. Thus, the initial likelihood surface contains all the possible values of likelihood.
3. While $\mathcal{L}_{max} w_i / \mathcal{E}_i > e^{-5}$:
   - i = i + 1
   - $\mathcal{L}_{min}$ = min $(\{\mathcal{L}_\alpha\})$
   - log(w_i) = log$(w_{i-1}) - N^{-1}$
   - $\mathcal{E}_i = \mathcal{E}_{i-1} + \mathcal{L}_{min} w_i$
   - Replace $\boldsymbol{\theta}_{min}$ with a $\boldsymbol{\theta}$ drawn from remaining prior volume, i.e, $\boldsymbol{\theta} \sim p(\boldsymbol{\theta}, \mathcal{H})$: $\mathcal{L}(\boldsymbol{\theta}) > \mathcal{L}_{min}$
4. Compute the evidence integral.

As the nested sampling algorithm proceeds, the list of points used in approximating the evidence, their likelihood values and parameter vectors are stored. The samples for prior mass X_i are drawn from the prior volume enclosed by the corresponding likelihood contour. This means that the prior density of the samples within the volume is boosted by a fraction proportional to the prior mass at that iteration. If the nested sampling prior probability is given by $p(\boldsymbol{\theta}|NS)$, then,

$$p(\boldsymbol{\theta}|NS) = \frac{p(\boldsymbol{\theta}, \mathcal{H})}{\mathrm{X}_i}. \tag{1.48}$$

The posterior is $\propto$ Likelihood $\times$ Prior, Eq: 1.38. We can replace the prior in there with Eq: 1.48 to give,

$$p(\boldsymbol{\theta}_i|\boldsymbol{d},\mathcal{H}) \propto p(\boldsymbol{\theta}_i|NS)p(\boldsymbol{d}|\boldsymbol{\theta}_i,\mathcal{H})\mathrm{X}_i. \tag{1.49}$$

Thus, post-processing the output of nested sampling gives the joint posterior probability distribution from which the posteriors of individual parameters could be computed by marginalizing over the other parameters.

Chapter 2

Coalescing Black Hole Binary Waveforms

Any source of matter with a time varying quadrupole moment can generate gravitational waves (see Eq: 1.16). Binary (or trinary etc.) systems, supernovae, deformed neutron stars (or black holes) and early universe phase transitions are just some of the possible astrophysical sources [18]. In the sensitive frequency band of LIGO though, the strongest signals are expected to come from coalescing black-hole (BH) binary systems, binary neutron star (NS) systems and binary BH-NS systems. During the second observation run of LIGO (O2), the detectors were sensitive to a binary NS merger at a distance of up to 80 Mpc (LHO) and 100 Mpc (LLO) [8].

To infer the physical parameters of the GW source, waveform models are required that predict the GW strain for all possible configurations of all classes of sources. Solving Einsteins equations for sources that can generate GWs is analytically impossible due to the non-linear structure of those differential equations. There exist a gamut of numerical techniques to solve these equations, but all are computationally expensive and not feasible for parameter estimation techniques. So, various approximate models have been developed, which employ different methods of construction for different types of systems.

For a binary BH system, the waveform would depend on the mass-ratio (q) of the system, the individual spins of the black hole $(\vec{S_1}, \vec{S_2})$ [1] and the eccentricity of the orbit. For most cases, it can be shown that the eccentricity of the orbit would be radiated off as the system nears merger and the orbit would be quasi-circular [57], [58]. Although work on eccentric waveforms is ongoing and interesting (as presence or absence of eccentricity could help in inferring formation mechanisms), we will concentrate on quasi-circular binaries.

[1] No charge will be considered on the black hole. As it is, most black holes are expected to loose any charge in vacuum before the merger actually occurs

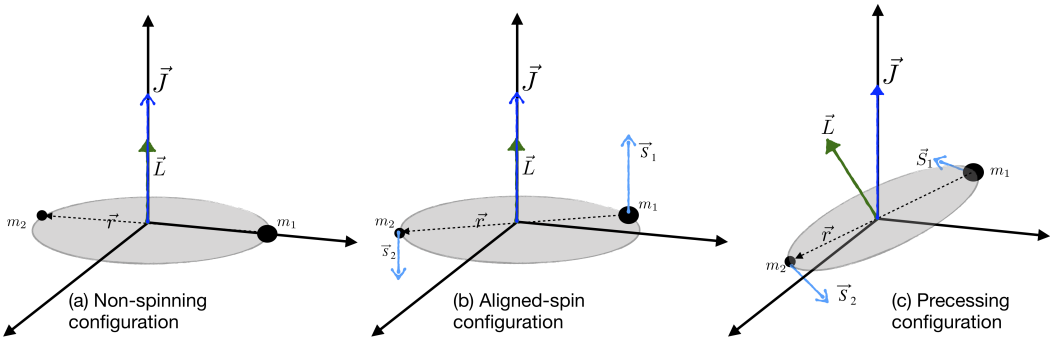

FIGURE 2.1: All three configurations of a coalescing binary system.

If a NS is present as one (or both) of the binary objects, it would start undergoing tidal deformations as it nears merger and these deformations would leave their imprint on the final waveform. The actual deformations and their imprint depend largely on the equation of state (EOS) of the NS [59]–[61](and references therein).

Binary black hole systems can be classified into three categories, depending on the direction (or presence) of spins.

- **Non-spinning systems:** As the name implies, these systems are where both of the BHs are non-spinning. The direction of the angular momentum vector($\hat{L}$) is unchanging in time and the orbital plane of such a system remains fixed. These systems have only two intrinsic parameters, i.e., the individual masses m_1 and m_2.
- **Aligned-spin systems:** In these configurations, both spins of the BHs are aligned (anti-aligned) to $\hat{L}$. Along with the mass parameters, the two spins add two extra dimensions to the intrinsic parameter space. The presence of spins (anti-)parallel to $\hat{L}$ (decreases) increases the total time to merger as compared to a corresponding non-spinning system. This is also called the orbital hangup effect [62].
- **Precessing systems:** These systems fall under all other possible spin configurations. When the spins are randomly oriented, the spins couple with orbital angular momentum and each other causing $\vec{L}$ to precess around the total angular momentum $\vec{J}$. This causes a wobbling of the orbital plane of the binary, which results in an overall modulation of the gravitational waveform. The intrinsic parameter space is 8 dimensional (2 mass and 6 spin) for precessing systems.

See Fig: 2.1 for the three configurations and Fig: 2.2 for how the waveforms differ for different configurations. Given a physical BBH system, the total mass ($M(M_\odot)$) acts as an overall

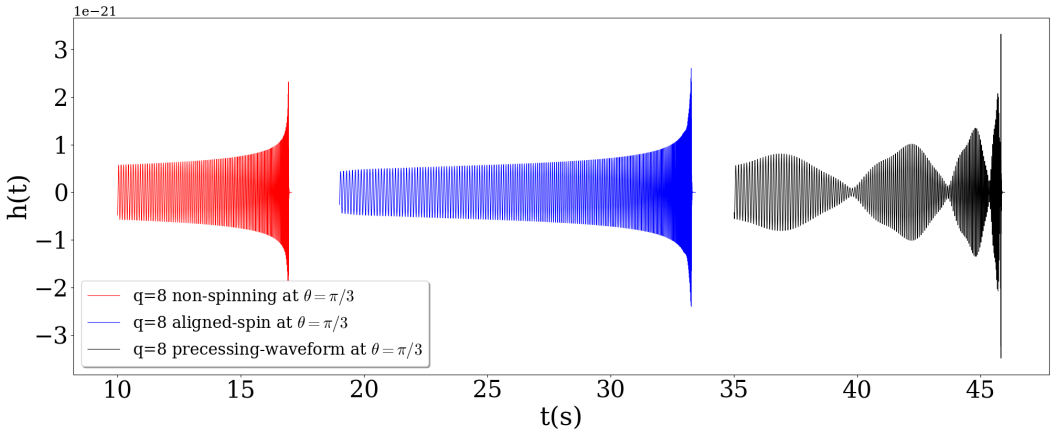

FIGURE 2.2: Representative time-domain waveforms from a non-spinning (red), aligned-spin (blue) and precessing (black) q=8, $90M_{\odot}$ system at 100MPc inclined at $\theta = 60^{o}$. The aligned spin waveform has $\vec{S_1} = \vec{S_2} = (0, 0, 0.9)$ and the precessing waveform has $\vec{S_1} = (0.8, 0.2, 0.5)$ and $\vec{S_2} = (0.8, 0.2, 0.)$. Notice the increased length of the aligned-spin waveform as compared to the non-spinning system (consequence of the orbital hang-up effect) and the extra modulations to the amplitude of the precessing system (consequence of the wobbling of the orbital place). These waveforms were created using the `IMRPhenomPv2` model [63].

scale and so, for waveform modelling, the intrinsic parameter space dimension reduces by one. For eg: for precessing systems, the intrinsic parameters would be defined by the mass ratio (q) and the six components of the spins.

GWs from a coalescing binary system can be split into three regions: the inspiral phase, merger phase and ringdown phase. During the inspiral phase, the masses are far away from each other and the characteristic velocity (v_c) of the system is small, i.e., $v_c << c$. For the inspiral phase, the black holes are considered as two point particles and the equations of motion are expanded beyond the leading Newtonian order in terms of the Post-Newtonian (PN) parameter $v/c << 1$. Equations of motion obtained in this way are called the PN equations and the corresponding waveforms the PN waveforms (see [64] for a review on PN theory and its applications in GW waveform modelling). The PN equations become less accurate when the system nears merger as $v/c \sim 1$.

Post merger, the final BH will be deformed and the deformities are radiated off until the BH settles down to a stationary Kerr solution. This signal can be modelled as a set of damped functions with frequencies as predicted from Teukolsky's equations [65]. These frequencies are called the Quasi-Normal mode (QNM) frequencies and the final signal is colloquially termed as the ringdown signal [66]. Using information from NR simulations, the binary parameters can be mapped to QNM frequencies and amplitudes leading to a model for the ringdown signal [67] [68] [69].

For the merger phase, different strategies have been developed. One is to rewrite the Hamiltonian of the two-body system as the Hamiltonian of an effective one-body system in deformed Kerr space-time [70] [71] and add corrections to the solution during the plunge-merger phase [72], [73]. These corrections are tuned to Numerical Relativity (NR) waveforms. Waveform models built using the effective one body (EOB) approach, and tuned to NR simulations are generally called `EOBNR` waveforms [74], [75]. Another strategy is to phenomenologically model the merger part (amplitude & phase), tune the model to NR waveforms and attach the merger waveform to the inspiral and ringdown [76]. We will discuss the phenomenological family of waveform models in more detail in Section 2.6 since these are the models used predominantly in this thesis. Both strategies have had success in modelling inspiral-merger-ringdown (IMR) waveforms for non-spinning, aligned-spin and precessing BH systems.

In general, a coalescing binary system is fully specified by a total of 15 parameters.

1. Two masses of the individual black holes, m_1 & m_2. Generally, the individual masses are re-parametrised in terms of chirp mass and symmetric mass-ratio $(\mathcal{M}, \eta)$ where $\mathcal{M}_c = M\eta^{3/5}$ and $\eta = \frac{m_1 m_2}{(m_1+m_2)^2}$.
2. Six spin parameters, $\vec{\chi}_i$ defined as $\vec{\chi}_i = \frac{\vec{S}_i}{m_i^2}$ where $\vec{S}_i$ and m_i are the angular momentum and mass of the ith black-hole and $0 \leq |\vec{\chi}| \leq 1$
3. Luminosity distance to the source d_L.
4. Right ascension α and declination δ of the source.
5. The inclination angle θ_{JN} between the total orbital angular momentum vector and line of sight.
6. The polarisation angle ψ that describes the relative orientation between the GW polarisation axes and detector axes.
7. The reference phase ϕ_c at the reference time t_c.

In this chapter, I will first describe the expected gravitational waveform from a BH binary in the quadrupole limit, Post-Newtonian (PN) waveforms, Numerical Relativity (NR), construction of PN-NR multimode Hybrid waveforms, and end with a description of the `IMRPhenom` family of waveforms.

2.1 Quadrupole radiation from quasi-circular binary

Consider a binary system of two objects of mass m_1 and m_2 going around each other in a circular orbit with frequency ω and separation R. For the solution below, we will not be considering higher-order effects like radiation reaction, etc. Choosing the reference frame as the centre of mass (COM) frame and the z-axis along $\hat{L}$ (so that the orbital plane is in the x-y plane), the co-ordinates [2] can be written as,

$$x(t) = R\cos(\omega t), \tag{2.1}$$

$$y(t) = R\sin(\omega t), \tag{2.2}$$

$$z(t) = 0. \tag{2.3}$$

In the COM frame, the mass moment (see Eq: 1.15) is,

$$M^{ij} = \frac{m_1 m_2}{m_1 + m_2} x^i x^j. \tag{2.4}$$

Defining $\frac{m_1 m_2}{m_1+m_2} = \mu$, the above equation gives the moment derivatives,

$$\ddot{M}_{11} = -2\mu R^2 \omega^2 \cos(2\omega t), \tag{2.5}$$

$$\ddot{M}_{12} = -2\mu R^2 \omega^2 \sin(2\omega t), \tag{2.6}$$

with $M_{11} = -M_{22}$. Plugging the above quantities in Eq: 1.17 and Eq: 1.18 gives the GW to be,

$$h_+ = \frac{4G}{c^4 r} \mu R^2 \omega^2 \cos(2\omega t), \tag{2.7}$$

$$h_\times = \frac{4G}{c^4 r} \mu R^2 \omega^2 \sin(2\omega t). \tag{2.8}$$

Now, from Keplers third law, $\omega = \sqrt{M/R^3}$, the velocity $v^2 = M/R$ and defining the symmetric mass ratio $\eta = m_1 m_2/(m_1+m_2)^2$ gives us the signal amplitude as $h_{+,\times} \propto M\eta v^2/r$.

2.2 PN waveforms

The calculation in Section 2.1 does not take into account the energy radiated from the binary system by gravitational waves. The energy flux reduces the orbital separation and increases the orbital frequency in time. This characteristic increase in frequency is why coalescing binary signals are also colloquially known as *chirp signals*. Previous studies have shown that for accurate parameter measurements, the template and signal waveform should not

[2] Disregarding any reference phase/time

de-phase by more than one cycle over the detection band [77]. Hence, it is important to accurately model the total accumulated phase of the coalescing binary.

In Post-Newtonian (PN) theory, the idea is to expand the equations of motion for two point particles in terms of the parameter $v/c << 1$ beyond the leading Newtonian order and include terms consistent in PN order to solve them.

The instantaneous frequency at time t $(\omega(t))$ is,

$$\omega(t) = \frac{\mathrm{d}\phi(t)}{\mathrm{d}t}. \tag{2.9}$$

Integrating this gives the phase to be,

$$\phi(t) = \int_{t_0}^{t} \omega(t')\mathrm{d}t' = \int_{\omega_i}^{\omega f} \frac{\omega}{\dot{\omega}}\mathrm{d}\omega. \tag{2.10}$$

Let the energy of the system be $\mathrm{E}(t)$ and the outgoing flux be $\mathcal{F}(t)$. These two quantities are related by the energy-balance equation,

$$\mathcal{F}(t) = -\frac{\mathrm{dE}(t)}{\mathrm{d}t}. \tag{2.11}$$

Defining the parameter $x = \left(\frac{GM\omega}{c^3}\right)^{2/3}$ as our PN parameter, we can rewrite Eq: 2.11 as [78],

$$\frac{\dot{\omega}}{\omega} = -\frac{3}{2x}\left(\frac{\mathrm{dE}(x)}{\mathrm{d}x}\right)^{-1}\mathcal{F}(x). \tag{2.12}$$

So, if we have the functional forms of $\mathcal{F}(x)$ and $\mathrm{E}(x)$, the term $\left(\frac{\mathrm{dE}(x)}{\mathrm{d}x}\right)^{-1}$ can be Taylor expanded in x, and Eq: 2.12 can be solved by keeping terms up to consistent PN order beyond the leading PN order.

As a demonstrative example, the energy and flux to 1PN for non-spinning binaries is [3],

$$E(x) = -\frac{\mu c^2 x}{2}\left(1 + x\left(-\frac{7}{4} + \frac{\eta}{4}\right)\right), \tag{2.13}$$

$$\mathcal{F}(x) = -\frac{32c^5}{5G}\eta^2 x^5\left(1 + x\left(-\frac{1247}{336} - \frac{35\eta}{12}\right)\right), \tag{2.14}$$

using which we get,

$$\frac{\dot{\omega}}{\omega^2} = \frac{96}{5}\eta x^{5/2}\left(1 + x\left(\frac{-743}{336} - \frac{11}{4}\eta\right)\right), \tag{2.15}$$

giving,

$$\phi(x) = \phi_0 - \frac{1}{32\eta}\left(x^{-5/2} + x^{-3/2}\left(\frac{3715}{1008} + \frac{55}{12}\eta\right)\right). \tag{2.16}$$

[3] See Eq: (6.4), (6.5), (8.3) and (8.4) of [78]

There are various strategies in which the above equations are expressed in terms of time (t) or velocity (v) and then the solutions are computed accordingly. Depending on how the solution is obtained, the PN waveform models are called `TaylorT1`, `TaylorT2`, `TaylorT4` [64], [79] etc. and are available in the `LALSimulation` package [53]. Studies of non-spinning binaries have shown that these different models agree with each other at 3.5PN and are good enough for detection purposes at low total masses (M$< 12M_{\odot}$) [80]. Comparisons between the PN models and numerical relativity waveforms show a very low amount of dephasing (within numerical uncertainty) and amplitude differences ($\lesssim$ 1% within the regime of PN validity) [81] [82].

Eq: 1.12 gives the expansion of the stress-energy tensor in the weak-field limit with the first term being identified as the dominant quadrupole moment. For accurate inspiral waveforms, the higher order terms need to be considered as well. Depending on the symmetry of those tensorial terms, they are classified as *radiative* mass-type $(\mathcal{U}_L)$ or current-type $(\mathcal{V}_L)$ moments (see [64] [83] [84] for more details). In this formalism, the GW strain as observed from direction $\hat{n}$ and distance R from the source, can be written as (up to any multipolar order l),

$$h_{ij}^{TT} = \frac{4G}{c^2 R}\Lambda_{ij,kl}^{TT}(\hat{n})\sum_{l=2}^{\infty}\frac{1}{c^l l!}\left\{\mathrm{N}_{L-2}\mathcal{U}_{klL-2}(t_r) - \frac{2l}{c(l+1)}\mathrm{N}_{aL-2}\epsilon_{ab(k}\mathcal{V}_{l)bL-2}(t_r)\right\}, \quad (2.17)$$

with t_r being the retarded time. In this notation, $L = i_1, i_2, \ldots, i_l$ is a multi-index of l multipolar spatial indices (not to be confused with gravitational wave mode l) $(1 \leq i_i \leq 3)$ with $L-1 \to i_1 \ldots i_{l-1}$; $\mathrm{N}_L = N_{i_1}, \ldots, N_{i_l}$ gives the product of l spatial vectors N_i and ϵ_{ijk} is the usual Levi-Civita antisymmetric symbol.

Gravitational waves, being a tensor field, can be decomposed into spin-weight -2 spherical harmonic basis $(Y_{lm}^{-2}(\theta,\phi))$. This allows us to write a gravitational waveform in terms of its spherical harmonic modes (or simply GW modes h_{lm}). Any gravitational wave strain $h(t)$ composed of plus (h_+) and cross $(h_\times)$ polarisations can be written as,

$$h(t,\theta,\phi) \equiv h_+(t,\theta,\phi) - ih_\times(t,\theta,\phi) = \sum_{l,-l\leq m\leq l} Y_{lm}^{-2}(\theta,\phi)h_{lm}(t). \quad (2.18)$$

In [85], the author relates the multipole moments of GW strain to mass and current radiative moments as,

$$h_{lm} = \frac{2G}{\sqrt{2}Rc^{l+2}}\left(\mathcal{U}_{lm}(t_r) - \frac{i}{c}\mathcal{V}_{lm}(t_r)\right), \quad (2.19)$$

where $\mathcal{U}_{lm}(t_r)$ and $\mathcal{V}_{lm}(t_r)$ are related to their symmetric trace-free components as given in Eq.(13) and Eq.(14) of [85]. This allows us a PN based method to obtain the higher-order multipole moments for GW strain in the inspiral regime.

For accurate PN waveforms, multiple different effects need to be considered, for example: radiation reaction, spin-orbit couplings, spin-spin couplings, tidal effects, eccentricity [86], [87], gravitational wave tails [88], [89], memory effects [90], [91] (and references therein) etc. Whereas effects of tidal deformation are applicable only when one of the binary object is a neutron star, all other effects arise naturally from either expanding the above PN expressions to higher orders (for eg: spin-spin coupling) or from inclusion of non-linearities in the PN equations (for eg: gravitational wave tails). Work is ongoing to obtain expressions to consistent higher PN orders, but the author will leave it for the reader for further reading on PN waveform formalism and current status (see [64]).

2.3 Numerical Relativity

The Post-Newtonian approximation is an accurate description of the orbital dynamics and waveform during the inspiral regime for a binary coalescence. As the system nears merger, $v/c \sim 1$, the PN approximation no longer remains valid. Where for the inspiral region (when $M\omega < 0.1$) the amplitude differences between NR and PN waveform (with amplitude corrections up to 3PN) are $\lesssim 1\%$, the errors $\gtrsim 4\%$ as the system nears merger (see Fig:21 of [81]). For high mass BBH systems observable by LIGO, most of the signal power will be contained in the merger part and so it is important to have accurate merger signals. The basic approach used to obtain NR waveforms is to decompose the full space-time manifold $\mathcal{M}$ into slices of 3 dimensional space-like hypersurfaces each defined at a particular time. Such a splitting of the full manifold into slices of hypersurfaces is called the 3+1 decomposition. See [92] for a complete treatment of NR.

In this formalism, Einstein's equations are split into constraint equations at each slice along with time evolution of the induced metric (γ_{ij}) and extrinsic curvature (K_{ij}). Solving the constraint equations on the zeroth hypersurface allows us to determine the initial data, and then the metric on all other hypersurfaces can be found by solving the evolution equations. The standard method of writing 3+1 decomposition evolution equations is in the Arnowitt-Deser-Misner (ADM) [93], [94] co-ordinate basis (see Eq: A.19), but these equations (see Eq: A.22 and Eq: A.23) are ill-posed and weakly hyperbolic leading to unstable solutions while solving numerically. I would like to refer the interested reader to Appendix:A or Chapter 2 of [92] for a more extensive treatment of the 3+1 decomposition.

The 3+1 constraint and evolution equations can be reformulated in terms of conformally rescaled variables $(\psi, \tilde{\gamma}_{ij}, \tilde{A}_{ij}, K)$ where ψ is the conformal factor and $(\tilde{\gamma}_{ij}, \tilde{A}_{ij}, K)$ are the rescaled intrinsic metric, trace-free part of K_{ij} and trace of the extrinsic curvature respectively. In this formulation, three extra connection functions, $\tilde{\Gamma}_i = -\partial_j \tilde{\gamma}^{ij}$, are introduced and with this, the evolution equations reduce to wave equations for the conformal metric coupled

to evolution of the $\tilde{\Gamma}_i$'s. The evolution equations reformulated in this way are strongly hyperbolic, which allows the numerical evolution to be robust. This way of writing the equations is called the *Baumgarte-Shapiro-Shibata-Nakamura* (BSSN) formulation ([95], [96] or Sect. 11.5 of [92]). The conformally related factors are,

$$\gamma_{ij} = \psi^4 \tilde{\gamma_{ij}} \quad A_{ij} = \psi^{-4} \tilde{A_{ij}} \quad K = \tilde{K} \text{ and } K_{ij} = A_{ij} + \frac{1}{3}\gamma_{ij}K. \tag{2.20}$$

The quadrature, $(\psi, \tilde{\gamma}_{ij}, \tilde{A}_{ij}, K)$ will provide us with all the required data on one time-slice.

Another major issue is dealing with the black-hole singularities. The Schwarzschild metric (in Schwarzschild co-ordinates) for a BH has a co-ordinate singularity at $R = 2M$ and a physical singularity at $R = 0$. There are two ways of dealing with the BH singularity; i) to remove the region of BH from the computational domain (BH excision method [97] [98] [99]) or ii) to conformally map the singularity to a wormhole or trumpet topology (BH moving puncture method) [100] [101] [102] [103].

2.3.1 Initial data for BBH systems

Appendix:A shows how Einstein's equations can be reformulated in the 3+1 decomposition formalism. To evolve the system, we need a set of initial conditions on the initial hypersurface Σ_0 and then we need to solve the Hamiltonian (Eq: A.16) and momentum (Eq: A.17) constraint equations to provide (γ_{ab}, K_{ab}). Multiple strategies for solving constraint equations to obtain the initial data and to find solutions of evolution equations have been developed, see [104] for a review on various methods of solving initial data.

In the transverse-traceless frame, under the assumption of conformal flatness ($\tilde{\gamma_{ij}} = \eta_{ij}$) and maximal slicing ($K = 0$), the momentum and Hamiltonian constraint equations get decoupled from each other in vacuum. Under this assumption, the momentum constraints can be solved analytically for black holes with linear momentum and spins, with numerical solutions for the Hamiltonian constraint. The data obtained via this approach is called the *Bowen-York* [105] data. (See Sec:3.2.1 of [104] and Sec:12.2.1 of [92] and references therein)

Geometry of space in the exterior of a non-spinning black-hole is given by the Schwarzschild metric. The line element is,

$$ds^2 = -f(r)\mathrm{d}t^2 + f(r)^{-1}\mathrm{d}r^2 + r^2\mathrm{d}\Omega^2 \quad \text{where,} \quad f(r) = 1 - \frac{2M}{r}. \tag{2.21}$$

As mentioned before, this metric has a co-ordinate singularity at $r = 2M$ and a physical singularity at $r = 0$. A co-ordinate transformation is then needed to remove the singularity from

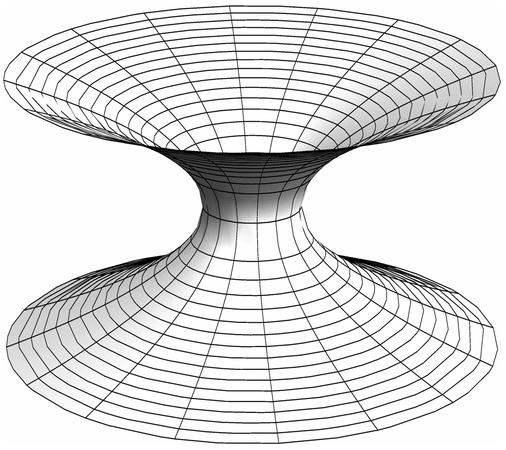

FIGURE 2.3: 2D embedding diagram of BH on the initial slice in wormhole puncture where the singularity is mapped to an asymptotically flat end [103].

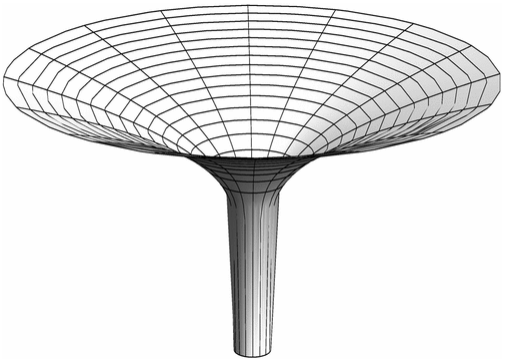

FIGURE 2.4: 2D embedding diagram of BH on the initial slice in the "trumpet" solution where the singularity at r=0 maps to a infinitely long cylinder of radius 3M/2 [103].

the evolution code. We can go to the *isotropic* co-ordinates where the physical singularity at $r = 0$ is mapped to another conformally flat sheet, which leads to a two sheet topology connected by a wormhole at $r = 2M$ (see Fig: 2.3). When this initial data is evolved using the "1+log" slicing for the lapse and Gamma-driver condition for shift function (see Fig: A.3 and Eq: A.18 for a explanation of the lapse and shift functions), the second conformally flat sheet settles to a infinitely long cylinder (or a "trumpet") of $R \sim 1.3M$ [106](see Fig: 2.4). In these co-ordinates, the lapse function is negative on the second sheet which can lead to instabilities during numerical evolution of the data. It has been found that using "trumpet" co-ordinates data leads to stable evolutions [103]. In these co-ordinates, the region around the physical singularity is converted into an infinitely long cylinder. For maximally sliced data ($K = 0$), this cylinder has a radius of $\sim$ 1.5 M [107].

In the evolution equations, the choice of shift (β^i) and lapse (α) functions are arbitrary, due to the gauge freedom of the problem. As given in [103], for trumpet solutions, the initial lapse and shift are,

$$\alpha = \sqrt{1 - \frac{2M}{R} + \frac{C^2}{R^4}}, \tag{2.22}$$

$$\beta^R = \frac{\alpha C}{R^2}, \tag{2.23}$$

where $C = 3\sqrt{3}M^2/4$ and $R \in [1.5M, \infty]$. The lapse function is then evolved with the "1+log" slicing condition and the shift function is evolved by the Gamma-driver condition [108],

$$(\partial_t - \beta^i \partial_i)\alpha = -2\alpha K, \tag{2.24}$$

$$\partial_t \beta^i = \frac{3}{4} B^i, \quad \partial_t B^i = \partial_t \tilde{\Gamma}^i - \eta B^i, \tag{2.25}$$

where η is a positive function of space and time [109].

2.3.2 BAM Code

Currently, there exist multiple codes that simulate the late stages of a BBH merger: i) the Bi-functional Adaptive Mesh (BAM) code [110], [108], ii) Spectral Einstein code (SpEC) [111], [112], iii) The Einstein Toolkit [113] to name a few. See [114] for a review of the current state of numerical relativity codes. Different groups use different codes for numerical simulations and public catalogues of the waveforms are available: SXS waveforms [115], RIT waveforms [116] and a database of NR waveforms from the LIGO-Virgo Collaboration (LVC) are available at [117]. In this thesis, I used the BAM code to generate NR waveforms, and so will briefly summarise its working. We also use the publicly available SXS waveform for constructing hybrid waveforms in Chapter- 5.

For the BAM code, wormhole puncture initial data are computed using the conformal transverse-traceless decomposition method. Initially, the background metric is assumed to be conformally flat with maximal slicing, i.e., $\gamma_{ij} \propto \eta_{ij}$ and $K = 0$. Under these conditions, the constraint equations are solved using a pseudo-spectral elliptic solver [118].

The initial data are then evolved using the BSSN formulation of the 3+1 decomposition equations with the χ-variant of the moving puncture method [100], [101]. The spatial derivatives are computed using sixth-order finite differencing [119] and the time integrals with a fourth order Runge-Kutta time integrator with Berger-Oliger type adaptive mesh refinement [120]. The lapse function is evolved with the "1+log" slicing condition and the shift vector with Γ-driver shift conditions [108].

In BAM, the computational domain consists of a set of moving and non-moving nested Cartesian grid boxes with different grid resolutions (to be specified by the user). So, there are $L_{max}+1$ (L=0,1,2,3...,L_{max}) boxes with N_l (user determined) grid points along each axis, the 0^{th} box being the level with coarsest resolution and the boxes at level L_{max} having the finest resolution.

For BAM, the *Newman-Penrose* formalism [121] is used for gravitational wave extraction where the Weyl scalar (Ψ_4) is computed at pre-specified extraction radii [108]. The scalar Ψ_4 is constructed from the 4D Riemann tensor by contracting under a complex null-tetrad basis. The code provides the Ψ_4 information and the gravitational wave strain $h(t)$ and Ψ_4 are related as,

$$\Psi_4(t) = \partial_t^2 \left(h_+(t) - ih_\times(t)\right). \tag{2.26}$$

Generally, $\Psi_4(t)$ is decomposed in the spin weight -2 spherical harmonic basis to give its modes ($\Psi_4^{lm}(t)$),

$$\Psi_4(t) = \sum_{l,m} Y_{lm}^{-2}(\theta,\phi)\Psi_4^{lm}(t). \tag{2.27}$$

2.4 Hybrid waveforms

Post-Newtonian (PN) waveforms are fast to compute and provide a very accurate model for the inspiral waveform, although the PN approximation becomes less accurate as the binary nears merger. Numerical Relativity (NR) waveforms are computationally very expensive, but give the most accurate waveforms for late-inspiral, merger and ringdown phases of a BBH coalescence. For detection and parameter-estimation purposes, we require waveform models that are fast and accurate and describe the full inspiral-merger-ringdown(IMR) of a BBH coalescence. In building such waveform models, we require a target set of accurate IMR waveforms and the best way to do that is to build *Hybrid waveforms* [4].

Assume we have PN and NR waveforms for the same system. If the NR waveform is long enough, there would be a common region where both the waveforms are accurate and agree with each other. The basic idea behind constructing hybrid waveforms is to *stitch* together the PN and NR waveforms within the valid region to get a full IMR waveform.

Suppose we have infinitely accurate PN and NR waveforms ($h^{PN}(t)$,$h^{NR}(t)$) for a given system. Let t_0 be a time in the region where the waveforms overlap. Then, the two waveforms *should* be the same up to an overall time and phase shift, i.e.,

$$h^{PN}(t_0) = h^{NR}(t_0+\tau)e^{i\phi_0}. \tag{2.28}$$

The frequency of the waveform, $\omega_i(t) = \mathrm{d}\phi_i(t)/\mathrm{d}t$ ($i = PN, NR$). Instead of choosing a reference time, we can choose a reference frequency ω_0 and given $t(\omega)$ for both, we can see τ would be,

$$\tau = t_{NR}(\omega_0) - t_{PN}(\omega_0), \tag{2.29}$$

with ,

$$\phi_0 = \frac{h^{PN}(t_{PN}(\omega_0))}{h^{NR}(t_{NR}(\omega_0))}. \tag{2.30}$$

2.4.1 Quadrupole hybridisation

Eq: 2.28 will not be perfectly valid for actual PN/NR waveforms as there will be both numerical inaccuracies during waveform computation and inaccuracies in the PN approximation.

[4] The description given in Section 2.4.1 and Section 2.4.2 closely follows the one in [122]

So, we need a way to find the *optimal* time and phase shift so that the two waveforms would match accurately over some interval. Suppose we wish to hybridise over the time interval $[t_0, t_0 + dt]$ where t_0 can be chosen arbitrarily or it could be the time at the reference frequency $t_{PN}(\omega_0) = t_0$. Define the quantity $\Delta(t_0, dt, \tau)$ as,

$$\Delta(t_0, dt, \tau) = \int_{t_0}^{t_0+dt} (\omega_{PN}(t) - \omega_{NR}(t-\tau))^2 \, \mathrm{d}t. \tag{2.31}$$

For a given set of (t_0, dt), the hybrdisation time shift (τ_0) would be the one that minimizes $\Delta(t_0, dt, \tau)$, i.e., $\tau_0 = \min_{\tau} \Delta(t_0, dt, \tau)$. Once we have τ_0, the phase shift (ϕ_0) could be defined as either $\phi_0 = \phi_{NR}(t_0 - \tau_0) - \phi_{PN}(t_0)$ or one that minimizes,

$$\Phi(\phi) = \int_{t_0}^{t_0+dt} (\phi_{NR}(t-\tau_0) - \phi_{PN}(t) + \phi)^2 \mathrm{d}t. \tag{2.32}$$

With these quantities, we can define the hybrid waveform as,

$$h_{hyb}(t) = \begin{cases} e^{i\phi_0} h_{PN}(t+\tau_0) & \text{if } t < t_0 - \tau_0 \\ w^-(t) e^{i\phi_0} h_{PN}(t+\tau_0) + w^+(t) h_{NR}(t) & \text{if } t_0 - \tau_0 < t < t_0 - \tau_0 + dt \\ h_{NR}(t) & \text{if } t_0 - \tau_0 + dt < t \end{cases} \tag{2.33}$$

where $w^{-,+}(t)$ are blending functions. The choice of the blending function is arbitrary. In [123] a cosine blending function is used, whereas in [122] a linear function was used. For this thesis, we use a Planck taper windowing function for blending the PN and NR waveforms. This procedure could be used to hybridise the (2,2) modes of PN/EOB and NR waveforms for any system. See Fig: 2.5 for a plot of the hybridized (2,2) mode waveform for a q=8 non-spinning system.

2.4.2 Multi-mode hybridisation

Eq: 2.18 gives the expansion of gravitational wave strain ($h(t, \theta, \phi)$) data into its spherical harmonic modes ($h_{lm}(t)$). Any PN or NR waveform is computed in a specific coordinate system, which are not the same in general. Two waveforms for the same system $h_a(t, \theta, \phi)$ and $h_b(t, \theta, \phi)$, computed in different co-ordinate systems, should be the same up to a overall time, phase and polarisation shift. For the (2,2) mode construction, the polarisation shift is not considered as it could be absorbed in the phase-shift, but the same idea does not carry forward to multi-mode hybrids. The phase of any h_{lm} mode would be $\sim m * \phi_{orb}(t)$ where $\phi_{orb}(t)$ is the orbital phase. Thus, a phase shift of ϕ_0 that would hybridize the (2,2) mode, would be $\sim \frac{m}{2}\phi_0$ for the (l,m) mode. The polarisation shift is required to align the

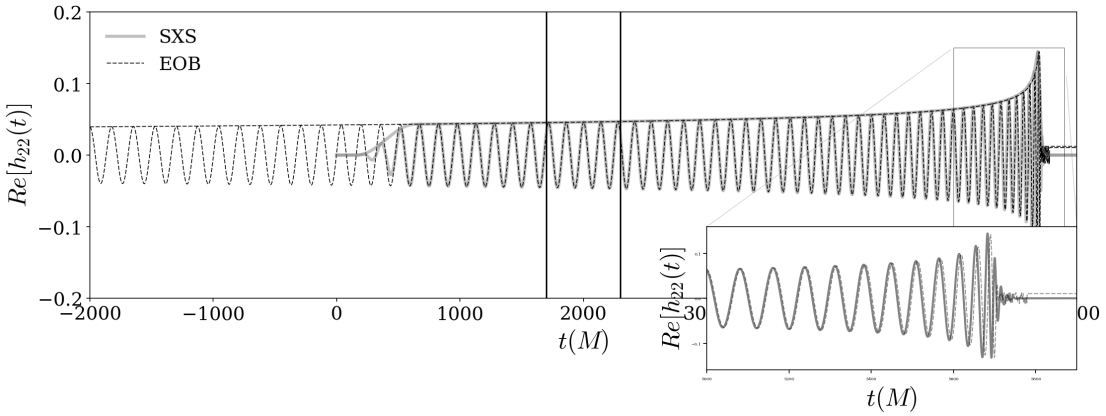

FIGURE 2.5: The plot shows the h_+ polarisation for a q=8 non-spinning system. The NR (SXS_BBH_0063 [116]) waveform is shown in grey and the inspiral waveform obtained from a Effective One Body (EOB) solver is shown with a black-dashed line. The region of hybridisation is shown by the two vertical black-lines. In the zoomed-in box, observe the de-phasing between the NR/EOB waveform and different post-merger signal morphology.

$(h_+, h_\times)$ axes of the two waveforms. Thus,

$$h_a(t, \theta, \phi) = e^{i\psi_0} h_b(t + \tau, \theta, \phi + \phi_0), \tag{2.34}$$

giving the individual modes,

$$h^a_{lm}(t) = e^{i(\psi_0 + m\phi_0)} h^b_{lm}(t + \tau). \tag{2.35}$$

So, to construct multi-mode hybrids, we require three quantities; (τ, ϕ_0, ψ_0). Any mode h_{lm} is related to h_{l-m} by $h_{lm}(t) = (-1)^l h^*_{l,-m}(t)$, which implies $\psi_0 \in \{0, \pi\}$.

For the time shift, we can use the same procedure as for the (2,2) mode and find the τ that minimizes Eq: 2.31. Once τ_0 is determined, we need to find ϕ_0 and ψ_0. Define $\Delta\phi_{lm}$ as,

$$\Delta\phi_{lm} = \phi^{NR}_{lm}(t_0 - \tau_0) - \phi^{PN}_{lm}(t_0). \tag{2.36}$$

Under the condition of Eq: 2.35, for the (2,2) mode, the quantities $(\psi_0, \phi_0, \Delta\phi_{22})$ follow,

$$\psi_0 + 2\phi_0 + \Delta\phi_{22} = 0 \text{ mod } 2\pi, \tag{2.37}$$

giving,

$$\phi_0 = -\frac{(\Delta\phi_{22} + \psi_0)}{2} \text{ mod } \pi. \tag{2.38}$$

Now, we have already argued for $\psi_0 \in (0, \pi)$; and with that condition for polarisation, we get 4 possible solutions,

$$(\psi_0, \phi_0) = \left(\kappa\pi, -\frac{\Delta\phi_{22}}{2} + (\kappa' - \kappa/2)\,\pi \text{ mod } 2\pi\right), \tag{2.39}$$

with $\kappa \in (0, 1)$ and $\kappa' \in (0, 1)$. So, we need to break the degeneracy of the possible solutions for a given set of modes. This can be done by using the modes other than the dominant quadrupole. If we have a non-zero mode h_{l^*,m^*} with $(l^*, m^*) \neq (2, 2)$, we can re-write Eq: 2.37 for this mode as,

$$\psi_0 + m^*\phi_0 + \Delta\phi_{l^*m^*} = 0 \text{ mod } 2\pi. \tag{2.40}$$

Using this information, we can obtain the phase and polarisation shifts for multi-mode hybrids.

2.5 Precessing systems

In the introductory section of this chapter I have mentioned the differences between non-spinning, aligned-spin and precessing BBH systems and Fig: 2.2 highlights the morphology of precessing waveforms compared to the other two. This section will discuss precessing BBH systems in more detail.

For BBH systems with no spins or with spins aligned along the direction of the orbital angular momentum ($\vec{L}$), $\dot{\hat{L}} = 0$, so the orbital plane of the binary is unchanging. When the spins have some component perpendicular to $\vec{L}$, $\dot{\hat{L}} \neq 0$ and $\vec{L}$ starts precessing around the total angular momentum ($\vec{J}$) and the orbital plane precesses. This precessional motion adds extra modulation to the phase and amplitude of the gravitational waveform (see Fig: 2.2). Throughout the coalescence, the spins and angular momentum vector precess around the total angular momentum $\vec{J}$, which changes slowly over the whole coalescence timescale. This type of precession is called *simple precession*. For simple precession, $\vec{J}$ is a approximate constant of motion.

For some systems though, it is possible that $|\vec{L}| \sim |\vec{S}|$ and $\hat{L} \sim -\hat{S}$. During inspiral, the spins change slowly, but $|\dot{L}| < 0$ due to radiation of the angular momentum. As $\vec{L} \sim -\vec{S}$, $|\vec{J}|$ is small and small changes in $|\vec{L}|$ during the inspiral strongly affect the evolution of $\vec{J}$. For such cases, $\vec{J}$ can cross the x-y plane (see Fig: 2.6). This type of precession is called *transitional precession* [125], [126]. Systems that could undergo transitional precession must have finely tuned parameters, so that $\vec{J}$ can flip across the orbital plane, and it would be a rare occurrence for an astrophysical system within the detectors sensitivity band to

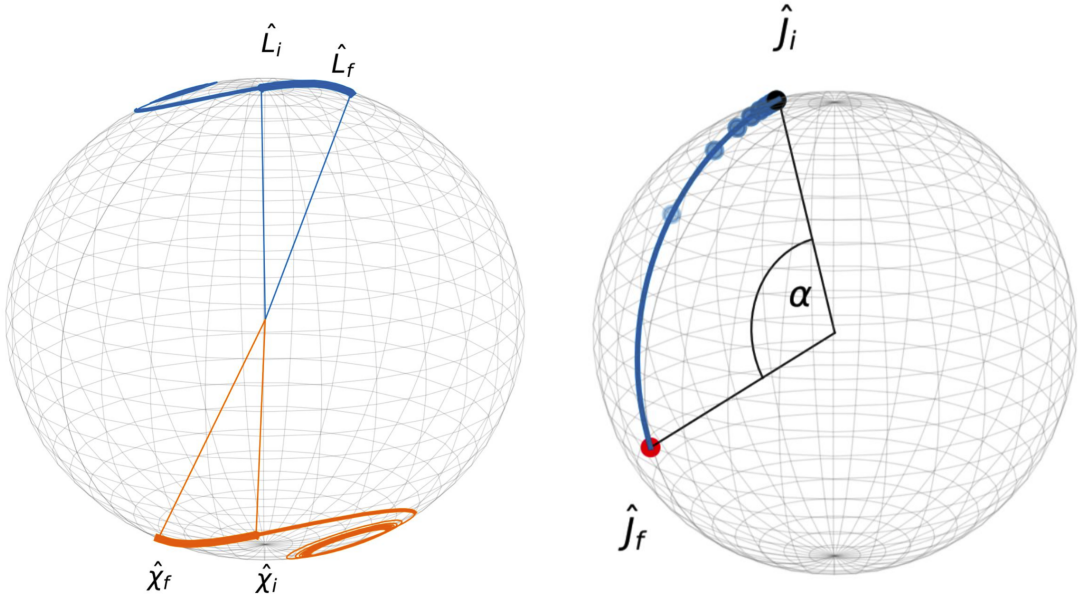

FIGURE 2.6: The left plot shows the evolution of $\vec{L}$ and $\vec{\chi}$ and the right plot shows the evolution of $\vec{J}$ for a system undergoing transitional precession. Image used for reference purpose only from [124].

have such parameters [126]. In this thesis we will not be dealing with transitional precession and so will end the discussion here.

During inspiral, precessing BBH dynamics have two intrinsic (but largely different) time scales, the time scale of one precession cycle (t_{prec}) and the time scale of one orbit (t_{orb}) with $t_{prec} \gg t_{orb}$ [5]. This allows us to define a frequency associated with precessional motion (ω_{prec}) along with the orbital frequency (ω_{orb}) for the system. From Eq: 2.10, we understand the phase of the waveform to be the integrated frequency over some time period. For precessing systems, the phase gets a contribution from ω_{prec} along with ω_{orb}, i.e.,

$$\phi_{prec}(t) = \int_{t_0}^{t} (\omega_{orb}(t') + \omega_{prec}(t'))\mathrm{d}t'. \tag{2.41}$$

From dynamical considerations, in [127] the precessing phase is shown to be,

$$\phi_{prec}(t) = \int_{t_0}^{t} (\omega_{orb}(t') - \cos(\iota(t'))\dot{\alpha}(t'))\mathrm{d}t', \tag{2.42}$$

where the angles α and ι define the instantaneous position of $\vec{L}$ w.r.t $\vec{J}$ (see Fig: 2.7).

[5] Note that there is also the radiation reaction time-scale, but it is not needed for the discussion here.

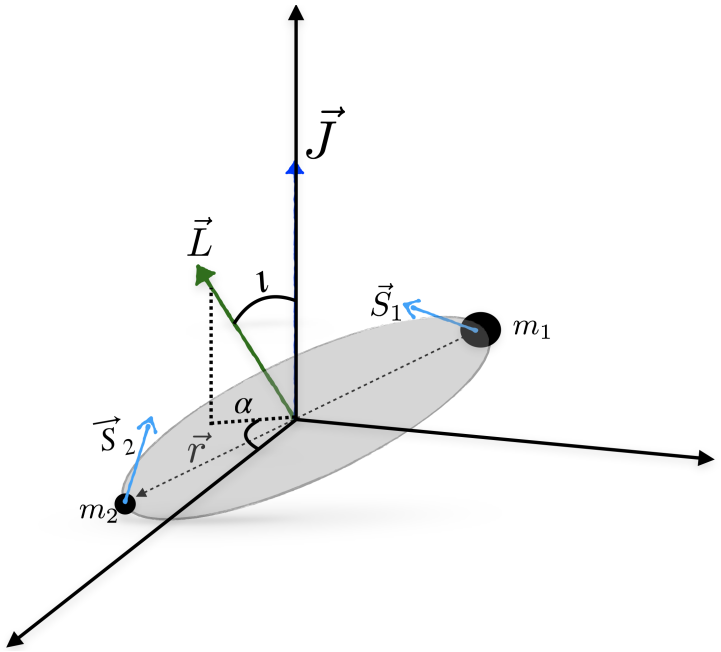

FIGURE 2.7: Generic configuration of a precessing binary black hole system with the total angular momentum $\vec{J}$ aligned along $\hat{z}$. The angle ι and α define the instantaneous position of $\vec{L}$ with respect to $\vec{J}$.

The evolution equation of spins averaged over one orbit (up to 3PN) is shown to be in [128](and references therein),

$$\dot{\vec{S}}_1 = \left\{\eta\left(2+\frac{3}{2}q\right) - \frac{3v}{2}\left[(q\vec{S}_1+\vec{S}_2)\cdot\hat{L}\right]\right\} v^5\left(\hat{L}\times\vec{S}_1\right) + \frac{v^6}{2}\vec{S}_2\times\vec{S}_1 + \mathcal{O}(v^7), \quad (2.43)$$

$$\dot{\vec{S}}_2 = \left\{\eta\left(2+\frac{3}{2}q\right) - \frac{3v}{2}\left[(\vec{S}_1+\frac{1}{q}\vec{S}_2)\cdot\hat{L}\right]\right\} v^5\left(\hat{L}\times\vec{S}_2\right) + \frac{v^6}{2}\vec{S}_1\times\vec{S}_2 + \mathcal{O}(v^7), \quad (2.44)$$

and

$$\dot{\hat{L}} = -\frac{v}{\eta}\left(\dot{\vec{S}}_1+\dot{\vec{S}}_2\right) + \mathcal{O}(v^7), \quad (2.45)$$

where $q = m_2/m_1 < 1$, $\eta = m_1m_2/M^2$, $v \equiv (M\omega)^{1/3}$ is the PN expansion parameter and ω is the orbital angular frequency of the system in a frame that is fixed to the orbital plane.

Here, note that Eq: 2.45 gives the evolution of the *direction* of $\vec{L}$. The evolution of the angular momentum magnitude is governed by the radiation reaction effects up to the known PN order [129](and references therein). From Eq: 2.43 and Eq: 2.44, we can see that the evolution of spins is driven by the spin-orbit couplings at 2.5PN order and by spin-spin couplings at 3PN. From the fact that $t_{prec} \gg t_{orb}$ and the arguments above, for inspiral dynamics it is possible to decouple the radiation reaction effects and precession effects from spin-orbit and spin-spin couplings.

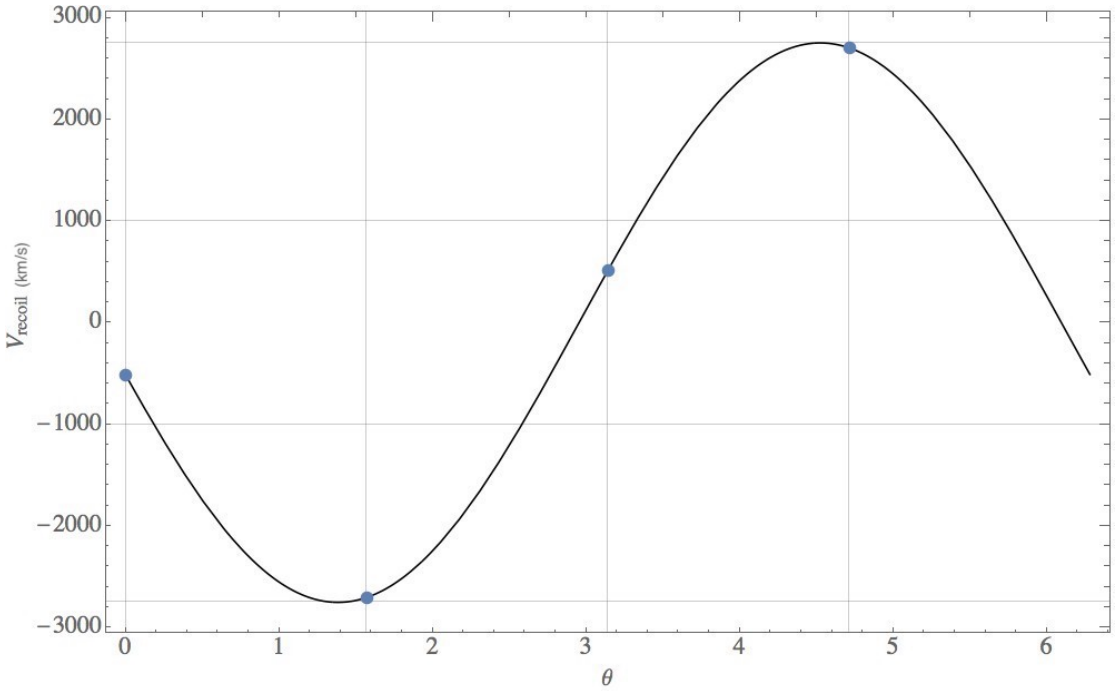

FIGURE 2.8: Recoil velocities of equal mass systems with the spins given by $\vec{S}_1(\theta) = 0.8[\sin(\theta), \cos(\theta), 0]$ and $\vec{S}_2(\theta) = -0.8[\sin(\theta), \cos(\theta), 0]$. The x-axis shows the angle θ with the resulting recoil velocity V_{recoil} plotted on the y-axis. The simulations used here are given in Tab: 4.1.

In [127] the gravitational wave polarisations have been computed up to 1.5PN for radiation reaction effects and 1.5PN for spin-orbit interactions with the strain given as,

$$h_{+,\times} = \frac{2M\eta v^2}{D_L}\left[H^{(0)}_{+,\times} + H^{(1/2)}_{+,\times} + H^{(1)}_{+,\times} + H^{(3/2)}_{+,\times} + H^{(1/2,SO)}_{+,\times} + H^{(1,SO)}_{+,\times} + H^{(3/2,SO)}_{+,\times}\right]. \tag{2.46}$$

See Eq:(3.16a)-(3.17g) and Eq:(4.17a)-(4.17r) of [127] for functional forms of $H^i_{+,\times}$ and resulting gravitational mode (h_{lm}). In [128], the authors presented closed-form analytic expressions for the inspiral phase of precessing BBH coalescence for generic masses, spin magnitudes and spin orientations. The authors provided analytic solutions of the precession equations including the radiation reaction effects to precessional motion using a *multiple scale analysis* technique where the leading order contribution from precession is averaged over the precessional time scale and then integrated over the radiation time scale with the higher-order terms acting as corrections to the leading order effects. This two spin model for the precession inspiral was then used towards building an improved precession phenomenological model, `IMRPhenomPv3` in [130].

The orbital plane of non-spinning and aligned-spin binaries remains steady during coalescence. If we define that plane as the x-y plane and decompose the waveform in the spin -2 weighted spherical harmonic basis for that co-ordinate system, the waveform modes $h_{l,m}$

and $h_{l,-m}$ are related as,

$$h_{lm} = (-1)^l h^*_{l,-m}, \tag{2.47}$$

with the phase of $h_{lm} \propto e^{-im\phi}$ during inspiral. Eq: 2.47 implies that the gravitational radiation is equal along $+\hat{z}$ and $-\hat{z}$ axes. The above relationships do not hold for precessing binaries due to the wobbling of the orbital plane. This introduces an inherent *asymmetry* in the precessional waveform modes. As shown in [131], to leading PN order, the relative amplitude difference between the (2,2) and (2,-2) modes of a precessing binary is,

$$\frac{|h^{2,2}| - |h^{2,-2}|}{|h^{2,2}| + |h^{2,-2}|} \approx -v^2 \frac{\vec{\Sigma} \cdot \hat{\lambda}}{2M^2}, \tag{2.48}$$

where $\vec{\Sigma} = M(M_2\vec{\chi}_2 - M_1\vec{\chi}_1)$ is a mass-weighted spin vector and $\hat{\lambda}$ is a unit vector in the orbital plane that is perpendicular to the separation vector. So, the gravitational radiation is different along the $+\hat{z}$ and $-\hat{z}$ axes and the radiated energy will be beamed along a particular direction. Due to the anisotropic gravitational wave emission, the final remanent black hole receives a kick away from the original centre of mass of the system [132], [133], [134].

Does this mean that systems for which Eq: 2.47 is valid receive no recoil? Eq: 2.47 indicates a symmetry of the system about the x-y plane when $\hat{L} \parallel \hat{z}$. This symmetry between the modes will not hold for arbitrary choice of $\hat{z}$ other than for equal mass non-spinning systems. In Chapter: 4 we will discuss a frame-independent way of characterising the mode asymmetry. Any system with unequal masses or non-zero spins will have some recoil velocity. Non spinning black holes with unequal masses can have recoil velocities up to ~ 175 km s^{-1} [135] and for generic aligned spins, the recoil velocities are found to go up to ~ 450 km s^{-1} [136], [137].

For special cases, the recoil velocity can be $\sim \mathcal{O}(10^3)$ km s^{-1} [138], [139], [140]. These *superkick* configurations are systems with equal masses and equal but opposite in-plane spins so that the total spin vanishes, $\vec{S} = \vec{S}_1 + \vec{S}_2 = 0$. For the study in Chapter: 4, we performed a series of NR runs for the superkick configurations (see Tab: 4.1), the recoil velocities of which are shown in Fig: 2.8. In [138] [141], the authors found that the recoil velocities can go up to ~ 4000 km s^{-1} for maximally spinning superkick configurations.

The centre of mass velocity v_{CM} computed from NR simulations will be independent of the total mass of the system. The velocity along direction x^i will be,

$$v^i_{CM} = \frac{\mathrm{d}x^i}{dt} = -\frac{1}{M}\int \mathrm{d}t \frac{\mathrm{d}P^i_{GW}}{\mathrm{d}t}, \tag{2.49}$$

where $\mathrm{d}P^i_{GW}/\mathrm{d}t$ gives the momentum radiated along x^i.

In [142], the authors found an active galactic nucleus (AGN) offset by $\sim$ 11kpc from the centre of the host galaxy moving at a velocity of $\sim$ 2100 km/s and spectroscopic data indicates that this galaxy is the result of a galaxy merger. So, this supermassive black-hole (with mass of $3 \times 10^9 M_\odot$) is possibly a remnant of the merger of the two galactic centres which received a large recoil due from GW emission. Chapter: 4 of this work will be devoted to exploring the effects of in-plane spin directions on precessional GWs, mode-asymmetries, super-kick simulations and their effects on detectability.

2.6 IMRPhenom waveforms

Waveform models describing the inspiral-merger and ringdown (IMR) phases of a BBH coalescence are important for GW searches and for parameter estimation routines with the effectualness of the searches and faithfulness of PE depending on the accuracy of the waveform models. Currently, two of the most common strategies employed to build IMR waveform models are, i) The Effective One Body (EOB) formalism, which leads to the waveform models termed `SEOBNRv4` [75], `SEOBNRv4HM` [143], `SEOBNRv3` [144] etc.; ii) The phenomenological approach that results in the aligned-spin waveform models `IMRPhenomD` [145], `IMRPhenomHM` [146] and precessing waveform models `IMRPhenomPv2` [147], `IMRPhenomPv3` [130]. As we will be using the waveforms from `IMRPhenom` family in this thesis, we will describe the relevant models in some detail in this section.

The basic idea behind the phenomenological approach of waveform model building is to use the information regarding the late-inspiral, merger and ringdown waveforms for a range of systems obtained from NR simulations and then polynomial functions are fitted to that data, with the coefficients of the polynomial fit tuned to the NR simulations across the relevant parameter space. This idea was used to build the first phenomenological waveform model for non-spinning systems `IMRPhenomA` [76], which is calibrated to q $\in (1, 4)$ for NR simulations. A waveform model for aligned-spin BBH systems called `IMRPhenomB` was constructed in [148] and was made more accurate for the model `IMRPhenomC` in [149].

In this section, we will describe i) the most recent aligned-spin waveform model `IMRPhenomD` [145] (Section 2.6.1), ii) Waveform model for precessing systems `IMRPhenomPv2` [147] (Section 2.6.2) and iii) a multi-mode waveform model for aligned-spin systems `IMRPhenomHM` [146] (Section 2.6.3).

2.6.1 IMRPhenomD Waveform

`IMRPhenomD` [145] is a phenomenological waveform model for aligned-spin systems that has been calibrated to SXS and BAM NR waveforms for $1 \leq q \leq 18$ and for spins $|a/m| \sim 0.85$ (0.98 for $q = 1$). Within the calibration region, the model shows mismatches of less than 1%.

As mentioned earlier, a BBH system can be described completely by its individual masses (m_1, m_2) and the individual spins ($\vec{S}_1, \vec{S}_2$). For gravitational waves, the mass parameters are reparametrised to the symmetric mass ratio $\eta = m_1 m_2/M^2$ and the chirp mass $\mathcal{M}_c = M\eta^{3/5}$, where $M = m_1 + m_2$ is the total mass of the binary. In the frequency domain, at the leading order, the inspiral amplitude is $\propto \mathcal{M}_c^{5/6}$ and the phase is $\propto 1/(\eta M^{5/3}) \equiv 1/(\mathcal{M}_c^{5/3})$. Due to the leading order dependency of phase on $\mathcal{M}_c$, it is the best measured parameter for GWs of low-mass systems [150], [151].

The spins are parallel to $\vec{L}$ for aligned spin systems and these systems can be completely described by $\mathcal{M}_c, \eta, \chi_1$ and χ_2, where χ_i are the dimensionless spin parameters defined as,

$$\chi_i = \frac{\vec{S}_i \cdot \hat{L}_i}{m_i^2}. \tag{2.50}$$

By construction, $\chi_i \in [-1, 1]$. In aligned-spin phenomenological models, the spin dependence is characterized by one effective spin parameter χ_{eff}. For `IMRPhenomB` and `IMRPhenomC`, the effective spin parameter is defined as $\chi_{eff} = (m_1\chi_1 + m_2\chi_2)/(m_1 + m_2)$. On the other hand, the spin parameter for `IMRPhenomD` is defined as,

$$\hat{\chi} = \frac{\chi_{PN}}{1 - 76\eta/113}, \tag{2.51}$$

where χ_{PN} is the leading order spin dependence in the PN waveform phase([152], [77], [153]),

$$\chi_{PN} = \chi_{eff} - \frac{38\eta}{113}(\chi_1 + \chi_2). \tag{2.52}$$

In Eq: 2.51, χ_{PN} is scaled by the denominator so that $\hat{\chi} \in [-1, 1]$ for all mass-ratios. For the final BH, the spins are parameterized by the combination $S_1 + S_2$ [69].

During the construction of this model, as set of hybrid EOB-NR waveforms are produced, which are then used for calibrating the amplitude and phase model ansatz. For the model construction, the waveform from BBH coalescence is split into three regions, the amplitude and phase for each region is modelled independently (with continuity restrictions) and the parameters of the model are then fit to NR data (see Fig: 2.9). The target waveform is split as:

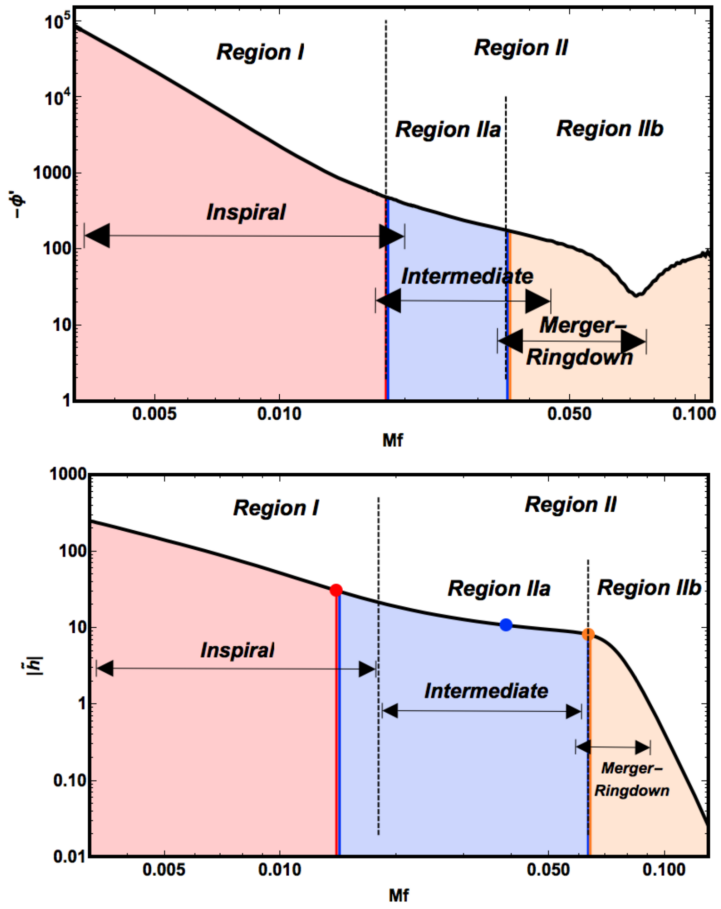

FIGURE 2.9: This plot shows the three regions defined for modelling of `IMRPhenomD` waveform. The top row shows the phase derivative $(\phi'(f))$ with the amplitude $(|h(f)|)$ in the bottom row. The dashed black lines show the starting frequency of the intermediate region, $Mf = 0.018$. Region II is split separately for the phase and amplitude to model the different morphologies seen in those regions. For eg: the dip in the phase derivative at $Mf \sim 0.07$ vs the Lorentzian behaviour of amplitude from $Mf \sim 0.065$. See text for further information of how the regions are defined. Figure from [145] for illustration purposes only.

- Region I : This region consists of the inspiral part of the waveform and lasts up to $Mf = 0.018$. Region I ends at $Mf = 0.018$ as this is the lowest common starting frequency of the NR waveforms used.

- Region IIa : This is the intermediate region between the inspiral and merger-ringdown phases. For modelling, Region IIa is defined separately for amplitude and phase construction. Defining f_{RD} as the ringdown frequency of the system, for phase this region is where $Mf \in [0.017, 0.75 f_{RD}]$ and for the amplitude, it is defined as the region where $Mf \in [0.018, 1/1.15 f_{RD}]$.

- Region IIb: As with Region IIa, the regions used to fit the amplitude and phase ansatz are defined separately, and model the merger-ringdown part of binary coalescence.

For the phase, Region IIb is where $Mf \in [0.45 f_{RD}, 1.15 f_{RD}]$ and for the amplitude, it is defined as the region where $Mf \in [1/1.15 f_{RD}, 1.2 f_{RD}]$.

Region II is defined separately for amplitude and phase modelling due to the different frequencies at which the amplitude or phase morphologies show changes. See Sec: VB and VC of [145] for more details of the model construction.

Defining a step function as,

$$\theta(f - f_0) = \begin{cases} -1, & f < f_0 \\ 1, & f \geq f_0, \end{cases} \tag{2.53}$$

and,

$$\theta^{\pm}_{f_0} = \frac{1}{2}[1 \pm \theta(f - f_0)], \tag{2.54}$$

the full IMR phase is given as,

$$\Phi_{IMR}(f) = \phi_{Ins}\theta^{-}_{f_1} + \theta^{+}_{f_1}\phi_{Inter}\theta^{-}_{f_2} + \theta^{+}_{f_2}\phi_{MR}(f), \tag{2.55}$$

where $f_1 = 0.018$ and $f_2 = 0.5 f_{RD}$ are the transition frequency for the phase. See Eq: (28), Eq: (16) and Eq: (14) of [145] for the functional forms of ϕ_{Ins}, ϕ_{Inter} and ϕ_{MR} respectively. The full IMR amplitude is given as,

$$A_{IMR}(f) = A_{Ins}\theta^{-}_{f_1} + \theta^{+}_{f_1}A_{Inter}\theta^{-}_{f_2} + \theta^{+}_{f_2}A_{MR}(f), \tag{2.56}$$

for which $f_1 = 0.014$ and $f_2 = f_{peak}$ are the transition frequency for the amplitude. The quantity f_{peak} is defined as,

$$f_{peak} = \left| f_{RD} + \frac{f_{\text{damp}}\gamma_3\left(\sqrt{1-\gamma_2^2} - 1\right)}{\gamma_2} \right|. \tag{2.57}$$

where f_{damp}, γ_2 and γ_3 are defined in the ansatz for the amplitude merger-ringdown phase (see Eq:19 of [145]). See Eq: (30), Eq: (21) and Eq: (19) of [145] for the functional forms of A_{Ins}, A_{Inter} and A_{MR} respectively. See [69] and [145] for further information on the construction and validation of the `IMRPhenomD` waveform model. Although the spins in `IMRPhenomD` are parameterized by one effective spin value, the inspiral parts of the model (A_{Ins}, ϕ_{Ins}) gets contribution from two-spin effects and `IMRPhenomD` has been found to accurately model two spin systems [154].

2.6.2 IMRPhenomPv2 Waveform

As previously described, the orbital plane of a binary black hole system with generic spins precesses about the total angular momentum vector. This precessional motion leaves its imprint as modulations to the amplitude and phase of the GW signal with the time scale of precession (which is larger than the orbital time scale). The sub-dominant modes (l = 2, m = $\pm$ 1, 0) for precessing systems are typically strong. A frame in which the quadrupole mode ($l = |m| = 2$) is maximised (the $|m| = 1$ modes are ~ 0) is the one that closely tracks the motion of orbital angular momentum $\vec{L}$ [125], [155], [156]. In this frame, the precessing quadrupole (2,$\pm$ 2) mode can be approximated by the quadrupole mode of the corresponding aligned spin system, i.e., the same system with the in-plane spins set to zero. This frame is called either the *"co-precessing"* frame or Quadrupole-Aligned (QA) frame. In the QA frame, the seven-dimensional intrinsic parameter space of precessing binaries $(q, \vec{S}_1, \vec{S}_2)$ can be mapped to aligned-spin waveforms described by q and χ_{eff}.

The motion of the QA frame with respect to the source frame is described by the three Euler angles $(\gamma(t), \beta(t), \epsilon(t))$, which in turn depend on the dynamics of the system. Two of the Euler angles describing the co-precessing frame, $(\gamma(t), \beta(t))$ can be approximated to be the polar angles (α, ι) of $\vec{L}$, see Fig: 2.7 for details. The third Euler angle gives an over-all rotation around the z-axis after the rotations with $(\gamma(t), \beta(t))$ are done, without which, there could remain unphysical modulations in the modes in the co-precessing frame. The angular momentum $\vec{L}$ will be along the z-axis in this frame. The angle $\epsilon(t)$ is [157],

$$\epsilon(t) = -\int \dot{\gamma}(t')\cos(\beta(t'))\mathrm{d}t'. \tag{2.58}$$

Although the choice of $\epsilon(t)$ can be arbitrary, a physical motivation behind defining the angle this way can be seen from Eq: 2.42 (Note that : $\beta \leftrightarrow \iota$ and $\gamma \leftrightarrow \alpha$).

Once we have the dominant (2,2) modes of the aligned-spin waveform in the QA frame, the time domain precessing waveform can be obtained by "twisting-up" the former. If the l=2 modes of the non-precessing waveform are given by $h_{2m'}(t)$, then the l=2 modes of the precessing system are,

$$h^P_{2m}(t) = e^{-im\alpha(t)} \sum_{m'} e^{im'\epsilon(t)} d^2_{mm'}(-\iota(t)) h_{2m'}(t), \tag{2.59}$$

where d^l_{mn} are the Wigner d-matrices [158], [159].

For a given mass-ratio, the inspiral-rate of the binary is largely dictated by the components of spin parallel to $\hat{L}$ ($\vec{S}^i_{\parallel}$) with the precession of the system driven by the in-plane spin components, i.e., components of spin perpendicular to $\hat{L}$; $\vec{S}_{1\perp}, \vec{S}_{2\perp}$. In Schmidt et al. [63],

the authors combined the in-plane spin components to define an effective spin precession parameter χ_p that can capture the precession dynamics. I would refer the interested reader to [63] for further discussions on motivation behind the choice of χ_p and its validity as a parameter capturing precession effects. χ_p is defined as,

$$\chi_p = \frac{S_p}{m_2^2} \equiv \max\left(A_1 S_{1\perp}, A_2 S_{2\perp}\right), \tag{2.60}$$

where $A_1 = 2 + \frac{3m_2}{2m_1}$ and $A_2 = 2 + \frac{3m_1}{2m_2}$. Here, it is assumed that $m_2 > m_1$. The precession spin-parameter χ_p is assigned to the larger black-hole. The effective spin-parameters χ_{eff} and χ_p map to a large number of physical spin configurations. The resulting degeneracies indicate the difficulty of measuring all spin components in a GW observation. Thus, the 6 dimensional spin vector space is mapped to the two dimensional space of effective spin parameters, via,

$$\vec{\chi}_1 \longrightarrow (0, 0, 0), \tag{2.61}$$

$$\vec{\chi}_2 \longrightarrow (\chi_p, 0, \frac{M}{m_2}\chi_{eff}) \tag{2.62}$$

`IMRPhenomPv2` is an analytic phenomenological frequency domain waveform model capturing the basic phenomenology of precessing binaries with three parameters, mass ratio (η), a effective spin parameter (χ_{eff}) and effective precessional spin parameter (χ_p). The total mass of the system and distance to the binary act as overall scales for the waveform. `IMRPhenomPv2` uses a modified version of the aligned-spin model `IMRPhenomD` as the model for quadrupole modes in the QA frame. The Euler angles for the QA frame $(\gamma(f), \beta(f), \epsilon(f))$ are computed from PN theory and that prescription for the angles is used through merger and ringdown phases. This approximation works well enough for lower mass-ratio and spins [147], but can lead to unphysical effects at higher mass-ratios. For a detailed discussion, see Sec. II.D of [130].

Using the quadrupole (2,2) mode of a corresponding aligned-spin binary from `IMRPhenomD` and a model for the Euler angles, the `IMRPhenomPv2` model generates all other l=2 modes for a precessing system using Eq: 2.59. Any gravitational wave waveform can be written as,

$$h(f) = h_+(f) - ih_\times(f) = \sum_{l}^{-l\leq m\leq l} Y_{lm}^{-2}(\theta, \phi) h_{lm}(f) \tag{2.63}$$

where $Y_{lm}^{-2}(\theta, \phi)$ are the spin-weighted (with spin -2) spherical harmonic functions. Thus, once we have all the $l = 2$ modes, the plus and cross polarisations can be obtained using Eq: 2.63.

Once we have the plus and cross GW polarizations, $h^P_{+,\times}(Mf, \eta, \chi_{eff}, \chi_p, \theta, \phi)$ the final strain as seen at a detector is given by:

$$h(f) = F_+(\alpha, \delta, \psi)h_+(f) + F_\times(\alpha, \delta, \psi)h_\times(f) \tag{2.64}$$

where $F_{+,\times}$ are the detector response functions which depend on sky-position and polarisation.

2.6.3 IMRPhenomHM waveform model

`IMRPhenomHM` [2] is a phenomenological waveform model for aligned spin binary black hole systems that models all the $l = 2, 3, 4$ and $m = |l|, |l-1|$ modes. For this model, the dominant quadrupole (2,2) mode is mapped to the sub-dominant modes using appropriately tuned scaling relations. Technically, these scaling relations can be applied to any quadrupole only waveform model to obtain the sub-dominant modes, but for `IMRPhenomHM` the aligned-spin `IMRPhenomD` is used as the base model. This mapping is approximate and does not include mode-mixing effects. See Fig: 2.10 for a comparison between the modes as obtained from an NR simulation and the `IMRPhenomHM` model.

For the construction of `IMRPhenomHM` , the idea is to map the dominant mode *(2,2)* phase, amplitude and frequency (ϕ_{22},A_{22},f_{22}) to the phase, amplitude and frequency (ϕ_{lm},A_{lm}, f_{lm}) of any sub-dominant mode (l, m). Thus, the frequency domain strain ($\tilde{h}_{\ell m}(f)$) of a sub-dominant mode is given by,

$$\tilde{h}_{\ell m}(f) = A_{\ell m}(f) \times \exp\{i\,\varphi_{\ell m}(f)\} \tag{2.65}$$

$$\approx |\beta_{\ell m}(f)|\, A_{22}(f^{\rm A}_{\ell m}) \times \exp\left\{i\left[\kappa(f)\varphi_{22}(f^{\varphi}_{\ell m}) + \Delta_{\ell m}(f)\right]\right\}, \tag{2.66}$$

where $f^{\varphi}_{\ell m}(f)$ and $f^{\rm A}_{\ell m}(f)$ denote the frequency mapping functions for the phase and amplitude frequencies. The function $\beta_{lm}(f)$ (see Eq: 2.68) is to scale the quadrupole amplitude to amplitude of mode (l, m), $\kappa(f)$ (see Eq: 2.70) relates the phase of quadrupole mode to mode (l, m) and the quantities $\Delta_{\ell m}(f)$ (see Eq: 2.71) capture the multipole dependent phase-offsets.

Mapping the quadrupole mode to the sub-dominant modes can be done for the following reasons:

- During inspiral phase, frequency of any multipole (l, m) is approximately $m\omega$, with ω being the orbital frequency of motion. Thus, the we can map frequency *f* of a multipole *m* to the (2,2) frequency by $2f/m$. This provides a mapping between the frequencies for the inspiral phase.

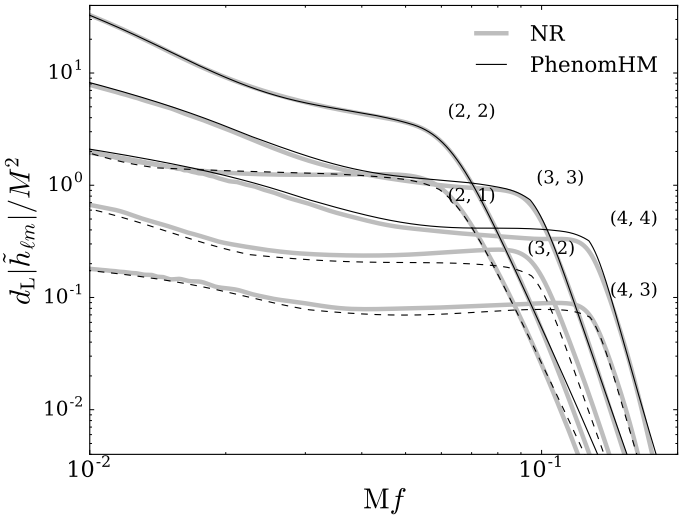

FIGURE 2.10: The figure shows the multipole moments of an aligned spin BBH system with q=8 and spin on larger BH of $\chi_z = -0.5$. The NR moments are shown as the thick gray lines. The modes computed from `IMRPhenomHM` are shown in thick (dashed) black lines for $m = l$ ($m = l - 1$) modes [2]. The modes computed from `IMRPhenomHM` have amplitude errors of a few $\mathcal{O}(1\%)$ to a few $\mathcal{O}(10\%)$ for the sub-dominant modes, but the phase errors are always $< 10\%$ for the non-spinning systems considered in Chapter:5.

- From QNM theory we get that the frequencies of mode (l, m) is related to the difference between the fundamental ringdown frequencies of (l, m) $f^{\rm RD}_{\ell m}$ and $(2, 2)$ $f^{\rm RD}_{22}$.
- From the PN theory, there exist analytical expressions for time-domain amplitudes of different modes (up to different PN orders) which can then be transformed to the frequency domain ($\hat{H}_{\ell m}(f)$) via the stationary phase approximation (SPA) [160], [161]. These expressions can be used to find scaling relations between the A_{22} and other $A_{\ell m}$s.

The above observations lead us to a physically motivated ansatz the for rescaling function,

$$\beta_{\ell m}(f) = \frac{\hat{H}_{\ell m}(f^{\rm A}_{22})}{\hat{H}_{22}(f^{\rm A}_{22})}. \tag{2.67}$$

To recover the correct behaviour of $\hat{H_{lm}}(f)$ at low frequencies, an extra factor of $\left(\frac{\hat{H}_{\ell m}(f)}{\hat{H}_{\ell m}(2f/m)}\right)$ is required. So, the final amplitude scaling relation used is,

$$\beta_{\ell m}(f) = \frac{\hat{H}_{\ell m}(f^{\rm A}_{22})}{\hat{H}_{22}(f^{\rm A}_{22})} \left(\frac{\hat{H}_{\ell m}(f)}{\hat{H}_{\ell m}(2f/m)}\right). \tag{2.68}$$

For `IMRPhenomHM` PN amplitudes are computed up to leading order in f for $l = |m|$ modes and upto 1.5 PN (to include the spin effects) for $l = |m - 1|$ modes.

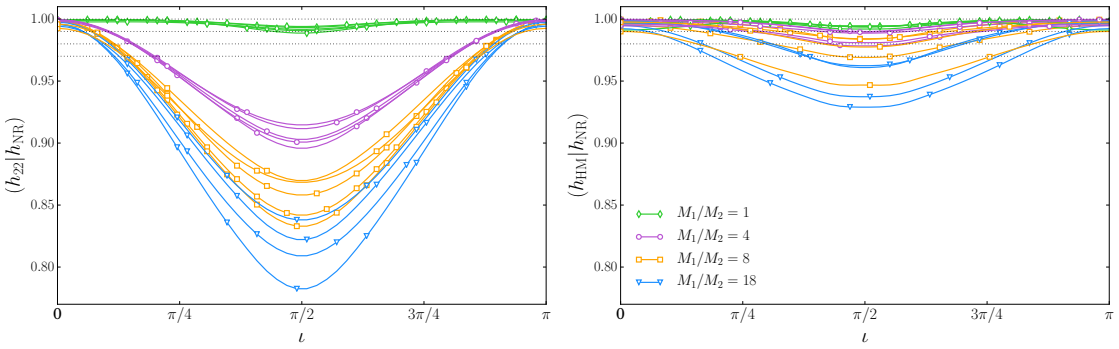

FIGURE 2.11: Matches of NR waveforms with varying mass ratio (q) with `IMRPhenomD` *(Left Panel)* and `IMRPhenomHM` *(Right Panel)* for varying inclination values. Its apparent that `IMRPhenomHM` provides much better matches than `IMRPhenomD` for almost all the cases [2].

The scaling relations from PN and QNM theory are used for frequency scalings for the inspiral and ringdown phases of the BBH coalescence. The frequency range between the PN and QNM frequency is mapped via a linear interpolation. The overall frequency mapping is as below,

$$f_{22}(f) = \begin{cases} \frac{2}{m} f, & f \leq f_0 \\ \frac{f_{22}^{\rm RD} - 2f_0/m}{f_{\ell m}^{\rm RD} - f_0}\,(f - f_0) + \frac{2f_0}{m}, & f_0 < f \leq f_{\ell m}^{\rm RD} \\ f - (f_{\ell m}^{\rm RD} - f_{22}^{\rm RD}), & f > f_{\ell m}^{\rm RD}. \end{cases} \tag{2.69}$$

For the frequency mappings, f_0 used is different for amplitude and phase frequency scaling. f_0 is fixed by optimizing the agreement with NR data for the amplitude and phase which leads to $f_0^A = 0.018 f_{lm}^{RD}/f_{22}^{RD}$ and $f_0^\phi = 0.014 f_{lm}^{RD}/f_{22}^{RD}$.

Using the frequency scaling relations, we can get the phase of multipole (l, m) by equating the derivatives of the multipole phase with scaled $(2, 2)$ phase, i.e., $\phi'_{lm}(f) \approx \phi'_{22}(f_{22}^{\rm A})$. Integrating once gives the phase relation that contains the inverse of the derivative of f_{22}, giving $\kappa = 1/f'_{22}(t)$. The other phase offsets are obtained via imposing continuity and from PN relations. This gives us the functional form for κ and $\Delta_{\ell m}$,

$$\kappa(f) = \frac{1}{f'_{22}(f)}, \qquad (\text{piecewise constant}), \tag{2.70}$$

$$\Delta_{\ell m} = \begin{cases} \frac{\pi}{2}\,[\,3\ell + \mathrm{mod}(\ell + m, 2)\,] - \pi, & f \leq f_0^\varphi \\ \varphi_{\ell m}(f_0^\varphi) - \kappa\,\varphi_{22}[f_{22}^\varphi(f_0^\varphi)], & f_0^\varphi < f \leq f_{\ell m}^{\rm RD} \\ \varphi_{\ell m}(f_{\ell m}^{\rm RD}) - \varphi_{22}[f_{22}^\varphi(f_{\ell m}^{\rm RD})], & f > f_{\ell m}^{\rm RD}. \end{cases} \tag{2.71}$$

These equations and relations provide a straightforward way of scaling the quadrupole amplitude and phase to their subdominant counterparts to obtain an aligned-spin waveform model with higher mode effects. Before this, the only multipole mode model was an EOB model for non-spinning systems `EOBNRv2HM` [162]. Recently, an EOB multimode model for aligned-spin systems (`SEOBNRv4HM`) was published in [143]. Studies have shown that although use of multi-mode templates for searches will give similar or slight improvements over a quadrupole only search, non-inclusion of sub-dominant modes can lead to large biases over the inferred parameters for high-mass/ high mass-ratio systems during analysis of detector data [163]–[169]. Thus having a fast, analytic multipole waveform model will be very useful. Fig: 2.11 shows the match between NR waveforms and `IMRPhenomD` and `IMRPhenomHM` . There are some more fine adjustments made to construct `IMRPhenomHM` from `IMRPhenomD` but the I would like to refer the reader to the [2] for more details. We will be studying the parameter estimation capabilities of `IMRPhenomHM` in Chapter: 5.

Chapter 3

IMRPhenomPv2 model and its systematic errors for GW150914

Advanced LIGO started its first observational science run in September of 2015, and the first direct detection of gravitational waves from coalescing binary black hole (BBH) system was achieved on the 14$^{\text{th}}$ of September of the same year. This transient gravitational wave signal (GW150914) was observed at 09:50:45 UTC at both LIGO detector sites with a matched-filter signal to noise ratio (SNR) of 24 and a false alarm rate of less than 1 event per 203000 years [3]. The initial source masses were estimated to be $36^{+5}_{-4}M_{\odot}$ and $29^{+4}_{-4}M_{\odot}$ with the final black-hole mass being $62^{+4}_{-4}M_{\odot}$. The effective aligned-spin parameter was estimated to be $\chi_{eff} = -0.07^{+0.16}_{-0.17}$ whereas the posterior of the effective precession spin parameter χ_p was approximately the same as the prior [3], [170]. All intervals are 90% credible intervals. The above parameters were estimated using phenomenological aligned-spin model IMRPhenomD [145], phenomenological precessing model IMRPhenomPv2 [147] and aligned-spin EOBNR model SEOBNRv2 [74] in the parameter estimation studies. Due to the high computational cost of the precessing EOBNR model, SEOBNRv3, that model was not used in [170], but the PE results using this model were published separately in [171]. An updated analysis of the parameters of GW150914 was given in [8], where, along with the aforementioned waveform models, analysis with the double-spin precessing EOBNR model (SEOBNRv3 [144], [74]) was included.

It is not assured that the parameters we infer from parameter estimation techniques will be the *true* parameters of the GW source. The total errors on recovered parameters can be split into statistical and systematic errors.

- **Statistical Errors:** The posterior distributions on any physical parameter from PE techniques will have a characteristic distribution around the mean value. The width of this distribution, due to the presence of detector noise, can be thought of as the source of *statistical* errors on the measured parameters.
- **Systematic Errors:** As described in Ch: 2, full IMR waveform models are built under certain approximations. These approximations *could* lead to a shift between the true parameter value and measured value, i.e., inaccuracies in the waveform model can lead to *biased* parameter measurements. Such errors are called *systematic errors*.

GW150914 was the first ever detection of a gravitational wave from a BBH source and there are several inherent approximations in the way the waveform models are built. So, to better understand the physical system, it was imperative to understand the systematic behaviour of the waveform models used for PE of GW150914. This study was undertaken by members of the LIGO-Virgo waveform group and was published as a full LVC collaboration paper in [1]. In the paper, systematics of precessing models `IMRPhenomPv2` along with aligned-spin phenomenological (`IMRPhenomD`) and `EOBNR` (`SEOBNRv2`) models were studied with the effects of varying inclination value, polarisation value, mode-content in NR waveforms and different detector noise on the same. My contribution to this study, was to study the systematics of the `IMRPhenomPv2` model using BAM-NR waveforms and this chapter presents the results of that work (see Section 2.3.2 for a description of the BAM code).

In Section 2.6.2, I have described the `IMRPhenomPv2` waveform model. In this chapter, I will first detail the motivations behind performing this study (Section 3.1), details of the NR waveforms and injections used for the PE studies (Section 3.2), the results are presented in Section 3.3 and will end with the conclusions in Section 3.4.

3.1 Motivation for the systematics study of `IMRPhenomPv2`

There is a possibility that the physical parameters inferred from PE are biased due to inaccuracies and/or missing physics in the waveform model. Before looking at the setup for and results of the systematics study, it would be instructive to note *why* the inaccuracies exist and *where* they might come from. As already noted in Ch: 2, it is impossible to obtain analytic solutions of the non-linear Einstein's equations for the full IMR phases of a BBH coalescence, which leads to approximations in waveform model building and the high computational cost of NR waveforms deters their use in PE studies. Although, efforts are underway to speed up parameter inference, as first presented in [172] and improved upon in [173]. In [174] and [175], it was shown that the above technique can be used to infer source parameters by comparing the signals with NR waveforms. For this study though,

ID	q	$\vec{\chi}_1$	$\vec{\chi}_2$	χ_{eff}	χ_p	M Ω	N_{orbits}	e
CFUIB0020	1.2	(-0.2594, -0.5393, -0.0458)	(-0.0276, -0.2194, 0.3622)	0.220	0.595	0.0276	6.6	3.6×10^{-3}
CFUIB0012	1.2	(-0.1057, 0.2362, 0.1519)	(0.1269, -0.5130, 0.4139)	0.274	0.417	0.0268	7.4	7.7×10^{-3}
CFUIB0029	1.2	(-0.2800, -0.2896, -0.1334)	(0.3437, 0.2283, 0.0989)	-0.026	0.406	0.0268	6.5	3.7×10^{-3}

TABLE 3.1: The parameters of the three BAM waveforms used for injections. $q, \vec{\chi}_1$ and $\vec{\chi}_2$ give the mass-ratio of the system and spin vectors at the start of the waveform with χ_{eff} and χ_p giving the corresponding effective spin parameters as defined for `IMRPhenomPv2`. The reference frequency at the start of the waveform is given by MΩ with the estimated eccentricity given by 'e'. The eccentricity of the BAM waveforms was estimated by following the procedure as outlined in [177]. Values of 'e' $\sim 10^{-3}$ ensures that the binary system is quasi-circular.

all the parameter estimation (PE) runs were performed using the samplers available in the `LALInference` package of `LALSuite`, specifically, the lalinference_nest sampler (nested-sampling) with 'lalinference_o2' version of `LALSuite` [53].

See Section 2.6.2 for a description of the `IMRPhenomPv2` waveform. A few approximations made during the construction of `IMRPhenomPv2` are:

- The Euler angles used to rotate the aligned-spin waveform from the QA frame to the source frame use PN expressions for inspiral, merger and ringdown phases of a BBH system whereas the PN expressions are expected to be applicable only until the late-inspiral phase of a coalescing binary. Although the PN angles do not behave pathologically at high frequencies, as compared to some PN expressions (for eg: leading order GW frequency tending to ∞ as $t \to t_c$, see Eq:3.2(c) of [176]), they consist of not more than an analytic continuation of the inspiral results.
- The effects of the six components of the two spin vectors on waveform morphology are captured by an effective alinged-spin parameter (χ_{eff}) and effective precession spin parameter (χ_p). The former characterizes effects of spin components parallel to orbital angular momentum, the latter of spin components perpendicular to the same.
- As an aligned-spin waveform is used to model the (2,2) mode in the co-precessing frame, the mode-asymmetry effects that are present for precessing systems are not included. See Section 4.1 for further discussions on mode-asymmetry.
- The model does not include the effects of higher order modes, i.e., modes with $\ell \geq 3$, or modes with $|m| < |\ell - 1|$ [1].

[1] The last two points mentioned here are also applicable to the precessing `EOBNR` model `SEOBNRv3` [144], [74].

3.2 Setup for the systematics study of IMRPhenomPv2

To assess the systematic errors induced due to inaccuracies in the waveform model, we perform parameter estimation studies with IMRPhenomPv2 as the model hypothesis using numerical relativity (NR) waveforms as signals. NR waveforms are chosen for injections as they are obtained by numerically solving Einstein's equations and they capture all the GR effects. In the BAM code, these equations are solved on a discrete grid and the waveforms are extracted at various *extraction radii*. There is a possibility that there could be inherent errors due to the discretization effects, but as was shown in [178], the mismatch ($[1-\mathcal{M}]$ where $\mathcal{M}$ is the match, see Section 1.4.2) between waveforms at different extraction radii are $\sim \mathcal{O}(10^{-4})$. For a gravitational wave detector to distinguish these effects, the SNR (ρ) of the detected gravitational wave would have to be ($\rho \geq \sqrt{D/2(1-\mathcal{M})}$ [179]–[181] using $D = 8$) larger than 200. As was shown in [182], [183], gravitational waves obtained from different commonly used NR codes have amplitudes accurate within 5% and the phase has an accumulated uncertainty of no more than 0.5 rad over the full course of inspiral, merger and ringdown. Hence, if systematic errors are present, at SNR of 25, it is unlikely that they would be due to the numerical errors from NR waveforms.

The NR waveforms used for injections have parameters close to those of GW150914 (see Table 3.1 for the list of NR waveforms used for injections). The NR waveforms are injected in zero-noise (detector noise is set to zero) and the Power Spectral Density (PSD) used for likelihood computations is obtained using the aLIGO detector data around the time of GW150914. Injecting the signal in zero-noise ensures that there are no errors due to random detector noise and the results can then be interpreted as an average over many Gaussian noise realizations. In [1], along with the BAM waveforms, a set of SXS [111], [112] waveforms were used as well; but I will focus only on the results of injecting the waveforms in Table 3.1 recovered with IMRPhenomPv2.

For the initial data, a PN evolution code (the code used for obtaining the inspiral parameters is the same one as used in [125], [178], [69]) is used to generate the Bowen-York quasi-circular parameters and the initial data is obtained via single-domain spectral elliptic solver described in [184] for the NR simulations. The system is then evolved with the BAM code (see Section 2.3.2 for a description of the BAM code). The nested boxes were grid with 80 points for the coarsest grid and 320 points for the finest grid, with the other grid values ranging from 96 to 240. The ψ_4 data is extracted over a range of radii from 80 M to 180M. The simulated systems have low mass-ratios ($q \sim 1.2$) and spins, so we can expect high accuracy based on the results in [178].

Numerical Relativity waveforms are commonly decomposed on a sphere using the spin weighted spherical harmonics basis, Y^s_{lm} with spin weight $s = -2$. These waveforms could

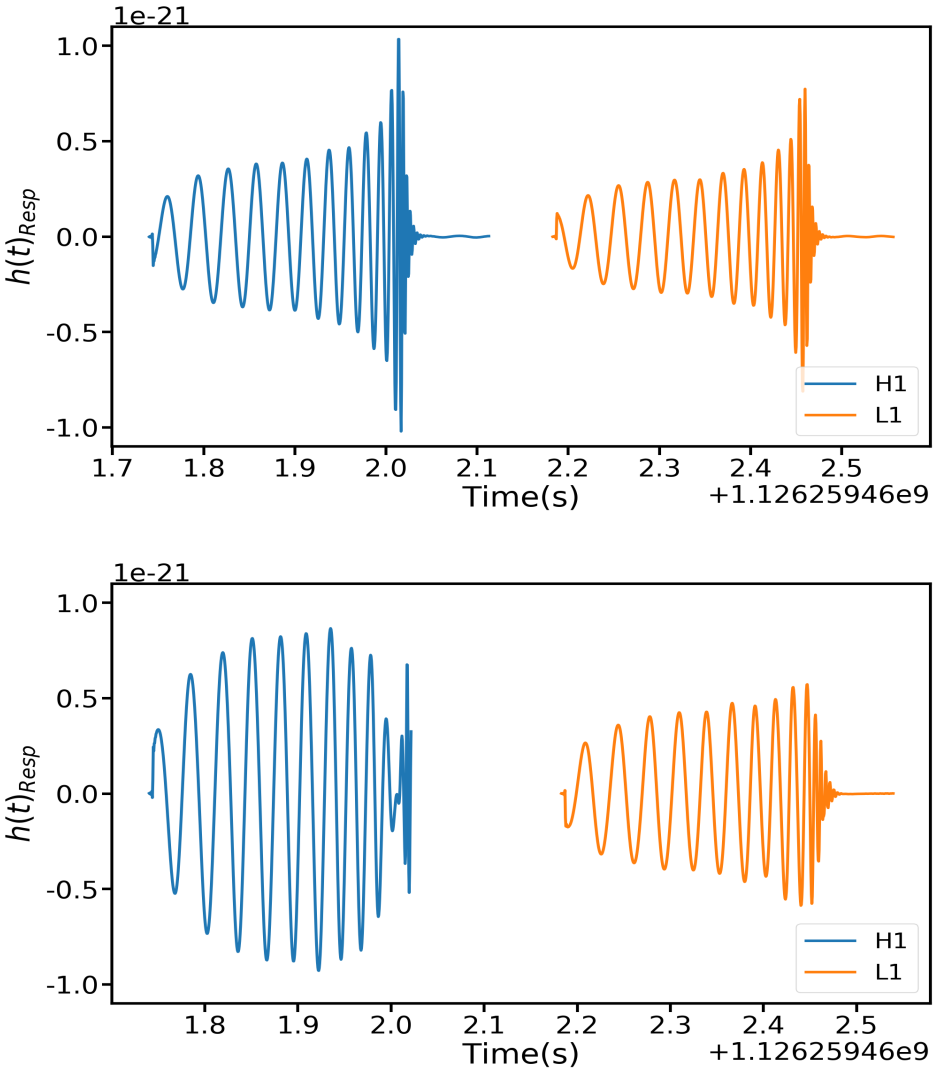

FIGURE 3.1: Response $h(t)$ as given in Eq: 2.64 for the NR waveform CFUIB0020 as computed by the frame-injection code for face-on ($\iota = 0$; top row plot) and edge-on ($\iota = 90$, bottom row plot) systems. The solid blue line (solid yellow line) is the response at H1 (L1) with injected SNR of 25. The morphology of the signal is markedly different for the two inclinations. This is expected as precession effects are more pronounced for edge-on inclinations than for face-on.

include all higher modes of the GW (h_{lm}), depending on the accuracy of the simulation. NR waveforms are described by the mass ratio (q) and spin vectors $(\vec{S}_1, \vec{S}_2)$ with total mass (M) acting as an overall scale factor. Given the spherical harmonic modes $(h'_{lm}s)$, we can calculate the plus and the cross polarisations of the waveform using Eq: 2.63. Using $(h_+, h_\times)$ with the extrinsic parameters like sky-position and polarisation, we can calculate the strain at each detector using Eq: 2.64. The total mass of the binary, the SNR value required for the injections (ρ_{inj}) and the PSD determines the distance at which the source is to be placed. This ensures that if a physical system with those parameters were to emit a signal, it will be observed at the LIGO detectors with a SNR = ρ_{inj}. For further details

regarding the framework for NR injections see [185]. We use the three NR waveforms given in Table 3.1, which are obtained using the BAM code. The response at each detector of the CFUIB0020 waveform for face-on and edge-on inclinations $(\iota = 0^{\circ}, 90^{\circ})$ using the NR injection code is shown in Fig: 3.1. Note that the inclination is the angle between $\vec{L}$ and $\vec{N}$ at a reference epoch (time or frequency), where $\vec{L}$ and $\vec{N}$ are the angular momentum vector of the system and the line-of-sight to the observer from the system.

For the injections, we used the estimated parameters from GW150914 (see Tab:1 of [1]). All waveforms were injected with a SNR of 25 with the sky-position at $07^{h}26^{m}50^{s}$ and -72.28° (right-ascension, declination). At the start of this study, the source frame mass for GW150914 was estimated at $\sim 74M_{\odot}$ (the numbers were then improved upon by further analysis in [170]) and so the NR waveforms were injected with similar source-mass values. The fiducial inclination (ι) and polarisation (ψ) are chosen to be 162° and 82° respectively. The polarisation angle for GW150914 is not well constrained, but we will study the effects of different polarisation values of the signal. For the inclination (polarisation) series of runs, the waveforms are injected with a total mass of $70M_{\odot}$ $(80M_{\odot})$. The lower cut-off frequency for the PE runs was fixed at 30Hz for both detectors. All the PE runs were done on the Cardiff cluster "ARCCA" [186].

3.3 Results and Discussion

As explained in Chapter: 2, for precessing systems, effects of precession become stronger from face-on to edge-on configurations. Fig: 3.1 showcases the different detector response of the CFUIB0020 NR waveform at face-on and edge-on inclination values. Hence, if systematic biases should exist in the model waveform, we can expect them to manifest in regions of strong precession. Thus, we performed a set of NR injections across the inclination space to study the effects of inclination on parameter recovery.

First, we perform a series of injections with the three NR waveforms at various inclination values. The total source frame mass of the system was set to $70M_{\odot}$. All three NR waveforms were injected with inclinations = (0°, 30°, 45°, 60°, 90°, 120°, 135°, 162°, 180°). Inclination of 162° was included as that was the estimated inclination of GW150914. For this inclination series, the polarisation for all the injections was fixed at $\psi = 82^{\circ}$.

We observe appreciable biases on a few of the parameters (masses and sky-position) at edge-on inclinations, but for other inclinations, the recovered parameters are consistent with injected values. Following [187] (see Eq:4 of [187]), we define the bias amount $(\delta\beta_{\theta})$ as the ratio between the systematic error and standard deviation, where the systematic error is the

difference between the recovered mean of the posterior [2] and the injected value (θ_0). So, defining systematic error as $\beta_\theta = |\theta_{\text{mean}} - \theta_0|$ and standard deviation as σ_θ, $\delta\beta_\theta = \beta_\theta/\sigma_\theta$. The value of $\delta\beta_\theta$ indicates the amount of bias.

3.3.1 Effect of Inclination on estimation of mass parameters

Fig: 3.2 gives the results for total mass and chirp-mass recovery for the runs in the inclination series. M_{total} and $\mathcal{M}_c$ measurements are accurate for all non edge-on inclinations, with these parameters showing a slight bias for CFUIB0020 and CFUIB0012, and a strong bias for CFUIB0029.

Fig: 3.3 shows the recovered values of η (along with their 90% credible interval values) for the NR waveform inclination series. The recovered η is close to the true value for all inclinations; other than at $\iota = 90^\circ$ (edge-on) where η is biased for all three NR waveforms.

In order to investigate the bias of recovered η for near edge-on configurations, CFUIB0020 was injected at extra inclination values of $(70^\circ, 80^\circ, 85^\circ, 90^\circ, 95^\circ, 100^\circ, 110^\circ)$. The results of these runs show that the bias on η starts at $\sim 80^\circ$ and persists until $\sim 100^\circ$ (see Fig: 3.4).

The results of the inclination series indicate that for near edge-on configurations, recovered mass parameters can be biased. Precession effects become more pronounced for edge-on configurations, and to recover the true parameters, `IMRPhenomPv2` should model the same. Also, as the priors placed on the inclination strongly disfavour edge-on systems, the PE codes tend to overestimate the distance of a binary which might then lead to a higher value to total mass to account for the decrease in signal strength. So, the bias over the mass-parameters could be from; i) inaccuracies between `IMRPhenomPv2` and NR waveforms and ii) effect of observational priors. We now wish to know how these inaccuracies manifest across the polarisation space.

To answer that, we inject CFUIB0020 at two different polarisation values $\psi = 82^\circ, 135^\circ$ across the inclination values and the results for recovered η are given in Fig: 3.5. We see that the strong bias present for $\psi = 82^\circ$ ($\delta\beta_\eta \sim 3$) reduces drastically at $\psi = 135^\circ$ ($\delta\beta_\eta \sim 1$). Where for $\psi = 82^\circ$ the true value was outside the 90% CIs, the same is not the case for $\psi = 135^\circ$. This suggests that; i) bias amount due to observational priors *could* be small and ii) although the inaccuracies in `IMRPhenomPv2` may manifest at some choices of ψ, the effect may be localized. We investigate this behaviour further in the next section, where we inject the above three NR waveforms at edge-on inclination over a range of polarization values. At $\psi = 82^\circ$, the detector response gets more contribution from $h_\times$ than h_+, and the opposite at $\psi = 135^\circ$.

[2] Note that in [187], the authors use the maximum a-posteriori (MAP) value

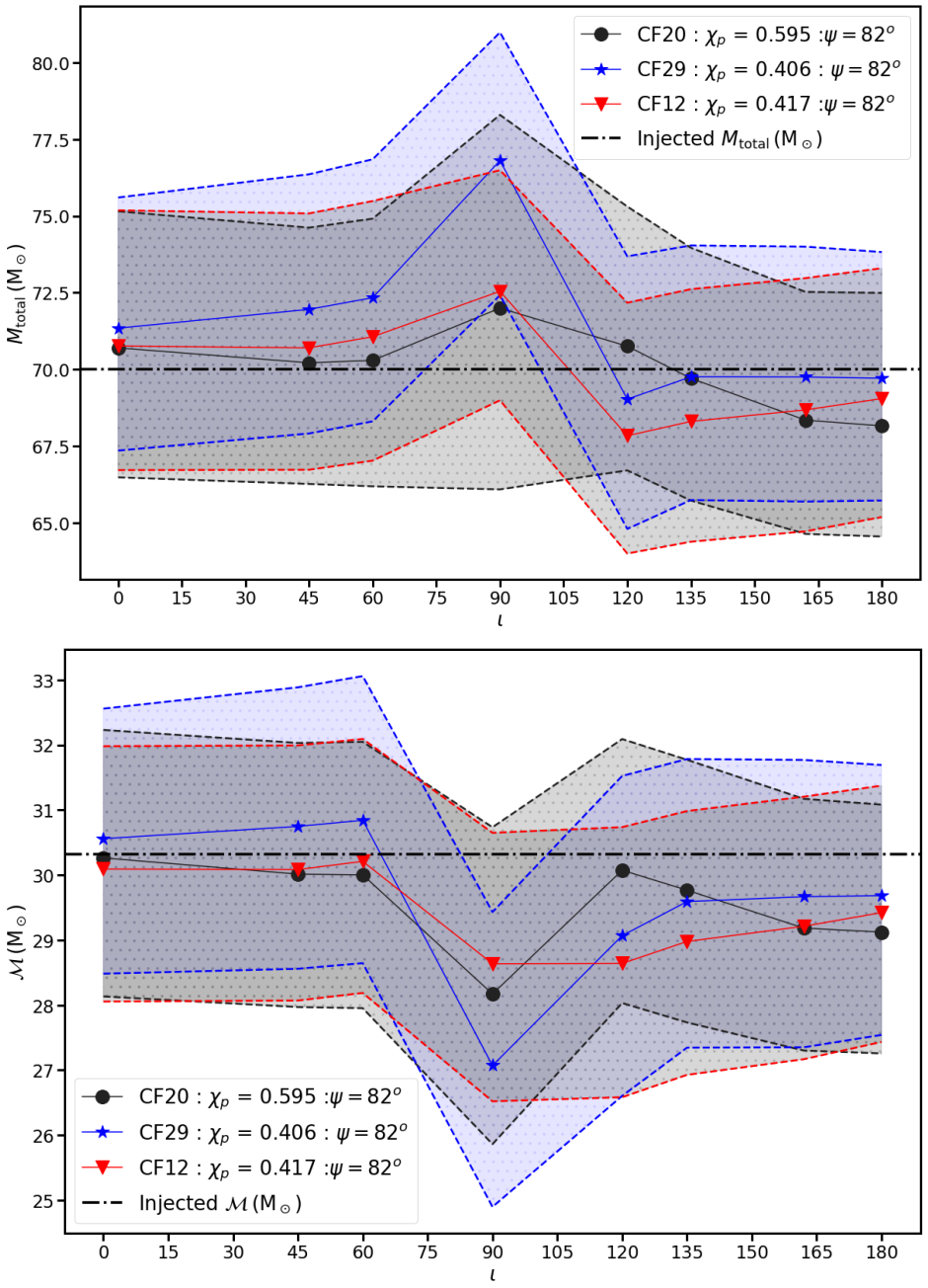

FIGURE 3.2: Recovered posterior over a range of inclination values with fixed polarization, of M_{total} (top panel) and $\mathcal{M}_c$ (bottom panel) for NR waveforms CFUIB0020 (black-dot), CFUIB0012 (red-lower triangle) and CFUIB0029 (blue-star) where the dot-dashed black line gives the value of injected (true) parameter. The solid lines show the mean value of the posterior with the dashed-lines showing the range of the 90% credible intervals. At edge-on inclination, $\delta\beta_{M_{total}}$ is 1.3 [2.5] (1) and $\delta\beta_{\mathcal{M}_c}$ is 1.5 [2.3] (1.3) for CFUIB0020 [CFUIB0029] (CFUIB0012) respectively, with the same values smaller than 1 for all other inclinations. Given that GW150914 had an inclination of $\sim 162^\circ$, these systematics errors are not likely to dominate the inferred parameters.

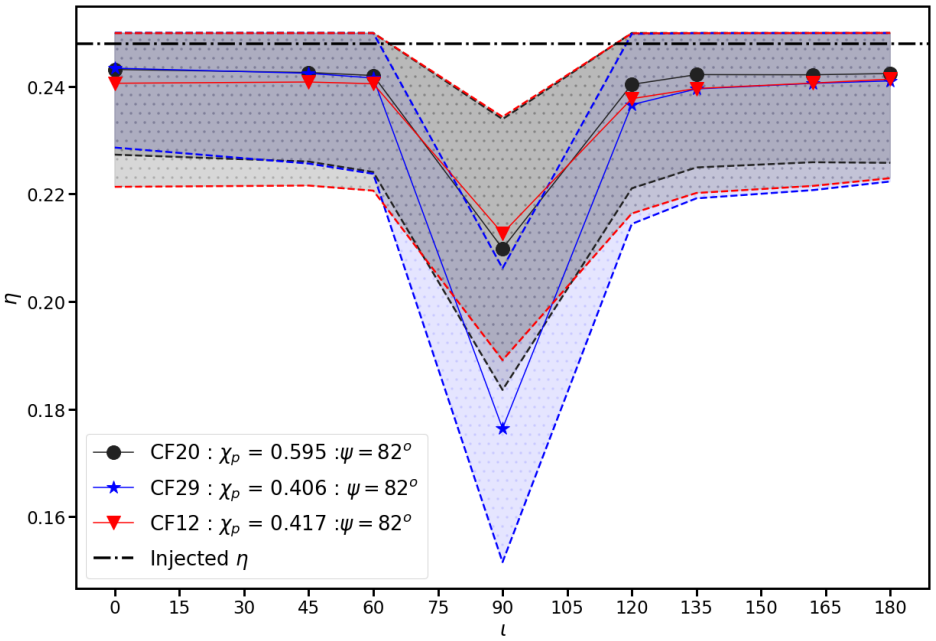

FIGURE 3.3: Recovered posterior of η for NR waveforms CFUIB0020 (black-dot), CFUIB0012 (red-lower triangle) and CFUIB0029 (blue-star) over a range of inclination values with fixed polarization. The dot-dashed black line gives the (true) value of injected η. The solid lines show the mean value of the posterior with the dashed-lines showing the range of the 90% credible intervals. At edge-on inclination, $\delta\beta_\eta$ is 3 [4.3] (2.5) for CFUIB0020 [CFUIB0029] (CFUIB0012) respectively, with the same values smaller than 1 for all other inclinations.

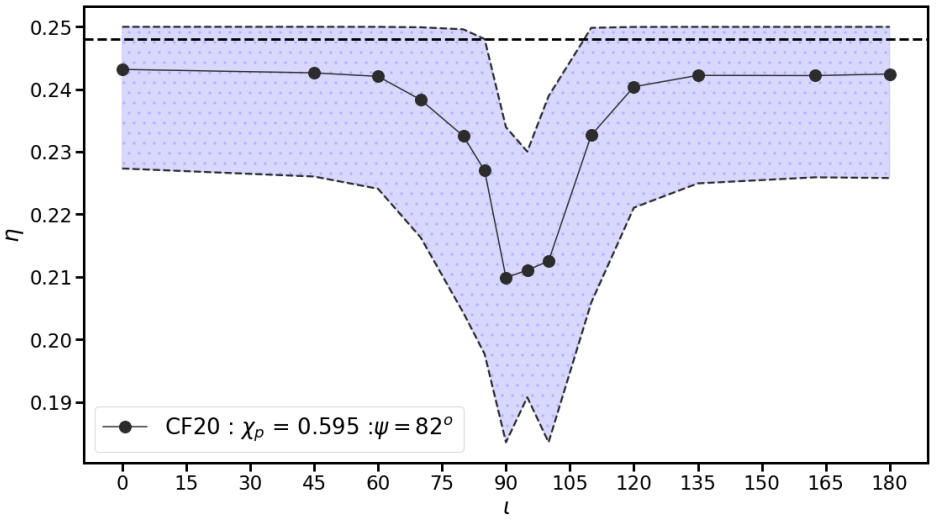

FIGURE 3.4: Recovered posterior of η CFUIB0020 (black-dot) with extra inclination points around $\iota = 90°$ where the dot-dashed black line gives the value of injected η. The solid black-line shows the mean values of the recovered posteriors with the 90% credible region shown by the blue-dotted region.

3.3.2 Effect of Polarisation on estimation of mass parameters

The detector polarisation parameter controls the overall orientation between the detector arms and GW polarisation axes, affecting the detector response (see Eq: 2.64). It is an

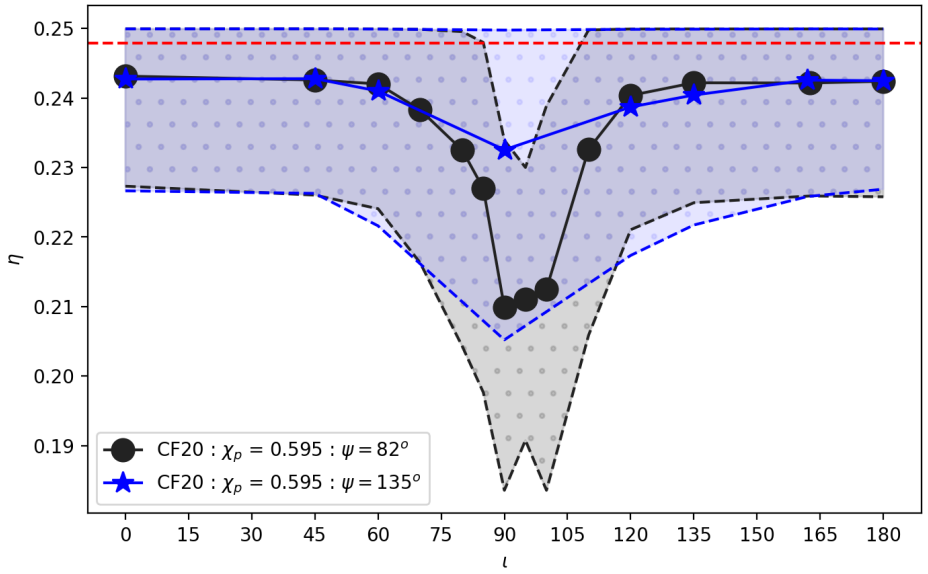

FIGURE 3.5: Recovered posterior of η for NR injection CFUIB0020 : $\psi = 82°$ (black-dot), and CFUIB0020 : $\psi = 135°$ (blue-star) where the dashed red line gives the value of injected η. The solid lines show the mean values of the recovered posteriors with the 90% credible region shown by the dashed-lines. Where for $\psi = 82°$, $\delta\beta_\eta = 3$, at $\psi = 135°$ it is 1.

extrinsic parameter, i.e., it depends on the relative position of Earth and source and is independent of the source dynamics. But, in the previous section (see Fig: 3.5) we saw that the polarisation value can have a (sometimes major) effect on the recovered parameters. So, the question then becomes, across how much of the polarisation space can we expect to see a bias? To check for this, we performed a series of PE runs where all three NR waveforms were injected at an inclination of 90° and polarisation values of $(\psi_{inj} = 0°, 45°, 82°, 90°, 100°, 135°, 180°)$. The total mass of the system is fixed at 80 $M_\odot$.

Fig: 3.6 gives the M_{total} and $\mathcal{M}_c$ recovery for edge-on injections with varying polarisation values for the three NR waveforms. Other than a slight bias for $\psi = 82°$ on total mass recovered for CFUIB0029 system, all other configurations show a slight or no bias (based on $\delta\beta_\lambda$ values), but contain the injected values on within the 90% CIs for recovered total mass and chirp mass.

From Fig: 3.7 we see that η_{rec} has a strong bias at ψ_{inj} = 82° ($\delta\beta_\eta \sim 3$), which is consistent with the results in Fig: 3.3 - Fig: 3.5. There exists a slight bias at $\psi_{inj} = 0°, 90°, 180°(\delta\beta_\eta \sim 1.3)$, but it is smaller than that observed at $\psi_{inj} = 82°$.

As mentioned earlier, at $\psi_{inj} = 82°$, the detector response is dominated by $h_\times$. Based on the specific combinations of (ι, ψ), the detector response can be composed by partially constructive or destructive interference between the two polarisations, which is why we see the strange signal morphology for H1 in Fig: 3.1. To recover accurate parameters,

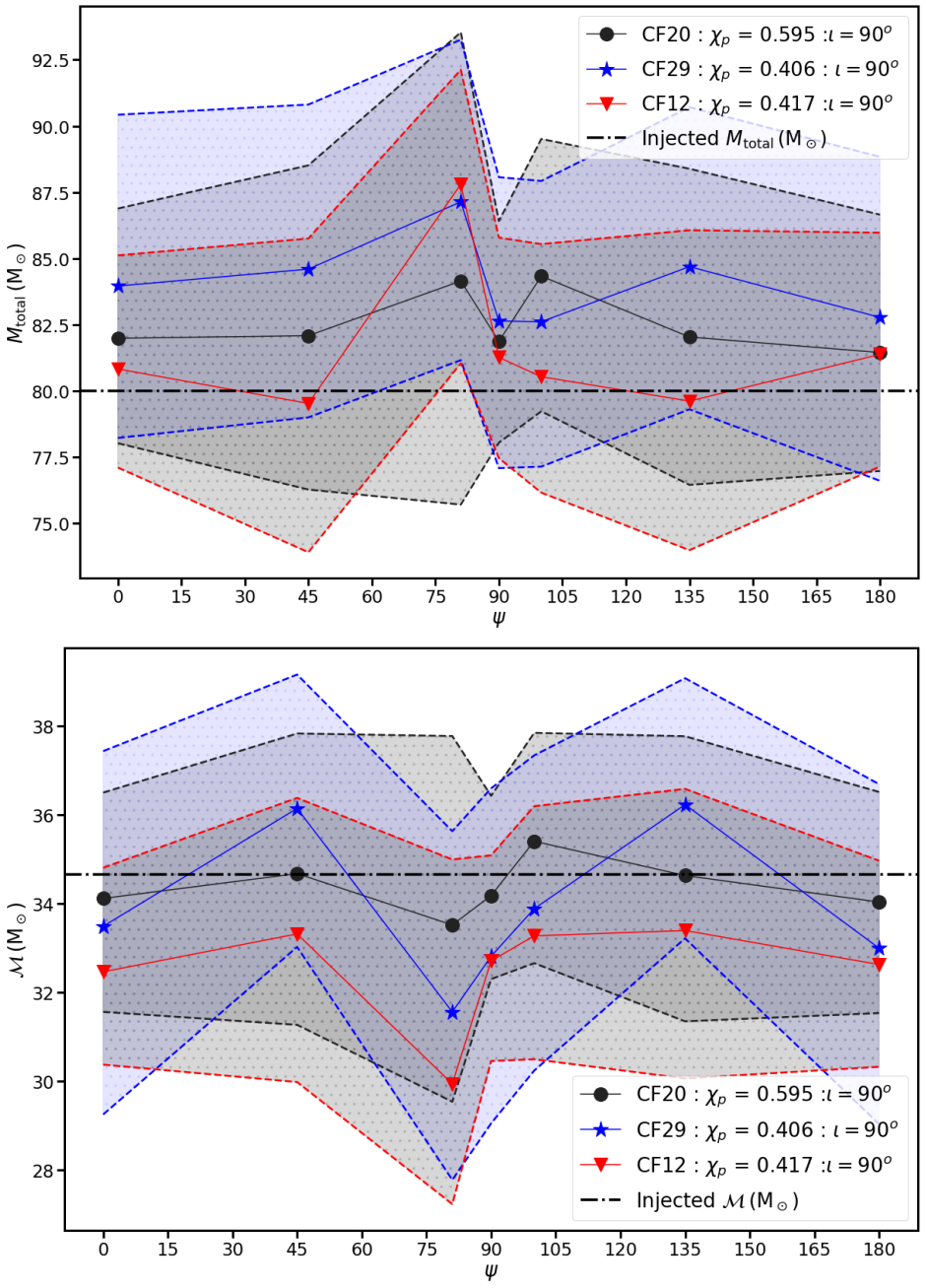

FIGURE 3.6: Recovered posterior of M_{total} and $\mathcal{M}_c$ for NR waveforms CFUIB0020 (black-dot), CFUIB0012 (red-lower triangle) and CFUIB0029 (blue-star) where the dot-dashed black line gives the value of injected M_{total} and $\mathcal{M}_c$. The solid lines show the mean values of the recovered posteriors with the 90% credible region shown by the dashed-lines. For CFUIB0020 and CFUIB0012 systems, $\delta\beta_{\mathcal{M}_c} < 1$, but for CFUIB0012 $1 \leq \delta\beta_{\mathcal{M}_c} \leq 1.7$. Other than $\psi_{inj} = 82°$ recovery (for which $\delta\beta_{M_{total}}$ is 2.3 (1.8) for CFUIB0012 (CFUIB0029)), $\delta\beta_{M_{total}}$ shows slight bias for all three across the polarisation space. Hence, for these parameters, the maximum bias is at $\psi_{inj} = 82°$.

the model should then accurately model h_+ and $h_\times$. Now, the NR waveform polarisations are constructed from all $\ell = 2$ sub-dominant modes, whereas the sub-dominant modes of `IMRPhenomPv2` ($\ell = 2, |m| = 1, 0$) are a consequence of the twisting up of the aligned-spin

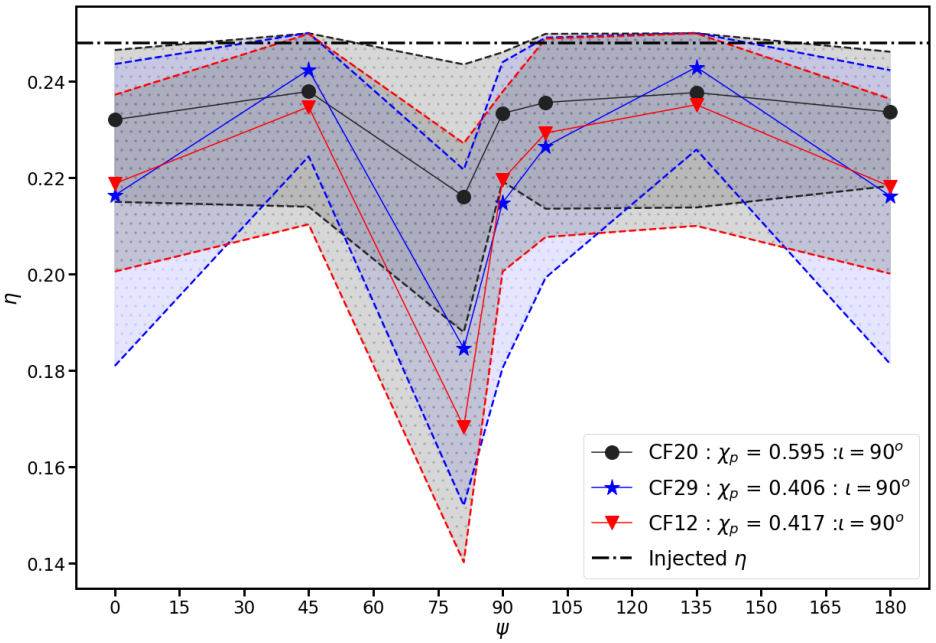

FIGURE 3.7: Recovered posterior of η for NR waveforms CFUIB0020 (black-dot), CFUIB0012 (red-lower triangle) and CFUIB0029 (blue-star) where the dot-dashed black line gives the value of injected η.

$(\ell, m) = (2, 2)$ modes. As we will see in Section 3.3.5, accurate parameters are recovered by `IMRPhenomPv2` for `IMRPhenomPv2` injections (even at edge-on configurations). These results, with the results from the inclination series, suggest that the amount of bias incurred from inaccuracies in `IMRPhenomPv2` waveform at recreating NR signal dominate over biases due to observational priors.

To have a better idea of the behaviour of errors on η in the (ι, ψ) space, extra runs were done where CFUIB0020 was injected over a range of inclination-polarisation values. Fig: 3.8 gives the combined results of these runs. Here, we compute the relative percent error ($\Delta\eta$ %) between mean of recovered posterior of symmetric mass ratio η_{rec} with its injected value η_{inj} and plot them across the (ι, ψ) parameter space. We see that we can expect high bias on recovered η ($8\% \leq \Delta\eta < 15\%$) in a small region of the (ι, ψ) parameter space centred around (ι, ψ) = (90°,82°). All edge-on inclination systems, irrespective of polarisation value, show mild biases whereas the posteriors recovered in the sampling of all other regions are consistent with the injected value.

GW150914 was estimated to have a nearly face-off inclination with $\psi \sim 82°$. From the above results, we see that for a small region in the $\iota - \psi$ parameter space ($\sim 30° \times 30°$ region centred around ($\iota - \psi$ = 90°,82°)), parameters recovered by `IMRPhenomPv2` can have a strong bias, but the estimated inclination of GW150914 does not lie in that region. Also, from the publicly available posteriors samples [188], GW150914 has ~ 10 times more support for $120° < \theta_{JN} < 180°$ compared to $60° < \theta_{JN} < 120°$. A simple calculation

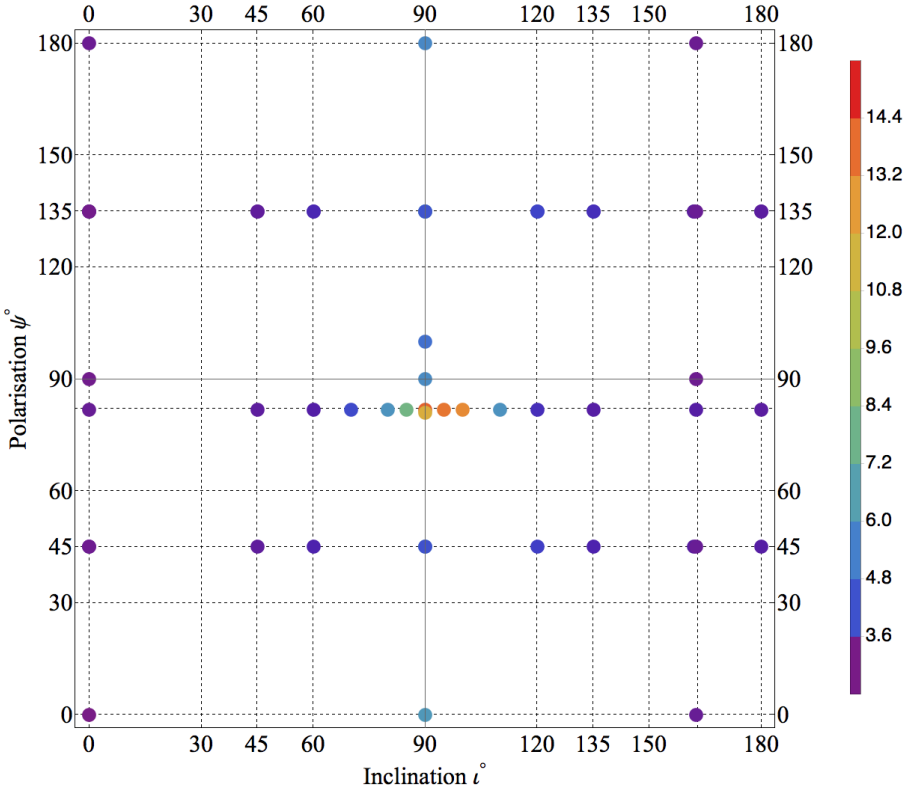

FIGURE 3.8: The above plot gives relative percent error between recovered posterior mean η_{mean} and η_{inj} over the inclination-polarisation parameter space ($\Delta\eta = 100(\eta_{mean} - \eta_{inj})/\eta_{inj}$). The coloured circular dots show the sampling in the parameter space. The colour legend on the right shows $\Delta\eta$% value.

shows that about only $\sim 0.3\%$ of all possible detectable signals fall into the region of high bias (See Appendix:B of [1] for the calculation). So, it is highly unlikely for GW150914 be at edge-on and for the mass parameters, we do not expect the systematic errors to dominate over errors from random noise [3].

3.3.3 Recovery of spin parameters

If the GW source is precessing, we would like to know how well `IMRPhenomPv2` can measure the precession and effective spin parameters (χ_p, χ_{eff}). The NR injections CFUIB0020, CFUIB0029, CFUIB0012 have the parameters (χ_{eff}, χ_p) = (0.220, 0.598), (-0.026, 0.406) & (0.274, 0.417) respectively.

[3] All these computations are performed for signals with parameters close to those estimated for GW150914. Changing the mass-ratio and spins (where precession effects become stronger) will change the behaviour.

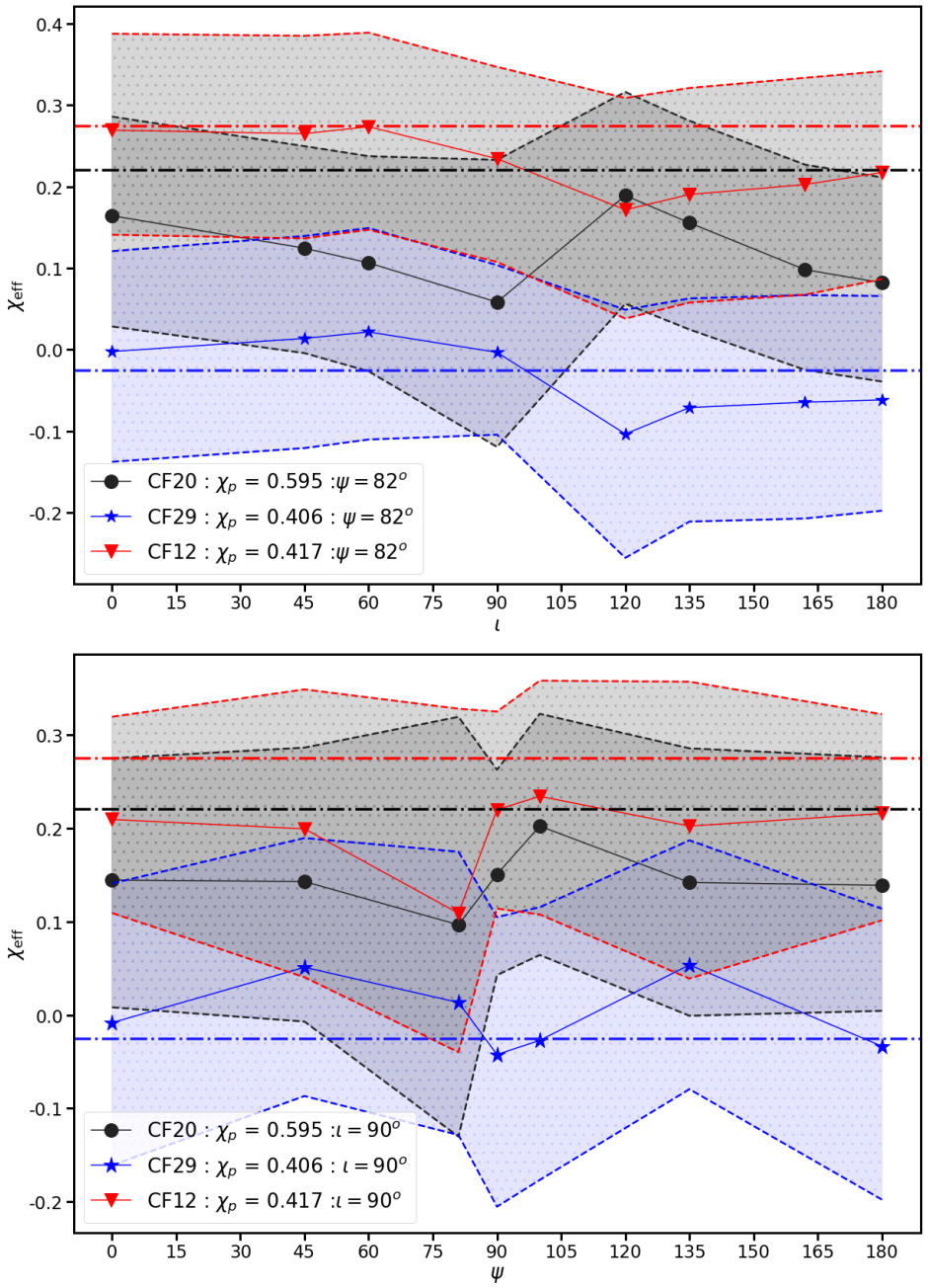

FIGURE 3.9: Recovered posterior of χ_{eff} for NR injection CFUIB0020 (black-dot), CFUIB0012 (red-lower triangle) and CFUIB0029 (blue-star) where the dot-dashed black, blue and red lines give the value of true χ_{eff} for CFUIB0020, CFUIB0029 and CFUIB0012 respectively. The solid lines show the mean of the recovered posterior with the bands between the dashed-lines show the 90% CIs. (Note: The difference between the two recoveries can be attributed to different total mass used for injection.)

Fig: 3.9 shows the results for χ_{eff} recovery across the inclination space (with fixed $\psi = 82°$) and polarisation space (with fixed $\iota = 90°$) for the three NR waveforms. Note that the inclination series waveforms were injected at $70M_\odot$ and the polarisation series at $80M_\odot$. Other than $\sim$ edge-on inclination of CFUIB0020 ($\delta\beta_{\chi_{eff}} \sim 2$ for $[\iota, \psi] = [90°, 82°]$), recovered χ_{eff}

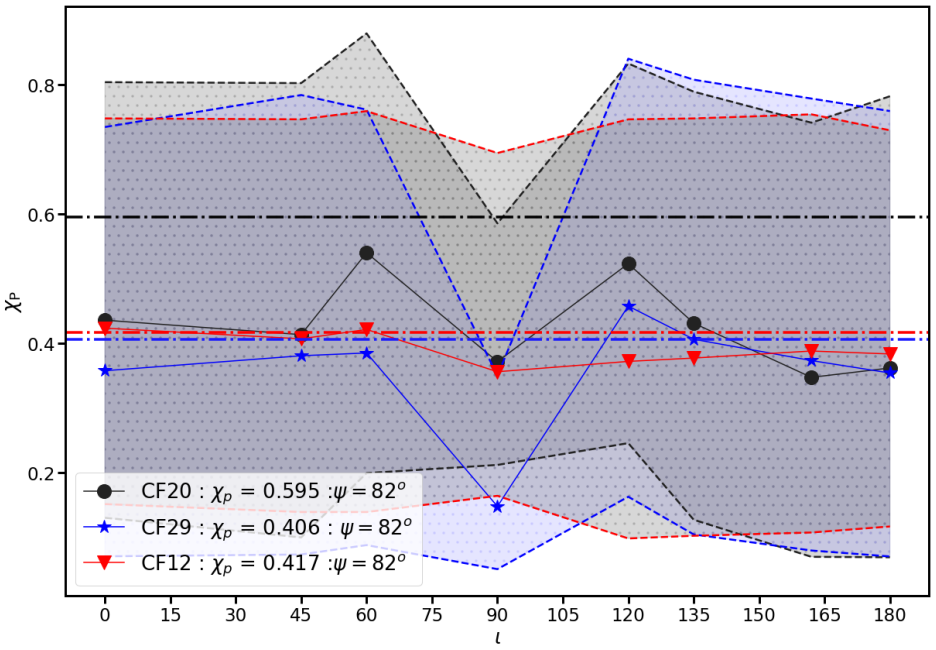

FIGURE 3.10: Recovered posterior of χ_p for NR injection CFUIB0020 (black-dot), CFUIB0012 (red-lower triangle) and CFUIB0029 (blue-star) where the dot-dashed black, blue and red lines give the value of true χ_p for CFUIB0020, CFUIB0029 and CFUIB0012 respectively. The solid lines show the mean of the recovered posterior with the bands between the dashed-lines show the 90% CIs.

is well-bounded and unbiased. The results of recovered χ_{eff} are consistent with what we see for the mass-parameters recovery, i.e., biased recovery at the same (ι, ψ) combinations.

Given the partial degeneracy between η and χ_{eff} (that enters via the binary phase [181]), we expect a bias on η to translate to a bias on χ_{eff}. Specifically, the biased recovery of η (Fig: 3.3 and Fig: 3.4) and χ_{eff} for the CFUIB0020 (Fig: 3.9). However, the bias on η is stronger than the bias on χ_{eff} and although we observe a biased η recovery for CFUIB0029 and CFUIB0012, the recovered χ_{eff} for these configurations contains the true value within its 90% CIs with $\delta\beta_{\chi_{eff}} < 1$.

Fig: 3.10 shows the results of χ_p recovery over the inclination space. For all NR configurations, the posteriors recovered for non edge-on injections are pretty broad and basically recover the prior over χ_p. χ_p has better bounds for edge-on configurations and is biased for CFUIB0020 and CFUIB0029 waveforms. Bounds on posteriors for χ_p for edge-on are better than for face-on as precession effects are the strongest at edge-on inclinations, but this is also where we see the largest bias. Biases on recovered mass parameters with the results for χ_p, suggest that for accurate edge-on precession measurement, accuracy of the models should be improved. For non edge-on inclinations, the 90% credible regions of χ_p span over almost 70% of the parameter space whereas those for χ_{eff} are bounded within 10% . This

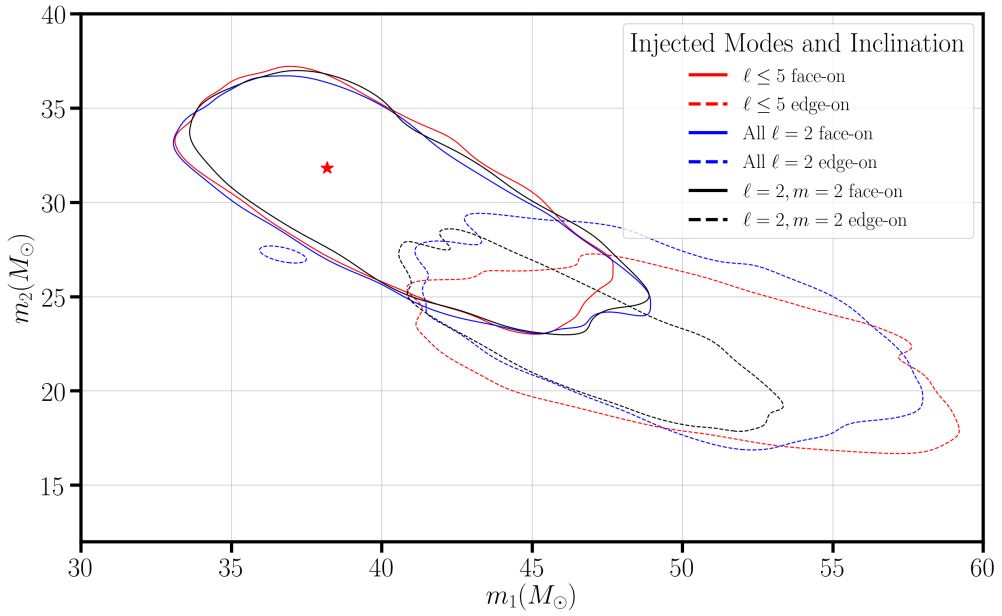

FIGURE 3.11: The figure shows the recovered mass posteriors in the $m_1 - m_2$ parameter space for injections with different mode content, with the contours showing the 90% credible interval. Results for face-on and edge-on inclination are shown in solid and dashed lines with the results for injections with i) All Higher Modes ($\ell \leq 5$) are shown in red, ii) All $\ell = 2$ and $-2 \leq m \leq 2$ modes are shown in blue and iii) only ℓ = $|m|$ = 2 modes are shown in black. The red star shows the injected values of $m_1 - m_2$. Consistent with previous results, we observe a biased mass parameter recovery for edge-on configuration.

shows that, unless the system is near edge-on, at $q \sim 1.2$, the effective precession spin parameter cannot be measured.

3.3.4 Effect of Higher Modes

`IMRPhenomPv2` waveform models all $\ell = 2$ modes of a precessing binary system. A real GW signal will be composed of all $\ell = 3, 4, 5 \ldots$ modes and non-inclusion of higher-mode content could result in another source of systematic errors. To check for that, we inject the CFUIB0020 waveform (70 $M_\odot$ total mass, $\psi = 82^o$) with different mode content; i) All Higher Modes (HM) (all modes up to $\ell = 5$), ii) All $l = 2$ modes, i.e., -2 $\leq$ m $\leq$ 2 and iii) only l = $|m|$ = 2 modes (l2m2); at face-on and edge-on inclinations and compare the posteriors recovered by `IMRPhenomPv2` .

Fig: 3.11 shows the contours of recovered mass posteriors (clipped between the 90% credible intervals) in (m_1, m_2) space for the above injections. We do not observe a large difference between the posteriors recovered for higher-mode injections and $\ell = 2$ injections for any of the parameters. The behaviour of the bias of (m_1, m_2) (i.e., overestimated m_1 and underestimated m_2) can be attributed to the overestimation of M_{total} combined with

recovered $\eta < 0.247$ and the fact that for the waveform models, $m_1 > m_2$. So, for face-on and edge-on inclinations, at q=1.2, exclusion of higher-mode content does not result in appreciable biases.

3.3.5 Results of `IMRPhenomPv2` injections

In the previous sections we saw a recovery bias towards high mass ratios for edge-on or nearly edge-on NR injections at a particular polarisation value. So, we wanted to check if we see such biases for zero-noise `IMRPhenomPv2` injections recovered with the `IMRPhenomPv2`. This would give an idea of the amount of bias over the inferred parameters due to observational priors (for eg: for edge-on inclinations). So, we started a set of PE runs sampling the inclination space with fixed $\psi = 82^\circ$, and polarisation space with a fixed $\iota = 90^\circ$. The gps trigger time and sky-position were kept the same as for the NR injections. For the inclination (polarisation) series, we use the physical parameters of CFUIB0020 (CFUIB0029) for `IMRPhenomPv2` waveform injections with the value of polarisation (inclination) being that of the largest bias seen for NR injections.

From Fig: 3.12, we can see that all the recovered parameters are unbiased over the inclination and polarisation space for `IMRPhenomPv2` injections. Recovered η for $(\iota, \psi) = (60^\circ, 82^\circ)$ are further from the mean than others, but not so much as to constitute a true bias and this effect is considerably less than that for the corresponding NR injections.

The aligned-spin parameter is unbiased and well constrained in all situations. Recovered χ_p (inclination series) is slightly better measured at $\iota \sim 90^\circ$ than at small inclinations, where precession effects are not that strong. In the polarisation series, `IMRPhenomPv2` was injected at $\chi_p \sim 0.4$ (0.6 for inclination), and although these runs are at edge-on, the recovered χ_p is not well measured. Thus, for these parameter space values $(q, \vec{S}_1, \vec{S}_2)$, `IMRPhenomPv2` cannot measure precession to a great accuracy. The highly consistent results between `IMRPhenomPv2` injections indicate that the biases seen by `IMRPhenomPv2` waveform for NR injections are due to the various approximations that went into building the model.

3.4 Conclusions

The physical parameters of GW150914 were measured using various waveform models, with one of them being `IMRPhenomPv2` . The mass parameters (M, η) of the BBH were measured to be $\sim (65M_\odot, 0.247)$ [170] with small anti-aligned spin (~ 0) and no evidence of precession. To investigate possible contributions of errors on the recovered parameters due to `IMRPhenomPv2` waveform model inaccuracies (see Section 3.1), a set of precessing

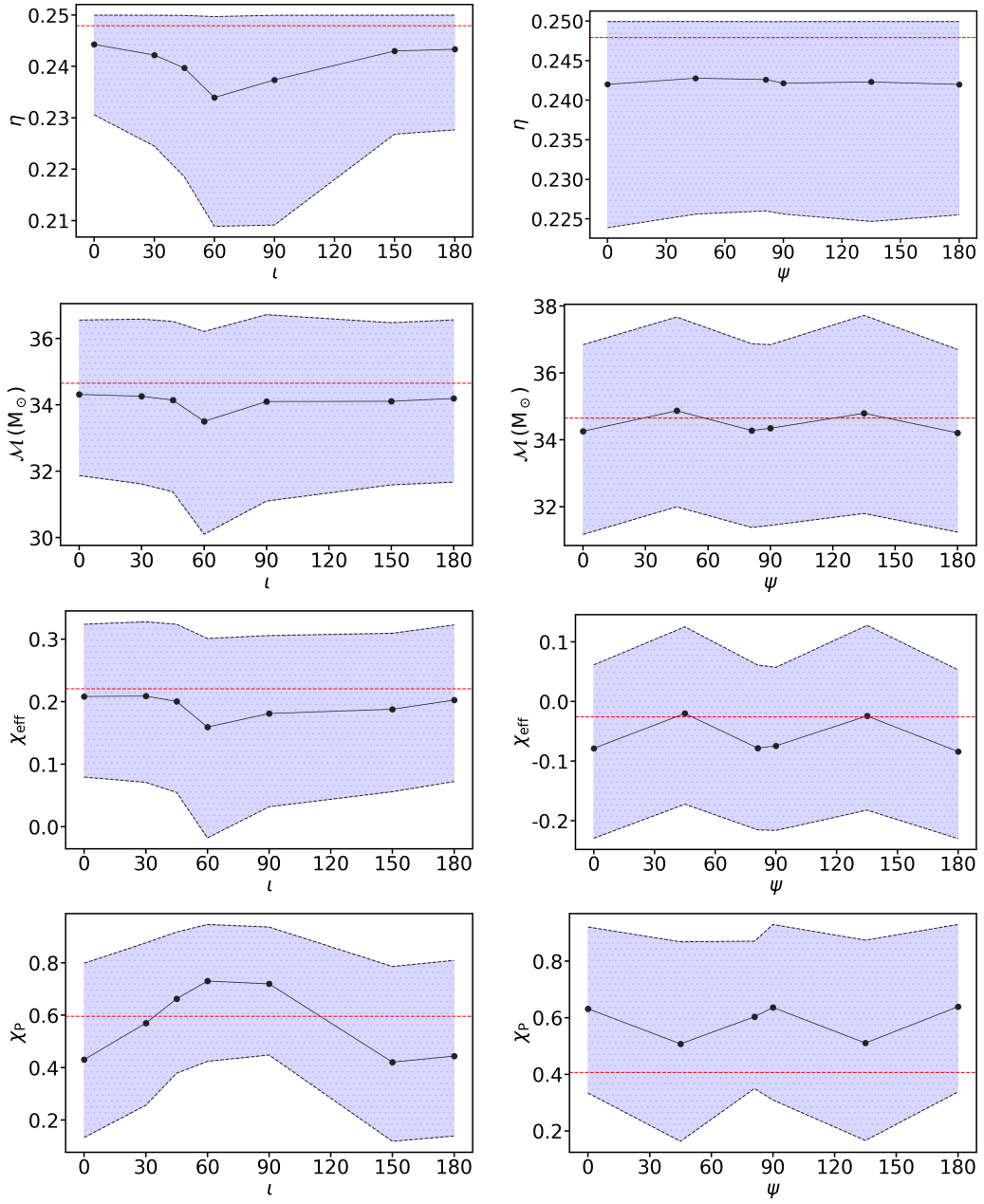

FIGURE 3.12: The above figure gives the recovered posteriors of the intrinsic mass and spin parameters $(\eta, \mathcal{M}_c, \chi_{eff}, \chi_p)$ of `IMRPhenomPv2` injections recovered with `IMRPhenomPv2` . The red-dashed line denotes the true value of each parameter, the black dots show the mean value of recovered posterior with the blue area denoting the 90% confidence regions of the same. The left column shows the results for the inclination series runs with a fixed injected $\psi = 82°$ and the right column shows the results of the polarisation runs with a fixed injected $\iota = 90°$.

NR waveforms with similar mass-ratio and aligned-spin parameters to that of GW150914 were injected over a range of inclination and polarisation values to check the behaviour of posteriors recovered by `IMRPhenomPv2`. NR waveforms are obtained via numerically solving Einstein's equations and replicate true GR waveforms from binary black-holes. The waveforms used for injections contained all $l = 2, 3, 4, 5$ and $-l \leq m \leq l$ modes. We find that errors on GW150914 parameters due to waveform inaccuracies are much smaller than those due to random noise. Overall, parameters estimated by `IMRPhenomPv2` are close to the true value with the outliers at edge-on inclinations.

Effects of precession (wobbling of binary plane) are weak for face-on or face-off signals and increase with inclination up to edge-on configurations. The inclination series runs (fixed $\psi = 82°$) show that recovered mass parameters by `IMRPhenomPv2` are close to the true parameters for most inclinations, with the largest bias observed for edge-on configurations. Bias on recovered η for CFUIB0020 waveform at $\iota = 90°$ vanishes on changing the injected polarisation value from $\psi = 82°$ to $\psi = 135°$ (see Fig: 3.5). The polarisation series runs (fixed $\iota = 90°$) show that for edge-on inclinations, the amount of bias observed for all three injections change with the polarisation value, the maximum bias being at $\psi = 82°$ (see Fig: 3.7). For a two detector network, the sky-position and polarisation values are degenerate. So exploration in the polarisation space can also be mapped to exploring the sky-positions for fixed polarisation values. The series of runs with CFUIB0020 over the inclination-polarisation space shows that (for q ~ 1.2, $0. \leq |\chi_{eff}| \leq 0.5$ & $\chi_p \sim 0.5$) there is $\sim 30° \times 30°$ region of the parameter space centered around $(90°, 82°)$ where we can expect the largest biased values to occur (see Fig: 3.8). As a very small number of signals from that region could actually be detected and as the inferred parameters of GW150914 are not in this region [170], these systematics will not dominate the errors on mass-parameters recovered for GW150914 and are unlikely to induce biases in most GW observations.

Effects of spin on the gravitational waveform are captured by two spin parameters (χ_{eff} & χ_p) in `IMRPhenomPv2` . The recovered effective spin parameter χ_{eff} is unbiased over most of inclination-polarisation space, the outlier being recovered χ_{eff} for CFUIB0020 waveform at $(\iota, \psi) = (90°, 82°)$. GW150914 was found to have $\chi_{eff} \sim 0$ and the unbiased spin recovery for CFUIB0029 ($\chi_{eff} = -0.02$) waveform over the (ι- ψ) space show that `IMRPhenomPv2` recovered spins would be consistent with the true value.

The effective precession spin parameter χ_p (see Fig: 3.10), for most inclinations recover the prior and is badly constrained. For near edge-on configurations of CFUIB0020 though, `IMRPhenomPv2` can better constrain the measured χ_p, although the parameter is still weakly constrained for the examples considered here. Constrained χ_p posteriors at near edge-on configurations can be explained by the increasing precession effects on final observed waveform when binary is highly inclined. To better understand the systematic errors from

IMRPhenomPv2 due to precession effects would require a study of injections at much higher SNRs and higher mass-ratio and spin combinations, as the precession effects would then be more pronounced and clearly measurable.

To confirm that the source of bias is from the IMRPhenomPv2 waveform inaccuracies, we injected IMRPhenomPv2 at various inclination (fixed ψ) and polarisation (fixed ι) values and recover with IMRPhenomPv2, with the intrinsic parameters set to those of CFUIB0020 (for inclination series) and CFUIB0029 (for polarisation series). Parameter recovery is good for all the runs done in this series. This indicates that the source of bias that we see is due to inaccuracies between the waveform model and real GR waveforms.

A gravitational wave signal observed from a real black hole coalescence will have all the modes present other than only the dominant quadrupole ($\ell = 2$) modes. At high mass-ratio, high-spins and near edge-on configurations, these subdominant modes are strong and their non-inclusion in the waveform model could lead to biased parameter recovery. For these reasons, the CFUIB0020 NR waveform was injected with differing mode content at face-on and edge-on inclinations but the posteriors recovered by IMRPhenomPv2 remain consistent with each other (see Fig: 3.11). So, for this mass-ratio, we conclude that the effect of higher-order modes will not be particularly important in parameter recovery and the contribution to total bias from higher-order modes can be neglected.

In this study, NR waveforms with parameters close to those of GW150914 were injected in zero-noise over a range of inclinations, polarisations and with varying mode content to check for systematic errors from using IMRPhenomPv2 waveform for parameter inference. For GW150914, we conclude that the statistical errors dominate over the systematic, and hence model waveform inaccuracies are not a major source of error. Note that these results hold only for systems with q ~ 1.2 as for larger mass-ratio values the effects of precession and sub-dominant modes would become stronger.

Chapter 4

Effects of in-plane spin direction on final waveform

In Chapter 2, we discussed precessing systems (see Section 2.5) along with a description of the `IMRPhenomPv2` waveform model (see Section 2.6.2). To recap, when the spins of the individual black holes are not (anti-)aligned to the orbital angular momentum direction $\hat{L}$, $\hat{L}$ (i.e, the orbital plane) precesses around the total angular momentum ($\vec{J}$), leading to modulations on the final amplitude and phase of the gravitational waveform. There exists a non-inertial frame wherein these precession modulations are minimized, called the Quadrupole Aligned (QA) frame. The QA frame is one for which $\hat{L}$ is approximately parallel to $\hat{z}$ $\forall t$, i.e., it approximately tracks the precession during the BBH coalescence [125], [155], [156], [189]. In this frame, almost all of the signal power is in the (2,2) and (2,-2) modes (see Fig: 4.1). In the QA frame, the fractional power in each mode corresponds to a non-precessing binary and the precessing waveform in the QA frame can be approximated by a corresponding aligned-spin waveform [125], [190], [63], at least during inspiral (see Fig: (1) of [190]).

The `IMRPhenomPv2` waveform model generates a precessing waveform by *twisting up* the aligned-spin waveform in the QA frame back to the inertial frame using a model for the Euler angles. For `IMRPhenomPv2`, the precession modulation effects are captured by a single effective spin parameter (χ_p), which is a weighted average of the in-plane spin parameters (spin parameters perpendicular to $\hat{L}$) (see Section 2.6.2 for an introduction to the `IMRPhenomPv2` waveform and definitions of the spin parameters). For the `IMRPhenomPv2` waveform, the opening angle (angle between $\hat{L}$ and $\hat{J}$) $\beta \propto S_{\perp}/(L + S_{\parallel})$, where $S_{\perp}$ and $S_{\parallel}$ are the magnitude of component of spin in the plane of the orbit and parallel to $\hat{L}$ respectively. The angle α depends on the in-plane spin components averaged over one orbit, with the initial orientation of the in-plane spin acting as an overall constant, i.e., the orientation of

the in-plane spin determines the initial direction of $\hat{L}$ about $\hat{J}$ (given a β) (see [191] for details on the implementation of the `IMRPhenomPv2` waveform model). The third angle is given as defined in Eq: 2.58. So, for this waveform model, the four dimensions of the in-plane spin are mapped to one effective precession spin parameter. This approximation works very well towards approximating precessing waveforms and the posteriors recovered with this model are consistent with other precessing models for all BBH events detected to date, although it should be noted that so far precession effects have not been strong enough to be measured. Another phenomenological waveform model for precessing systems that models effects of both spins during inspiral, `IMPhenomPv3`, has recently been developed in [130]. Work is currently ongoing to tune the merger-ringdown precession angles to NR data.

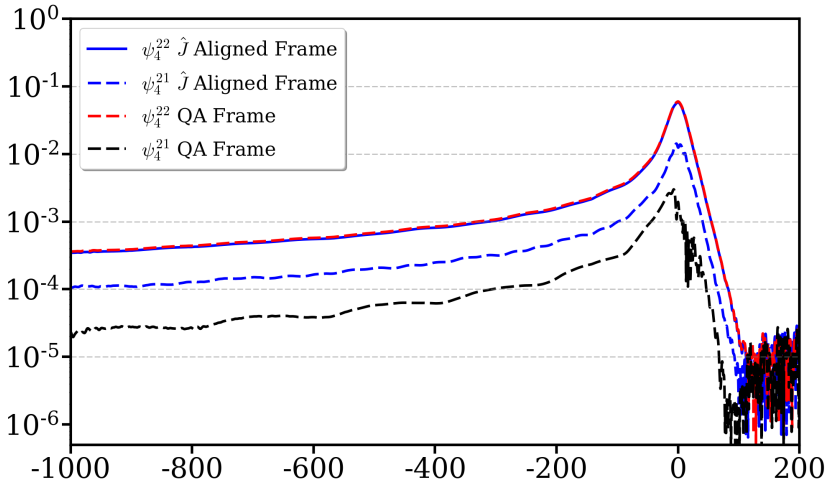

FIGURE 4.1: (2,2) and (2,1) ψ_4 modes of a precessing system in the QA frame and $\vec{J}$-aligned frame. The strength of the (2,1) mode, in the QA frame, reduces drastically due to which most of the signal power lies in the quadrupole mode. The waveforms are aligned so that $t = 0$ is the time of maximum amplitude.

One approximation in the current precession models (`IMRPhenomPv2`, `SEOBNRv3`) is the treatment of effect of the direction of the in-plane projection of the spin. We denote the angle between the in-plane projection of the spin $\vec{S}$ (for a single spin system) and the position vector $\hat{r}$ by ϕ_{SR}. In current models the only effect of changing ϕ_{SR}, is an overall phase shift at a given reference time. The other effect that is not modelled, is the radiation of linear momentum perpendicular to the orbital plane. Other than in equal mass non-spinning systems, gravitational waveforms from all systems have a inherent asymmetry in the modes, the behaviour of which is quite different for precessing systems (for details see Section 4.1). In this study, we wish to determine the effects of modifying the direction of the in-plane spin on the final gravitational waveform and attempt to place bounds on when it could be possible to observe and distinguish these variations. We also check for effects of including and removing the mode-asymmetry content from the waveforms on distinguishability of the signals from two systems and check how disregarding mode-asymmetry content from precessing waveforms affects the results.

To do that, I performed a set of NR simulations of unequal mass single-spin BBH systems with the spin lying in the orbital plane and at varying orientations with respect to $\vec{r}$ at the reference frequency. For a given mass-ratio, one of these NR waveforms is chosen as the proxy *template* waveform, with the others being the *signal* waveforms. We then compute the match (Section 4.3.1) between the two waveforms over the (θ, ϕ) space where the match is maximised over the time and phase of arrival, signal and template polarisation values and over the template (θ, ϕ) space (Section 4.3.2). From the maximised match values, we determine the critical (minimum) SNR of the signal at which the template waveform will be able to distinguish the signal source as a different one from itself (Section 4.3.4). For these cases with different spin directions, we wished to investigate *if* we could decouple the effect of mode asymmetry and orbital precession effects and attempt to estimate the dominant contributions towards the overall match (and hence, the measurability of a signal). Such a study is not conclusive, because without a full waveform model, we are unable to maximise over the intrinsic parameters $(M_{total}, \eta, \chi_{eff}, \chi_p)$ and so cannot comment on the full bias that might be incurred by using a model that ignores these physical effects.

To generate the NR waveforms for this study, we wished to generate the initial data of the BBH systems so that all start at a given reference frequency with the required spin orientations. To obtain the initial data, I modified a code in `Mathematica` of the simulations that use the PN equations of motion to obtain the initial data for the required configurations (the modified code is the same one as used in [125], [178], [69] to generate the initial parameters). In Section 4.1, I will explain the mode-asymmetry for precessing systems and provide some examples of the same. Section 4.2 provides an explanation of the implementation of the initial data generation code and details of the NR waveforms used in this study. Section 4.3 explains the match computation procedure for precessing waveforms, the connection between the match values and distinguishability condition and the maximisation procedure employed to get the final match. The results of the study are given in Section 4.4 with the conclusions of the study in Section 4.5.

4.1 Mode asymmetry

Gravitational wave signals can be decomposed in the spin weight -2 spherical harmonic basis (${}^{-2}Y_{lm}(\theta, \phi)$) to obtain the gravitational wave modes (h_{lm}). For non-spinning and aligned-spin waveforms the orbital plane remains steady. In a frame where the orbital plane lies in the x-y plane ($\hat{L} \parallel \hat{z}$), there exists a reflection symmetry about the x-y plane. Due to this symmetry, for models constructed in this frame, the waveform modes are related as,

$$h_{lm}(t) = (-1)^l h^*_{l-m}(t), \tag{4.1}$$

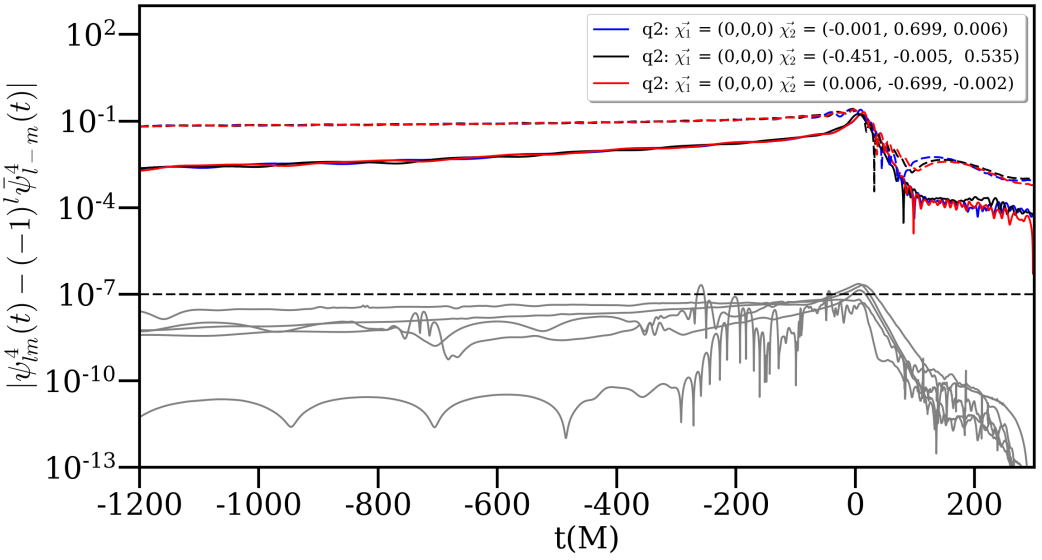

FIGURE 4.2: The figure plots the quantity $|\psi^4_{lm} - (-1)^l \psi^{4*}_{l-m}|$ for the ψ_4 modes of the publicly available SXS waveforms (`SXS:BBH:0001`, `SXS:BBH:0184`, `SXS:BBH:0182`, `SXS:BBH:0257` and `SXS:BBH:0242`) [116] for different non-spinning and aligned-spin configurations (shown in grey). The Blue, Black and Red lines plot the same quantity for a set of BAM precessing waveforms. The solid [dashed] lines give the difference in the (2,2) [(2,1)] modes. The waveforms are aligned so that $t = 0$ is the time of maximum amplitude.

with $\phi_{lm} \propto m\phi_{orb} \implies \phi_{22} + \phi_{2-2} = 0$. For precessing systems, due to the wobbling of the orbital plane, these relationships do not hold.

Let me demonstrate this in slightly more detail. The relation in Eq: 4.1 will hold for the ψ_4 modes of the NR waveform and the quantity $|\psi^4_{lm} - (-1)^l \psi^{4*}_{l-m}|$ would give an idea of the validity of the relationship.

As we can see from Fig: 4.2, the quantity $|\psi^4_{lm} - (-1)^l \psi^{4*}_{l-m}|$ is non-zero for precessing systems, whereas for aligned-spin and non-spinning systems, we just see numerical noise. Also, the value for the (2,1) mode differences of the precessing system are almost 100 times larger than their corresponding (2,2) mode differences. Fig: 4.3 plots the quantity $\phi_{22} + \phi_{2-2}$ for an aligned spin and a precessing system. Whereas $\phi_{22} + \phi_{2-2} = 0$ throughout the coalescence for aligned-spin waveforms, the same is not true for the precessing waveform. This equality holds precisely for the aligned-spin case, and this symmetry is exploited in the BAM numerical simulations by evolving only the $z > 0$ half of the simulation domain.

For Fig: 4.2, Fig: 4.3 and Fig: 4.4, the NR modes of non-spinning and aligned-spin binaries are defined in the $\hat{L}$ aligned frame while the precessing modes are defined in the $\hat{J}$ aligned frame. It is pretty straightforward to see that if the wave frame is rotated to an arbitrary direction, the behaviour between the modes for all systems would change. Also, we see that in a special frame, there exists a symmetry between the modes of a non-spinning and

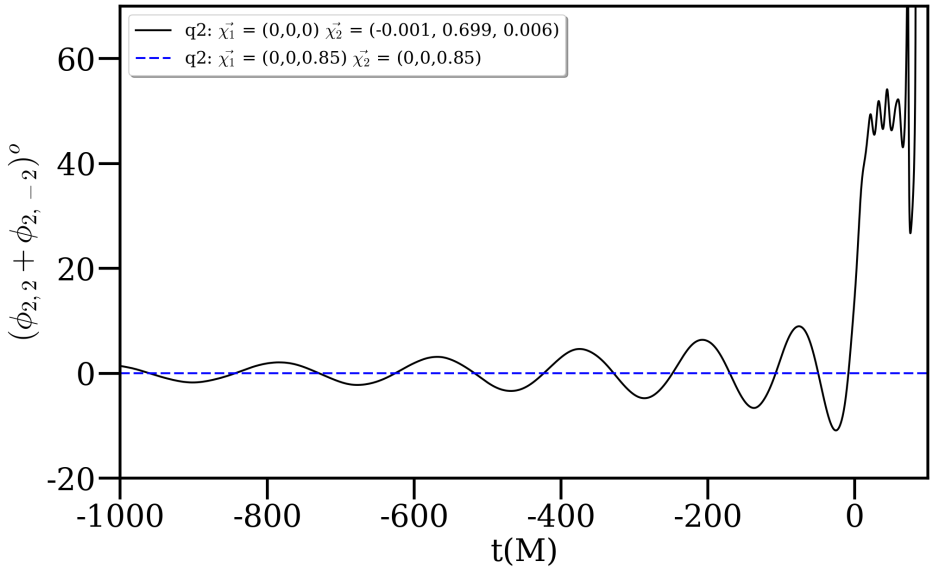

FIGURE 4.3: The quantity, $\phi_{22} + \phi_{2-2}$ for an aligned-spin (SXS:BBH:0257 [116]) shown in dashed-blue and the q2a07p0 precessing system shown in black(see Tab:4.1). The waveforms are aligned so that $t = 0$ is the time of maximum amplitude.

aligned-spin system which does not exist for precessing systems. So, we need a frame-independent way to characterize these asymmetries in the modes.

As mentioned earlier, the relation Eq: 4.1 holds for non-spinning and aligned-spin systems due to the choice of initial axes during the model construction ($\hat{L} \parallel \hat{z}$). Other than for equal mass non-spinning systems, there exists a inherent asymmetry in the emission of gravitational radiation from the system which leads to the final black hole obtaining a non-zero momentum along some direction. For non-precessing systems, this asymmetry is captured by the higher-harmonics and the recoil velocity can be computed via the overlap of different harmonics (see Fig:6 of [136]).

In Sec. IIB of [131], the authors provide a way of defining a rotationally invariant measure for mode-asymmetries, which I will briefly explain here. Let $f(\hat{r})$ be a function defined on a unit sphere. Define an operator A such that,

$$A[f(\hat{r})] = f(-\hat{r}). \tag{4.2}$$

For spin weighted fields, A reverses the sign of the spin weight. Taking a complex conjugate of the spin weighted field reverses the sign of the spin weight. Thus, to keep the spin weight constant, define another operator $\bar{A}$ such that,

$$\bar{A}[f(\hat{r})] = f^*(-\hat{r}). \tag{4.3}$$

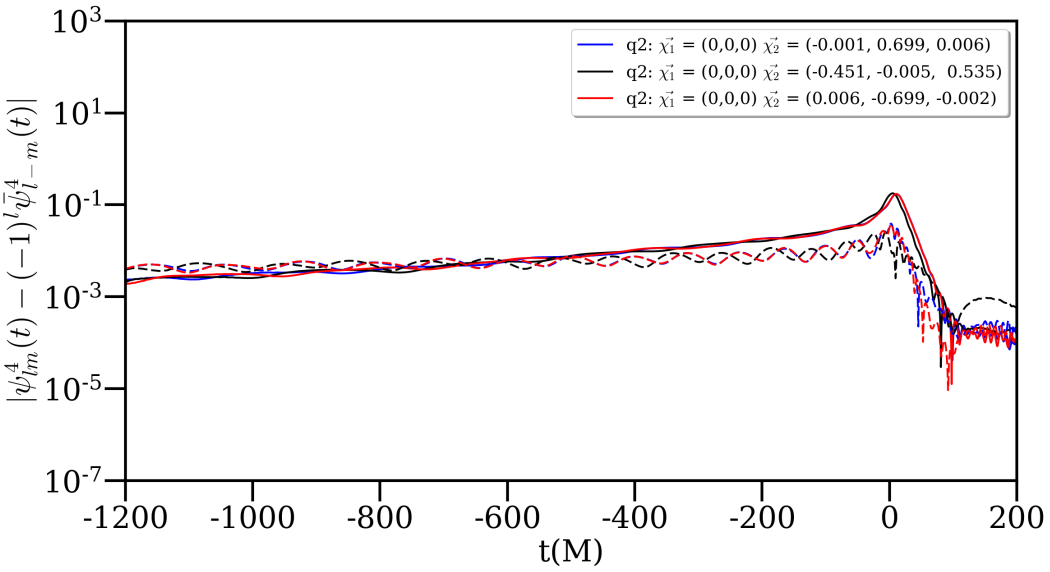

FIGURE 4.4: $|\psi^4_{lm} - (-1)^{l+m}\psi^{4*}_{l-m}|$ for the precessing systems plotted in Fig: 4.2. Note that the (2,1) and (2,2) mode differences are now of the same order. The waveforms are aligned so that $t = 0$ is the time of maximum amplitude.

So, for any gravitational wave mode $h_{lm}(t)$, operation of $\bar{A}$ gives [1],

$$\bar{A}[h_{lm}(t)] = (-1)^{l+m} h^*_{l-m}(t). \tag{4.4}$$

As shown in Appendix C of [131], the operator $\bar{A}$ is the parity operator P_- and the relation Eq: 4.4 is a consequence of,

$$P_- h_{lm}(t) = (-1)^{l+m} h^*_{l-m}(t). \tag{4.5}$$

So, the quantity $|\psi^4_{lm} - (-1)^l \psi^{4*}_{l-m}|$ plotted in Fig: 4.2 gives the difference in modes as reflected about the x-y plane and $|\psi^4_{lm} - (-1)^{l+m}\psi^{4*}_{l-m}|$ will give the difference along $\hat{r}$ and $-\hat{r}$. In Fig: 4.4, I plot the quantity $|\psi^4_{lm} - (-1)^{l+m}\psi^{4*}_{l-m}|$ for a precessing NR simulation; and now we see that the mode differences for (2,2) and (2,1) modes are of the same order.

Consider the operator, $\Pi = \frac{1}{2}(1 - \bar{A})$. Now, $\Pi[f(\hat{r})] \propto f(\hat{r}) - f^*(-\hat{r})$. So, we can understand Π as the operator that gives the difference in the gravitational wave emission along opposite directions of a sphere. With this, the authors in [131] define the normalized asymmetry as,

$$a = \sqrt{\frac{\int |\Pi[h]|^2 \mathrm{d}\Omega}{\int |h|^2 \mathrm{d}\Omega}} = \sqrt{\frac{\sum_{l,m} |h_{lm} - (-1)^{l+m} h^*_{l,-m}|^2}{4 \sum_{l,m} |h_{lm}|^2}}. \tag{4.6}$$

[1] See Appendix C of [131] for a thorough derivation.

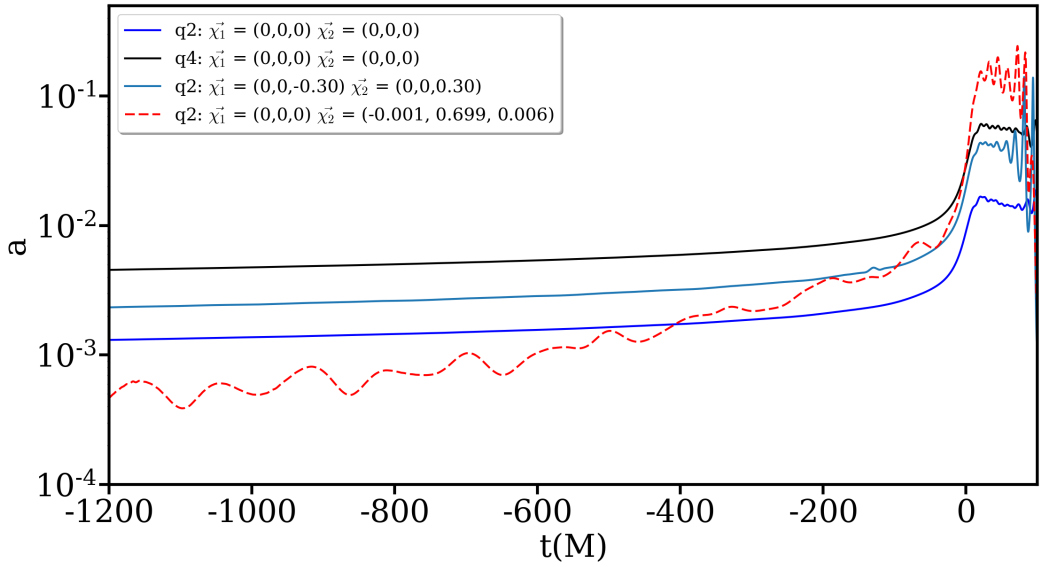

FIGURE 4.5: Normalized mode asymmetry (see Eq: 4.6) for the SXS systems (`SXS:BBH:0184`, `SXS:BBH:0182` and `SXS:BBH:0242` [116]) and q2a07p0 simulation (see Tab:4.1). The waveforms are aligned so that $t = 0$ is the time of maximum amplitude.

Fig: 4.5 shows the plots of the normalized mode asymmetry for two non-spinning, one aligned-spin and one precessing system, where $'a'$ is computed with only the l=2 modes. For equal mass non-spinning systems, $a = 0$, but as we can see from the figure, for non-equal mass systems such mode-asymmetries are an inherent part of the waveform behaviour and cannot be removed by any frame transformation. For precessing systems, the behaviour of a across time is not smooth (unlike the others) and as the system nears merger, a increases drastically. The mode-asymmetry is $\sim \mathcal{O}(10)$ larger for the precessing waveform at merger than the corresponding non-spinning waveform and about $\sim$ 3 to 4 times than the corresponding aligned-spin system.

Current waveform models twist-up an aligned-spin waveform from the QA frame to an inertial frame, and as Fig: 4.5 shows, this procedure will not capture the mode-asymmetric content of the true waveform.

4.2 NR Waveforms Generation

For this work, we produce single-spin NR waveforms such that all systems start at the same reference frequency and with pre-specified spin directions. For a single spin precessing system, we can completely specify the spin direction by two angles, i) the angle between the spin-vector ($\hat{S}$) and angular momentum vector ($\hat{L}$) which we call θ_{SL}, and ii) the angle

between the position vector and the projection of spin on the orbital plane, which we call ϕ_{SR}.

In previous works ([125], [178], [69]), the code used to generate the initial parameters for precessing systems would evolve the PN expressions from a given initial condition with the parameters read off at the reference frequency. By construction, we could specify the spin orientation only at the start of the PN waveform and there was no control over the direction of spin at the starting point of the NR evolution. For this work, we need to obtain the data such that the spin vectors have the specified (θ_{SL}, ϕ_{SR}) angles at the reference frequency.

4.2.1 Initial Data Code

Over the course of early inspiral, the angle between $\hat{S}$ and $\hat{L}$ (or value of $S_{\|}$) is almost constant (it changes by $\sim 1^o$) for most systems, the exception being the systems with transitional precession. As we will not be considering systems showing transitional precession, once we specify θ_{SL}, we expect it to stay approximately constant [125]. To obtain the *exact* final parameters, we technically also should iterate over the $S_{\|}$ component, but this then makes the problem 2-dimensional which would increase the overall computational time and cost of the root finding procedure. Hence, we fix θ_{SL} at the start of the evolution and do not iterate over this parameter.

We employ a brute-force strategy to get the initial parameters. This is required for these systems because the frequency with which $S_{\perp}$ rotates around $\vec{r}$ increases over the course of the inspiral. Thus it is hard to pinpoint the exact direction of the initial spin ($\vec{S_{ini}}$) to obtain the required ϕ_{SR} at f_{start}.

Step 1:

This step consists of two iterations.

Iteration 1: At the start of this iteration, the spin vector is only along the x-axis (S_{ini}), i.e, $S_y = S_z = 0$, and as the two black holes are initially placed along the x-axis; $\phi_{SR} = 0$ at $t = 0$. The spin is placed on the heavier black-hole. Then, this spin vector is rotated counterclockwise by angle ($\theta_{SL} - \frac{\pi}{2}$) about the y-axis (to get the correct angle between $\vec{L}$ and $\vec{S}$, as $\vec{L} \parallel \hat{z}$ at the start of the simulation) and the PN solver is run until we reach f_{start}. The separation between the black holes at the start of the PN evolution is user specified and we place the black holes $\sim$ 40M apart. The PN solver, along with other quantities, returns the time (t_0) at which the orbital frequency reaches f_{start}, the time (t_1) around t_0 at which $\phi_{SR}(t_1) = \phi_{SR}^{target}$, $\phi_{SR}(t_0)$ and the relative error (ω_{err}) between the orbital frequencies at t_0 and t_1. At each iteration, $\phi_{SR}^{t_0,i}$ is stored. If ϕ_{SR} at t_0 is not ϕ_{SR}^{target} and if ω_{err} is larger than a pre-specified threshold (ω_{err}^{F}), then we record the value of $\phi_{SR}^{t_1}$, let's call it ϕ_{SR}^{1}. The

threshold error is set by the user, and for the initial data generated for this study, we set $\omega_{err}^{F} = 1\%$.

Iteration 2: For the second iteration, the spin vector S_{ini} is rotated by $(\theta_{SL} - \frac{\pi}{2})$ about the y-axis and then by $(-\phi_{SR}^{1})$ about z-axis and the PN solver is run again. If the above two conditions are satisfied ($\omega_{err} < \omega_{err}^{F}$ & $\phi_{SR}^{t_1}$ = ϕ_{SR}^{target}) then the parameters are read off at the time t_1; if not, we head to the second step. Also, if we need to head to step two, we call the value of $\phi_{SR}^{t_1}$ stored during this second iteration as ϕ_{SR}^{2}.

Step 2:

This step can consist of one iteration or multiple iterations depending on the parameters obtained. Note that in all the future iterations, the spin (S_{ini}) is first rotated by $(\theta_{SL} - \frac{\pi}{2})$ about the y-axis and then by angle $(-\phi_{SR}^{i})$ for each future iteration.

Iteration 3: If the correct parameters are not obtained in iteration 2 of the first step, we define a angle correction parameter, let's call it ϕ_{corr}. The term $\omega_{err} - \omega_{err}^{F}$ gives a indication of how close the parameters are to the required value and the value of ϕ_{corr} is determined by the same. Noting that, if the condition $(\omega_{err} - \omega_{err}^{F} > \frac{1}{2}\omega_{err}^{F})$ is satisfied, then $\phi_{corr} = 10^{o}$, else $\phi_{corr} = 5^{o}$. Once ϕ_{corr} is defined, we define $\phi_{SR}^{3} = \phi_{SR}^{2} + \phi_{corr}$. Because this system is not convergent, the choice of either adding or subtracting the correction is arbitrary. Using this angle ϕ_{SR}^{3} to rotate (S_{ini}), the PN solver is run again and the output parameters recorded.

Iteration *n* > 3 : Before we start these iterations, we check if $\phi_{SR}^{t_0,3} > \phi_{SR}^{t_0,2}$. If that is the case then it is an indication that the initial spin is being rotated in the wrong direction, and for each subsequent iteration we define $\phi_{SR}^{i} = \phi_{SR}^{2} - (n-3) \times \phi_{corr}$, if not, $\phi_{SR}^{i} = \phi_{SR}^{2} + (n-2) \times \phi_{corr}$. Based on these angles, we keep on rotating (S_{ini}) until the right parameters are obtained.

Once the parameters are within the specified tolerances at f_{start}, the system is rotated so that the black holes lie along the y-axis. This has to be done as the solver that produces the initial data (Section 2.3.1) on a grid to be used by BAM (Section 2.3.2) and the BAM code require the black holes to be along the y-axis. But, this rotation does not ensure that the total angular momentum, $\vec{J}$, will be along the z-axis. The parameters generated in this manner can then be passed to the BAM code to obtain the numerical relativity waveform through late-inspiral, merger and ringdown stages.

The BAM code returns, along with other physical quantities, the ψ_4 modes of the gravitational wave, which can be used to compute the strain. As mentioned before, the data returned by the initial data code does not have $\vec{J}$ along z-axis. Due to that, during the coalescence, along with the precession of $\hat{L}$ about $\hat{J}$, $\hat{J}$ also precesses about the fixed $\hat{z}$ axis leading to extra (unphysical) modulations on the precessing waveform. It is cleaner to

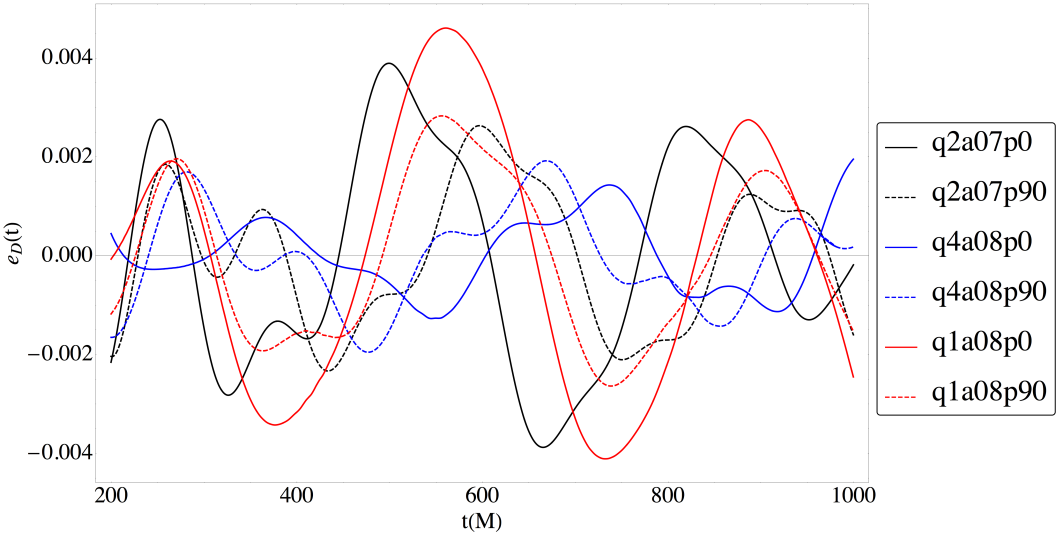

FIGURE 4.6: The eccentricity $(e_D(t))$ estimated from the the co-ordinate separation for the cases q1a08p0 (q1a08p90), q2a07p0 (q2a07p90) and q4a08p0 (q4a08p90) which are shown in Red (dashed-red), Black (dashed-black) and Blue (dashed-blue) respectively.

perform the analysis of the strain data in a frame where the total angular momentum ($\vec{J}$) is along the z-axis as the extra modulations in the waveform due to precession of $\vec{J}$ are muted. We can do this rotation without loss of generality as this is a inertial rotation, i.e., the Euler angles are computed only once at from the data at the start of the simulation and the same rotation is applied throughout the coalescence. Hence, in this frame, modulations due to precession of $\vec{J}$ are muted, but modulations due to precession of $\hat{L}$ remain. So, I wrote a `Mathematica` code that would parse through the folder containing the ψ_4 mode data, calculate the rotation angles to align $\vec{J}$ along the z-axis with the third angle fixed so that $\vec{L}$ lies in the x-z plane at the start of the simulation and rotate all the modes and the other physical quantities to this frame. These rotated data are exported to another folder and these are the data used for analysis.

4.2.2 Details of the simulations

For this study, a set of 12 new NR simulations were performed with the BAM code, which are split into three sets based on mass-ratio of the system; q=2, q=4 and q=1 series. The q2 series is a set of four q=2 NR waveforms with a total in-plane spin of $|\chi| = 0.7$ with (θ_{SL})=90° and (ϕ_{SR}) = (0°, 90°, 180°, 270°). The q4 series is a set of four q=4 NR waveforms with $|\chi| = 0.8$ and the same (θ_{SL}, ϕ_{SR}) configurations as q2. The series q1 is a set of four equal mass systems where both black holes are spinning and with equal and opposite in-plane spins of $|\chi_i| = 0.8$, also known as the *super-kick* configurations [138], [139], [140](see Fig: 2.8 for the final recoil velocities from this series of runs). The super-kick configurations

are non-precessing and due to the symmetry of the system, the final recoil is along $\pm\hat{z}$. In the configurations below, $m_2 > m_1$ and $\vec{S_1}$ = (0,0,0) for the q2 and q4 series. For the names, we use the following convention : q(mass-ratio of system)a(total spin of system)p(angle between in-plane spin and position vector ϕ_{SR}), so the first simulation in q2 series would be q2a07p0. The angle, θ_{LS}, between $\hat{L}$ and $\hat{S}$ is always 90° for these systems. For the q1 series waveforms, remember that total spin ($\vec{S_1} + \vec{S_2}$)=0, but we follow the above convention naming for simplicity. We also use three extra NR simulations with different total in-plane spin values (with same θ_{SL} and $\phi_{SR} = 0$), which are used as comparison cases.

The initial data for the q=2 series of runs was generated by running the initial data code from Section 4.2.1 for $\phi_{SR} = 0$ and the spins were then rotated by hand around $\hat{L}$ to get the data for $\phi_{SR} = 90, 180, 270$. For all the q=1 and q=4 systems though, the initial data was generated from the code separately for each simulation.

It is possible that there exists some residual eccentricity once the NR simulation is started with the quasi-circular parameters obtained from Section 4.2.1. So, we need to i) estimate the eccentricity (e) and ii) if the eccentricity is above a given threshold ($e > \mathcal{O}(10^{-3})$), modify the momenta until the estimated e is within the threshold. We estimate the eccentricity from the co-ordinate separation (as given in Eq: (3) of [177]). There have been various studies where the authors have looked at reducing the eccentricity for NR simulation by modifying the tangential/radial component of the momenta (see [177], [192] and more recently [193]). For these simulations though, we choose to change the overall momenta by some percent of itself (for eg: either add or reduce the $\vec{p}$ by 1% of $|\vec{p}|$). For the q=2 system, we did not require to change the momenta (as the first set of parameters gave low eccentricity), but for q4a08p0 (q4a08p90) system we changed the momenta by -1% (+2.5%)$|\vec{p}|$ and for the q1a08p0 (q1a08p90) we changed the momenta by -1% (0%)$|\vec{p}|$ to get the low-eccentricity parameters. See Fig: 4.6 for the eccentricities of the simulations generated for this study. Note that the eccentricities for systems with an angle difference of $\phi_{SR} \pm \pi$ have the same values, for e.g., the parameters required for q4a08p0 and q4a08p180 are the same.

Config	q	$\vec{S_1}$	$\vec{r} = D/M$	$\vec{p} = \vec{p_1} - \vec{p_2}$	$\omega_{start}(fM)$	ϕ_{SR}	θ_{SL}
q1a08p0	1	(0, -0.799, -0.001)	(0, 11.552, 0)	(-0.174, -0.001, 0)	0.0225	0	90
q1a08p90	1	(0.7999, 0, -0.0012)	(0, 11.623, 0)	(-0.174, -0.001, 0)	0.0225	90	90
q1a08p180	1	(0, 0.7999, -0.0012)	(0, 11.623, 0)	(-0.174, -0.001, 0)	0.0225	180	90
q1a08p270	1	(-0.7999, 0, -0.0012)	(0, 11.623, 0)	(-0.174, -0.001, 0)	0.0225	270	90
q2a07p0	2	(-0.001, 0.699, 0.006)	(0., 10.810, 0.)	(-0.105, -0.001, 0.123)	0.025	0	90
q2a07p90	2	(-0.451, -0.005, 0.535)	(0., 10.810, 0.)	(-0.105, -0.001, 0.123)	0.025	90	90
q2a07p180	2	(0.006, -0.699, -0.002)	(0., 10.810, 0.)	(-0.105, -0.001, 0.123)	0.025	180	90
q2a07p270	2	(0.448, -0.005, -0.537)	(0., 10.810, 0.)	(-0.105, -0.001, 0.123)	0.025	270	90
q4a08p0	4	(0.0007, 0.799, -0.005)	(0. , 11.486, 0.)	(-0.111, -0.0004, 0.014)	0.0225	0	90
q4a08p90	4	(-0.793, 0, 0.099)	(0. , 11.486, 0.)	(-0.111, -0.0005, 0.014)	0.0225	90	90
q4a08p180	4	(-0.0007, -0.799, -0.005)	(0. , 11.486, 0.)	(-0.111, -0.0004, 0.014)	0.0225	180	90
q4a08p270	4	(0.792, 0, -0.110)	(0. , 11.486, 0.)	(-0.111, -0.0005, 0.0147)	0.0225	270	90
q4a04p0	4	(-0.001, 0.399, -0.00007)	(0. , 11.486, 0.)	(-0.111, -0.0004, 0.014)	0.0299	0	90
q2a04p0	2	(-0.00008, 0.3999, -0.0008)	(0. , 11.6299, 0.)	(-0.153, -0.0009, 0.015)	0.0224	0	90
q2a08p0	2	(0.0005, 0.799, -0.003)	(0. , 11.5709, 0.)	(-0.153, -0.0009, -0.0243)	0.023	0	90

TABLE 4.1: Table of NR simulations used for this study. From left to right, the columns show the name of the simulation, the mass-ratio of the system, value of the spin on the larger black hole at the reference frequency, the separation between the black-holes at the reference frequency, the total momenta of the system at the reference frequency, the reference frequency at which the simulation starts and the values of the ϕ_{SR} and θ_{SL} angles respectively. For the q1 series, note that $\vec{S_2} = -\vec{S_1}$.

4.3 Analysis of the data

We have performed the above three sets of simulations (the simulations for the comparison set were done at Caridff [194] in an attempt to investigate the effects of varying the spin-angle parameter (ϕ_{SR}) on the final gravitational waveform. Such a study would enable us to determine whether the effect of this parameter would be large enough to be detectable in GW observations, how strong the signal should be for detectability and thus whether such a parameter would be essential to model. To do that, we require to quantify the level of agreement/disagreement between different waveforms and this is done by computing the *match* between two waveforms.

Given two NR waveforms, we can calculate the match $\mathcal{M}(h_1, h_2)$, where the match between two waveforms, $h_1(f)$ and $h_2(f)$ is given as,

$$\mathcal{M}(h_1, h_2) = 4\mathrm{Max}_{t_0,\phi_0}\left[\mathrm{Re}\int_0^\infty \frac{h_1(f)h_2^*(f)}{S_n(f)}\right], \tag{4.7}$$

where the integral is maximised over time (t_0) and phase shifts (ϕ_0). The normalized match between two waveforms is 1 if both are exactly the same, and less than unity otherwise. This allows us to quantify the effect of a given parameter on the waveform by comparing

waveforms within a set with each other. For precessing systems, the match computations are a bit more involved, but we defer further discussion to Section 4.3.1.

Once we have the match maximised over the relevant parameters, we wish to check *if* the in-plane spin effects can be measured and estimate how strong the signal should be so that it is distinguishable from the template. To do that, we use a relation between the match value of a signal and template waveform and the corresponding critical SNR required for the template waveform to distinguish the signal as a different system. For example: for the q2 series analysis, suppose we use the q2a07p0 (q2a07p90) waveform as the template (signal). The only difference between q2a07p0 and q2a07p90 is the initial in-plane spin direction with all other parameters being the same. For a particular signal coming from (θ_s, ϕ_s), we can get the maximum match $\mathcal{M}_{max}$ with the template that gives us a corresponding SNR value (ρ_c) for the signal. The SNR (ρ_c) then is an estimate of how strong the signal (q2a07p90) should be for the template (q2a07p0) to distinguish the system as a different one from itself.

In the following sections we will discuss how we compute the matches for the precessing systems, the maximisation procedure of obtaining the maximised match and the connection between match values and critical distinguishability SNR.

4.3.1 Match calculation

Given a signal and model waveform, the agreement between the two can be gauged from the match value [2]. This number is given by the noise-weighted inner product of the signal $(h^S(f))$ and model $(h^M(f))$ detector response (see Eq: 4.7 with $h_1(f) \equiv h^S(f)$ and $h_2(f) \equiv h^M(f)$).

The detector response of a gravitational wave arriving from directly overhead a detector (so that the sky position $(\alpha, \delta) = (0, 0)$ in Eq: 1.27 and Eq: 1.28) is given by (see Eq: 1.29),

$$h_{resp}(t) = h_+(t)\cos(2\psi) + h_\times(t)\sin(2\psi), \tag{4.8}$$

where ψ is the polarisation value of the waveform. Defining the complex waveform as,

$$h_{comp}(t) = h_+(t) - ih_\times(t), \tag{4.9}$$

gives us a way to write the total response in terms of the complex waveform and polarisation as,

$$h_{resp}(t) = \mathrm{Re}\left[h_{comp}(t)e^{2i\psi}\right]. \tag{4.10}$$

[2] This way of computing matches noted below between precessing waveforms is described in Appendix B of [63] and we closely follow that prescription here.

Using the above form of response in the match function [3],

$$\mathcal{M}(h^S(f), h^M(f)) = \mathrm{Re}\left[\int_{-\infty}^{\infty} \frac{h^S(f)h^{M*}(f)}{S_n(|f|)} e^{2i(\psi_S - \psi_M)} \mathrm{d}f\right] + \mathrm{Re}\left[\int_{-\infty}^{\infty} \frac{h^S(f)h^M(-f)}{S_n(|f|)} e^{2i(\psi_S + \psi_M)} \mathrm{d}f\right], \tag{4.11}$$

where ψ_S and ψ_M are the polarisation values of the signal and model waveform respectively and $S_n(|f|)$ is the noise power spectral density.

Once we have the form of the inner product (i.e., match) between two waveforms, it provides us a straightforward way to define the norm of a waveform as,

$$\langle h(f)|h(f)\rangle = ||h(f)||^2 = \mathrm{Re}\left[\int_{-\infty}^{\infty} \frac{h(f)h^*(f)}{S_n(|f|)} \mathrm{d}f\right] + \mathrm{Re}\left[\int_{-\infty}^{\infty} \frac{h(f)h(-f)}{S_n(|f|)} e^{4i\psi} \mathrm{d}f\right]. \tag{4.12}$$

Now, we need the normalized match maximised over ψ_M, i.e.,

$$\mathrm{Max}_{\psi_M} \left\langle \frac{h^S(f)}{||h^S(f)||} | \frac{h^M(f)}{||h^M(f)||} \right\rangle = \mathrm{Re}\left[\frac{1}{||h^S(f)|| \times ||h^M(f)||} \int_{-\infty}^{\infty} \frac{h^{M*}(f)e^{-2i\psi_M}}{S_n(|f|)} \left[h^S(f)e^{2i\psi_S} + h^{S*}(-f)e^{-2i\psi_S}\right] \mathrm{d}f\right]. \tag{4.13}$$

Let us define the quantities $(N_1, N_2, O, \sigma_N, \sigma_o)$

$$N_1 = \int_{-\infty}^{\infty} \frac{|h^M(f)|^2}{S_n(|f|)} \mathrm{d}f, \tag{4.14}$$

$$N_2 e^{i\sigma_N} = \int_{-\infty}^{\infty} \frac{h^M(f) * h^M(-f)}{S_n(|f|)} \mathrm{d}f, \tag{4.15}$$

$$O e^{i\sigma_o} = \int_{-\infty}^{\infty} \frac{h^{M*}(f)}{S_n(|f|)} \left[h^S(f)e^{2i\psi_S} + h^{S*}(-f)e^{-2i\psi_S}\right] \mathrm{d}f. \tag{4.16}$$

Now,

$$||h^M(f)||^2 = \mathrm{Re}\left[\int_{-\infty}^{\infty} \frac{h^M(f)h^{M*}(f)}{S_n(|f|)} \mathrm{d}f\right] + \mathrm{Re}\left[\int_{-\infty}^{\infty} \frac{h^M(f)h^M(-f)}{S_n(|f|)} e^{4i\psi_M} \mathrm{d}f\right], \tag{4.17}$$

$$= N_1 + N_2 e^{i(\sigma_N + 4\psi_M)}, \tag{4.18}$$

and we can rewrite the integral in Eq: 4.13 as $O e^{-i(2\psi_M - \sigma_o)}$.

[3] Note that we can get Eq: 4.11 from Eq: 4.7 by noting $4\mathrm{Re}\left[\int_0^{\infty} a(f)b^*(f)\right] \equiv \left[\int_{-\infty}^{\infty} a(f)b^*(f) + \int_{-\infty}^{\infty} a^*(f)b(f)\right]$

Using the above relations, we can analytically compute the match maximised over model polarisation ψ_M by first rewriting the match function in terms of the quantities $(N_1, N_2, O, \sigma_N, \sigma_o)$. We can optimize the match value for different values of signal polarisation, and the maximum match we get is,

$$\mathrm{Max}_{\psi_M}\left\langle \frac{h^S(f)}{||h^S(f)||} | \frac{h^M(f)}{||h^M(f)||} \right\rangle = \mathrm{Max}_{\psi_M}\left[\frac{O}{||h^S(f)||}\frac{\cos(2\psi_M - \sigma_o)}{\sqrt{N_1 + N_2\cos(\sigma_N + 4\psi_M)}}\right], \tag{4.19}$$

$$= \frac{O}{||h^S(f)||}\sqrt{\frac{N_1 - N_2\cos(\sigma_N + 2\sigma_o)}{N_1^2 - N_2^2}}, \tag{4.20}$$

for optimal ψ_M being,

$$\psi_M^{opt} = \frac{1}{2}\tan^{-1}\frac{N_1\sin(\sigma_o) + N_2\sin(\sigma_N + \sigma_o)}{N_1\cos(\sigma_o) - N_2\cos(\sigma_N + \sigma_o)}. \tag{4.21}$$

Now, we want that match value which is maximised over the time and phase shift of the model waveform compared to the signal. Calculating the match optimized over template polarization is equivalent to the maximising the match over an overall phase-shift. To obtain the time-shift optimized match, notice that the Fourier transform of a time-shifted function behaves as,

$$\mathcal{F}\left[x(t - t_0)\right](f) = \int_{-\infty}^{\infty} x(t - t_0)e^{2\pi i f t}\mathrm{d}t = \mathcal{F}\left[x(t)\right](f)e^{2\pi i f t_0} = x(f)e^{2\pi i f t_0}. \tag{4.22}$$

Time shifting the model waveform $h^M(f)$ by t_0 adds an additional factor of $e^{-2\pi i f t_0}$ to Eq: 4.11. Optimization over the time shift can then be done by taking the inverse Fourier transforms of the integrals and then finding the maximum value of the same.

Computing matches between two precessing waveforms then follows the algorithm below:

Algorithm to compute precessing match:

1. Input $\rightarrow$ Frequency series of model waveform $(h^M(f))$, signal waveform $(h^S(f))$ and PSD $(S_n(f))$ with the signal polarisation ψ.
2. $\sum \mathrm{df} * \frac{|h^S(f)|^2}{S_n(f)} \rightarrow N_1$
3. $\sum \mathrm{df} * \frac{h^S(f)h^S(-f)}{S_n(f)} \rightarrow N_2^c$
4. $|N_2^c| \rightarrow N_2$ :: $\arg(N_2^c) \rightarrow \sigma_N$

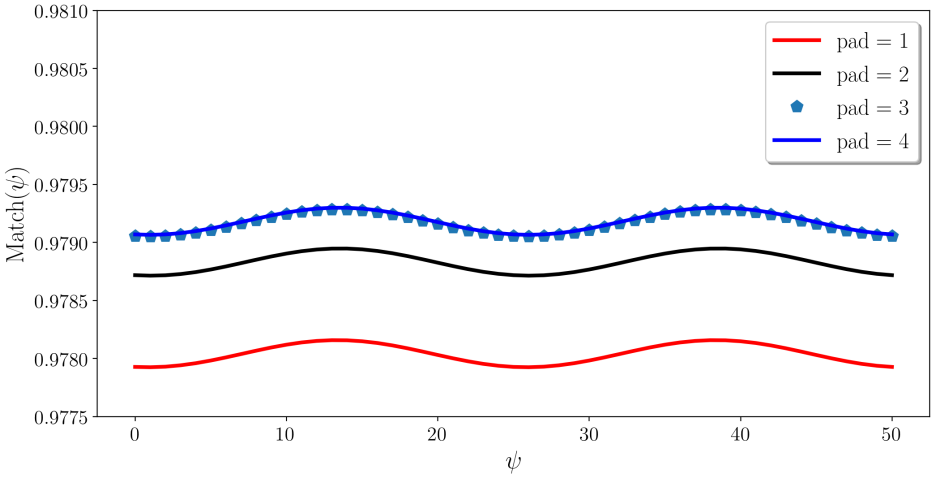

FIGURE 4.7: Variation of match as a function of the signal polarisation at different padding values for signal q2a07t0 (θ, ϕ) = (175^o, 0^o) and template q2a07t0 (θ, ϕ) = (0^o, 0^o).

5. $\sum \text{df} * \frac{|h^M(f)|^2}{S_n(f)} \rightarrow S_1$
6. $\sum \text{df} * \frac{h^M(f)h^M(-f)}{S_n(f)} \rightarrow S_2^c$
7. iFFT$(\frac{h^{*S}(f)h^M(f)}{S_n(f)}) \rightarrow M_1^c$
8. iFFT$(\frac{h^{*S}(f)h^{*M}(-f)}{S_n(f)}) \rightarrow M_2^c$
9. $|M_1^c e^{2i\psi} + M_2^c e^{-2i\psi}| \rightarrow M$
10. arg$(M_1^c e^{2i\psi} + M_2^c e^{-2i\psi}) \rightarrow \sigma_M$
11. $\sqrt{S_1 + \text{Re}(S_2^c e^{4i\psi})} \rightarrow \rho$
12. Match = max$\left[\frac{M}{\rho}\sqrt{\frac{N_1 - N_2\cos(\sigma_N + 2\sigma_M)}{N_1^2 - N_2^2}}\right]$

For the algorithm above, the model, signal and PSD have to be sampled at the same frequencies. These series are masked between the low and high frequency cut-off and before computing the inverse FFTs the data are padded with extra zeroes to improve the sampling. Increasing the padding amount increases the computational cost of the match computation. For my code, the extra padding amount is in powers of 2, so pval=1 would mean the padding would increase by a overall factor of 2, pval=2 means 4 and so on. See Fig: 4.7 for variation of the match with different paddings. We see that beyond pval=3, the match values do not change, and hence, for the result computations, we choose a padding value of 3. Typically, the signals are constructed so that there are $\sim 8192 - 16384$ samples in the frequency domain.

4.3.2 Maximisation procedure

Given a set of intrinsic parameters (total mass, mass-ratio, spins etc.) the match value depends on the signal and template inclination, coalescence phase and polarisation values. Let the signal and template extrinsic parameters be given by $(\theta_1, \phi_1, \psi_1)$ and $(\theta_2, \phi_2, \psi_2)$ respectively, where the (θ_i, ϕ_i) are the inclination and coalescence phase of the binary that go into the spin weighted spherical harmonic functions while composing $h_+(t)$ and $h_\times(t)$ from the h_{lm} modes (see Eq: 4.23). For a given value of ψ_1, the match procedure described in the previous section gives the match maximised over ψ_2 [4] and initial time.

Given a signal (θ_1, ϕ_1), we compute the match maximised over all the extrinsic template parameters $(\theta_2, \phi_2, \psi_2)$ as well as the signal polarisation. Although the signal polarisation is not a parameter one can control for real GW observations, we present results where the match is maximised over the signal polarisation as this would give us a estimate of the *best-case* match between the waveforms, with the match for all other points in the extrinsic parameter space being lower than the maximised match. The maximisation procedure to get the match between the signal and template waveforms for a given (θ_1, ϕ_1) goes through these steps:

- Grid the template $(\theta_2, \phi_2) \in ([0, \pi], [0, 2\pi])$ with 41 uniform points in θ_2 space and 81 uniform points in ϕ_2 space.
- For each value of template θ_{2i}, we compute the match across template ϕ_{2j}. For each (θ_{2i}, ϕ_{2j}) combination, the code gives the match as a function of the signal polarisation value. We compute the match across signal $\psi_1 \in (0, \pi/2)$ and record the maximum match over ψ_1 for each of the template ϕ_{2j}.
- We then interpolate the match maximised over template and signal polarisations across each ϕ_{2j} value (fixed θ_{2i}) and, for a given θ_{2i}, that is the maximised match.
- Thus, we get a set of match values across the template θ_{2i} values, which are then interpolated to obtain the maximum match over template $(\theta_2, \phi_2, \psi_2)$ and signal ψ_1.

For the results, the match maximised over the extrinsic parameters as described above is computed over a 25x25 grid in the signal $(\theta, \phi \in ([0, \pi], [0, \pi]))$ space. As I did not isotropically grid the (θ_i, ϕ_i) parameters during this procedure, I will re-weight the results accordingly.

[4] Note that maximising over the polarisation effectively maximises the match over an overall phase

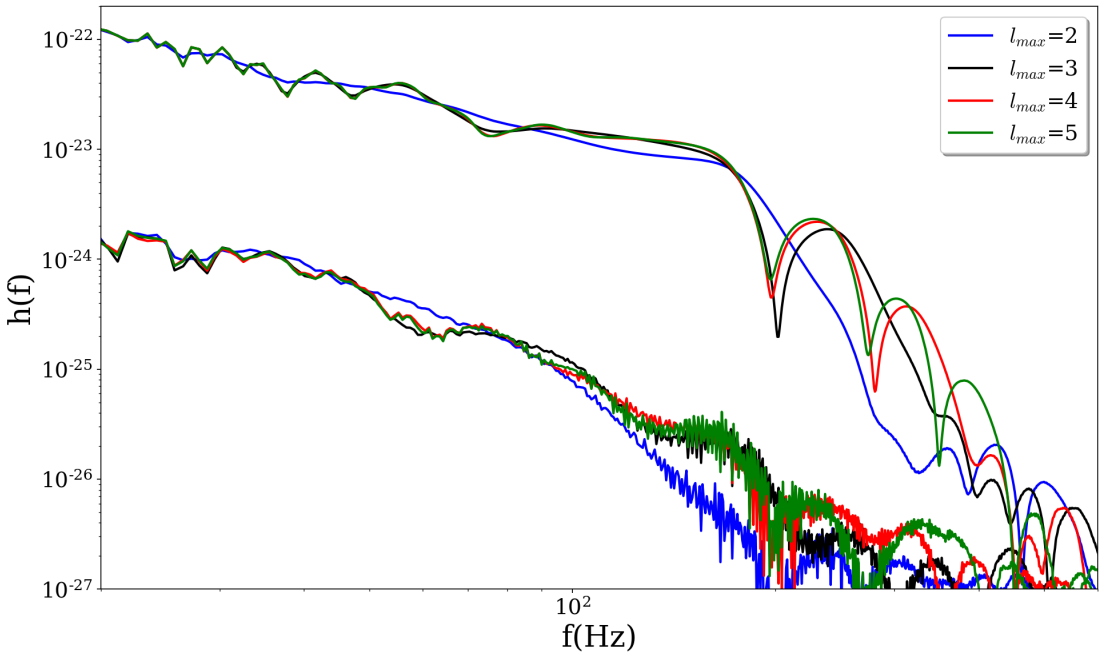

FIGURE 4.8: Detector response from recomposed NR waveform with varying l_{max} modes for system q4a08p0 with total mass 90$M_{\odot}$, distance of 550 MPc and (θ, ϕ) = (0,0). The transition of inspiral to merger occurs at $\sim$ 170Hz for this system.

4.3.3 Choice of Modes

As mentioned earlier, the time (frequency)-domain gravitational waveform can be expanded in a spherical harmonic basis as,

$$h(t, \vec{\lambda}) = h_{+} - ih_{\times} = \sum_{l,m} {}^{-2}Y^{l,m}(\theta, \phi) h_{lm}(t, \vec{\lambda}), \tag{4.23}$$

where h_{lm} are the gravitational wave modes and $m \leq |l|$. For non-spinning equal mass BBH systems, the dominant mode is the $l = 2$ quadrupole mode with the sub-dominant modes ($l = 3, 4, 5 \ldots$) having almost zero signal power. But, the sub-dominant mode contribution becomes stronger for precessing high-mass ratios and high-spin systems and for non face-on inclinations.

To examine the impact of including sub-dominant modes on the frequency domain waveform, I construct the NR waveform from simulation q4a08p0 while including l=2, 3, 4 and 5 modes respectively. From Fig: 4.8, we can see that the higher-order modes do add extra structure to the waveform in the merger/post-merger phase (the waveform is defined in the $\hat{J} \parallel \hat{z}$ frame).

As most of the current waveform models only model the quadrupole mode, we present the results with only l_{max} = 2 modes for both template and signal and defer the study with

higher-order mode contribution for the future.

4.3.4 Connecting match value with distinguishability SNR

Let the detector data ($d(t)$) with noise ($n(t)$) have a signal ($h(t,\vec{\lambda_0})$) present; giving us [5],

$$d(t) = h(t,\vec{\lambda_0}) + n(t), \tag{4.24}$$

where $\vec{\lambda_0}$ is the vector of source parameters.

Any GW signal $h(t,\vec{\lambda})$ with $\vec{\lambda} \sim \vec{\lambda_0}$ can be Taylor expanded to first order in terms of parameters,

$$h(t,\vec{\lambda}) = h(t,\vec{\lambda_0}) + \Delta\lambda^i \partial_i h(t), \tag{4.25}$$

with $\partial_i h(t)$ being the partial derivative of $h(t)$ w.r.t parameter λ_i.

Given the detector data and a waveform template, we can write the likelihood for a given set of $\vec{\lambda}$ as,

$$p(d|\vec{\lambda}) \propto \exp\left\{-\frac{\left\langle d(t) - h(t,\vec{\lambda}) \middle| d(t) - h(t,\vec{\lambda}) \right\rangle}{2}\right\}. \tag{4.26}$$

Substituting the expressions for $d(t)$[Eq:4.24] and $h(t,\vec{\lambda})$[Eq:4.25] in Eq: 4.26 and keeping terms up to first order in λ_i,

$$p(d|\vec{\lambda}) \propto \exp\left\{-\frac{\langle n(t)|n(t)\rangle}{2} + \lambda_i \langle n|\partial_i h(t)\rangle - \frac{\lambda_i\lambda_j \langle \partial_i h(t)|\partial_j h(t)\rangle}{2}\right\}. \tag{4.27}$$

Given a likelihood, within Bayesian analysis, the posterior probability is,

$$p(\vec{\lambda}|d(t)) \propto p(d|\vec{\lambda})p(\vec{\lambda}), \tag{4.28}$$

where $p(\vec{\lambda})$ is the prior over the parameters, which can be assumed to be flat for detectable signals. The flat prior assumption, although not physically motivated, is a reasonable approximation as the likelihood function would be highly peaked in a very small region of the full parameter space.

Once we have a posterior distribution, we can define a region in parameter space (Θ) that contains a given probability p of the posterior distribution,

$$p = \int_\Theta \mathrm{d}\lambda p(\vec{\lambda}|d). \tag{4.29}$$

[5] This discussion closely follows the one given in Section V.A of [181]

Such confidence intervals can be computed by obtaining the posteriors from a full parameter estimation computation, but here we will derive the confidence intervals within the Fisher matrix approximation.

Before computing the confidence intervals, we would like to point out the expressions for mean $(< \lambda_i >)$ and variance $(< \lambda_i \lambda_j >)$ of given parameters [181],

$$\begin{aligned} < \lambda_i > &= \int \mathrm{d}\lambda \lambda_i p(\vec{\lambda}|d(t)) = \langle \partial_i h | \partial_j h \rangle^{-1} \langle n | \partial_j h \rangle \,, \\ < \lambda_i \lambda_j > &= \langle \partial_i h | \partial_j h \rangle^{-1} \,. \end{aligned} \tag{4.30}$$

Using the above expressions along with Eq:4.27 and the assumption of a flat prior, we can re-express the posterior distribution (Eq:4.28) as,

$$\begin{aligned} p(\vec{\lambda}|d(t)) \propto \exp\left\{ -\frac{1}{2} \langle \lambda_i - < \lambda_i > \rangle \langle \partial_i h | \partial_j h \rangle \langle \lambda_j - < \lambda_j > \rangle \right\}, \\ \sim \exp\left\{ -\frac{1}{2} \left\langle |h(\vec{\lambda}) - h(< \vec{\lambda} >)|^2 \right\rangle \right\}. \end{aligned} \tag{4.31}$$

The region that contains a given probability p of posterior distribution is the one where,

$$|h(\vec{\lambda}) - h(< \vec{\lambda} >)|^2 < \chi^2_k (1-p), \tag{4.32}$$

where $\chi^2_k(1-p)$ is the chi-square value wherein there is a probability $(1-p)$ of obtaining the given value or larger with k being the number of dimensions for the problem which are dependent on the number of physical parameters.

For two waveforms close to each other in the parameter space; i.e.; for $h_1(\vec{\lambda_1})$ and $h_2(\vec{\lambda_2})$ with $\vec{\lambda_1} \sim \vec{\lambda_2}$; $|h_1|^2 \sim |h_2|^2 \sim \rho^2$ with ρ being the SNR of the signal,

$$|h_1(\vec{\lambda_1}) - h_2(\vec{\lambda_2})|^2 = 2|h_1|^2 \left[1 - \frac{\langle h_1 | h_2 \rangle}{|h_1||h_2|} \right] \sim 2\rho^2 [1 - \mathcal{M}]. \tag{4.33}$$

This gives a condition on confidence intervals in terms of match values as ,

$$\mathcal{M}[h_1, h_2] \geq 1 - \frac{\chi^2_k (1-p)}{2\rho^2}. \tag{4.34}$$

Two waveforms would be distinguishable from each other if the posteriors recovered for the two are peaked at different values with non-overlapping confidence intervals. So, given a match value, Eq: 4.34 gives us a condition for the SNR at which the waveforms would be

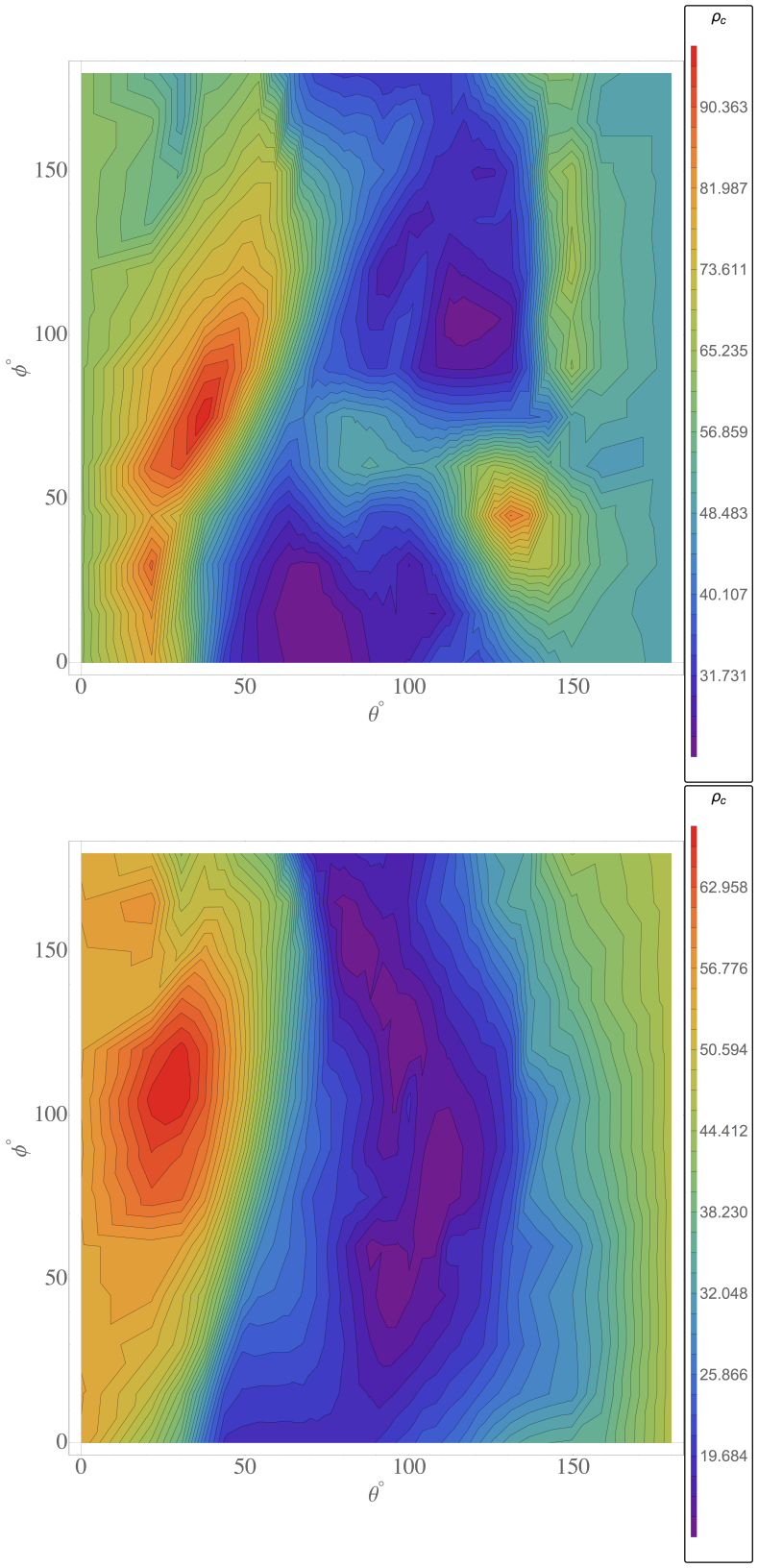

FIGURE 4.9: Variation of the critical SNR (ρ_c) over the signal (θ, ϕ) space for the q2a07p90 signal as seen by q2a07p0 template. For these plots, we compute the match maximised over template (θ, ϕ, ψ) for a range of signal polarisations between $[0, \pi/2)$. The top (bottom) panel shows the maximum (minimum) of the detected SNR variation over the signal polarisations. For the plot, the x-axis gives the inclination variation with the y-axis showing the coalescence phase variation for each signal (θ, ϕ) value. For a given inclination, variation of ρ_c across ϕ is small for small θ which increases slightly for near edge-on systems. For a given ϕ, SNR variation is large over θ, which is expected. Due to precessing effects dominating at edge-on, ρ_c is lower near $\pi/2$ as compared to other inclinations.

distinguishable,

$$\rho \geq \sqrt{\frac{\chi_k^2(1-p)}{2(1-\mathcal{M})}}. \tag{4.35}$$

For the systems under consideration, the dimensionality of the problem is seven, one mass-ratio dimension (q) and 6 spin parameters ($\vec{S}_1, \vec{S}_2$). For 7 dimensions, the value $\frac{\chi_k^2(1-p)}{2}$ = 6.01 for 90% credible interval estimates.

4.4 Results

Fig: 4.9 shows the variation of the critical SNR (ρ_c) over the signal (q2a07p90) $(\theta_s, \phi_s) \in ([0,\pi],[0,\pi])$ space with the template being q2a07p0 waveform. For Fig: 4.9, the match is maximised over template (θ, ϕ, ψ) for a fixed signal polarisation, the signal polarisation is varied over $[0, \pi/2)$ and the distinguishability SNR is computed using Eq: 4.35. Using that, I compute the maximum match over the signal polarisations (top panel of Fig: 4.9) and the minimum value of match over all polarisations (bottom panel of Fig: 4.9). The variation of ρ_c for both the plots show similar qualitative behaviour; i) for a given θ_s, variation of ρ_c along ϕ_s is small; ii) it is harder to distinguish near face-on/face-off signals (larger ρ_c) as compared to signals near edge-on inclinations and iii) distinguishability SNR is strongly affected by the signal polarisation as we see a maximum SNR difference of ~ 30 over signal polarisations for a given signal (θ, ϕ). Distinguishability SNR being lower for edge-on systems is expected as the precession effects become more pronounced as the inclination varies from face-on to edge-on.

Now, although the contour plots as shown in Fig: 4.9 are interesting and provide a good idea of ρ_c variation over the (θ, ϕ) space, we find it more instructive to plot the relative percentage of total signals distinguishable at a given SNR for a given template (id2) - signal (id1) combination. So, we compute the quantity,

$$\Gamma(\rho) = 100\frac{\text{len}(\mathcal{S}_{\text{id2:id1}}[\rho < \rho_c], N(\theta))}{\text{len}(\mathcal{S}_{\text{id2:id1}})}, \tag{4.36}$$

where $\mathcal{S}_{\text{id2:id1}}$ is the list of the SNR values and $N(\theta)$ is a function that re-weights the number of samples from each θ value. It is defined as,

$$N(\theta) = \begin{cases} 1 & \text{if } \theta = 0 \text{ or } \pi \\ N_l * \text{Sin}(\theta) & 0 < \theta < \pi \end{cases} \tag{4.37}$$

with N_l being 25. This means that, if $\theta = 0$, then we will randomly choose one sample from the available samples at $\theta = 0$, and at $\theta = \pi/2$, we choose all 25 samples available at $\theta = \pi/2$. For all the results from now, we will be plotting $\Gamma(\rho)$.

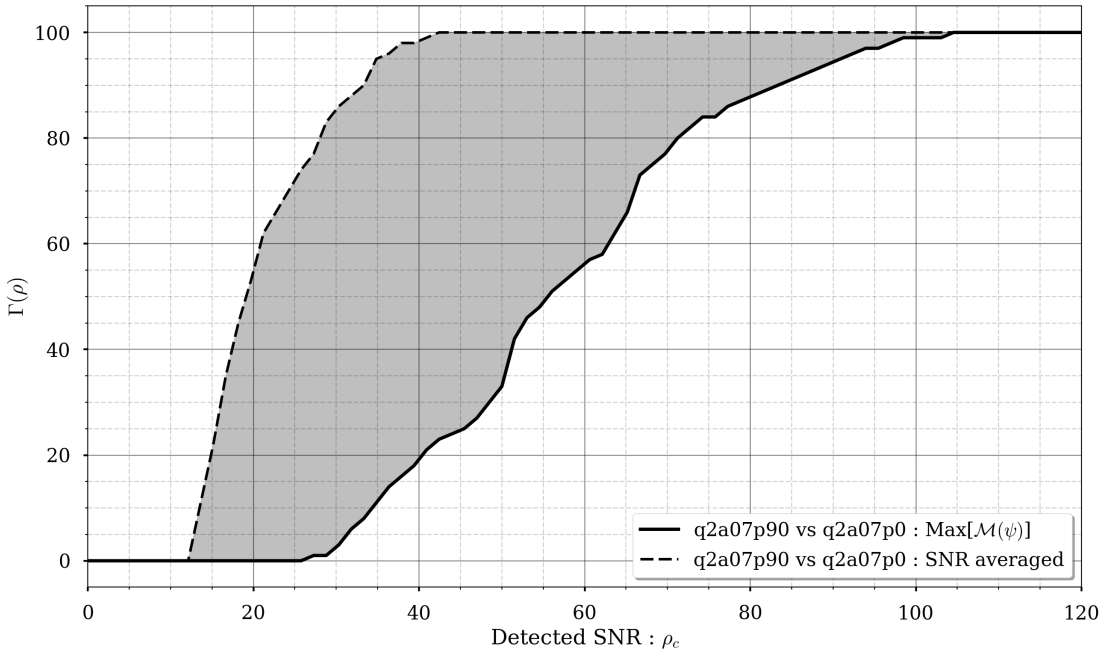

FIGURE 4.10: Relative percent of signals detected at a given SNR as a function of ρ_c for signal q2a07p90 and template q2a07p0, where the ρ_c is computed from the SNR averaged match (see Eq:4.38) for a range of signal polarisation (maximised over template (θ, ϕ, ψ)) and the match maximised over template (θ, ϕ, ψ) and signal ψ. The dashed line gives the SNR averaged match and the solid line gives the match maximised over signal polarisation. For fixed signal polarisations, the ρ_c is always smaller than when the match is maximised over signal polarisations. Hence, the signal polarisation maximised ρ_c profiles should give us an estimate of the worst case scenarios of distinguishability of the in-plane spins for these systems with the understanding that for most physical cases (i.e., fixed signal ψ's) it would in-fact be easier to distinguish the effects of in-plane spins.

Now, given a set of matches, we can also compute the *orientation averaged match* [130], [165], [195] and its corresponding SNR. This way of re-weighting the match accounts for the likelihood of the signal being detected. The orientation averaged match (or SNR averaged match) is defined as,

$$\overline{\mathcal{M}} = \left(\frac{\sum_i \rho_i^3 \mathcal{M}_i^3}{\sum_i \rho_i^3} \right)^{1/3} . \tag{4.38}$$

In Fig: 4.10, we plot the $\Gamma(\rho)$ profiles of the SNR averaged match and the match maximised over signal polarisation for signal q2a07p90 and template q2a07p0. Comparing Fig: 4.9 and Fig: 4.10 shows that the lower ρ_c points in Fig: 4.10 are from near edge-on signals, with the high ρ_c signals from near face-on/face-off inclinatons. For the SNR averaged match over signal polarisation, 50% (100%) of the signals can be distinguishable up to $\rho_c \sim 20(40)$ whereas when maximised over signal polarisation the same value goes up to $\rho_c \sim 55(100)$. This plot again points how strong the signal polarisation can affect the matches. For all the plots from Fig: 4.11 onwards, for each signal $(\theta, \phi) \in ([0, \pi], [0, \pi])$, the distinguishability SNR is computed from the match that is maximised over template (θ, ϕ, ψ) and signal ψ; as

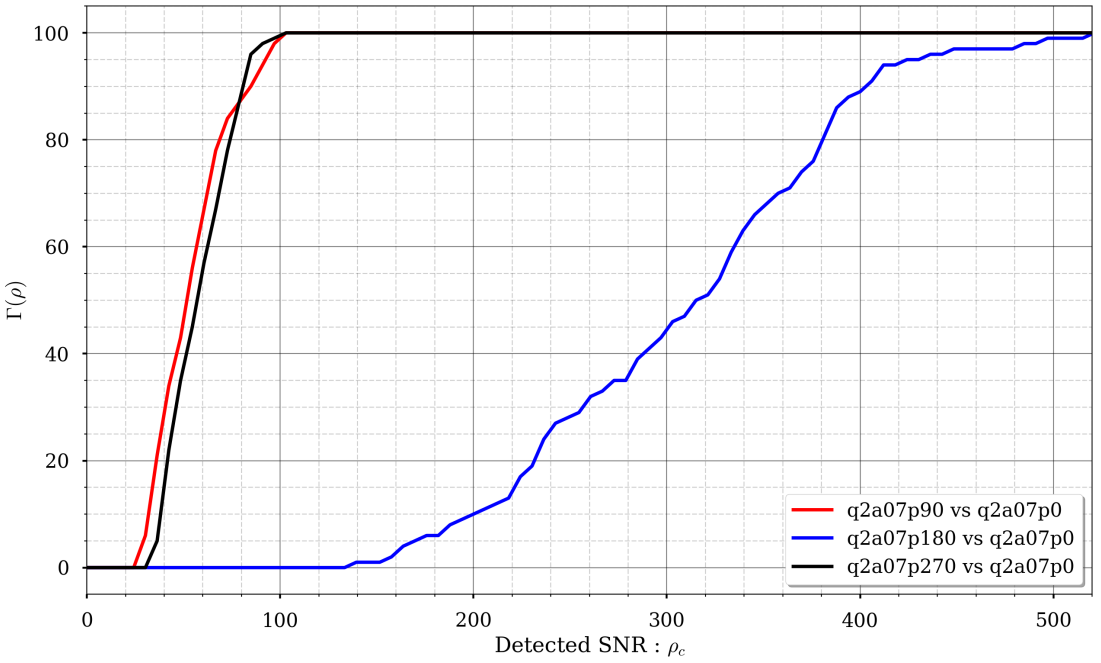

FIGURE 4.11: Relative percent of distinguishable signals as a function of ρ_c for the signals q2a07p90 (Red), q2a07p180 (Blue), q2a07p270 (Black) with q2a07p0 as template. The $\Gamma(\rho)$ profiles are very similar for q2a07p90 and q2a07p270 due to the symmetry in the system, which is also what causes the extremely high ρ_c for q2a07p180 signals as seen by q2a07p0.

that will give an idea of the *worst-case* scenario for the detectability SNR. Also, computing the match maximised over signal ψ is computationally less expensive (by $\sim$ 4 times) than varying the signal ψ over a range of values and maximising only over template (θ, ϕ, ψ).

For each of the results from now, we use one waveform from the q2 (q2a07p0), q4 (q4a08p0) or q1 (q1a08p0) series as the proxy template waveform and compute the match maximised over template inclination, coalescence phase and polarisation and signal polarisation. The results are computed over a 25x25 equidistance grid over the signal $(\theta, \phi) \in ([0, \pi], [0, \pi])$ and the SNR distribution is computed from Eq: 4.36; where the SNRs are re-weighted to count for isotropic distribution of (θ, ϕ).

4.4.1 Full waveform analysis

Previous studies have shown the agreement between precessing waveforms in the QA frame and corresponding aligned-spin waveform [125], [190]. For each of the q1, q2 and q4 systems under consideration, the only variation within each choice of mass-ratio and spin-magnitude is the spin direction (ϕ_{SR}) or (for the comparison cases) only the spin magnitude with the same (ϕ_{SR}) as the proxy template. For cases with different ϕ_{SR}, the QA waveforms should be similar as they correspond to the same aligned-spin waveform. Hence, in the

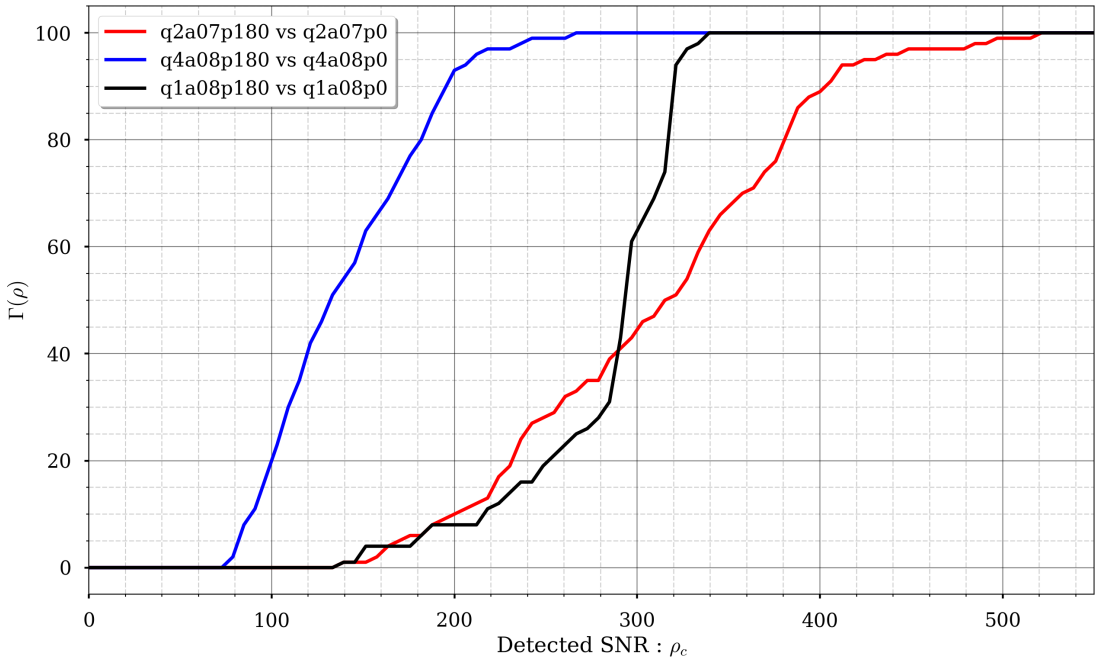

FIGURE 4.12: Relative percent of distinguishable signals as a function of ρ_c for the signals q2a07p180 (q4a08p180) [q1a08p180] and template q2a07p0 (q4a08p0) [q1a08p0]. For q=1, q=2 and q=4 systems, we see a symmetry between the $\phi_{SR} = 0, 180$ systems but to different degrees.

inertial frame, the differences will primarily arise from the precession dynamics and the waveform mode-asymmetries.

Considering *both* the aforementioned effects in signal and template waveforms would give an estimation of the measurability of ϕ_{SR} at a given mass-ratio, if the parameters are estimated by a template waveform that models all the precession physics. In the next sections, we will discuss the effects of removing one or both of these effects.

The q1 series systems have equal but opposite spins, so the total in-plane spin $\vec{S} = \vec{S}_1 + \vec{S}_2$ is zero, and show no precession. Although the orbital plane shows no precessional motion, the presence of spins causes the orbital plane to starting bobbing along $\hat{z}$ (i.e., the COM oscillates vertically along the $\hat{z}$ axis) due to the asymmetric gravitational radiation. This asymmetry in the radiated gravitational wave modes is what makes it possible to distinguish two different systems in the q1 series.

Fig: 4.11 gives the results for the q2 series waveforms where the system q2a07p0 is used as the template. The SNR variation profile for the q2a07p90 and q2a07p270 systems closely match each other. q2a07p180 system has a *quasi*-symmetry of rotation by π with q2a07p0 system and is almost impossible to distinguish. This symmetry also shows up during the match computation, where the maximum match for a q2a07p180 signal from (θ_s)

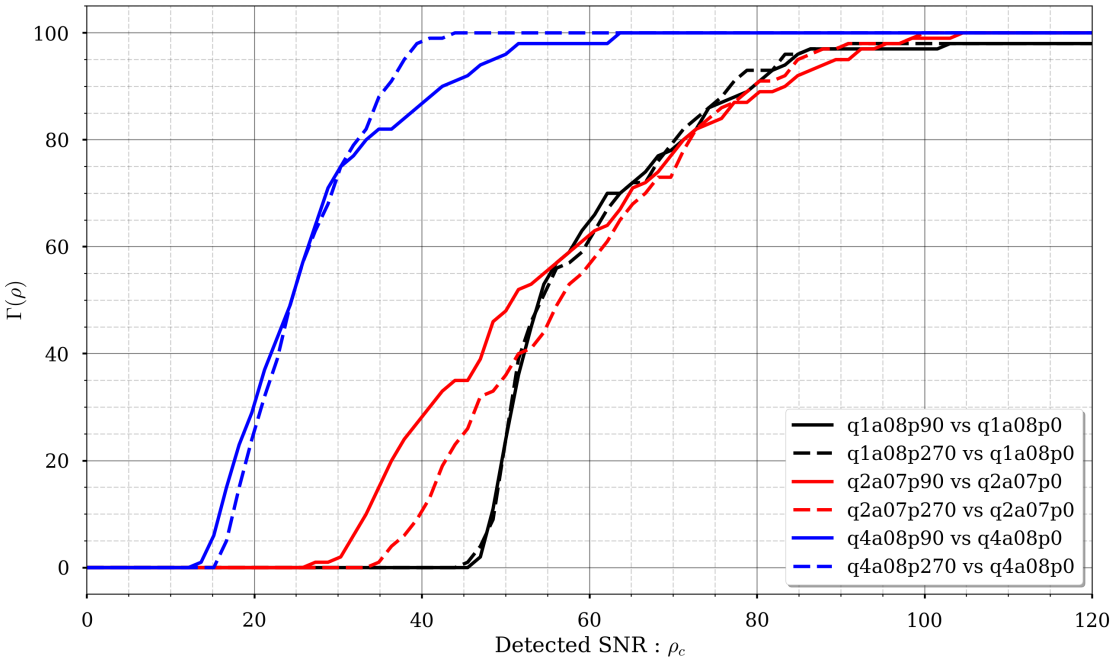

FIGURE 4.13: Relative percent of distinguishable signals as a function of ρ_c for the signals q1a08p90 (q1a08p270), q2a07p90 (q2a07p270), q4a08p90 (q4a08p270) matched with the corresponding proxy template is shown in Black (dashed-black), Red (dashed-red) and Blue (dashed-blue) respectively. For each system, the solid and dashed curves show the results for $\phi_{SR} = 90, 270$ signals, and as seen from Fig:4.12, there exists a symmetry between waveforms with ϕ_{SR} difference of $\pm\pi$. This is the reason for the similar profiles seen for $\phi_{SR} = 90, 270$ signals.

is at q2a07p0 template $(\theta_s + \pi)$. About 45% of q2a07p180 signals are distinguishable for 100<SNRs<300 and the remaining for SNRs>300.

From Fig: 4.11, an interesting question would be whether the quasi-symmetry between the $\phi_{SR} = 180$ and $\phi_{SR} = 0$ case exists for all systems. From Fig: 4.12, we can see that the symmetry exists (to varying degrees) for q1, q2 and q4 series at the SNRs we have to deal with for the ground based detectors. For the q4 system though, the distinguishability SNRs are lower, which suggest that the symmetry is not as strong as for the corresponding q2/q1 cases. Although a symmetry between the $\phi_{SR} = 180$ and $\phi_{SR} = 0$ case *does* exist, it is not exact and for that reason I refer to it as quasi-symmetry. In Section 4.4.2, we will compare the QA frame angles and mode-asymmetry between the different systems and will explain in more detail the quasi-symmetry between ϕ_{SR}=(0°, 180°) systems.

Fig: 4.13 gives the results of the required ρ_c so the $\phi_{SR} = 0$ template from each mass-ratio can distinguish a waveform (with the same mass-ratio) whose spins are rotated by $\pm\frac{\pi}{2}$ ($\phi_{SR} = 90, 270$). Of all signals considered here, we can tell 50% of the signals apart at SNRs of $\sim$ 20 (55) [55] for the q4 (q2) [q1] system with 100% $\sim$ 50 (100) [100]. Note

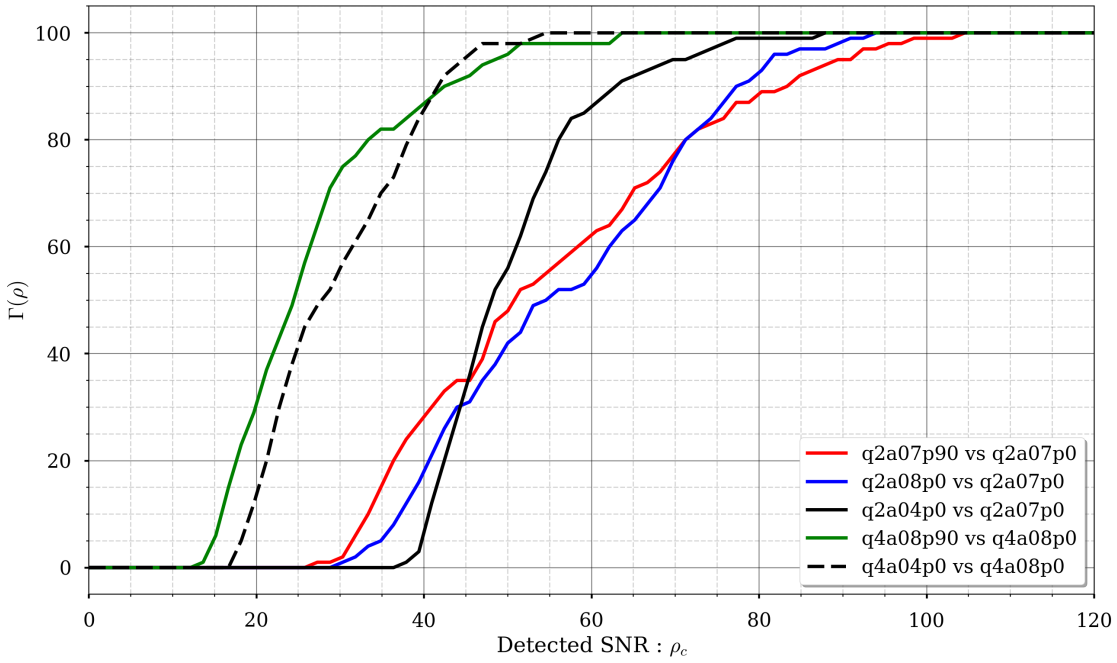

FIGURE 4.14: Relative percent of distinguishable signals as a function of ρ_c for the signals q2a04p0 (q4a04p0) and q2a08p0 with template q2a07p0 (q4a08p0).

that for these distinguishability SNRs are computed from the match maximised over signal polarisations and on average, we can expect to measure ϕ_{SR} at lower SNRs.

Fig: 4.13 shows the effect of changing the in-plane spin directions on distinguishability. We also want to understand how changing the total spin magnitude compares to changing spin direction. Fig: 4.14 gives the distinguishability between cases where ϕ_{SR} or the spin magnitude is varied. Let us first consider the q2 systems: we are using the waveform q2a07p0 as template and the only difference between q2a04p0 and q2a08p0 and the template is the amount of spin on the larger black-hole. For a small number of signals, q2a04p0 is harder to distinguish than q2a08p0 or q2a07p90, but overall ρ_c for q2a04p0 is lower. The ρ_c profiles for q2a08p0 or q2a07p90 are almost similar and indicate that effect of varying in-plane orientations could be as strong as changing the spin value by ~ 0.1. At SNRs $\sim$ 80, we could almost always measure ϕ_{SR} differences of $\pm\pi/2$, χ_p differences of 0.1 and always measure χ_p differences of 0.3 at mass-ratio 2. At SNR $\sim$ 50, we can measure χ_p difference of 0.3 for about 60% of the signals, the same goes to about 40% for q2a07p90 and q2a08p0. Hence, for q2 systems, the effect of changing the in-plane spin direction by $\pm\pi/2$ has a similar effect to that of changing the spin magnitude by 0.1, but not as strong as a spin magnitude difference of 0.3.

For q4 systems, the effect of changing ϕ_{SR} become more pronounced. About 80% of signals with different in-plane spin direction ($\phi_{SR} = 90$) are *easier* to distinguish than corresponding q4a04p0 signals. For 80% of the signals, we can measure ϕ_{SR} differences of 90° at SNR $\sim$

35 and χ_p difference of 0.4 at SNR $\sim$ 40. Though, the results of Fig: 4.10 suggest that on average we can expect to distinguish signals from q4a08p90 and q4a04p0 at similar SNRs.

4.4.2 QA Angles and mode-asymmetry

In Section 4.4.1 we saw that two systems with a $\pm\pi/2$ angle difference in the in-plane spin can be distinguished at moderate to high SNRs and that in some cases, it is easier to measure the ϕ_{SR} than a spin-magnitude change. As mentioned before, these differences can arise from the differences in the precessional dynamics and mode-asymmetric content. In this section, we will compare these two effects separately for systems with a given mass-ratio.

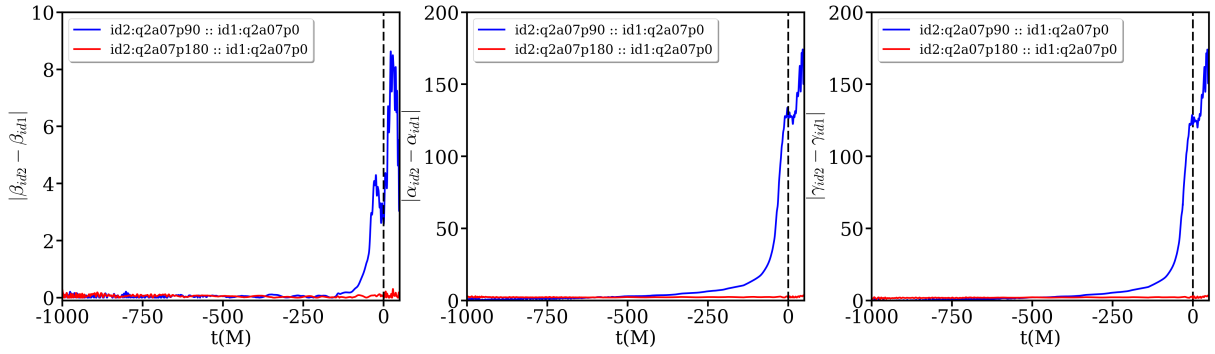

FIGURE 4.15: Here, we plot the differences in the QA frame angles (α, β, γ) for the system q2a07p90 with q2a07p0 (blue line) and q2a07p180 and q2a07p0 (red line) for the angles β (left panel), α (centre panel) and γ (right panel)

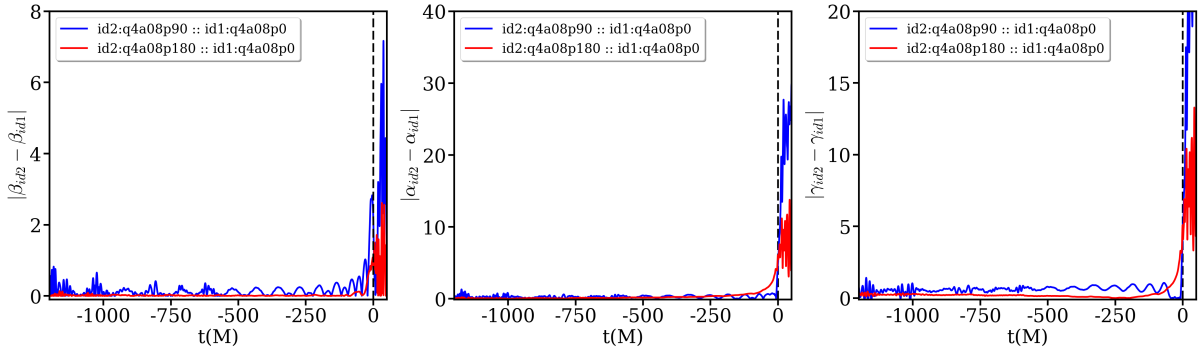

FIGURE 4.16: Here, we plot the differences in the QA frame angles (α, β, γ) for the system q4a08p90 with q4a08p0 (blue line) and q4a08p180 and q4a08p0 (red line) for the angles β (left panel), α (centre panel) and γ (right panel)

Fig: 4.15 and Fig: 4.16 show the differences in the Euler angles (call it δ_{ξ_i} for $\xi_i \in (\alpha, \beta, \gamma)$) required to transform the precessing system to the co-precessing frame. For the q=2 quasi-symmetric cases, δ_{ξ_i} is almost zero at all times; whereas between the $\phi_{SR} = (90, 0)$ cases, we see that δ_{ξ_i} increases as the system approaches merger. At q=4, δ_{ξ_i} between the

$\phi_{SR} = (180, 0)$ cases is not always zero, we see slight increase in δ_{ξ_i} as the systems merge. This is one factor for the *weaker* quasi-symmetry for q=4 as seen in Fig: 4.12.

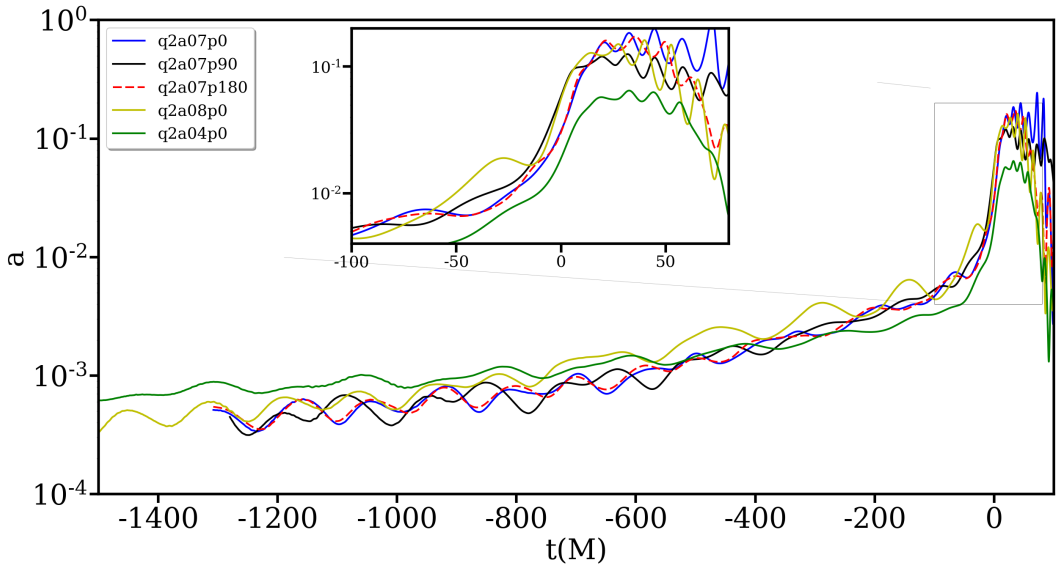

FIGURE 4.17: Plot of mode-asymmetry measure (a, see Eq: 4.6) throughout the coalescence for all the q=2 systems used in this thesis.

In Eq: 4.6, we have defined a rotationally invariant measure of mode asymmetry. Fig: 4.17 plots the mode asymmetry 'a' for all the q=2 systems used in this analysis. The symmetry between $\phi_{SR} = 180$ and $\phi_{SR} = 0$ systems shows up in the *almost* overlapping asymmetry in the modes. The asymmetry measure of q2a07p90 shows a similar (yet different) overall evolution in time as q2a07p0.

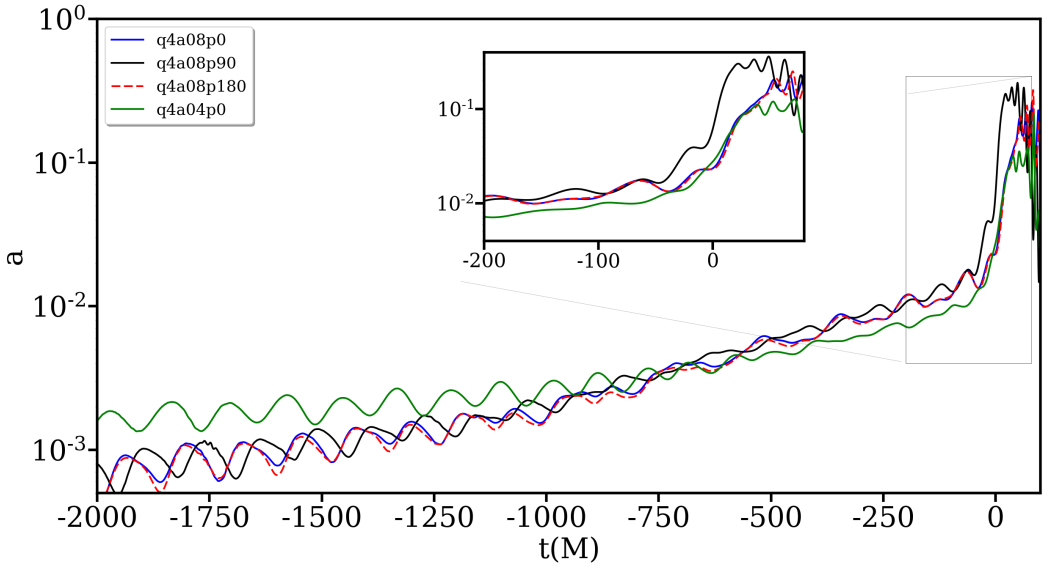

FIGURE 4.18: Plot of mode-asymmetry measure (a, see Eq: 4.6) throughout the coalescence for all the q=4 systems used in this thesis.

Fig: 4.18 gives the *a* for all the q=4 systems. We see the same behaviour between the $\phi_{SR} = 180$ and $\phi_{SR} = 0$ systems as for q2. The $\phi_{SR} = 90$ system shows a similar evolution during late-inspiral as $\phi_{SR} = 0$ system with a clear distinction between them at merger. For the q=2 and q=4 cases, the mode-asymmetric content between systems with ϕ_{SR} differences of $\pm\pi/2$ show a similar time-evolution (as compared to systems with a different spin-magnitude), which suggests that the major effect on distinguishability is from the differences in the precessional dynamics. We will check for this in Section 4.4.4 where we analyse waveform with and without mode-asymmetric content.

Fig: 4.19 plots the same for q=1 superkick configuration systems and we observe the same overall behaviour as for the q=2, 4 cases. The notable difference for the super-kick cases is that for the quasi-symmetric systems, as the systems near merger, a for $\phi_{SR} = 0, 180$ is exact up to numerical errors.

So, till now we have showed that waveforms with varying in-plane spins can be distinguishable from one other at moderate to high SNRs. In this section, we saw that varying in-plane spin direction can affect the precessional motion of the orbital plane as well as give rise to slightly different mode-asymmetry content. We conclude that it is the combination of the differences in the precessional motion of the system with the different mode-asymmetry content that allows for distinguishability between the ϕ_{SR} = (0, π/2) systems. We now want to see *if* the two effects (mode-asymmetry and differential precessional motion) could be decoupled from each other and how the results behave if one or both of them are turned off.

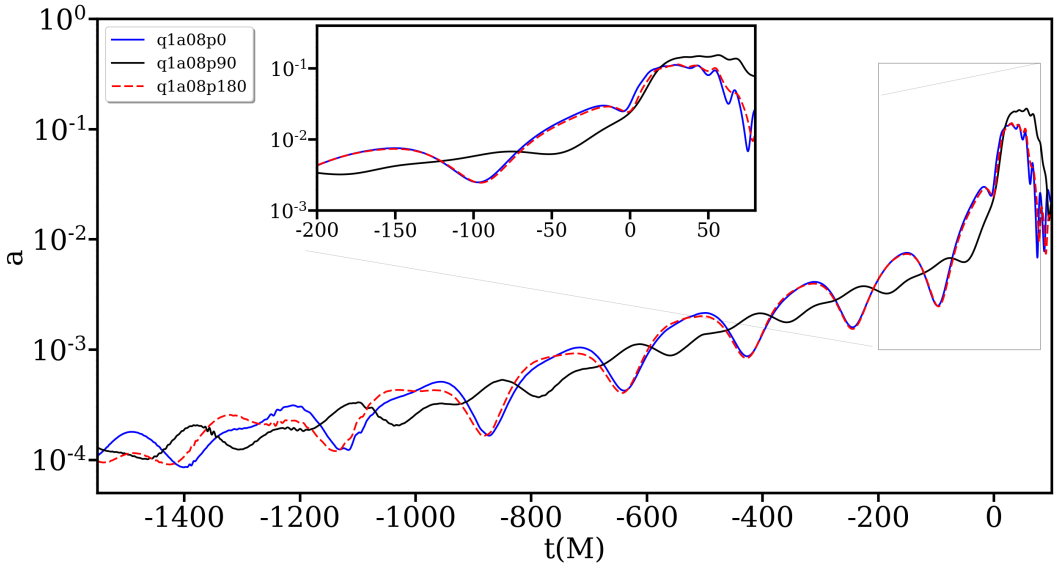

FIGURE 4.19: Plot of mode-asymmetry measure (a, see Eq: 4.6) throughout the coalescence for all the q=1 systems used in this thesis.

4.4.3 Analysis of QA symmetrized waveforms

In Section 4.4.2 we investigated the differences in mode-asymmetry content and precessional motion between the different waveforms. We first want to see how well the waveforms match when mode-asymmetry and precession modulations are removed. To do this, we first use the QA angles to transform each waveform to its co-precessing frame. In this frame, the (2,1) and (2,-1) modes are suppressed, with the precession modulations mostly removed. The mode-asymmetries are then removed by taking a symmetric combination of the (2,2) and (2,-2) modes as,

$$h_{22}^{symm}(f) = \frac{1}{2}\left(h_{22}^{qa}(f) + \bar{h}_{2-2}^{qa}(f)\right), \tag{4.39}$$

with the symmetric (2,-2) mode being the complex conjugate of Eq: 4.39.

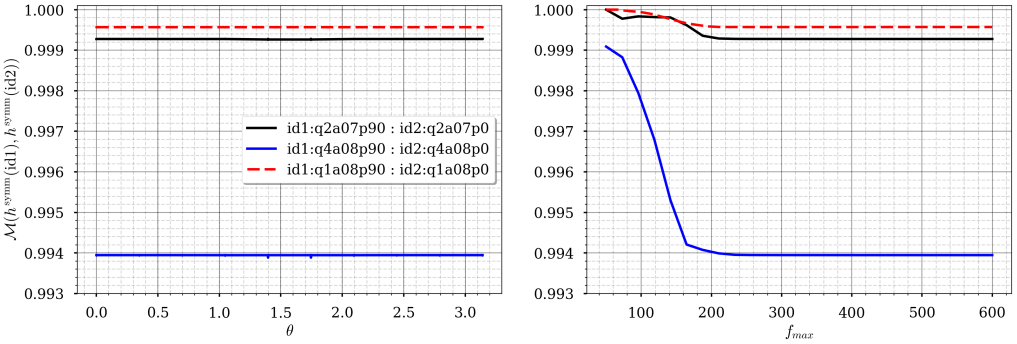

FIGURE 4.20: In the left panel, we plot the match between the symmetrized waveforms in the QA frame for q2a07p90 vs q2a07p0 (Black line), q4a08p90 vs q4a08p0 (Blue line) and q1a08p90 vs q1a08p0 (Red-dashed line) over a range of signal (θ, ϕ) values. There is hardly any variation of the match over signal inclination or coalescence-phase values. For the right plot, we fix the inclination and calculate the match as a function of f_{max}.

Using this symmetric waveform in QA frame, we compute the matches between $\phi_{SR} = 90$ and $\phi_{SR} = 0$ cases over a range of signal (θ, ϕ) values and compute the match maximised over the template extrinsic parameters and signal polarisation value. Note that the q1 series waveforms do not show precessional motion and so we only symmetrise it using Eq: 4.39 without first transforming it to the QA frame. The results of the same are given in Fig: 4.20. The maximised match for the symmetrized waveforms in the QA frame show no variation over the (θ, ϕ) space and remains constant at a match of $\sim$ 0.9996 (0.9994) [0.994] for the q1 (q2) [q4] system, which translates to $\rho_c \sim$ 120 (100) [35] (see the left panel of Fig: 4.20).

For the full waveform systems with ϕ_{SR} difference of $\pi/2$, we have 100% detectability at ρ_c < 100 (100) [60] for the q1 (q2) [q4]. The similar QA frame waveforms of $\phi_{SR} = 0, 90$ for q1 and q2 systems suggest that the detectability is majorly affected by both precessional dynamics and mode-asymmetric content. For the q4 system, the QA frame waveforms has a match value that is smaller than 20% of the full waveform cases, which suggests that for

a few cases, inclusion of the precessional dynamics and mode-asymmetric content *improve* the match, i.e, makes it harder to distinguish.

In the right panel of Fig: 4.20, we plot the match as a function of f_{max} for the symmetrized QA waveforms. The match value is $\sim$ 1 (1) [0.999] for q1 (q2) [q4] system at f_{max} of 50 Hz and settles down to the minimum match after f_{max} >200Hz. From the high match values at low f_{max} indicates that, in the co-precessing frame, the inspiral part of the $\phi_{SR} = 90$ and $\phi_{SR} = 0$ waveforms are *almost* the same with the majority of differences creeping in during (and post) the merger phase; with the differences being larger as we go from q=1 to q=4. This conclusion is reinforced by Fig: 4.21 where we plot the q2a07p0/q2a07p90 waveform and indicate the times at which the waveform has different f_{max}.

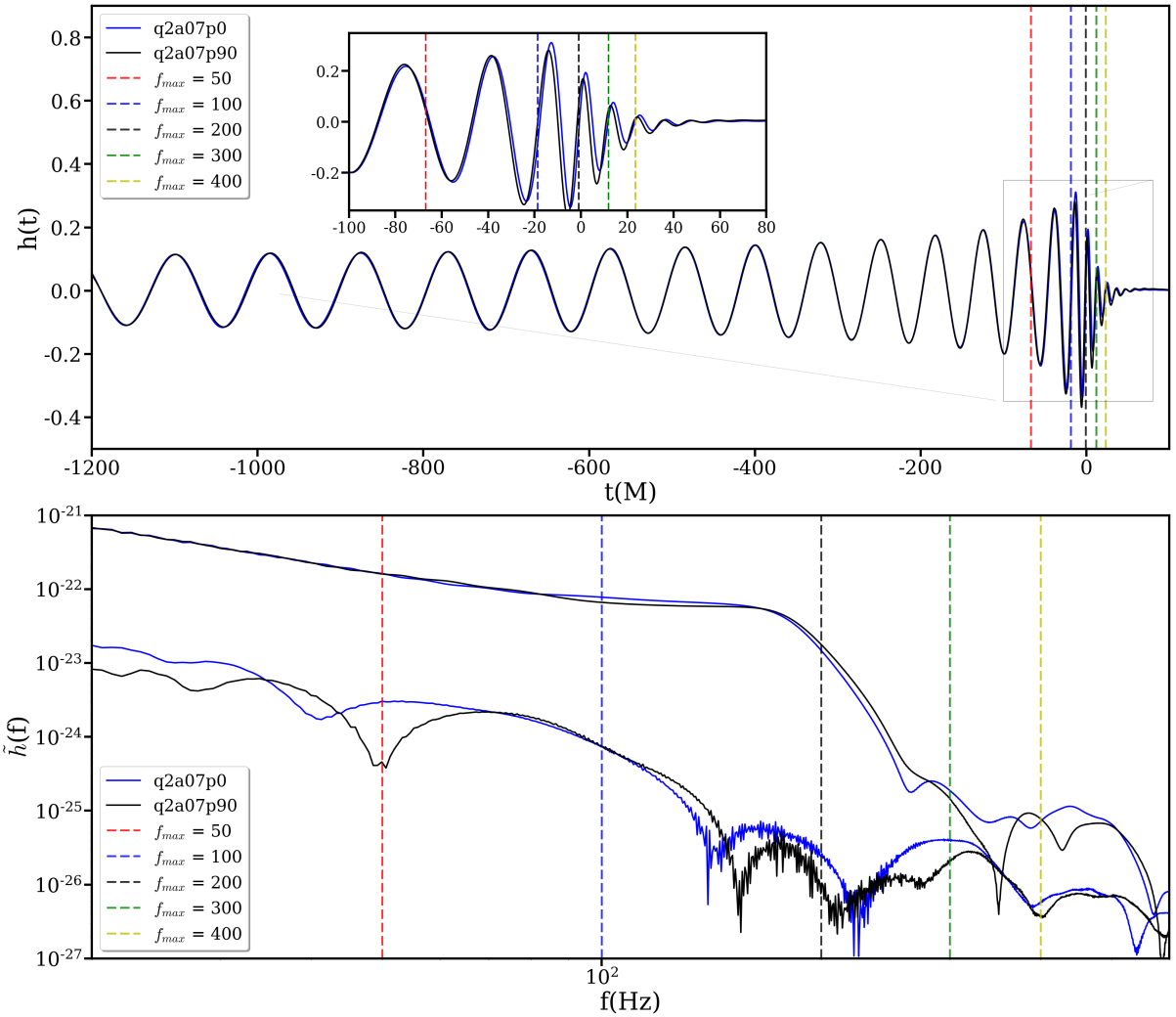

FIGURE 4.21: In the top [bottom] panel, we plot the q2a07p0 (blue) and q2a07p90 (black) time [frequency] domain waveforms. For the top panel, the dashed lines show the time at which the waveform has a specific frequency used as f_{max} value for right panel of Fig:4.20. For the bottom panel, the dashed lines show the position of that frequency with respect to the frequency domain waveform. Frequency values of (50, 100, 200, 300, 400) are given in dashed (red, blue, black, green, yellow) lines respectively.

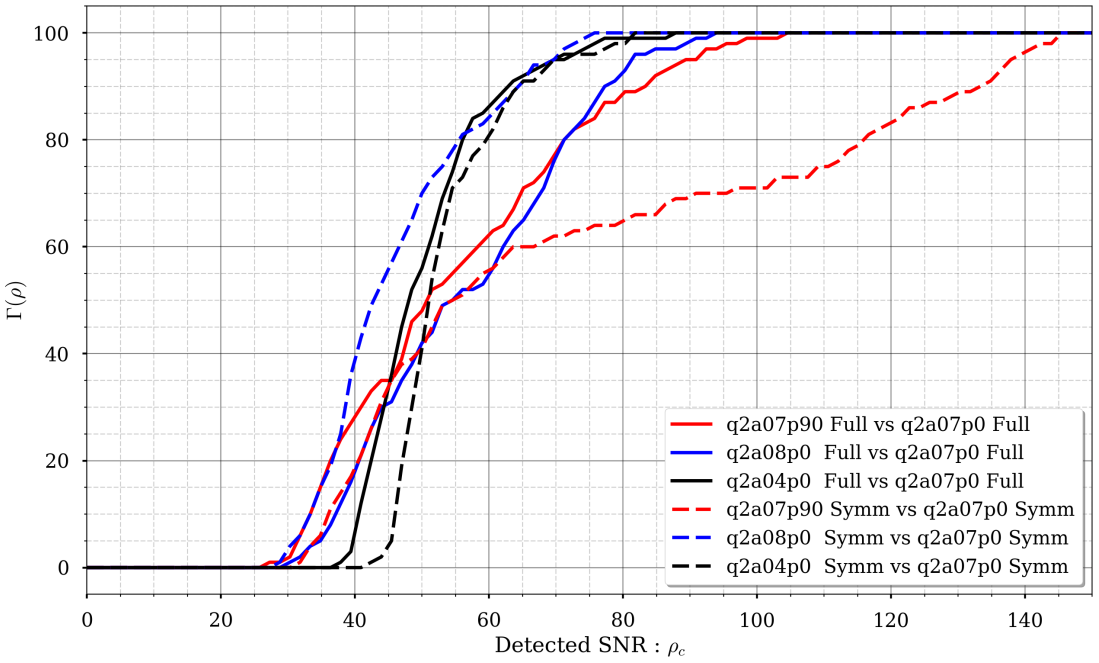

FIGURE 4.22: The figure plots the distribution of ρ_c of Full waveform vs Full waveform (solid lines) and Symmetrized waveform vs Symmetrized waveform (dashed lines) for q2 series waveforms. For q2a07p90 signals, a large percentage $(\sim 40\%)$ of the signals are *much* harder to distinguish with symmetrized signals and templates. Profiles for symmetrized q2a04p0 and q2a08p0 signals are similar to full signal profiles with the maximum ρ_c difference between them is ~ 20 for q2a08p0, with the symmetrized q2a08p0 signals easier to distinguish than the full signals. These results indicate at q=2, considering only precessional effects makes it harder to distinguish different ϕ_{SR} for some cases, and easier or harder to distinguish spin values.

4.4.4 Analysis of Inertial symmetrized waveforms

From Fig: 4.20 we see that, in the QA frame, the match between $\phi_{SR} = 90$ and $\phi_{SR} = 0$ cases is constant across the signal (θ, ϕ) space with the differences in the waveforms near merger leading to the corrsponding match value. In all of the current IMR precessing waveform models, mode-asymmetry is not considered. We now want to consider two things:

- How does the distinguishability SNR behave if mode-asymmetries are turned off for *both* template and signal waveforms (waveforms with only precession modulations)?
- How does the distinguishability SNR behave if mode-asymmetries are turned off for *only* the template with signal being the full waveform (mode-asymmetry + precession modulations)?

From the first check we might be able to gain some idea of the effect of precessional motion differences (QA angle differences) on ρ_c and the relative importance of modelling these

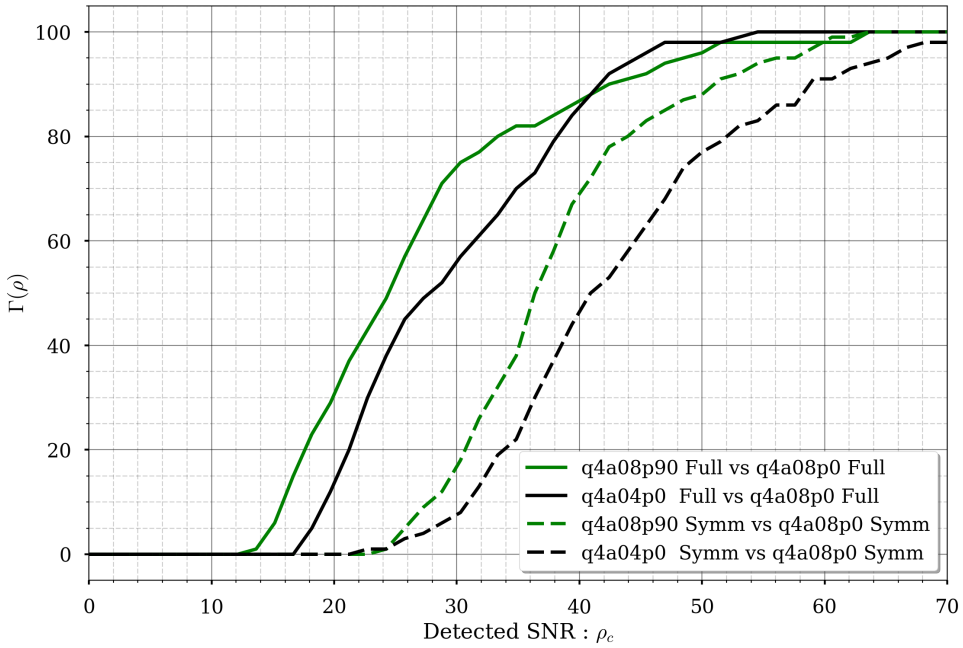

FIGURE 4.23: The figure plots the distribution of ρ_c of Full waveform vs Full waveform (solid lines) and Symmetrized waveform vs Symmetrized waveform (dashed lines) for q4 series waveforms. Symmetrized q4a08p90 and q4a04p0 signals are always harder to distinguish than full waveforms. Contrast this to the q2 results, where symmetrizing the waveform had different effects based on spin magnitude (see Fig:4.22).

effects. The second check would give an idea of effects of using templates without mode-asymmetry to distinguish full signals (mode asymmetry + precessional modulations), which is more of a realistic situation and is the case for current observations. These results might indicate the level of importance of mode-asymmetry for waveform modelling.

To check for precessional motion effects of distinguishable SNR, we use the waveforms symmetrized in the QA frame using Eq: 4.39, rotate them back to the inertial frame and then compute the matches. Here, "Full waveform" is one with both mode-asymmetries + precessional motion and "Symmetrized waveform" is one with only precessional motion. Fig: 4.22 gives the results for ρ_c for the q=2 series symmetrized waveforms and compares them to the full waveform results.

When mode-asymmetry is turned off, all of q2a07p90 signals are harder to distinguish than for full waveforms, with 100% distinguishability at SNR$\sim$150 whereas for full waveforms, 100% distinguishability is at SNR$\sim$100. For q2a04p0 and q2a08p0 systems though, the $\Gamma(\rho)$ profiles for waveform with precession+mode-asymmetry effects are similar to those of waveforms with only precession effects, with symmetrized q2a08p0 signals detected at lower ρ_cs than full q2a08p0 signals. This implies that for q=2, it is the mode-asymmetry differences that would dominate the measurability of in-plane spins and have different effects based on spin magnitudes. Note that in the QA frame, the symmetrized q=2 waveforms

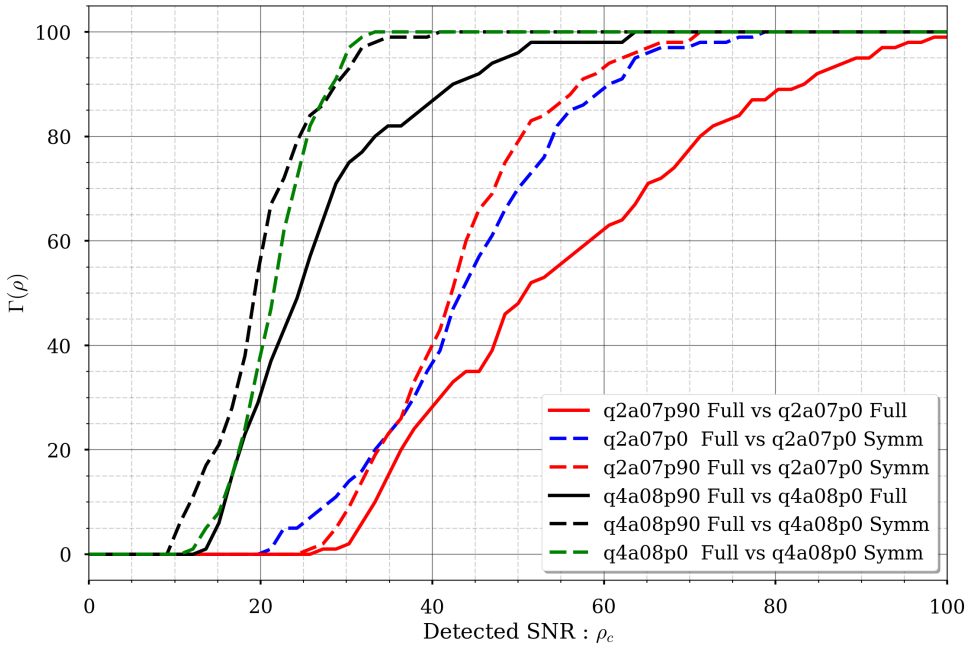

FIGURE 4.24: The figure plots the distribution of ρ_c of Full waveform vs Full waveform (solid lines) and Full waveform vs Symmetrized waveform (dashed lines) for q2 and q4 series waveforms. Notice that the symmetrized $\phi_{SR} = 0$ template sees the full $\phi_{SR} = 0$ signal as a different system for both q=2 (dashed-blue) and q=4 (dashed-green).

match with each other to give a $\rho_c \sim 100$ which suggests that for some cases, inclusion of only precessional dynamics makes it harder to distinguish the two systems.

Fig: 4.23 gives the same as Fig: 4.22, but for the q4 series waveforms. We observe a similar behaviour between the full and symmetrized waveforms for $\phi_{SR} = 90, 0$ case as for q2, i.e., ρ_c for symmetrized waveforms is higher for all symmetrized signals. Where for q2, the symmetrized waveforms with a different spin magnitude are easier (or similar to full waveform) to distinguish, the same does not hold for q4. We see that the symmetrized q4a04p0 symmetrized signal is always harder to distinguish than the full waveform. It is possible that this behaviour is a consequence of the stronger mode-asymmetric content for q=4 systems as compared to q=2.

From Section 4.4.3, we already know that symmetrized q1a08p90 can be distinguished at $\rho_c \sim 120$, which is near to the 100% ρ_c for the full system $\rho_c \sim 120$ (see Fig: 4.13). Hence, all results indicate that losing mode-asymmetry content information will affect detectability.

For Fig: 4.24, we use full waveforms of q2a07p90, q2a07p0, q4a08p90 and q4a08p0 systems as the signals and use the corresponding symmetrized waveforms as the proxy template (q2a07p0 and q4a08p0). The results are compared with the full waveform results. With the symmetrized templates, it is easier to distinguish the $\phi_{SR} = 90$ system from $\phi_{SR} = 0$

system for both q = 2,4. When the signal is the full q2a07p0 (q4a08p0) waveform, the corresponding symmetrized template sees it a different system with 100% distinguishability at $\rho_c \sim 75$ (40). These results imply that using a symmetrized template to estimate the source parameters could lead to biased parameter recovery.

4.5 Conclusions

All the results we have quoted above are for match values that are maximised over all the relevant extrinsic parameters, i.e., the template (θ, ϕ, ψ) and signal ψ. In Fig: 4.9 we see that over signal polarisations, ρ_c shows a SNR variation of ~ 30 at maximum and ~ 10 at the minimum. So, for all results shown here for the systems where we maximise the match over signal polarisations, there would exist signals with lower ρ_c than what is quoted in Section 4.4.

The results from Section 4.4.1 show that changing the direction of the in-plane spin *does* affect the final waveform and can be distinguished from the base waveform at moderate to high SNRs. All q1 (q2) [q4] signals with a ϕ_{SR} difference of $\pm\pi/2$ with respect to the template can be distinguished if the incoming SNR is $\sim$ 120 (100) [60] with 50% distinguishability at SNR $\sim$ 50 (55) [20] [see Fig: 4.13]. Also, comparing these results with results for signals with a different total spin value (same direction as template) show that, for q=2, varying the in-plane direction can have an effect as strong a change of 0.1 in the in-plane spin magnitude, but weaker than a change of 0.3. For q=4, changing ϕ_{SR} has a slightly stronger effect than spin magnitude change of 0.4, but on average we expect these effects to be comparable. Single spin systems with in-plane spins related by rotation of π about $\hat{L}$ are quasi-symmetric with each other, which shows up as the very high ρ_c. In the regime of a sensitive gravitational wave detector network, albeit rarely, we can expect signals of such high SNRs. From these results, we wish to indicate that future precessing waveform models, the description of the precession physics should incorporate the *direction* of in-plane spin at reference frequency instead of a single averaged precession spin parameter.

In Section 4.4.2 we showed the differences in the precessional motion and mode asymmetry content between the $\phi_{SR} = 90$ and $\phi_{SR} = 0$ cases and saw that the quasi-symmetry seen in the $\phi_{SR} = 180, 0$ case is reflected in the same. After symmetrizing the waveforms in the Quadrupole Aligned (QA) frame (see Section 4.4.3), we get a constant match across the signal (θ, ϕ) space that is higher than corresponding inertial frame match for q=1 & q=2, for q=4 the match is larger than for $\sim$ 80% of signals. This indicates that we can distinguish case $\phi_{SR} = 90$ from $\phi_{SR} = 0$ due to the different precessional modulations and mode asymmetry content, and for some q=4 cases, inclusion of both effects can improve the computed match.

We then rotate the QA symmetrized waveform back to the inertial frame and compute matches between the inertial symmetrized waveforms. For these waveforms, the mode-asymmetry content is essentially *turned-off*. Without mode-asymmetries in both signal and template, there is a overall increase in match (and consequently ρ_c) across the signal sky-position parameter space between the $\phi_{SR} = 90, 0$ cases. For q2 and q4, signals without mode-asymmetry with a different spin value can be easier or harder to distinguish as compared to full waveforms (see Fig: 4.22 and Fig: 4.23). So, for systems with the same total spin and varying spin directions, non-inclusion of mode-asymmetry information will make it harder to distinguish waveforms with different spin directions. For systems with a total different spin, non-inclusion of mode-asymmetry makes it easier or harder to distinguish the signals, depending on the mass-ratio of the system.

In Fig: 4.24, we plot the results of using a symmetrized template waveform to distinguish signal with precessional modulations and mode-asymmetry content. For the $\phi_{SR} = 90, 0$ cases, symmetrized template can find it *easier* to distinguish the signal than a full template waveform. Also, the signal from a system *with* mode-asymmetry content is seen as a different system by a template waveform of the same system but *without* mode-asymmetries. The distinguishability results are connected to the maximised match value between the template and signal. Now *if* the template waveform was from a waveform model, it is very likely that the waveform model obtains a better match at parameters different as that of the symmetrized q2a07p0 (q4a08p0) systems. If that happens to be the case, then using that waveform model in PE would very likely lead to biased parameter recovery.

The results above indicate that; i) it is possible to measure the in-plane spin direction at reference frequency at SNRs from 15 - 100 (depending on mass-ratio/spin magnitude combination) and ii) disregarding mode-asymmetry content in templates could lead to biased inferred source parameters. Towards building future IMRPhenom precessing models, the first priority is towards tuning the QA Euler angles to NR simulations; but the results from here indicate that inclusion of mode-asymmetric content could also help in improving capturing precessional effects. During the course of this study, surrogate models for precessing systems from NR waveforms have been built in [196], [197], where the symmetric and asymmetric parts of waveform modes (in the co-orbital frame) as used as "data-pieces" to build the model and this model should include the mode-asymmetry effects.

Chapter 5

Parameter estimation with multi-mode templates

The first ever detection of gravitational waves from a binary black hole source (BBH) was achieved on the 14$^{\text{th}}$ of September, 2015 [3] by the two aLIGO detectors at Hanford and Livingston. Till April 2019, there have been two observing runs by the aLIGO detectors and from the second half of 2017, the aVIRGO detector has joined the gravitational wave network facilitating the first three detector detection of a BBH source. During the first two observation runs of LIGO, a total of 10 binary black hole (BBH) mergers and one binary neutron star (BNS) merger were detected, with the total mass of the BBHs ranging between $18^{+3.1}_{-0.7}M_{\odot}$(GW170608) and $85^{+15.6}_{-10.9}M_{\odot}$(GW170729) [8]. Amongst the 10 BBHs, GW170729 and GW151226 show support for aligned spin binaries (non-zero measured χ_{eff}), but none of them show any evidence for precession. The inferred parameters are obtained by combining the posteriors recovered from `IMRPhenomPv2` and `SEOBNRv3` templates. In [198] the authors used (along with other models) multi-mode aligned-spin waveform models (`IMRPhenomHM` and `SEOBNRv4HM`) to determine the parameters of GW170729 and where the quadrupole models inferred the mass-ratio between $1 \leq q \leq 2.4$, the multi-mode models placed the limits between $1.3 \leq q \leq 3.2$. The third combined science run lasting for a year of the two aLIGO detectors and aVIRGO started from April 2019, with increased sensitivity towards detecting GW signals. With the inferred merger rates of $\approx 30-100$Gpc^{-3}yr^{-1} [199], we can expect a large number of BBH signals during this third observation run.

As mentioned in the previous chapters, the accuracy of measured parameters depends on the strength of the detector noise and the effectualness of the template waveform model. During the first two observation runs, almost all available waveform models for aligned-spin systems modelled only the dominant quadrupole mode and no higher-multipole models

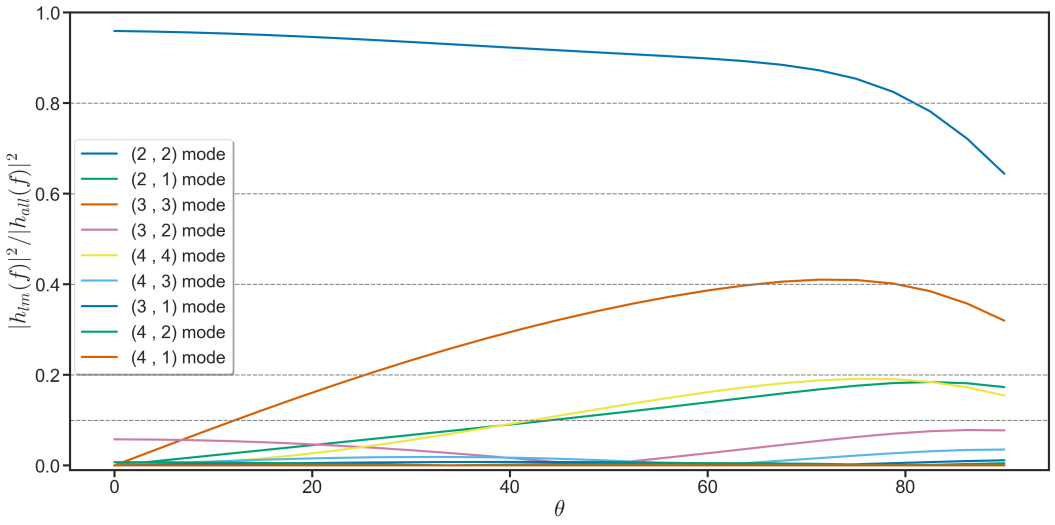

FIGURE 5.1: Behaviour of relative percent power in each mode w.r.t total signal power (y-axis) against the inclination of the binary system (x-axis) for a q=8 non-spinning system.

were used in the flagship LVC analyses ([200], [8]). Ref:[2] presented a multimode aligned-spin phenomenological waveform model (`IMRPhenomHM`) for BBHs that describes all $l = 2, 3, 4$ and $|m| = l, l-1$ modes (see Section 2.6.3 for a description of the `IMRPhenomHM` waveform model). Soon after, Ref: [143] presented a multi-mode aligned-spin waveform model (`SEOBNRv4HM`) employing the Effective One Body (EOB) description which models the modes $(l, |m|) = [(2, 2), (2, 1), (3, 3), (4, 4), (5, 5)]$.

Any gravitational wave ($h(\theta, \phi, \vec{\lambda}, t)$) can be decomposed in terms of a spherical harmonic basis with spin weight -2, ${}^{-2}Y_{lm}$,

$$h(\theta, \phi, \vec{\lambda}, t) = \sum_{l} \sum_{m=-l}^{m=l} {}^{-2}Y_{lm}(\theta, \phi) h_{lm}(\vec{\lambda}, t), \tag{5.1}$$

where $h_{lm}(\vec{\lambda}, t)$ are the gravitational wave modes. For equal mass (q=1) non-spinning system, all odd $|m|$ modes are zero, with $|m| = 2, 4, \ldots$ modes being much weaker than the dominant quadrupole mode. For systems with $q > 1$, all even and odd m modes are non-zero. The strength of the sub-dominant modes increases with increasing mass-ratio and spins. Also, for a given system with non-zero subdominant mode content, the contribution of sub-dominant modes to the signal power increases as the inclination goes from face-on to edge-on (see Fig: 5.1).

Previous studies have investigated the effect of employing higher-order mode models for gravitational wave searches [164], [165], [168], [169] and provided an estimate of the systematic errors that could be incurred from neglecting higher-order modes in the template waveforms [163], [166], [167]. In [187] and [201] the authors performed a full Bayesian

analysis of the effects of including and neglecting higher-order modes in template waveforms non-spinning systems. I now summarise some notable results relevant to the current study.

In [163], the authors used multi-mode NR-PN hybrids as signals and computed the expected statistical and systematic errors over a range of total mass and mass-ratio values using quadrupole templates, for a signal sky-averaged SNR of 8. The statistical errors are estimated from the Fisher Information Matrix, which is the noise weighted inner product between partial derivatives of the waveform. The authors compute the fitting factor maximised over the template mass parameters between the multimode signal (with fixed parameters) and quadrupole template waveform, and then, the effective systematic error is proportional to the difference between the best fit and true parameters. In this study, the authors found that non-inclusion of the subdominant modes in templates will lead to $\sim$ 10% loss in detection rate for q $\geq$6 and M $\geq 100M_{\odot}$ and will lead to systematic errors larger than statistical errors for q $\geq$4 and M $\geq 150M_{\odot}$. The results obtained from a Fisher information matrix approximation are valid for high SNR events. To study the waveform errors for low or moderate SNRs, a full Bayesian analysis is required (see Section 1.4.3 for a quick introduction to parameter estimation techniques).

In [187], the authors injected multimode non-spinning NR waveforms in zero-noise at different mass-ratios with a fixed inclination of $\pi/3$ and compared the systematic and statistical errors of the posteriors recovered by nonspinning quadrupole-only (`EOBNRv2`) and multimode waveform models for non-spinning systems (`EOBNRv2HM`). They found that up to q=6 and for SNRs $\leq$ 50, the systematic errors from `EOBNRv2HM` were smaller than or comparable to the statistical errors. The fractional systematic error (defined as the ratio between systematic bias and statistical error) for the intrinsic parameters are consistently lower for `EOBNRv2HM` than `EOBNRv2`. Also, the posteriors were recovered at a overall higher likelihood by `EOBNRv2HM` than `EOBNRv2` (see Fig:2 of [187]).

In [201], the authors performed a very comprehensive study of the effects of using `EOBNRv2HM` and `EOBNRv2` templates to recover `EOBNRv2HM` signals across a range of total mass values ($50 \leq M_{total}M_{\odot} \leq 500$) and SNRs ($6 \leq \rho \leq 18$) for q=1.25 and q=4 systems at two inclinations ($\theta_{JN} = 0, \pi/3$). Consistent with [187], the posteriors are recovered at an overall larger total evidence by `EOBNRv2HM` as compared to `EOBNRv2` (see Fig:5 of [201]) for inclined systems, the difference between which i) increases with increasing inclination, ii) increases at higher mass-ratios and iii) shows a overall increase with total mass (where the merger-ringdown contributions would increase). The posteriors are better constrained by the multi-mode model than quadrupole-only model (see Fig:7 of [201]) with lower systematic bias for inclined systems. They found that the multi-mode model constrains the inclination angle better than quadrupole-only model, which in turn leads to better constraints on the distance.

Note that this behaviour of the extrinsic parameters is expected as presence of higher-order modes in the templates allows for improved polarisation measurements that translate to improved constraints on the inclination and distance.

In the previous studies, the authors used non-spinning multi-mode and quadrupole only waveforms for the Bayesian analysis, and hence, were restricted in the (m_1, m_2) space for intrinsic parameters. In this study, we will use a multi-mode aligned-spin waveform template (`IMRPhenomHM`) and increase the dimensionality of the problem by one, i.e., (m_1, m_2 and χ_{eff}) space for intrinsic parameters. The behaviour of the systematic errors of the intrinsic recovered parameters in the (m_1, m_2) space will change in the (m_1, m_2, χ_{eff}) space due to the degeneracies between the masses and effective spin parameters [181]. Of course, the extrinsic parameter space remains the same.

One of the aims of this study is to explore the effects of using a multi-mode aligned-spin waveform template (`IMRPhenomHM`) on inferring source parameters from a multi-mode signal and to contrast it with an aligned-spin quadrupole-only model (`IMRPhenomD`). For this, we perform a set of injections at three different mass-ratios and three inclinations in zero-noise using the `IMRPhenomHM` waveform as the signal. This would give us an idea of parameter errors from both including and not-including the sub-dominant modes in templates. `IMRPhenomHM` is an approximate model of the sub-dominant modes and does not model a few of the higher harmonics, specifically, all modes with l$\geq$5 and the (3,1), (4,2), (4,1) and all the $m = 0$ modes. Other than for precessing systems, the $m = 0$ modes are generally zero. The sub-dominant modes of the model are not tuned to NR simulations and mode-mixing effects are not modelled. With that in mind, the other aim of the study is to determine the ability of `IMRPhenomHM` (`IMRPhenomD`) to recover parameters of real physical signals. For that, we perform injections with the same set of parameters as for `IMRPhenomHM` injections but with multi-mode PN-NR hybrid waveforms and compare the parameters recovered by `IMRPhenomD` and `IMRPhenomHM`. We inject non-spinning systems using both waveforms at q=2, q=4 and q=8 at inclinations of (0, $\pi/3$, $\pi/2$). As the sub-dominant strength increases as we go from lower to higher mass-ratio (or inclination), this set of runs should indicate the differences between using a quadrupole and multi-mode model at different sub-dominant mode content strength.

For this chapter, the first section will deal with the creation and validation of the multi-mode hybrids, the second section will detail the parameter estimation (PE) setup for this study and the chapter will end with the results and their discussion.

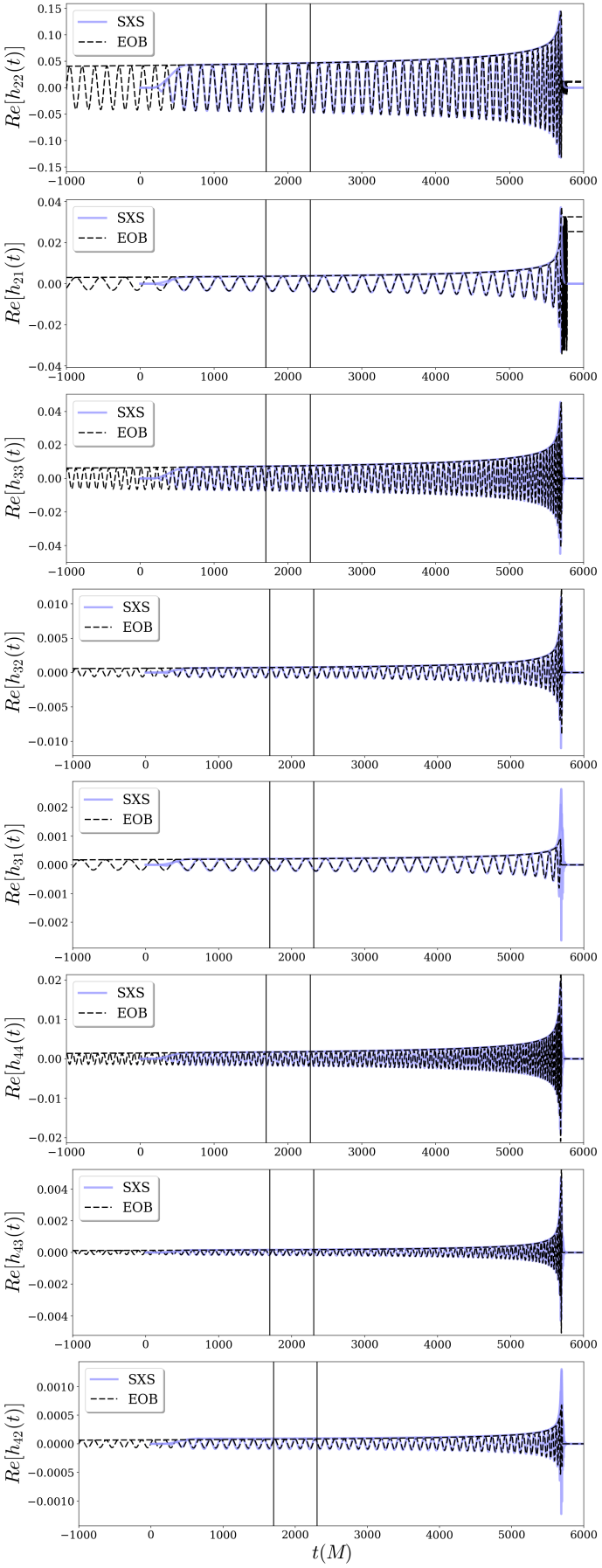

FIGURE 5.2: The figure shows the time-domain modes of the PN-EOB waveform used to construct the inspiral part of the hybrid waveform (black-dashed) with the corresponding SXS-NR mode (thick blue) shifted by the parameters (τ, ϕ_0, ψ_0) for a q=8 non-spinning system. The vertical black lines show the region of hybridisation for the modes.

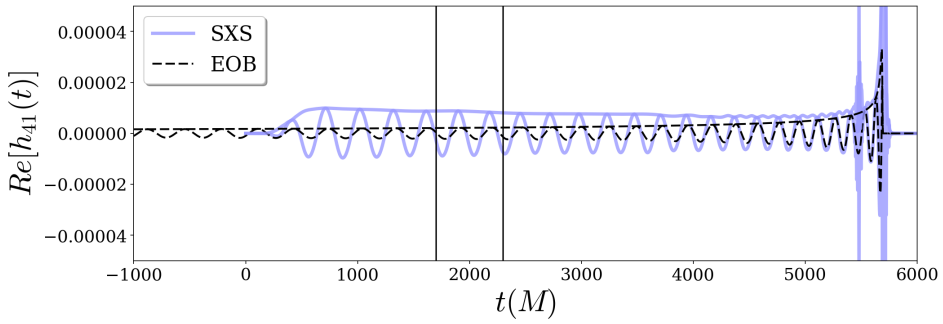

FIGURE 5.3: The figure shows the time-domain (4,1) mode for the inspiral EOB (black-dashed) and SXS-NR waveforms (thick-blue).

5.1 Construction and validation of the multi-mode hybrids

In Section 2.4.2 of Chapter: 2, I have already discussed the theory behind construction of multi-mode hybrids by using the inspiral information from PN-EOB codes and stitching them with corresponding NR waveforms. The EOB codes used to obtain the inspiral modes is based on the method described in [202] with the fits to the parameters as published in [203]. To construct a multi-mode hybrid, we require the time-shift (τ), phase and polarisation shift (ϕ_0, ψ_0) between the waveforms.

During inspiral, the frequency of mode (l, m) is related to the $(2, 2)$ mode frequency (f_{22}) via $mf_{22}/2$. So, for a NR waveform, modes with $m > 2$ will start at a higher frequency than the (2,2) mode. For example: if the NR waveform is such that its $(2, 2)$ mode starts at $f_{low} = 20$Hz for a $100M_{\odot}$ system, the $(4, 4)$ mode will start at $f_{low} = 40$Hz.

Generating NR waveforms is computationally expensive and so, the BHs are generally evolved only for the last few orbits for a given system. If we want all the modes to start at the same f_{low}, we would have to use overall high-mass values. For this study, we require that all modes of the injection waveform start at $f_{low} = 20$Hz and so, we constructed multi-mode hybrids for the systems under consideration. We construct multi-mode hybrids for all $l = 2, 3, 4$ modes, with the exception of the $(4, 1)$ mode (see Fig: 5.2). The inspiral (4,1) mode as obtained from the EOB code is very weak and does not match the NR data within the stitching region(see Fig: 5.3). Also, the relative power in the (4,1) mode is $\sim 10^{-3}$ times smaller than the (2,2) mode. For these reasons, we do not include the (4,1) mode in the hybrid.

Once we have the hybrid waveforms, for cross-validation, we compute the match between the hybrid waveform and its corresponding SXS-NR waveform at various inclinations, with the match value optimized over the phase. The total mass of the system is fixed at $100M_{\odot}$ for these systems and the match is computed with $f_{low} = 30$Hz and aLIGO PSD. We find

matches of > 0.999 across all inclinations. We also compute the matches between the hybrid-NR waveform and both `IMRPhenomHM` and `IMRPhenomD` over the inclination space and quote the range of matches over the phase (fixed inclination). In Fig: 5.4 we plot the matches. We see that `IMRPhenomHM` gives higher matches than `IMRPhenomD` across the mass-ratio and inclination space. The match values with `IMRPhenomHM` are lower than those with the hybrid-NR waveforms due to the approximate nature of the mode, but the results we see here are consistent with those presented in [2].

5.2 Setup for PE runs

For the injections, we constructed a set of hybrid-NR waveforms, of which frames were created using the `pycbc_generate_hwinj` function from the PyCBC library [204]. The infrastructure employed for generating NR frames is described in [185]. For the injections, the total mass of the system, low frequency cut-off, the gps-trigger time, the sky-position for the system, its polarisation and the required SNR of the signal have to be specified.

For all runs, we choose a total mass of $100M_{\odot}$ and low frequency cut-off of 20Hz. The choice of total mass is motivated by two factors; i) at high masses, where the majority of contribution to total signal power is from the merger phase, systematics due to the approximate nature of `IMRPhenomHM` should be apparent and ii) at lower masses the total CPU time required for PE runs will be larger due to the high computational cost of `IMRPhenomHM` waveform generation. The hybrids are created so that all subdominant modes start at frequencies less than 20Hz at $100M_{\odot}$. The SNR of the system is fixed to 25. For each inclination value, the injection code computes the distance at which the binary needs to be placed to obtain the required SNR. Hence, face-on systems are injected farther away than edge-on systems.

For the PE runs, we wanted a recovery PSD which would be like the O2 detector sensitivity. So, we choose a gps-time that is near the trigger time for GW170814 and set it to 1186741869. Using this gps-time, we create the median PSD for H1 and L1 using the BayesWave post-processing script following the instructions as provided in Ref: [205]. The PSD obtained from that is used for recovery during the PE runs.

The gravitational wave strain as seen by the detector depends on the sky-position and polarisation values, which enter via the detector response functions (see Eq: 1.27, Eq: 1.28 and Eq: 1.29). For the sky-position, we first fix the polarisation ($\psi = 1.4$) and the gps-trigger time (1186741869) and use those values of (ra, dec) where; i) neither F_{+} or $F_{\times} \sim 0$ and ii) the total detector response is neither too high or too low (see Fig: 5.5).

Once all the parameters are fixed, we generate signals using the hybrid-NR waveforms and `IMRPhenomHM` waveforms and the signals are injected in zero-noise. Injecting the signal in

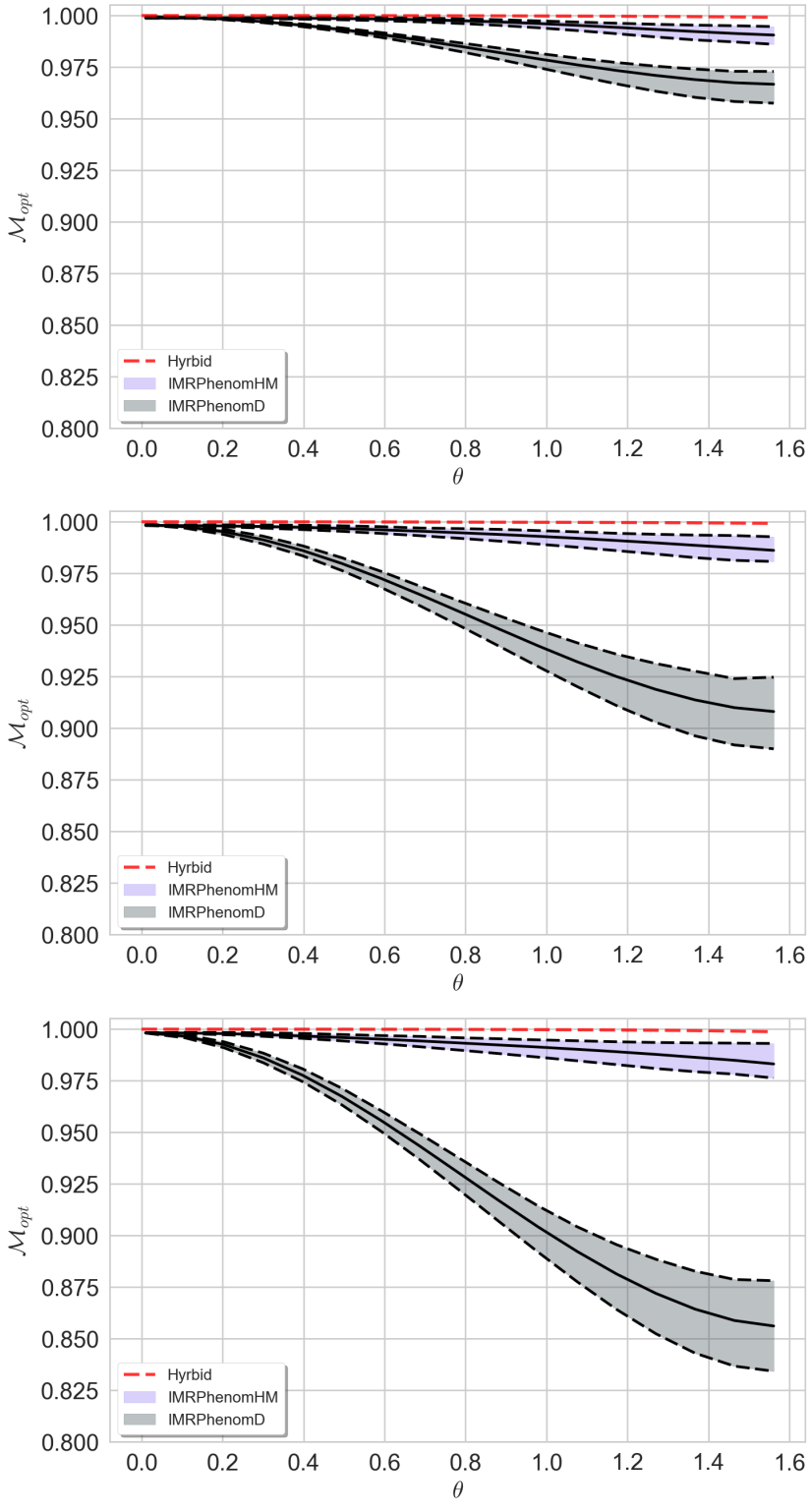

FIGURE 5.4: This figure gives the match between non-spinning q=2 (top panel), q=4 (middle panel) and q=8 (bottom panel) hybrid NR waveforms with `IMRPhenomD` (grey) and `IMRPhenomHM` (blue) waveforms. The dashed-red line gives the match between the hybrid-NR waveform and the corresponding SXS waveform optimized over overall phase. The match are computed with f_{min} = 30Hz and f_{max}=1000Hz with aLIGO PSD.

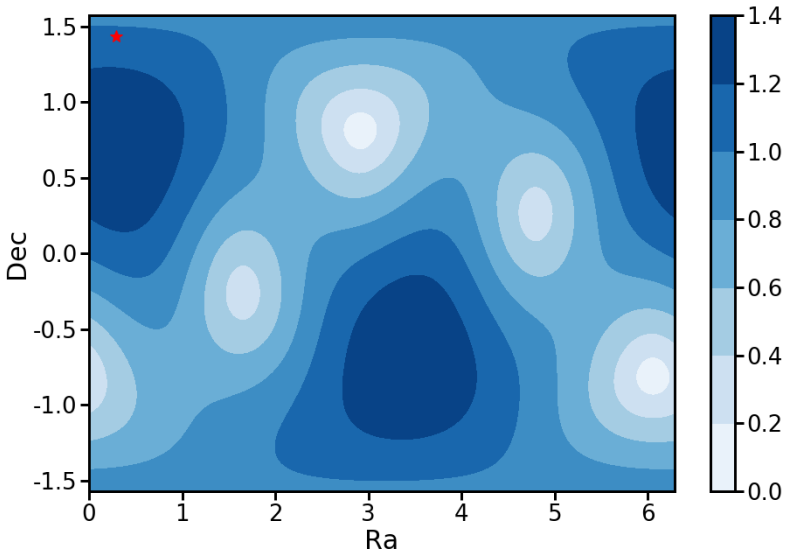

FIGURE 5.5: This figure plots the variation of total detector response ($F_{total} = \sqrt{F_+^2 + F_\times^2}$) across the sky-position [ra $\in [0, 2\pi]$ and dec $\in [-\pi/2, \pi/2]$] for gps time = 1186741869. The red star gives the sky-position used for the injections which has $F_{total} = 0.810$ and the ratio of F_+ to $F_\times$ is 2.3 (1.2) for H1 (L1).

zero-noise ensures that there are no errors due to random detector noise and the results can then be interpreted as an average over an ensemble of gaussian noise realizations.

For the PE runs, we use the `lalinference_nest` sampler from the `LALInference` package of `LALSuite` [53]. The number of live points was fixed at 1024 for all runs. All the PE runs were performed on the ARCCA [186] cluster at Cardiff.

5.3 Results

For this study, we performed a total of 36 PE runs. We injected both hybrid-NR and `IMRPhenomHM` waveforms for 3 different mass-ratios at 3 inclinations and the posteriors are recovered by `IMRPhenomD` and `IMRPhenomHM` for each injection. For the results, we will first discuss the recovery of the intrinsic parameters ($\mathcal{M}_c, q, \chi_{eff}, M_{total}$). For the intrinsic parameter recovery, we will first discuss the results of `IMRPhenomHM` injections and then hybrid-NR injections.

Then, we will discuss the recovery of the extrinsic parameters, i.e., the distance (d_L) and inclination (θ_{JN}). As these are non-spinning systems, $\vec{L} \parallel \vec{J}$ and so, $\theta_{JN} = \theta_{LN}$.

5.3.1 Recovery of intrinsic parameters:

For these plots, the posterior over a parameter from each run is clipped within its 90% credible intervals and then we plot them as a violin plot. For each parameter, the y-axis shows the value of the recovered posterior and the x-axis gives the injected inclination-recovery waveform combination. For example; if the recovery is for an edge-on injection by `IMRPhenomD`, it is labelled as $\iota = 90^o$PhnD. As we are splitting the results for `IMRPhenomHM` injections and hybrid-NR injections, there is no need to specify the injected waveform in the plot. Posteriors for q2, q4 and q8 systems are shown in Blue, Grey and Orange respectively. For reasons that we will discuss soon, the posteriors are shown at different opacities depending on the recovered maximum likelihood value of that particular run.

For a given (mass-ratio, inclination) configuration, the improved constraints on the inclination and distance parameters by using multi-mode templates might lead to better constraints on the intrinsic parameters. Let us define $d^{model}_{\lambda_i} = C^{upper}_{\lambda_i} - C^{lower}_{\lambda_i}$, where $C^{upper}_{\lambda_i}$ and $C^{lower}_{\lambda_i}$ are the upper and lower bounds of the 90% CI for a given parameter λ_i. Hence, $d^{model}_{\lambda_i}$ would provide a measure of the posterior width. Using this, we define the relative percent difference between the credible interval widths for a given configuration (Δ_{λ_i}) as,

$$\Delta_{\lambda_i} = 100 \left(\frac{d^{\texttt{IMRPhenomD}}_{\lambda_i} - d^{\texttt{IMRPhenomHM}}_{\lambda_i}}{d^{\texttt{IMRPhenomD}}_{\lambda_i}} \right). \tag{5.2}$$

For a given intrinsic parameter, Δ_{λ_i} would quantify the improvements on the parameter constraints from using multi-mode templates.

The Bayes factor measures how likely one model is compared to the other. From the PE codes, we get the log Bayes factor (B_i) of a signal hypothesis (which would be the template waveform used for that run) against the noise-only hypothesis. Hence, a difference of the log Bayes factors obtained from `IMRPhenomD` and `IMRPhenomHM` recovery will give an idea of how much better (if) `IMRPhenomHM` is at recreating the signal in the injection. For eg: if $Log(B^{PhnD}_i) = 190$ and $Log(B^{PhnHM}_i) = 195$, then $B^{PhnHM}_i / B^{PhnD}_i = e^5$, i.e., `IMRPhenomHM` is e^5 times more likely to recreate the signal as compared to `IMRPhenomD`. We will first discuss the results of `IMRPhenomHM` injections.

5.3.1.1 `IMRPhenomHM` Injections

The results of recovered intrinsic parameters for `IMRPhenomHM` injection are given in Fig: 5.6 (for $\mathcal{M}_c$ and q) and Fig: 5.7 (for M_{total} and χ_{eff}), with the Δ_{λ_i} plots in Fig: 5.8. At face-on inclinations, posteriors recovered by `IMRPhenomHM` and `IMRPhenomD` show no bias and the recovered posteriors are similar to each other. This is expected due to the *almost*

zero contributions of higher-order modes to total signal power at face-on inclination (see Fig: 5.1). Also, as the underlying quadrupole model for `IMRPhenomHM` is `IMRPhenomD`, they should show similar behaviour in situations where the higher-order mode content is weak. For face-on, we see slightly improved constraints on $(\mathcal{M}_c, M_{total}, \chi_{eff})$ for q=4 and q=8 ($\Delta_{\lambda_i} \geq 0$) and the mass-ratio recovered by `IMRPhenomHM` is always better constrained than the corresponding `IMRPhenomD` recovery for all q ($\Delta_q > 0$) (see the top-left plot of Fig: 5.8).

At higher inclination values, `IMRPhenomD` recovery starts being biased away from the true value and the parameters are recovered at comparatively lower likelihood. These effects are stronger with increasing sub-dominant mode contribution to total signal power. At q=2, the `IMRPhenomD` recovered $\mathcal{M}_c$ and M_{total} are slightly biased away from the true value towards overall higher total mass with a majority support for mass-ratio being more from near equal-mass systems. For a given q, the waveform length decreases (increases) at higher (lower) total mass or more negative (positive) χ_{eff}. For q2 then, the effect of an overall higher mass is compensated by positive χ_{eff} recovery. At q=4 and 8, mass-ratio recovery is accurate, but ($\mathcal{M}_c$, M_{total}) show a moderate bias towards overall lower mass, with the bias increasing with inclination, which then leads to a biased negative spin recovery. Also, as we go from q=2 to q=8, the maximum likelihood of the posteriors recovered by `IMRPhenomD` for a given inclination reduces.

Let us consider the likelihood in more detail. During the PE run, the recovered posterior depends on the likelihood for that run along with the prior over the parameters. The likelihood function is,

$$\mathcal{L} \propto - < d(t) - h(\vec{\lambda}) | d(t) - h(\vec{\lambda}) >, \tag{5.3}$$

where $d(t) = s(t) + n(t)$ is the detector response with $s(t)$ being the signal and $n(t)$ being the noise. In case of zero-noise, $n(t) = 0$, and so, $\mathcal{L} \propto < s(t) - h(\vec{\lambda}) | s(t) - h(\vec{\lambda}) >$. Now, if the template is able to model the signal in the data accurately, then $s(t) - h(\vec{\lambda}) \to 0$. So, a higher $|\mathcal{L}|$ means that the template is not able to model the signal present in the detector data and vice versa.

The most extreme case of low likelihood, is the q8 edge-on recovery of the `IMRPhenomHM` signal by `IMRPhenomD`, which shows a bi-modal distribution. For this injection, `IMRPhenomD` sees the signal as two completely different systems [$(M_{total}, q, \chi_{eff}) \sim (85, 7, -0.25)$, $(63, 11, -1.)$] with comparable (but overall very low) likelihood. We performed additional PE runs for q8 edge-on `IMRPhenomHM` injection with `IMRPhenomD` recovery, using a larger number of live points and effective samples, but this bi-modal posterior distribution persisted. Two more PE runs were then done where the sky-position of the signal was randomized, keeping the polarisation fixed and vice versa. Although the `IMRPhenomD` recovered parameters for these runs lost their bi-modal behaviour, they still were 1) highly biased and 2)

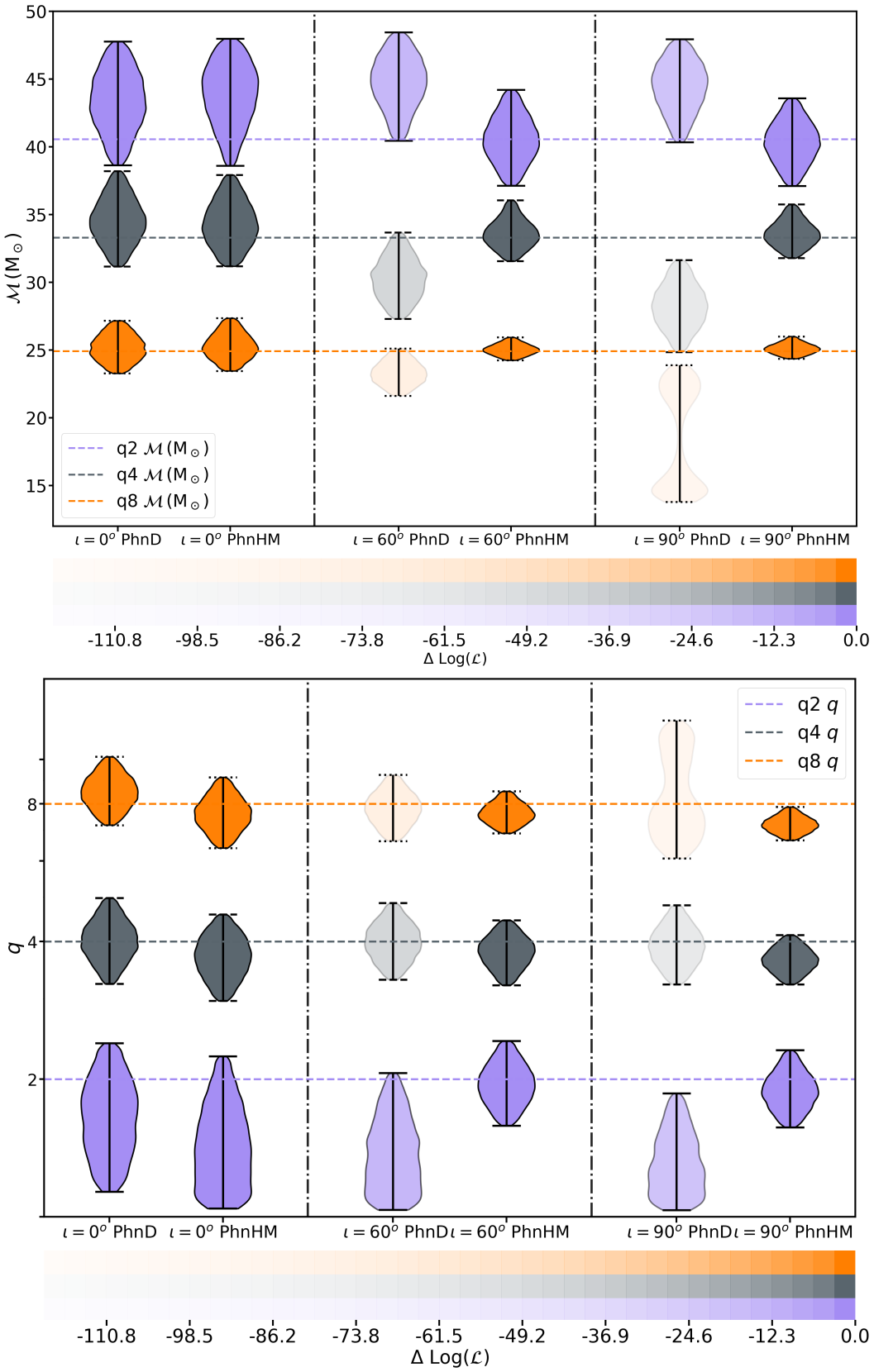

FIGURE 5.6: Posteriors of intrinsic parameters $(\mathcal{M}_c, q)$ for `IMRPhenomHM` waveform injected at q = 2, 4, 8 with $\theta_{JN} = 0, \pi/3, \pi/2$. Posteriors for q2 (q4) [q8] are shown in Blue (Grey) [Orange] with the opacity of each determined from the maximum likelihood value of that run. The variation of opacity over the likelihood values is shown at the bottom of each graph. Overall the posteriors recovered by quadrupole only model show increasing bias at higher θ_{JN} for a given q and vice-versa. This behaviour is not present for multi-mode model posterior recovery. See text for further discussion of the biases, especially the bi-modality of `IMRPhenomD` recovered posteriors for q=8 edge-on configuration.

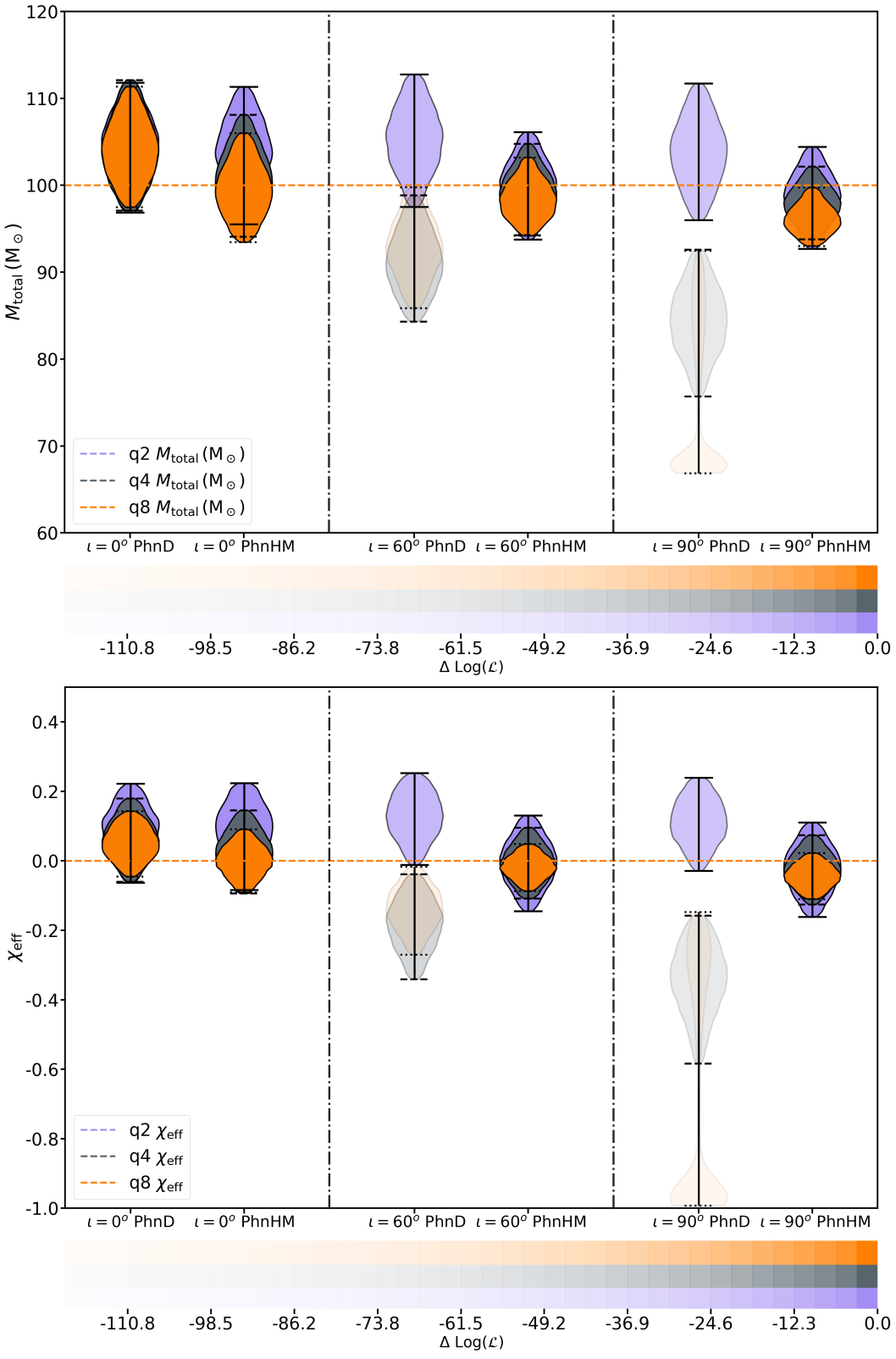

FIGURE 5.7: Posteriors of intrinsic parameters (M_{total}, χ_{eff}) for `IMRPhenomHM` waveform injected at q = 2, 4, 8 with $\theta_{JN} = 0, \pi/3, \pi/2$. Posteriors for q2 (q4) [q8] are shown in Blue (Grey) [Orange] with the opacity of each determined from the maximum likelihood value of that run. The variation of opacity over the likelihood values is shown at the bottom of each graph. At non-zero inclinations, the χ_{eff} recovered by `IMRPhenomD` drifts away from the injected value leading to biases on the total mass (see text for how these parameters affect each other). Posteriors recovered by the multi-mode mode for χ_{eff} and M_{total} are generally accurate, with a *slightly* biased M_{total} recovery at q=8 edge-on; which can be explained by observational priors (see text).

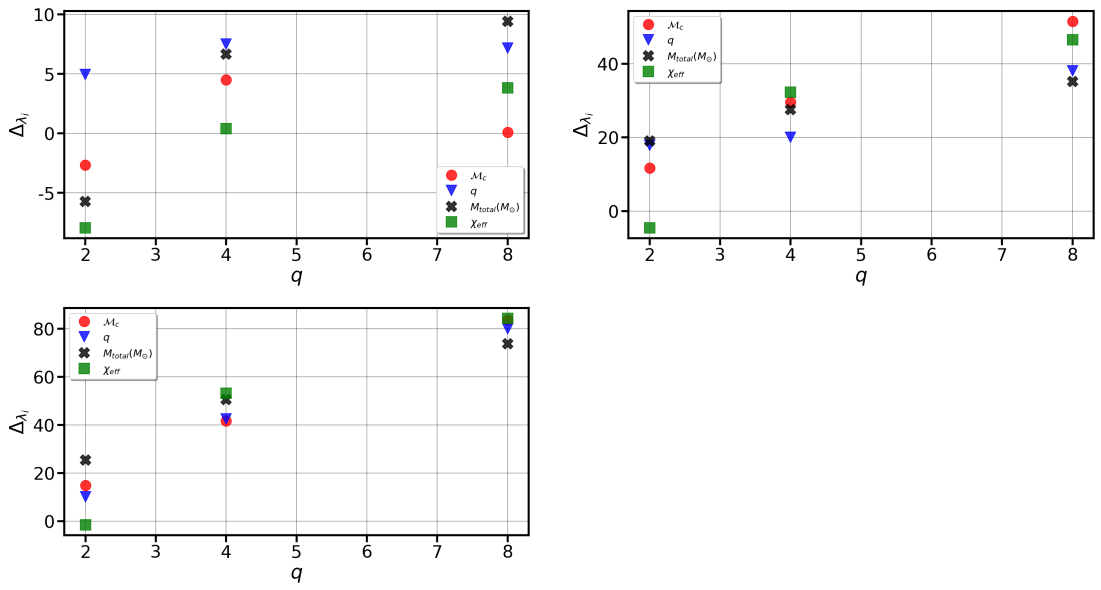

FIGURE 5.8: Plot of Δ_{λ_i} for all the `IMRPhenomHM` injections. Results for face-on, $\pi/3$ and $\pi/2$ inclination injections are shown in top left, top right and bottom left respectively. Δ_{λ_i} for the parameters $(\mathcal{M}_c, M_{total}, q, \chi_{eff})$ are shown with red-circle, black-cross, blue-lower triangle and green-square respectively. Generally, for a given parameter, Δ_{λ_i} improves with q for a given θ_{JN} or improves with θ_{JN} for a given q. Hence, recovered parameters tend to be more precise with multi-mode models as compared to quadrupole-only models.

recovered with similar maximum likelihood ($\sim$ -95). The bi-modality of recovered parameters in Fig: 5.6 and Fig: 5.7 is a consequence of `IMRPhenomD` seeing the signal as from two different but equally likely systems, which is lost when the signal morphology changes with changing sky-position and polarisation values. But, for all sky-position and polarisation combinations, parameters recovered by `IMRPhenomD` for q=8 edge-on system show a consistent bias towards lower total mass and negative χ_{eff}. Also, the difference in the log Bayes factor for the `IMRPhenomD` and `IMRPhenomHM` recovery for the bi-modal run is 94, which implies that the signal as seen by `IMRPhenomD` is highly unlikely as compared to what `IMRPhenomHM` recovers. All this suggests that the observed bi-modality is not real, but a combined effect of the priors over the physical parameters and the inaccuracy of `IMRPhenomD` towards recreating the true signal.

$\mathcal{M}_c$ posteriors recovered by `IMRPhenomHM` are accurate for all the cases. At face-on q=2, recovered q has a large support from near-equal mass systems, but this behaviour is lost at higher inclinations. At edge-on q=4 and 8, mass-ratio and M_{total} are slightly biased towards lower values. The inclination prior has very low support for edge-on inclinations, and hence, the recovered θ_{JN} posterior tends to have more support from non-edge-on inclinations, which leads to the distance being overestimated. The amplitude ($\mathcal{A}$) of a BBH source is $\mathcal{A} \propto \mathcal{M}_c^{5/6}/d_L \equiv M^{5/6}\sqrt{\eta}/d_L$. At higher masses, $\mathcal{M}_c$ and M_{total} are the better constrained mass parameters. Hence, overestimating d_L (with good constraints on

$\mathcal{M}_c$ and M_{total}) would lead to a higher value of η or equivalently, a lower q. This effect is what causes the slight bias on the IMRPhenomHM recovered q for edge-on q=4 and q=8 IMRPhenomHM injections.

At inclinations of $\pi/3$ and $\pi/2$, the mass parameters recovered by IMRPhenomHM are always better constrained than corresponding IMRPhenomD recoveries (see top right and bottom left panels of Fig: 5.8), i.e., $\Delta_{\lambda_i} > 0$. For a given inclination - parameter combination, Δ_{λ_i} increases with increasing q. For e.g., for $\theta_{JN} = \pi/3$ inclination, $\Delta_{\mathcal{M}_c} \sim 20, 30, 50$ for q=2, 4 and 8 respectively. The comparatively high Δ_{λ_i} values for edge-on q8 configuration is due to the bi-modality of IMRPhenomD recovered posteriors. Overall, we observe better constraints on the mass-parameters for inclined system across the mass-ratio space.

Where the quadrupole model tends away from zero spin at higher inclinations, IMRPhenomHM recovery does not. At $\theta_{JN} = \pi/3, \pi/2$; q=2 recovered χ_{eff} posteriors has almost the width for IMRPhenomD and IMRPhenomHM templates ($\Delta_{\chi_{eff}} \sim 0$), and although the spread of these posteriors are similar, χ_{eff} recovered by IMRPhenomHM are accurate whereas IMRPhenomD recovery is biased. At q=4 and q=8, $\Delta_{\chi_{eff}} \geq 0$ for all inclinations, IMRPhenomD recovers biased χ_{eff} posteriors for non face-on inclinations whereas IMRPhenomHM recovery is accurate for all configurations.

Although we expect IMRPhenomHM to recover accurate parameters for IMRPhenomHM injections, this study would also provide an indication of the possible measurement accuracy from using a multi-mode model. We see that other than for face-on configurations, the recovered mass and spin parameters are better constrained ($\Delta_{\lambda_i} > 0$), with the constraints improving with increasing mass-ratio or inclination.

5.3.1.2 Hybrid-NR Injections

This section gives the results of posteriors recovered by IMRPhenomD and IMRPhenomHM for hybrid-NR signals. The hybrid-NR waveforms i) contain extra (3,1) and (4,2) modes in the waveform and ii) contain the correct mode content for real physical systems. Where IMRPhenomHM injection results give an idea of the parameter recoveries by multi-mode compared to quadrupole-only templates in the presence of multi-mode signals, the hybrid-NR injections provide an estimate of the systematic errors of parameters recovered by IMRPhenomHM due to approximations in the model.

The results of recovered intrinsic parameters for Hybrid NR waveform injections are given in Fig: 5.9 and Fig: 5.10 and Fig: 5.11 shows the Δ_{λ_i} for these injections. For q=2, q=4 and q=8, at face-on inclinations, posteriors recovered by IMRPhenomHM and IMRPhenomD follow the same behaviour as what we had seen for IMRPhenomHM injections. Parameters

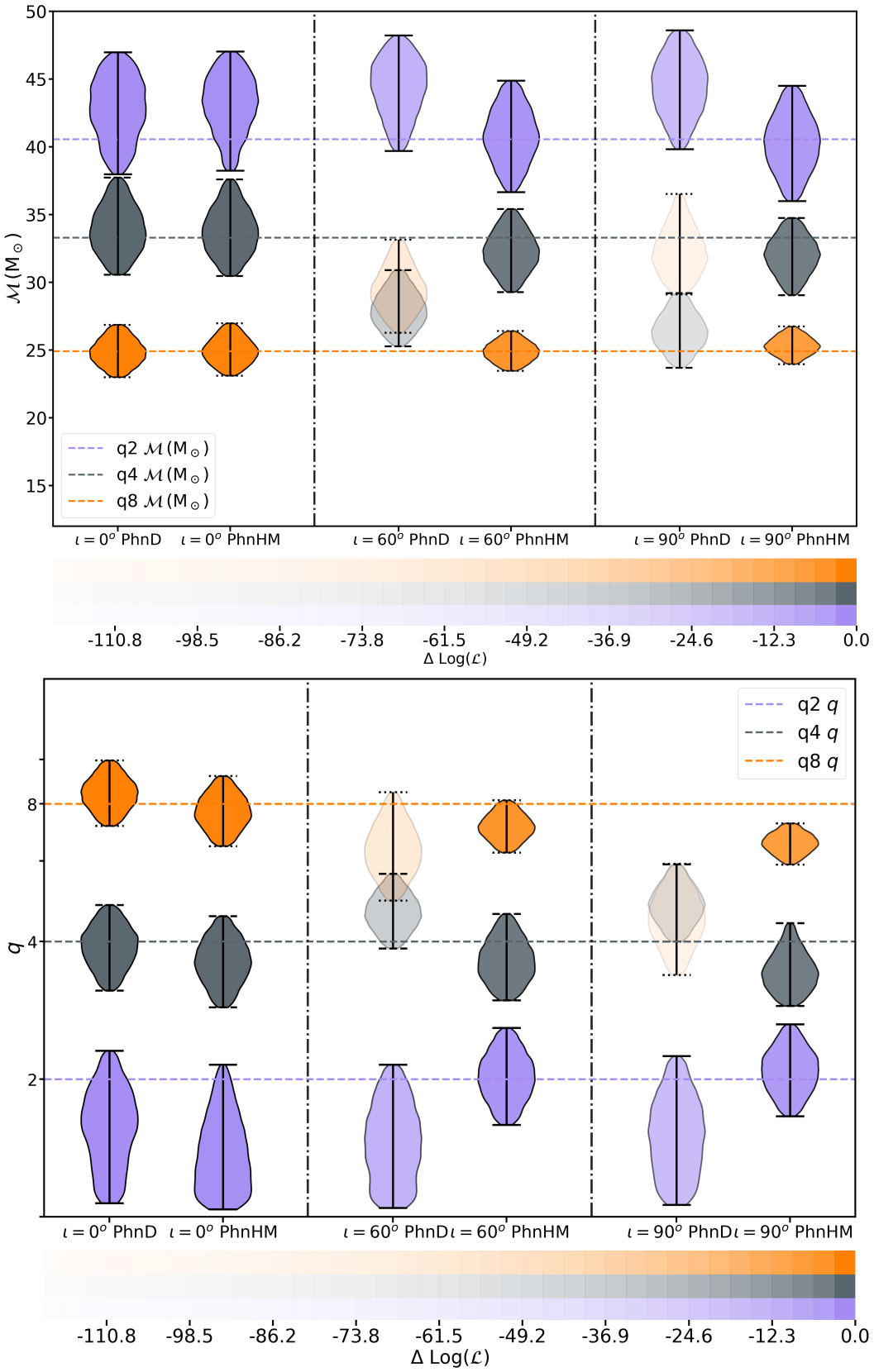

FIGURE 5.9: Posteriors of intrinsic parameters $(\mathcal{M}_c, q)$ for Hybrid-NR waveform injected at q = 2, 4, 8 with $\theta_{JN} = 0, \pi/3, \pi/2$. Posteriors for q2 (q4) [q8] are shown in Blue (Grey) [Orange] with the opacity of each determined from the maximum likelihood value of that run. The variation of opacity over the likelihood values is shown at the bottom of each graph. Posteriors recovered by quadrupole only model shows similar trends as seen for `IMRPhenomHM` injections, with differences in the amount and direction of the bias. Wherever `IMRPhenomHM` recovered posteriors are biased, the bias is always smaller than corresponding `IMRPhenomD` recovery.

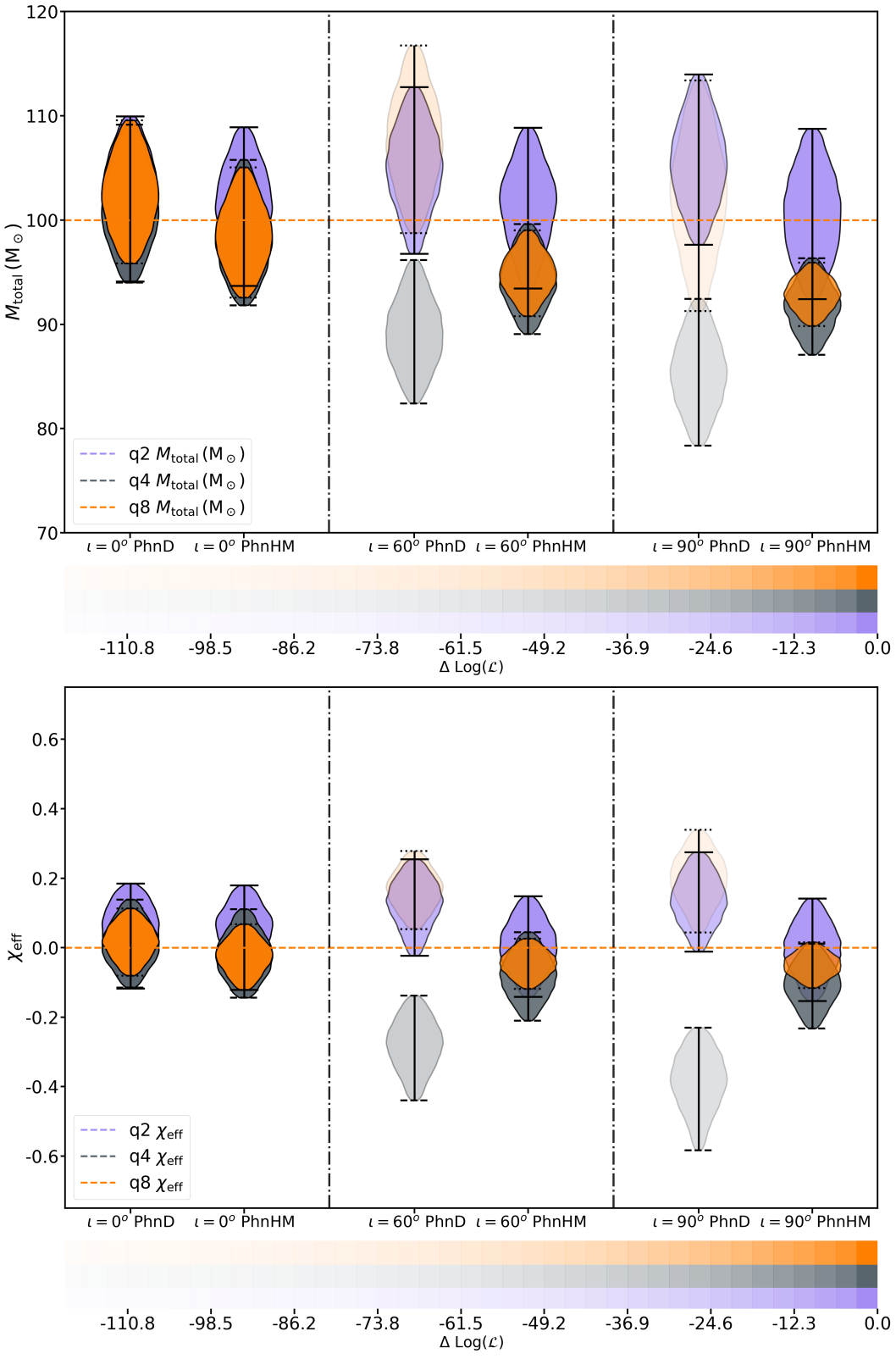

FIGURE 5.10: Posteriors of intrinsic parameters (M_{total}, χ_{eff}) for Hybrid-NR waveform injected at q = 2, 4, 8 with $\theta_{JN} = 0, \pi/3, \pi/2$. Posteriors for q2 (q4) [q8] are shown in Blue (Grey) [Orange] with the opacity of each determined from the maximum likelihood value of that run. The variation of opacity over the likelihood values is shown at the bottom of each graph. Posteriors recovered by `IMRPhenomD` and `IMRPhenomHM` for these Hybrid-NR injections show similar qualitative behaviour across the $q - \theta_{JN}$ space, with slight quantitative differences (see text for further discussion).

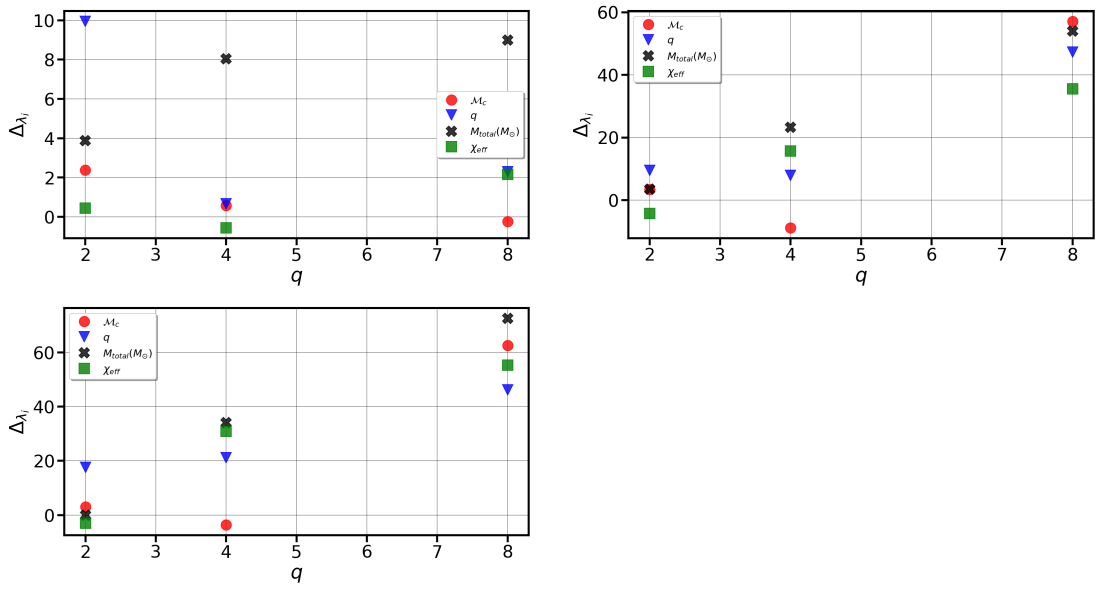

FIGURE 5.11: Plot of Δ_{λ_i} for all the hybrid-NR injections. Results for face-on, $\pi/3$ and $\pi/2$ inclination injections are shown in top left, top right and bottom left respectively. Δ_{λ_i} for the parameters $(\mathcal{M}_c, M_{total}, q, \chi_{eff})$ are shown with red-circle, black-cross, blue-lower triangle and green-square respectively. Behaviour of Δ_{λ_i} is qualitatively similar to that of the `IMRPhenomHM` injections across the parameter space, with some quantitative differences.

recovered by both the models are accurate, but the posteriors recovered by `IMRPhenomHM` show slightly improved constraints on the mass and spin parameters ($\Delta_{\lambda_i} \geq 0$).

At q=2 and inclinations of $\pi/3$ and $\pi/2$, `IMRPhenomD` recovered mass and spin parameters shows a slight bias and `IMRPhenomHM` recovery is unbiased. The behaviour of the bias (amount and direction) as seen by `IMRPhenomD` for the hybrid-NR injection is similar to that for q=2 `IMRPhenomHM` injections, for e.g., `IMRPhenomD` recovered χ_{eff} (M_{total}) tends towards positive χ_{eff} (higher M_{total}) but contains the true value within its 90% CIs . At high inclinations, the support towards equal-mass systems for q=2 injection as seen by `IMRPhenomD` is lost with `IMRPhenomHM`. For inclined signals, mass-ratio is better constrained by `IMRPhenomHM` ($\Delta_q \sim 20$), with the other posteriors recovered with similar widths, i.e, Δ_{λ_i} is near zero for $\lambda_i = (\mathcal{M}_c, M_{total}, \chi_{eff})$.

For q=4 and 8, at high inclinations, `IMRPhenomD` recovered mass and spin parameters show increasing bias and the posteriors are recovered at lower maximum likelihood. For example: for edge-on q=8 injection, `IMRPhenomD` recovers $\mathcal{M}_c$ and q consistent for q=4 injection. For q=4 at inclinations of $\pi/3$ and $\pi/2$, the spin is biased towards negative χ_{eff} and the recovered total mass is biased towards lower masses. For q=8, the behaviour of the bias (amount and direction) changes between the hybrid-NR injections and `IMRPhenomHM` injections for these systems.

The $\mathcal{M}_c$ recovered by IMRPhenomHM for hybrid NR injections is unbiased for all cases, with the total mass recovery for q=4 and q=8 at $\pi/3$ and $\pi/2$ shows a bias towards lower total mass. For edge-on q=4 injection, the mass-ratio recovered by IMRPhenomHM contains the real value within its 90% CI bounds, but the posterior has greater support from lower q. For q=8, the mass-ratio at $\pi/3$ and $\pi/2$ tends towards lower q values but this bias is always smaller than corresponding quadrupole recovery, but is larger than the corresponding IMRPhenomHM injection. For inclined q=8 hybrid-NR injections, the recovered θ_{JN} is *more* off the true value as compared to corresponding IMRPhenomHM injection which leads to the distance being over-estimated and hence, a larger bias on q as compared to the IMRPhenomHM injection. The same explanation can be applied for the q=4 mass-ratio bias.

For all cases, IMRPhenomHM is able to recover the true spin value within it's 90% CI bounds, though at q=4 and 8, the posterior has more support from anti-aligned spins. With multi-mode templates, at higher mass-ratios, the recovered posteriors are more constrained than the corresponding quadrupole recovery and recovered with overall higher likelihood.

For both IMRPhenomHM and hybrid-NR injections, the quadrupole recovery is biased at high inclination and mass-ratios, with the bias direction depending on the injected waveform. IMRPhenomHM recovers accurate $\mathcal{M}_c$ and consistent χ_{eff} for both injection waveforms. For q=8 systems at $\pi/3$ and $\pi/2$, IMRPhenomHM recovered M_{total} and q shows a bias towards overall lower total mass and lower mass-ratio, with the bias being larger for the hybrid-NR injections than IMRPhenomHM injections. Although the mass parameters inferred by IMRPhenomHM can show a bias for high inclination and high-mass ratio systems, the bias is consistently smaller than IMRPhenomD and the spin posteriors always contain the true value. At lower mass-ratios, IMRPhenomHM can recover the correct q at non-zero inclinations as compared to the large support from equal-mass systems as seen by IMRPhenomD. The mass-spin posteriors recovered by IMRPhenomHM are generally better constrained or have similar widths as compared to IMRPhenomD recovery. Overall, we see positive Δ_q and $\Delta_{M_{total}}$ for IMRPhenomHM recoveries and the values increase with mass-ratio (for a given inclination) and inclination (fixed mass-ratio). Hence, use of multi-mode templates lead to better measurements of the intrinsic parameters across the explored mass-spin space as compared to the quadrupole-only templates with the accuracy of measurements dictated by accuracy of sub-dominant mode content.

5.3.2 Recovery of extrinsic parameters

For intrinsic parameters, at face-on configurations, parameter recovery by the quadrupole and multi-mode models are similar to each other. This behaviour breaks down for the extrinsic parameters. For the distance plots, we show the 90% clipped posteriors for each

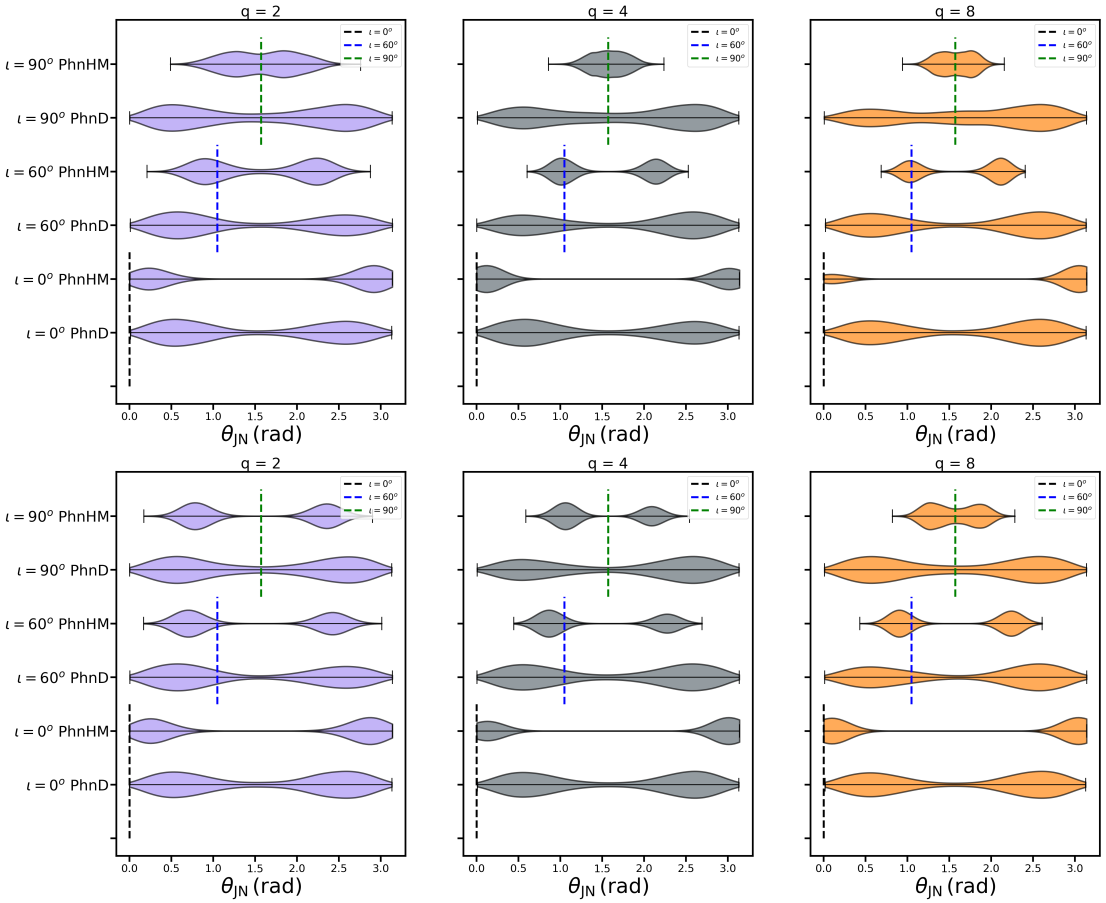

FIGURE 5.12: θ_{JN} recovery for `IMRPhenomHM` injection (top row) and hybrid NR injections (bottom row) for inclinations 0, $\pi/3$ and $\pi/2$ and with `IMRPhenomHM` and `IMRPhenomD` as recovery waveform models. Inclination recovery for q2, q4 and q8 configurations are shown in the left, center and right columns respectively and the posteriors are plotted in Blue, Grey and Orange respectively. The true value of the injected inclination are given in dashed Black, Blue and Green lines for 0 , $\pi/3$ and $\pi/2$.

configuration. The posteriors for q=2, q=4 and q=8 injections are given in Blue, Grey and Orange. The inclination recovery plots follow the same colour scheme and we plot all the posterior samples.

5.3.2.1 θ_{JN} recovery

Figure: 5.12 gives the results for inclination recovery. For both `IMRPhenomHM` and hybrid NR injections, at all mass-ratio and inclination configurations, θ_{JN} recovery by `IMRPhenomD` shows a similar bimodal behaviour and mostly follows the prior. Inclination recovery is unaffected by mass-ratio or inclination value for the quadrupole only model and thus it is not possible to differentiate between a non-inclined and inclined system. For the quadrupole-only templates, there exists a degeneracy between inclination (θ_{JN}), polarisation (ψ) and phase (ϕ), which leads to the similar bi-modal posteriors for θ_{JN} for any injected inclination.

For IMRPhenomHM recovery, the bi-modality for inclination posterior persists, but the posteriors are better constrained. At face-on configurations for IMRPhenomHM and hybrid NR injections, IMRPhenomHM sees the system as strongly face-on or face-off. The bi-modal structure of recovered θ_{JN} could be better constrained in the presence of multiple detectors due to the improved measurements of the polarisation and it is possible that this degeneracy could be broken in some instances. For the two-detector network though, just the presence of higher modes cannot break the degeneracy. For $\pi/3$ IMRPhenomHM injection, the recovered inclination is peaked near the true value and the constraint on the inclination improves with increasing mass-ratio. Edge-on IMRPhenomHM injection posteriors show a similar behaviour. For Hybrid NR injections, inclination recovery for $\pi/3$ is peaked just off the true value and for edge-on, the recovery is completely off. Due to the presence of higher-modes, IMRPhenomHM is able to capture inclination information better than IMRPhenomD.

5.3.2.2 Distance recovery

Figure: 5.13 gives the results for distance recovery. We plot the relative distance error, $\Delta d_L = d_L^{posterior} - d_L^{injected}$. For IMRPhenomHM injections, the true distance value lies within the 90% confidence intervals for most of IMRPhenomD and all of IMRPhenomHM recovered posteriors. At larger inclinations, the quadrupole model tends to overestimate the distance to the binary. For the q2 Hybrid NR injections, at inclination $\pi/3$ and $\pi/2$, 90% CIs for d_L recovered by IMRPhenomHM do not include the true value. For all other situations though, 90% CIs for d_L recovered by IMRPhenomHM contain the true injected value.

For quadrupole-only templates, as the recovered inclination is the same for all injected inclinations, the recovered distance for non-zero inclinations tend towards overall larger values. For IMRPhenomHM injection - IMRPhenomHM recovery, where injected θ_{JN} lies within the 90% CIs of recovered θ_{JN}, the real distance is recovered at all times. For the q=2 and q=4 hybrid-NR injection - IMRPhenomHM template, recovered θ_{JN} at $\pi/3$ ($\pi/2$) is slightly (completely) off the true value which causes the recovered distance to be overestimated from the true value, though for q=4, the injected distance is within the 90% CIs. This is likely due to the different mode content in the signal and template and the waveform inaccuracies in IMRPhenomHM. But, these results do indicate that use of multi-mode template waveform will lead to better distance measurements.

The improved constraints on inclination for IMRPhenomHM recovery translates to improved constraints on the measured distance of the system as compared to IMRPhenomD recovery. We see this behaviour for all the configurations. At face-on configurations, IMRPhenomHM

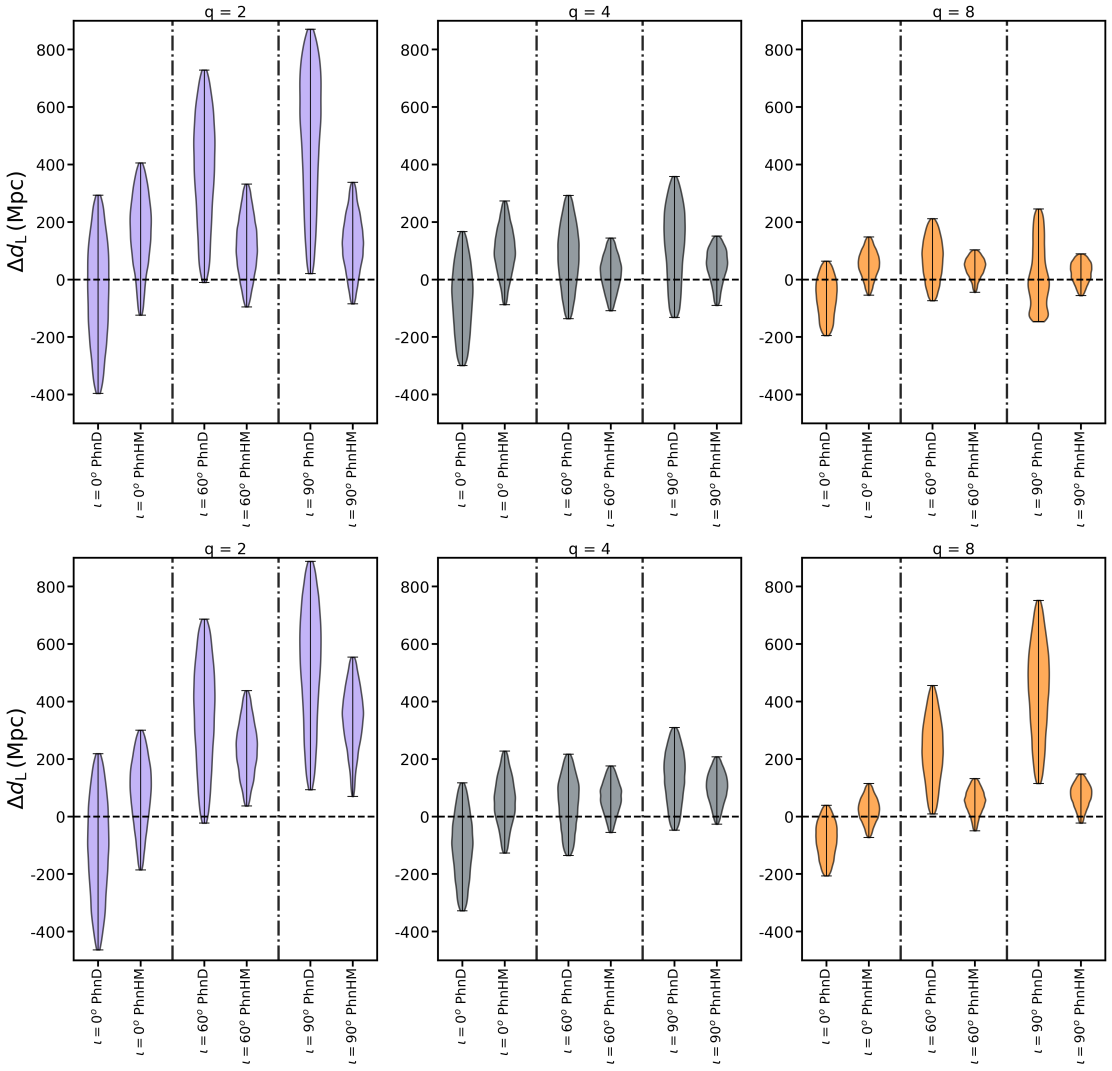

FIGURE 5.13: Recovered distance error Δd_L recovery for `IMRPhenomHM` injection (top row) and Hybrid NR injections (bottom row) for inclinations 0, $\pi/3$ and $\pi/2$ with `IMRPhenomHM` and `IMRPhenomD` as recovery waveform models. Inclination recovery for q2, q4 and q8 configurations are shown in the left, center and right columns respectively. Δd_L = 0 line is denoted by the dashed-black line. The injected distance value for `IMRPhenomHM` [NR] injection for q2-q4-q8 0 is 895-624-388 [880-639-398] Mpc, $\pi/3$ is 537-404-258 [523, 376, 249] Mpc and for $\pi/2$ is 387-307-199 [367, 253, 183] Mpc.

constraints the distance about $\sim$ 20% - 25% better as compared to `IMRPhenomD`. For higher inclinations, the constraint improves by about $\sim$ 30% - 60%.

Over the course of this study, we had performed PE runs with varying sky-positions which were chosen based on the total detector response (see Fig: 5.5). We observed that the distance constraints, for the same system, change with varying sky-position (and hence the total response). For a face-on q=4 injection at a sky-position with maximal response, we saw about $\sim$50% improvement in the distance as compared to $\sim$ 20% for a sky-position with near minimal response. Hence, for the results we quote here, we chose a sky-position with average total response. For [2], we had performed a PE run with the BAM q4a05a05

(aligned-spin) waveform where we observed $\sim$40% constraint improvement for face-on signal.

5.4 Conclusions

This is the first study that quantifies the behaviour of inferred source parameters by a multi-mode aligned-spin template waveform, where the parameters are estimated by a Bayesian analysis. For that, we inject two families of multi-mode signal waveforms (`IMRPhenomHM` and hybrid-NR) over a range of mass-ratios and inclinations (with fixed total mass) and then we compare the parameters recovered by multi-mode and quadrupole-only templates. We choose to fix the total mass of injected signals at $100M_{\odot}$ due to two reasons; i) `IMRPhenomHM` is an approximate waveform model of the sub-dominant modes, is not tuned to NR waveforms and the most uncertain part of the `IMRPhenomHM` modelling is in the merger and ringdown phases and hence, the choice of a high total mass allows us to get an idea of the systematic errors due to these waveform inaccuracies, and ii) as `IMRPhenomHM` is a computationally expensive model, signals with total mass $100M_{\odot}$ are short enough to allow an efficient PE study. An optimized version of this model is under development which will make it possible to repeat this study with low-mass signals with comparable computational time. Overall, we observe that the parameters recovered by the multi-mode templates are generally consistent with the true values and if the parameters are biased, the bias is always smaller (often significantly smaller) than for the corresponding quadrupole model. The posteriors recovered by `IMRPhenomHM` for the mass-spin parameters are better constrained than the corresponding `IMRPhenomD` recovery. The results we see here are consistent with those in [187] and [201] where non-spinning multi-mode models were used for PE.

The authors would like to point out that this study is not comprehensive enough to quantify the effects of higher-modes on parameter recovery across the entire mass-spin parameter space as we quote results for non-spinning systems with a fixed total mass while exploring the mass-ratio space. For gravitational waves, accuracy of parameter measurements vary with total mass of the system. For example: $\mathcal{M}_c$ (M_{total}) is better measured for low-mass (high-mass) systems. Also, there would be differences for high-spin or precessing configurations. That being said, the recovered parameters by a quadrupole and multi-mode model show broad trends across the parameter space, which we now attempt to describe and explain. We expect the same trends to continue for spinning systems, but given that astrophysical BBH populations favour small spins [8], [206] (based on current observations), the results here should hold for most likely GW observations.

A multi-mode model can constraint inclinations much better than a quadrupole model across the different mass-ratio and inclination values, leading to better constraints on distance measurements. For example, for a q2 face-on injection, the posteriors recovered by the multi-mode model strongly favour face-on or face-off systems whereas the quadrupole model gets support from all possible inclinations. The behaviour of recovered parameters between `IMRPhenomHM` and hybrid NR injections suggest that higher-order mode templates improve inclination measurements; with the accuracy of the measured inclination depending on the accuracy of model to recreate the sub-dominant modes.

For a given system, the contribution of sub-dominant modes towards total signal power increases with increasing inclination, peaking at $\theta = \pi/2$. The total mass of the system and distance to the system determine the strength of the signal amplitude and hence, signal power. For a signal with non-zero inclination, a quadrupole-only template model that gets more support from non-edge-on inclinations, would tend to find that the (comparatively) weak signal is from further off and tends to overestimate d_L. A multi-mode template model can better constraint the degeneracy between the inclination, phase and polarisation values leading to improved constraints on the inclination compared to quadrupole-only model, which then translates to better constrained measurement of distance. With improved multi-mode models, we can expect improved inclination constraints and hence, distance measurements. Especially for a three-detector network, where we can expect improved constraints on the extrinsic parameters as compared to a two-detector network [207], [208].

With multi-mode templates, we find that parameters can be better constrained as compared to quadrupole-only model with the constraints improving with increasing mass-ratio and inclination (see Fig: 5.8 and Fig: 5.11). The general behaviour of parameter constraints from our results are consistent with those seen in [201], but the posterior widths we see here are slightly larger due to the addition of the spin dimension. For example, the quantity $\Delta\mathcal{M}_{obs}/\mathcal{M}_{obs}$ for q=4, M = 100$M_{\odot}$, SNR=18 and $\theta_{JN} = \pi/3(0)$ in [201] is 0.056 (0.049) whereas the same quantity for these runs (note that SNR=25) is 0.168 (0.242).

If the source parameters of a BBH signal with strong sub-dominant mode contributions are estimated using a quadrupole-only waveform model, the recovered parameters will show a tendency to be biased away from the true value. This systematic error generally increases with increasing mass-ratio or inclination; situations where sub-dominant strength increases. For `IMRPhenomHM` injections, parameters recovered by `IMRPhenomHM` are generally unbiased and if a bias exists, it can be explained by the combined effect of distance being overestimated and the priors (for example, biased q `IMRPhenomHM` recovery for edge-on `IMRPhenomHM` injection).

For the hybrid NR injections, intrinsic parameters recovered by `IMRPhenomHM` can be biased for high mass ratio - large inclination combinations. For q2 configurations, `IMRPhenomHM`

recovery is accurate across the board whereas q4-$\pi/2$, q8-$\pi/3$ etc. parameters start showing a bias. Two places where this bias could come from are: i) the hybrid NR signals are composed with more sub-dominant mode content than `IMRPhenomHM`, specifically, the (3,1) and (4,2) modes and ii) `IMRPhenomHM` modes are not calibrated to NR waveforms. Given that the contribution of the (3,1) and (4,2) modes towards total signal power is small $(\sim 1\%)$, the dominant source of systematic error is probably from the sub-dominant modes not being tuned to NR waveforms. `IMRPhenomHM` recovery has the largest bias at the system where it has the worst match with the NR waveforms, i.e., q=8 edge-on. However, even if `IMRPhenomHM` recovered parameters are biased for some systems, the bias is always smaller than the corresponding quadrupole recovery (see Fig: 5.14).

In [187], the authors had injected NR waveforms at $\theta_{JN} = \pi/3$ and they quantify the bias amount ($\delta\beta_{\lambda_i}$) by the ratio of the systematic error (difference between the *maximum a posteriori* (MAP) value and true value) and the standard deviation of the recovered posterior. We plot the same quantity for the hybrid NR injection results of this study in Fig: 5.14 along with $\delta\beta_{\mathcal{M}_c}$ and $\delta\beta_{M_{total}}$ for the q=2 (6), M = 51 (56) , SNR = 48 (48) configurations of [187]. The bias trends across mass-ratio that we see in this study are consistent with [187] [1].

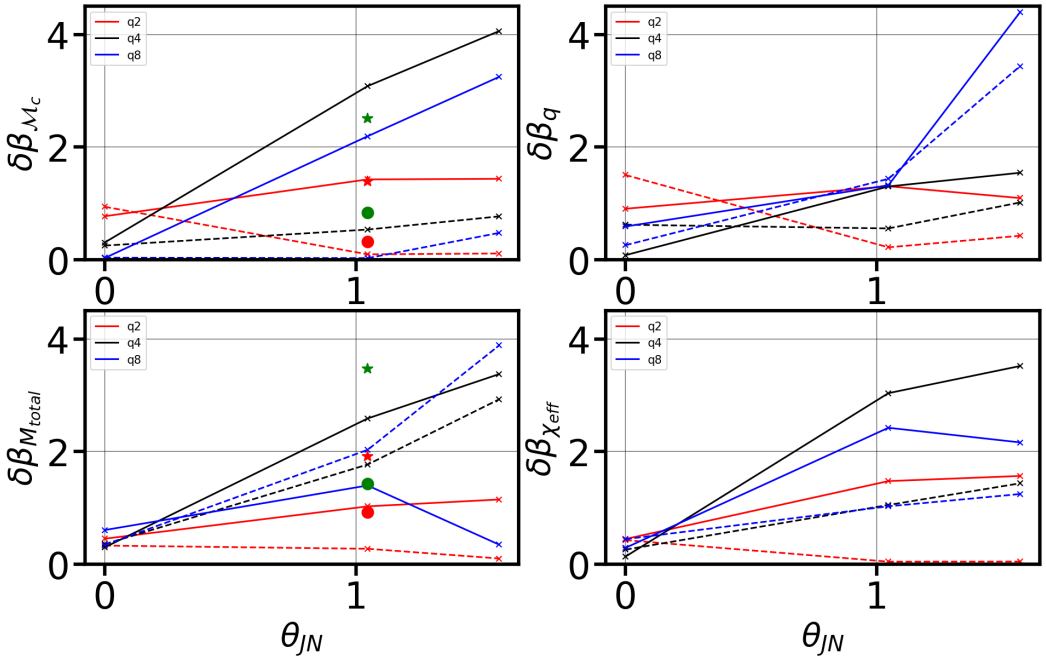

FIGURE 5.14: We plot the quantity $\delta\beta_{\lambda_i}$ for the parameters $(\mathcal{M}_c, M_{total}, q, \chi_{eff})$ for hybrid-NR injection results with the solid (dashed) lines indicating the bias value for `IMRPhenomD` (`IMRPhenomHM`) recovery. $\delta\beta_{\lambda_i}$ for q=2, 4 and 8 are shown in Red, Black and Blue respectively. The systematic bias for the q=2 (6), M = 51 (56) , SNR = 48 (48) configurations [187] is shown in red (green) with the quadrupole [multi-mode] recovered bias shown with a star [circle].

[1] Note: The total mass and SNRs used in [187] are quite different from this study. Also, the NR waveforms used in [187] do not contain the $(l, |m|)$ = (3,1),(4,3) and (4,2) modes, but include the $(l, |m|)$ = (5,5) and (6,6) modes.

The likelihood function used to estimate the source parameters $\propto -|d(t) - h(t, \vec{\lambda})|$. For a given PE run, the maximum likelihood would depend on how well the waveform model recreates $d(t)$. The low likelihood at which `IMRPhenomD` recovers the posteriors and the high bias over the parameters suggest that at large mass-ratio and inclinations, a quadrupole only template cannot be trusted for accuracy. For example, from the difference in the log Bayes factor (of $\sim$ 95) for the `IMRPhenomD` and `IMRPhenomHM` recovery for q8 edge-on `IMRPhenomHM` configuration and the bi-modal behaviour of `IMRPhenomD` recovered parameters for the same, parameters inferred by `IMRPhenomD` are highly unlikely as compared to those inferred by `IMRPhenomHM`.

For both `IMRPhenomHM` and hybrid NR injections, mass ratio recovered by `IMRPhenomD` for q2 systems tend to have a greater support from near-equal mass systems. `IMRPhenomHM` mass-ratio recovery shows a similar behaviour for face-on configurations. At $\theta_{JN} = \pi/3, \pi/2$ the mass-ratio posteriors recovered by `IMRPhenomHM` show no support from equal-mass and the posterior is peaked near q=2. This suggests that multi-mode templates could better resolve the mass-ratio for low mass-ratio systems as compared to a quadrupole only model. Our results here are in line with the observation for GW170729 [198] where the templates with quadrupole-only models resolved q between 2.5-1 at 90% CI and templates with higher-order modes placed the bounds on q between 3.3-1.25 within 90% CIs.

Effective spin recovered by `IMRPhenomD` tends to be biased at high inclination configurations, with the bias amount increasing with mass-ratio. `IMRPhenomHM` recovered spins for `IMRPhenomHM` injections is consistent for all systems. For hybrid NR injections, the true value of χ_{eff} just about lies within the 90% credible interval for q4/q8-$\pi/2$ configurations and is unbiased for all other configurations. So, `IMRPhenomHM` will consistently lead to better measurements of spins over quadrupole-only models (see the bottom right panel of Fig: 5.14).

For this study, we investigate the effects of using `IMRPhenomHM` over `IMRPhenomD` at recovering non-spinning multi-mode signals with a fixed total mass and SNR value. For a given template model, the accuracy of measured parameters depends on the total mass of the system (for e.g., measurement accuracy of $\mathcal{M}_c$ at low masses compared to high masses) and the posterior spread depends on the SNR. In the future, with optimized versions of `IMRPhenomHM` (or with models tuned to NR), it would be instructive to study the parameter recovery behaviour across a range of spins, total mass and SNR values; but we expect the overall trends of recovered parameters as mentioned here to remain unchanged.

Chapter 6

Conclusions and Future Directions

The aLIGO and aVIRGO detectors have started their third science observation run (O3) from April 2019 with increased sensitivity and hence, a larger distance reach. During the first two months of O3, there already have been more GW candidates than during the first two observation runs put together and we can realistically expect many more BBH detections before O3 ends in April 2020.

Given a GW detection, the parameters inferred from PE routines strongly depend on the template waveform model and the spread of posteriors is generally dependent on the detector noise content at that time and the strength of the signal. For the first GW detection, GW150914, `IMRPhenomPv2` was one of the template waveform models used for PE and it was necessary to check if using `IMRPhenomPv2` led to a systematic bias on the measured parameters and how the bias behaved, if it existed. As shown in Chapter: 3, at q~ 1.2 and for non-edge on systems, the systematic errors from using `IMRPhenomPv2` are much smaller than the statistical errors due to detector noise and hence, we can trust the estimated parameters for GW150914. Some of these results were summarised in [1].

`IMRPhenomPv2` generates the precessing modes in the inertial frame by wrapping up the aligned-spin (2,2) and (2,-2) modes from the QA frame using a model for the Euler angles. This model uses PN expressions for the Euler angles throughout the inspiral, merger and ringdown phases. As the PN approximation becomes less accurate as the system nears merger, the model for the angles does the same. While using `IMRPhenomPv2`, although the systematic bias is negligible for q~ 1.2, the same cannot be confidently said for high-mass ratio - high-spin precessing systems, where the precession effects are much stronger. Although we have not yet seen any systems with strong precession, it is highly likely that such systems exist and will be observed in the future and hence, we wish to improve the precession description for future models.

Towards improving a phenomenological description of precessing binaries, the first priority would be to build a model of the Euler angles for the merger-ringdown phases that is tuned to NR simulations. This work is currently ongoing at Cardiff, where the model is being tuned to a set of single-spin precessing systems. The NR simulations needed for this required the spins to be in a specific configuration at a given reference frequency and use the initial data generation process outlined in Section 4.2.1.

For the precessing waveform models, the precession information is captured by a single effective precession spin parameter χ_p (see Section 2.6.2), which is a weighted average of the in-plane spin components of the binary system. For the study in Chapter: 4, we wished to check *if* a change in the in-plane spin direction can be detectable. For that, we generated a set of NR waveforms with varying in-plane spins (same magnitude, different directions) and found that:

- For q=2 and $|S|$ = 0.7, a difference of $\pm\pi/2$ between the in-plane spins could be measurable at SNRs $\sim$ 50 and changing in-plane spin direction can have an effect *almost* as strong as changing the magnitude by $\sim$ 0.1.
- For q=4 and $|S|$ = 0.8, a difference of $\pm\pi/2$ between the in-plane spins could be measurable at SNRs $\sim$ 30 and changing in-plane spin direction can have an effect stronger than changing the magnitude by $\sim$ 0.4.
- There exists a *quasi-symmetry* between the systems for which in-plane spins are related by a $\pm\pi$ angle difference, which also shows up in the match values where the maximum match for signal with inclination (θ_s) is from a template with inclination ($\theta_s + \pi$).
- A change in the initial spin direction leads to slightly different precessional motion and mode-asymmetry content. These differences are what allows the systems with different in-plane spins to be differentiable from each other.

For current precession waveform models, the direction of the in-plane spin only determines the reference position of $\hat{L}$ about the precession cone, with all the other things being the same. As this is approximately degenerate with the binary phase(ϕ), waveforms with different ϕ_{SR} are difficult to distinguish from one another. From the results of Chapter: 4, we indicate that modelling the in-plane spin direction should be considered in the near future.

In Chapter: 4, we also check for the effect of (non-)inclusion of mode-asymmetry content in the signal and template waveforms. When mode-asymmetry is turned off for both signal and template, we see that it becomes harder to distinguish signals with different in-plane spins. For signals with different total spins, the results vary depending on the choice of

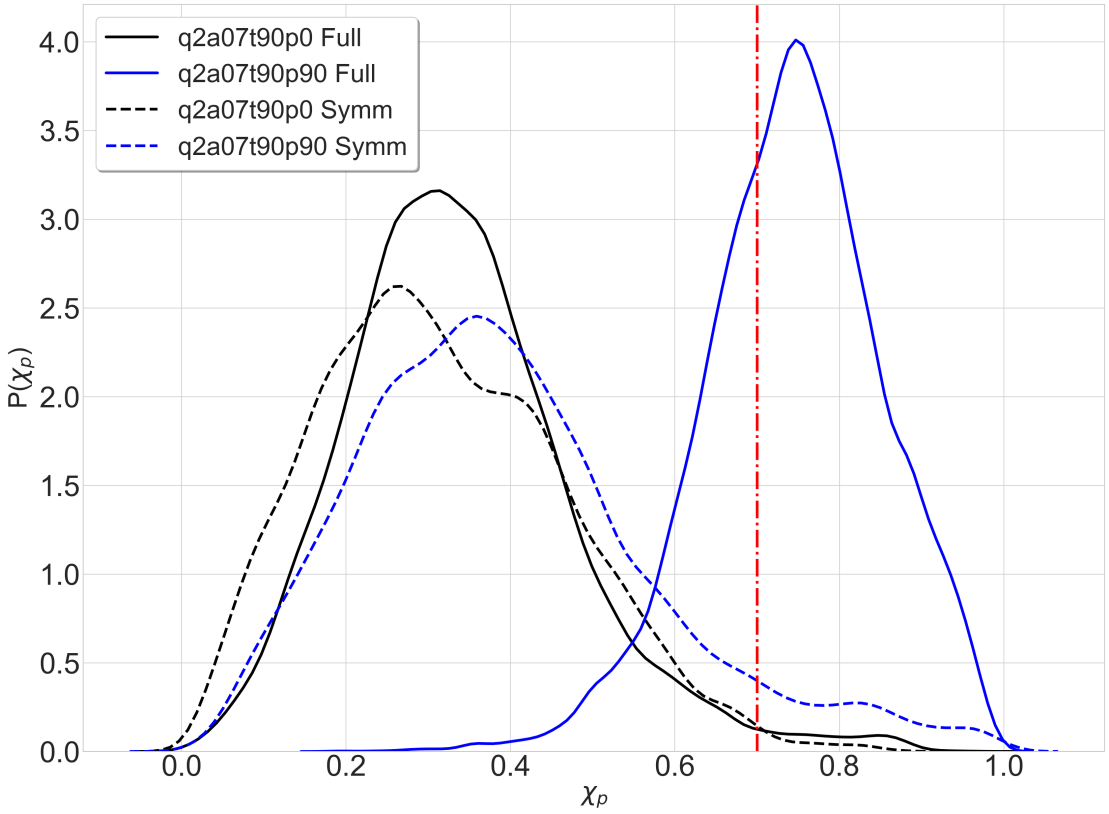

FIGURE 6.1: This figure shows the χ_p posteriors recovered by `IMRPhenomPv2` for the full (symmetrized) waveforms of the system q2a07t90p0 and q2a07t90p90 which are shown in sold-black (dashed-black) and solid-blue (dashed-blue) respectively. The true χ_p is shown by the dashed-dotted red line.

signal-template systems (see Fig: 4.22 and Fig: 4.23). When mode-asymmetry content is not included in only the templates, we see that:

- Systems with different in-plane spins ($\pm\pi/2$ angle difference) can be distinguished at a lower SNR than when templates contain mode-asymmetric content for q=1, q=2 and q=4 cases (see Fig: 4.24).
- For the same system, signals with mode-asymmetric content are seen as a different system at SNRs similar to those of systems with different in-plane spins (without mode-asymmetry in templates) (see Fig: 4.24).

These two results imply that disregarding mode-asymmetric content for template waveforms could lead to biased parameter measurements, specifically for high SNR signals (SNRs > 30). For systems with different ϕ_{SR}, mode-asymmetry and precessional motion variations are weak, yet changing ϕ_{SR} can have a comparable effect to total spin magnitude change. Given all the results above, we conclude that initial spin direction and mode-asymmetry effects may be important for future waveform modelling.

As a test, I injected the NR waveforms q2a07p0 (full and symmetrized) and q2a07p90 (full and symmetrized) at face-on inclination with SNR=40 and recovered the parameters with `IMRPhenomPv2`. For both the systems, the true value of the in-plane spin is $\chi_p = 0.7$. For the full (symmetrized) q2a07p0 waveform, the mean of the recovered $\chi_p \sim 0.3(0.3)$ and for q2a07p90 it is $\chi_p \sim 0.7(0.3)$ (see Fig: 6.1), with all other parameters being consistent within the 90% CIs. So, the `IMRPhenomPv2` measured χ_p is inconsistent for the two full waveforms (wrong recovery for q2a07t90p0) and consistent but biased for the symmetrized waveforms. With the above results, we wish to indicate that mode-asymmetry effects can be strong and that future precessing waveform models might want to consider modelling the mode-asymmetries. Note that these are preliminary results.

In Chapter: 5, we compared the posteriors recovered by a multi-mode (`IMRPhenomHM`) and quadrapole-only (`IMRPhenomD`) template waveform for multi-mode hybrid NR and `IMRPhenomHM` signals over three mass-ratio values (q=2, 4 and 8) and at three inclinations ($\iota = 0, \pi/3, \pi/2$), with a fixed SNR of 25. We found that using multi-mode templates allows for better measurements of the intrinsic parameters across the parameter space. Quite interestingly, where the quadrapole model consistently returns biased χ_{eff} measurements for inclined systems, the multi-mode model always recovers the correct spins. Even for low mass-ratio systems, `IMRPhenomHM` is better at constraining the mass-ratio at moderate inclinations and can completely rule-out equal mass systems. Using templates with higher-order modes breaks the degeneracy between the inclination, distance and polarisation parameters, allowing for better constraints on the same. We see that the distances can be better constrained by $\sim$ 20% - 60% as compared to `IMRPhenomD` or any other accurate quadrupolar model.

For systems with strong sub-dominant mode power, the parameters recovered by `IMRPhenomHM` show a slight bias, which is always smaller than the corresponding `IMRPhenomD` bias. This can be explained by the approximations made during the building of this model, viz., i) sub-dominant modes are not tuned to NR and ii) mode-mixing between the sub-dominant modes is not modelled. Although the multi-mode models are computationally more expensive ($\sim$ 30 times slower than `IMRPhenomD` at the moment), using multi-mode templates allows for better parameter measurements across the board and should be seriously considered as template models for future observations. It would be very helpful to build Reduced Order Models (ROM) for the multi-mode templates or to highly optimize the waveform generation codes to reduce the computational time of a given PE run.

Appendix A

3+1 decomposition of GR

Equations in General Relativity relating the spacetime metric to matter sources form a set of 10 coupled non-linear differential equations for which analytical solutions can be found for only some special cases (Schwarzschild metric, Kerr metric etc.). The expected gravitational wave signal from a coalescing binary source can be approximated by Post-Newtonian expansion methods, but this approximation holds only during the inspiral phase of the system. To obtain the GW signal during late inspiral and merger phases, we need to solve Einstein's equations numerically.

Dynamical evolution of a gravitational field can be posed as an initial value problem wherein time-evolution of the full space-time metric g_{ab} can be determined by specifying the metric ($g_{ab}(t_0)$) and its time derivative ($\partial_t g_{ab}(t_0)$) at a initial time t_0. In the 3+1 decomposition of Einstein's equations, the space-time is *foliated* by spacelike hypersurfaces labelled by the $x_0 = t$ co-ordinate. The metric can then be evolved to higher times by obtaining expressions for $\partial_t^2 g_{ab}$ from the Einstein equations at each point on the hypersurface and solving these to obtain $g_{ab}(t_0 + \delta t)$ and $g_{ab}(t_0 + \delta t)$ for hypersurface at time $t_0 + \delta t$.

The 10 Einstein equations are, $G_{ab} = \left(8\pi G/\ c^4\right) T_{ab}$, with the Bianchi identity $\nabla_b G^{ab} = 0$ gives,

$$\partial_t G^{a0} = -\partial_i G^{ai} - G^{bc}\Gamma^a_{bc} - G^{ab}\Gamma^c_{bc}, \tag{A.1}$$

since the RHS terms Eq: A.1 do not contain third time derivatives or higher of g_{ab}, the quantities G^{a0} do not contain any second-time derivatives of g_{ab}. Hence, 4 of Einstein's equations, $G_{a0} = \left(8\pi G/\ c^4\right) T_{a0}$ do not contain any information of dynamical time evolution of the system, but do provide a set of constraint equations for the initial data, $g_{ab}(t_0)$ and $\partial_t g_{ab}(t_0)$. The remaining 6 equations determine the time evolution of the metric. Due to the co-ordinate gauge freedom of general relativity, we can chose $g_{00} = -1$ and $g_{0i} = 0$ and thus have six metric components, g_{ij} which need to be solved for. Thus, given a set of initial

data, the time evolution of the spacetime metric can be solved via foliating the space-time with hypersurfaces at different times and solving for the six metric components g_{ij}.

The 3+1 decomposition provides a geometric outlook at the problem of solving Einstein's equations, in that the space-time is decomposed into the 3-dimensional space and a 1-dimensional time leading to populating the spacetime with spacelike hypersurfaces labeled by the time co-ordinate. Time evolution of the metric is then obtained by solving equations for the six metric components on each time-slice. This decomposition provides us with four constraint equations for g_{ab} and $\partial_t g_{ab}$ and the matter sources on each time slice and evolution equations of g_{ab} on each time slice.

Let the spacetime manifold ($\mathcal{M}$) have the metric g_{ab} defined over it. To decompose space-time, it's assumed that ($\mathcal{M}$, g_{ab}) can be foliated by spacelike hypersurfaces (Σ) which are level surfaces of the time co-ordinate (t). From t we can get a 1-form [1],

$$\Omega_a = \nabla_a t, \tag{A.2}$$

and ,

$$||\Omega||^2 = g^{ab}\nabla_a t \nabla_b t = -\frac{1}{\alpha^2}. \tag{A.3}$$

The quantity α, called the *lapse* function, measures amount of proper time elapsed between two time-slices along the normal Ω^a to the slice. Assume that $\alpha > 0$, so Ω^a is a time-like one-form leading to space-like hypersurface Σ. This allows us to define the normalized 1-form as $\omega_a = \alpha\Omega_a$ and unit normal to slices $n^a = -g^{ab}\omega_b$. As $n^a n_a = -1$, it is time-like and points in the direction of increasing t . See Fig: A.1 for a visual representation.

Given n^a, we can define the metric γ_{ab} induced on Σ by g_{ab} as,

$$\gamma_{ab} = g_{ab} + n_a n_b. \tag{A.4}$$

With the metric γ_{ab} so defined, its action on a tensor will project out any components along the time-like vector n^a. γ_{ab} is purely spatial and allows calculation of distance between two points on a hypersurface Σ.

Once we have the space-time foliation, we want to decompose the purely spatial (lying on hypersurface Σ) and time-like (along n^a) parts of tensors. For that, we need two projection operators. The operator projecting a tensor T_{ab} on a slice Σ, can be obtained by raising one index of the spatial metric,

$$\gamma^a_b = g^a_b + n^a n_b = \delta^a_b + n^a n_b. \tag{A.5}$$

[1] This whole discussion closely follows the one in [92]

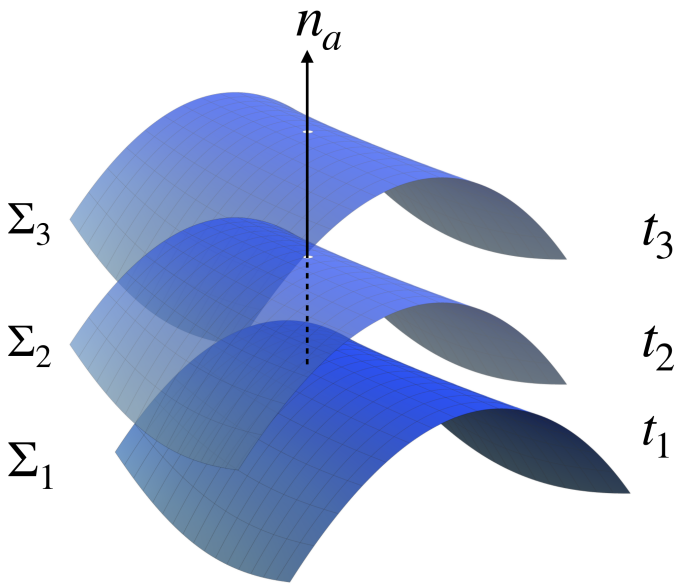

FIGURE A.1: Foliation of manifold M into space-like hypersurfaces (Σ_1, Σ_2, Σ_3 ..) each a level surface of time (t_1, t_2, t_3...). The normal to the hypersurfaces is given by n^a

To project T_{ab}, each index has to be contracted by the projection operator. Let us denote projection of T_{ab} on Σ as ${}_\perp T_{ab}$. Then,

$$ {}_\perp T_{ab} = \gamma_a^c \gamma_b^d T_{cd}. \tag{A.6} $$

The normal projection operator is defined as,

$$ N_b^a = -n^a n_b = \delta_b^a - \gamma_b^a. \tag{A.7} $$

Thus, we can now use the two projection operators given in Eq: A.5 and A.7. These projection operators can also be used to project the covariant derivatives of tensor quantities on Σ by the same logic. The co-variant derivative of a scalar function *f* on Σ is,

$$ D_a f = \gamma_a^b \nabla_b f \tag{A.8} $$

The covariant derivative on Σ can be expressed in terms of the 3-d connection coefficients Γ_{bc}^a which, in terms of γ_{ab} are,

$$ \Gamma_{bc}^a = \frac{1}{2}\gamma^{ad}\left(\partial_c \gamma_{bd} + \partial_b \gamma_{dc} - \partial_d \gamma_{bc}\right). \tag{A.9} $$

Using these, we can obtain the Riemann tensor associated with γ_{ab} as,

$$ 2D_{[a}D_{b]}w_c = R_{cba}^d w_d \qquad R_{cba}^d n_d = 0. \tag{A.10} $$

With this, we can then obtain the 3-dimensional Ricci tensor and Ricci scalar.

Einstein's equations relate the 4-dimensional Riemann tensor ${}^{(4)}R^a_{bcd}$ to the stress-energy tensor. We want to decompose ${}^{(4)}R^a_{bcd}$ into its spatial components for recasting the equations in 3+1 decomposition. Part of its spatial decomposition is the 3d Riemann tensor defined in Eq: A.10, but this contains information of the *intrinsic* curvature of slice Σ and tells nothing of it's shape while its embedded in the manifold $\mathcal{M}$. This information is contained in the *extrinsic* curvature.

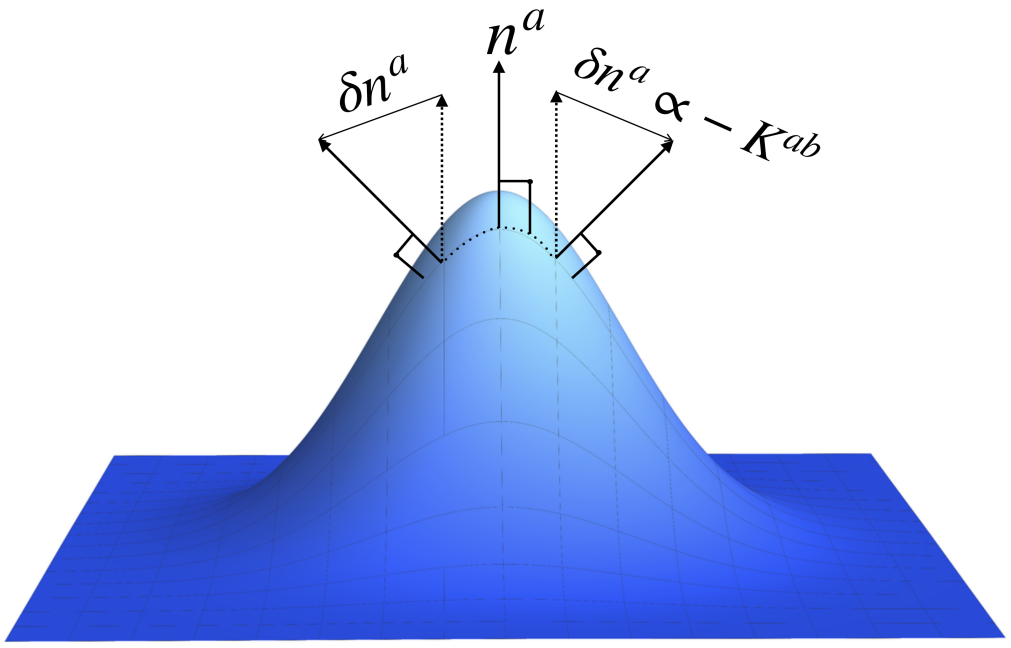

FIGURE A.2: The extrinsic curvature K^{ab} measures variation of normal vector n^a at different points on Σ. It measures the rate at which Σ gets deformed as it's evolved along n^a

The extrinsic curvature K_{ab} can be found by projecting covariant derivatives of the normal vector of Σ onto Σ. This gives,

$$K_{ab} = -\gamma^c_a \gamma^d_b \nabla_c n_d. \tag{A.11}$$

The extrinsic curvature, intuitively, gives a measure of by how much the normal n_a changes as it moves along Σ giving an idea of how the manifold curves; see Fig A.2. For eg:, a normal to the 2D surface of a sphere going along the line joining two opposite poles will keep on changing its direction and that rate of change would be dependent on the curvature of the sphere. We can also express the extrinsic curvature in terms of γ_{ab} as,

$$K_{ab} = -\frac{1}{2}\mathcal{L}_{\boldsymbol{n}}\gamma_{ab}, \tag{A.12}$$

where $\mathcal{L}_{\boldsymbol{n}}$ is the *Lie derivative* of along normal n^a. Thus, the two quantities, (γ_{ab}, K_{ab}) contain information of the instantaneous state of the gravitational field and serve as fundamental variables in our formulation.

The choice of (γ_{ab}, K_{ab}) cannot be arbitrary because they need to follow some constraints to foliate the manifold $\mathcal{M}$ completely. For that, we need to relate the 4-dimensional ${}^{(4)}R^a_{bcd}$ of $\mathcal{M}$ to the 3-dimensional Riemann tensor on Σ. These relations are given by the *Gauss, Codazzi* and *Ricci* equations. The Gauss and Codazzi equations depend only on the spatial derivatives of (γ_{ab}, K_{ab}) and are given as,

$$R_{abcd} + K_{ac}K_{bd} - K_{ad}K_{cb} = \gamma^p_a\gamma^q_b\gamma^r_c\gamma^s_d R^{(4)}_{pqrs}, \tag{A.13}$$

$$D_bK_{ac} - D_aK_{bc} = \gamma^p_a\gamma^q_b\gamma^r_c n^s R^{(4)}_{pqrs}. \tag{A.14}$$

These two equations will provide constraint equations for (γ_{ab}, K_{ab}). The Ricci equation relates time derivative of extrinsic curvature to a spatial projection of 4d Riemann tensor and is given as,

$$\mathcal{L}_{\boldsymbol{n}}K_{ab} = n^d n^c \gamma^q_a\gamma^r_b R^{(4)}_{drcq} - \frac{1}{\alpha}D_aD_b\alpha - K^c_bK_{ac} \tag{A.15}$$

To obtain the constraint and evolution equations of our variables (γ_{ab}, K_{ab}), we take the Gauss, Codazzi and Ricci equations (given in Eq: A.13, A.14 and A.15 respectively) and eliminate the 4d Riemann tensor using Einstein's equations. Doing the former on Gauss and Codazzi equations gives us the *Hamiltonian constraint* and *momentum constraint* which relate the 3+1 decomposition formalism variables to the *total energy density* and *momentum density* of the matter as observed by normal observer n^a.

The Hamiltonian constraint equation is,

$$R + K^2 - K_{ab}K^{ab} = 16\pi\rho, \tag{A.16}$$

where R and K are the 3d Ricci scalar and trace of extrinsic curvature. ρ is the total energy density of the matter.

The momentum constraint equation which relates the momentum density of matter (S_a) to the extrinsic curvature is,

$$D_bK^b_a - D_aK = 8\pi S_a \qquad S_a = -\gamma^b_a n^c T_{bc}. \tag{A.17}$$

The equations Eq: A.16 and A.17 provide the conditions for embedding the 3-dimensional hypersurfaces Σ in the four dimensional manifold M created by the matter source. For

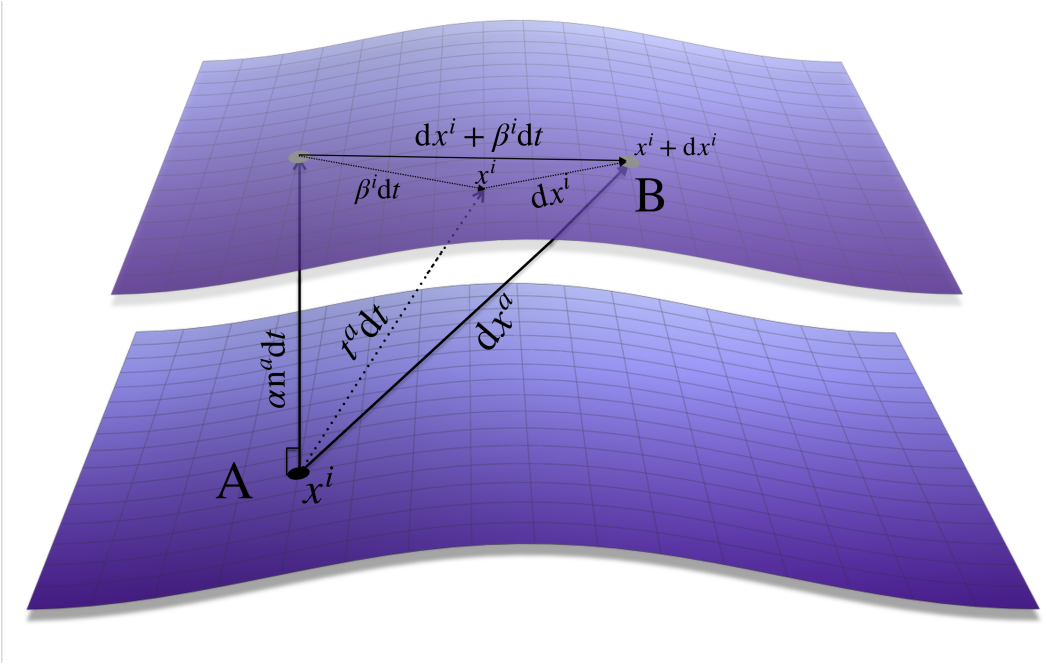

FIGURE A.3: The time vector t_a connects the point with spatial co-ordiante x^i on slice t to the same co-ordinate on slice t + dt. The lapse function α gives the amount of proper time passed and the vector β^a measures the shift of spatial co-ordinate between the slices.

evolving the metric of a physical system, we need to solve these equations to obtain the initial data.

Time evolution equations can be found from Ricci's equation Eq: A.15 and Eq: A.12 which relates the extrinsic curvature to the intrinsic metric of Σ. Taking a derivative along the normal n^a will not be a time derivative, as n^a is not the exact dual of the one-form on hypersurface Ω_a which defines the hypersurface time; $n^a\Omega_a = \alpha^{-1}$. We instead choose a vector, t^a, which is defined in Eq A.18. See Fig: A.3.

$$t^a = \alpha n^a + \beta^a \implies t^a\Omega_a = 1. \tag{A.18}$$

It's useful to use the vector t^a because it connects two points with the same spatial co-ordinates on the two slices, let's call it x^a. The term αn^a measures the amount of proper time elapsed between the slices and the shift vector β^a measures the amount by which the the point x^a has shifted along the surface between the two hypersurfaces. These two functions determine the evolution of the co-ordinates in time. The choice of the 4 quantities α and β^a are completely arbitrary in a problem. The co-ordinate gauge freedom of General Relativity is what allows the choice of these four functions to be arbitrary.

Now, we can obtain the evolution equations for (γ_{ab}, K_{ab}) in general co-variant form, but the equations are generally solved in the ADM co-ordinate basis and so we will look at that

basis first and state the equations in that basis. The ADM co-ordinates are chosen such that, $x^a = (t^a, e^a)$ where e^a form a set of basis vectors on slice Σ, so that $\Omega_a e^a = 0$. In this basis, the components of the vectors t^a and β^a are,

$$t^a = (1, 0, 0, 0) \qquad \beta^a = (0, \beta^i). \tag{A.19}$$

This ensures that the Lie derivative along t^a will essentially be a partial derivative w.r.t *t*. The co-variant (n_a) and contravariant (n^a) components of the normal vector are,

$$n^a = \left(\alpha^{-1}, -\alpha^{-1}\beta^i\right) \qquad n_a = (-\alpha, 0, 0, 0,)\,. \tag{A.20}$$

We can use these to give us the four-dimensional metric g_{ab} in terms of the lapse and shift vector using which we can write the line element in the 3+1 form as,

$$ds^2 = -\alpha^2 \mathrm{d}t^2 + \gamma_{ij}(\mathrm{d}x^i + \beta^i \mathrm{d}t)(\mathrm{d}x^j + \beta^j \mathrm{d}t). \tag{A.21}$$

In this basis, the evolution equations for extrinsic curvature reads,

$$\partial_t K_{ij} = \alpha\left(R_{ij} - 2K_{ik}K^k_j + KK_{ij}\right) - D_i D_j \alpha - 8\pi\alpha\left(S_{ij} - \frac{1}{2}\gamma_{ij}(S-\rho)\right) + \beta^k \partial_k K_{ij} + K_{ik}\partial_j \beta^k + K_{kj}\partial_i \beta^k, \tag{A.22}$$

and the evolution equation for spatial metric,

$$\partial_t \gamma_{ij} = -2\alpha K_{ij} + D_i \beta_j + D_j \beta_i. \tag{A.23}$$

The hamiltonian and momentum constraints coupled with the evolution equations are equivalent to Einstein's equations in a 4-dimensional space. To summarise, in 3+1 decomposition the 4 dimensional manifold M produced by the matter source is first split into slices at different times. Initial conditions on the first slice can be obtained by solving the constraint equations for a given system which would give us the metric and it's time derivative at the initial time, $g_{ab}(t_0)$ and $\partial_t g_{ab}(t_0)$. We constrain the co-ordinate gauge freedom of GR by choosing the ADM basis and find the metric at all other times by evolving the hypersurface slice to higher times.

Bibliography

[1] B. P. Abbott *et al.*, "Effects of waveform model systematics on the interpretation of GW150914," *Class. Quant. Grav.*, vol. 34, no. 10, p. 104 002, 2017. DOI: 10.1088/1361-6382/aa6854. arXiv: 1611.07531 [gr-qc].

[2] L. London, S. Khan, E. Fauchon-Jones, *et al.*, "First Higher-Multipole Model of Gravitational Waves from Spinning and Coalescing Black-Hole Binaries," *Phys. Rev. Lett.*, vol. 120, no. 16, 2018, ISSN: 10797114. DOI: 10.1103/PhysRevLett.120.161102.

[3] B. P. Abbott *et al.*, "Observation of Gravitational Waves from a Binary Black Hole Merger," *Phys. Rev. Lett.*, vol. 116, no. 6, p. 61 102, 2016, ISSN: 0031-9007. DOI: 10.1103/PhysRevLett.116.061102. arXiv: 1602.03837. [Online]. Available: http://link.aps.org/doi/10.1103/PhysRevLett.116.061102.

[4] *Image source*, https://en.wikipedia.org/wiki/File:PSR_B1913%2B16_period_shift_graph.svg.

[5] J. M. Weisberg and J. H. Taylor, "Relativistic Binary Pulsar B1913+16: Thirty Years of Observations and Analysis," pp. 1–7, 2004, ISSN: 1050-3390. arXiv: 0407149 [astro-ph]. [Online]. Available: http://arxiv.org/abs/astro-ph/0407149.

[6] J. Aasi *et al.*, "Advanced LIGO," *Class. Quant. Grav.*, vol. 32, p. 074 001, 2015. DOI: 10.1088/0264-9381/32/7/074001. arXiv: 1411.4547 [gr-qc].

[7] F. Acernese *et al.*, "Advanced Virgo: a second-generation interferometric gravitational wave detector," *Class. Quant. Grav.*, vol. 32, no. 2, p. 024 001, 2015. DOI: 10.1088/0264-9381/32/2/024001. arXiv: 1408.3978 [gr-qc].

[8] B. P. Abbott *et al.*, "GWTC-1: A Gravitational-Wave Transient Catalog of Compact Binary Mergers Observed by LIGO and Virgo during the First and Second Observing Runs," 2018. arXiv: 1811.12907 [astro-ph.HE].

[9] B. P. Abbott, R. Abbott, T. D. Abbott, *et al.*, "Gw170817: Observation of gravitational waves from a binary neutron star inspiral," *Phys. Rev. Lett.*, vol. 119, p. 161 101, 16 2017. DOI: 10.1103/PhysRevLett.119.161101. [Online]. Available: https://link.aps.org/doi/10.1103/PhysRevLett.119.161101.

[10] ——, "Gravitational Waves and Gamma-rays from a Binary Neutron Star Merger: GW170817 and GRB 170817A," *Astrophys. J.*, vol. 848, no. 2, p. L13, 2017. DOI: 10.3847/2041-8213/aa920c. arXiv: 1710.05834 [astro-ph.HE].

[11] A. Albert *et al.*, "Search for High-energy Neutrinos from Binary Neutron Star Merger GW170817 with ANTARES, IceCube, and the Pierre Auger Observatory," *Astrophys. J.*, vol. 850, no. 2, p. L35, 2017. DOI: 10.3847/2041-8213/aa9aed. arXiv: 1710.05839 [astro-ph.HE].

[12] B. P. Abbott *et al.*, "GW170814: A Three-Detector Observation of Gravitational Waves from a Binary Black Hole Coalescence," *Phys. Rev. Lett.*, vol. 119, no. 14, p. 141 101, 2017. DOI: 10.1103/PhysRevLett.119.141101. arXiv: 1709.09660 [gr-qc].

[13] T Uchiyama, K Kuroda, M Ohashi, *et al.*, "Present status of large-scale cryogenic gravitational wave telescope," *Classical and Quantum Gravity*, vol. 21, no. 5, S1161–S1172, 2004. DOI: 10.1088/0264-9381/21/5/115. [Online]. Available: https://doi.org/10.1088%2F0264-9381%2F21%2F5%2F115.

[14] Y. Aso, Y. Michimura, K. Somiya, *et al.*, "Interferometer design of the KAGRA gravitational wave detector," *Phys. Rev.*, vol. D88, no. 4, p. 043 007, 2013. DOI: 10.1103/PhysRevD.88.043007. arXiv: 1306.6747 [gr-qc].

[15] *Ligo india proposal*, http://www.gw-indigo.org/tiki-index.php?page=LIGO-India.

[16] C. S. Unnikrishnan, "IndIGO and LIGO-India: Scope and plans for gravitational wave research and precision metrology in India," *Int. J. Mod. Phys.*, vol. D22, p. 1 341 010, 2013. DOI: 10.1142/S0218271813410101. arXiv: 1510.06059 [physics.ins-det].

[17] B. P. Abbott, R. Abbott, T. D. Abbott, *et al.*, "Prospects for observing and localizing gravitational-wave transients with advanced ligo, advanced virgo and kagra," *Living Reviews in Relativity*, vol. 21, no. 1, p. 3, 2018, ISSN: 1433-8351. DOI: 10.1007/s41114-018-0012-9. [Online]. Available: https://doi.org/10.1007/s41114-018-0012-9.

[18] B. S. Sathyaprakash and B. F. Schutz, "Physics, Astrophysics and Cosmology with Gravitational Waves," *Living Rev. Rel.*, vol. 12, p. 2, 2009. DOI: 10.12942/lrr-2009-2. arXiv: 0903.0338 [gr-qc].

[19] B. Schutz, *A First Course in General Relativity*, 2nd ed. Cambridge University Press, 2009. DOI: 10.1017/CBO9780511984181.

[20] J. B. Hartle, *Gravity: An Introduction to Einstein's General Relativity*, illustrate. Benjamin Cummings, Jan. 2003, ISBN: 0805386629.

[21] R. M. Wald, *General relativity*. Chicago, IL: Chicago Univ. Press, 1984. [Online]. Available: https://cds.cern.ch/record/106274.

[22] M. Maggiore, *Gravitational waves. Volume 1: Theory and experiments*, First Edit. Oxford University Press, 2008, p. 572. DOI: 10.1007/s10714-009-0762-5. [Online]. Available: https://global.oup.com/academic/product/gravitational-waves-9780198570745?cc=gb{\&}lang=en{\&}.

[23] J. Weber, "Gravitational Radiation," *Physical Review Letters*, vol. 18, pp. 498–501, Mar. 1967. DOI: 10.1103/PhysRevLett.18.498.

[24] O. D. Aguiar, "The Past, Present and Future of the Resonant-Mass Gravitational Wave Detectors," *Res. Astron. Astrophys.*, vol. 11, pp. 1–42, 2011. DOI: 10.1088/1674-4527/11/1/001. arXiv: 1009.1138 [astro-ph.IM].

[25] B. Abbott *et al.*, "Detector description and performance for the first coincidence observations between LIGO and GEO," *Nucl. Instrum. Meth.*, vol. A517, pp. 154–179, 2004. DOI: 10.1016/j.nima.2003.11.124. arXiv: gr-qc/0308043 [gr-qc].

[26] *Enhanced ligo upgrades document*, https://dcc.ligo.org/public/0007/T060156/000/T060156-01.pdf.

[27] F Acernese *et al.*, "Status of virgo," *Classical and Quantum Gravity*, vol. 25, no. 11, p. 114 045, 2008. DOI: 10.1088/0264-9381/25/11/114045. [Online]. Available: https://doi.org/10.1088%2F0264-9381%2F25%2F11%2F114045.

[28] *Tama300 interferometer*, http://tamago.mtk.nao.ac.jp/spacetime/tama300_e.html.

[29] A. Abramovici, W. E. Althouse, R. W. P. Drever, *et al.*, "LIGO - The Laser Interferometer Gravitational-Wave Observatory," *Science*, vol. 256, pp. 325–333, Apr. 1992. DOI: 10.1126/science.256.5055.325.

[30] B. C. Barish and R. Weiss, "LIGO and the detection of gravitational waves.," *Physics Today*, vol. 52, no. 10, pp. 44–50, 1999. DOI: 10.1063/1.882861.

[31] B. P. Abbott *et al.*, "LIGO: The Laser interferometer gravitational-wave observatory," *Rept. Prog. Phys.*, vol. 72, p. 076 901, 2009. DOI: 10.1088/0034-4885/72/7/076901. arXiv: 0711.3041 [gr-qc].

[32] J. R. Smith, "The Path to the enhanced and advanced LIGO gravitational-wave detectors," *Class. Quant. Grav.*, vol. 26, p. 114 013, 2009. DOI: 10.1088/0264-9381/26/11/114013. arXiv: 0902.0381 [gr-qc].

[33] B. Abbott *et al.*, "Search for gravitational-wave bursts in LIGO's third science run," *Class. Quant. Grav.*, vol. 23, S29–S39, 2006. DOI: 10.1088/0264-9381/23/8/S05. arXiv: gr-qc/0511146 [gr-qc].

[34] ——, "Search for gravitational waves from binary black hole inspirals in LIGO data," *Phys. Rev.*, vol. D73, p. 062 001, 2006. DOI: 10.1103/PhysRevD.73.062001. arXiv: gr-qc/0509129 [gr-qc].

[35] ——, "Search for gravitational waves from binary inspirals in S3 and S4 LIGO data," *Phys. Rev.*, vol. D77, p. 062 002, 2008. DOI: 10.1103/PhysRevD.77.062002. arXiv: 0704.3368 [gr-qc].

[36] B. P. Abbott *et al.*, "Search for Gravitational Waves from Low Mass Compact Binary Coalescence in 186 Days of LIGO's fifth Science Run," *Phys. Rev.*, vol. D80, p. 047 101, 2009. DOI: 10.1103/PhysRevD.80.047101. arXiv: 0905.3710 [gr-qc].

[37] B. P. Abbott *et al.*, "Exploring the Sensitivity of Next Generation Gravitational Wave Detectors," *Class. Quant. Grav.*, vol. 34, no. 4, p. 044 001, 2017. DOI: 10.1088/1361-6382/aa51f4. arXiv: 1607.08697 [astro-ph.IM].

[38] S. Hild *et al.*, "Sensitivity Studies for Third-Generation Gravitational Wave Observatories," *Class. Quant. Grav.*, vol. 28, p. 094 013, 2011. DOI: 10.1088/0264-9381/28/9/094013. arXiv: 1012.0908 [gr-qc].

[39] *Lisa science requirements document*, https://lisa.nasa.gov/archive2011/Documentation/LISA-ScRD_v4.1a.pdf.

[40] S. A. Usman *et al.*, "The PyCBC search for gravitational waves from compact binary coalescence," *Class. Quant. Grav.*, vol. 33, no. 21, p. 215 004, 2016. DOI: 10.1088/0264-9381/33/21/215004. arXiv: 1508.02357 [gr-qc].

[41] C. Messick, K. Blackburn, P. Brady, *et al.*, "Analysis framework for the prompt discovery of compact binary mergers in gravitational-wave data," *Phys. Rev. D*, vol. 95, p. 042 001, 4 2017. DOI: 10.1103/PhysRevD.95.042001. [Online]. Available: https://link.aps.org/doi/10.1103/PhysRevD.95.042001.

[42] S. Sachdev *et al.*, "The GstLAL Search Analysis Methods for Compact Binary Mergers in Advanced LIGO's Second and Advanced Virgo's First Observing Runs," 2019. arXiv: 1901.08580 [gr-qc].

[43] S. Klimenko *et al.*, "Method for detection and reconstruction of gravitational wave transients with networks of advanced detectors," *Phys. Rev.*, vol. D93, no. 4, p. 042 004, 2016. DOI: 10.1103/PhysRevD.93.042004. arXiv: 1511.05999 [gr-qc].

[44] S. Klimenko, I. Yakushin, A. Mercer, *et al.*, "Coherent method for detection of gravitational wave bursts," *Class. Quant. Grav.*, vol. 25, p. 114 029, 2008. DOI: 10.1088/0264-9381/25/11/114029. arXiv: 0802.3232 [gr-qc].

[45] B. P. Abbott, R. Abbott, T. D. Abbott, *et al.*, "All-sky search for long-duration gravitational-wave transients in the second Advanced LIGO observing run," 2019. arXiv: 1903.12015 [gr-qc].

[46] ——, "Directional limits on persistent gravitational waves using data from Advanced LIGO's first two observing runs," 2019. arXiv: 1903.08844 [gr-qc].

[47] ——, "A search for the isotropic stochastic background using data from Advanced LIGO's second observing run," 2019. arXiv: 1903.02886 [gr-qc].

[48] ——, "All-sky search for continuous gravitational waves from isolated neutron stars using Advanced LIGO O2 data," 2019. arXiv: 1903.01901 [astro-ph.HE].

[49] T. Damour, B. R. Iyer, and B. S. Sathyaprakash, "Improved filters for gravitational waves from inspiralling compact binaries," *Phys. Rev.*, vol. D57, pp. 885–907, 1998. DOI: 10.1103/PhysRevD.57.885. arXiv: gr-qc/9708034 [gr-qc].

[50] T. Damour, B. R. Iyer, P. Jaranowski, *et al.*, "Gravitational waves from black hole binary inspiral and merger: The Span of third postNewtonian effective one-body templates," *Phys. Rev.*, vol. D67, p. 064 028, 2003. DOI: 10.1103/PhysRevD.67.064028. arXiv: gr-qc/0211041 [gr-qc].

[51] J Veitch, V Raymond, *et al.*, "Parameter estimation for compact binaries with ground-based gravitational-wave observations using the LALInference software library," *Phys. Rev. D - Part. Fields, Gravit. Cosmol.*, vol. 91, no. 4, pp. 1–25, 2010, ISSN: 15507998. DOI: 10.1103/PhysRevD.91.042003. arXiv: 1409.7215.

[52] J. Veitch *et al.*, "Parameter estimation for compact binaries with ground-based gravitational-wave observations using the LALInference software library," *Phys. Rev.*, vol. D91, no. 4, p. 042 003, 2015. DOI: 10.1103/PhysRevD.91.042003. arXiv: 1409.7215 [gr-qc].

[53] LIGO Scientific Collaboration, *LIGO Algorithm Library - LALSuite*, free software (GPL), 2018. DOI: 10.7935/GT1W-FZ16.

[54] *Nested sampling for general bayesian computation*, https://projecteuclid.org/euclid.ba/1340370944.

[55] *Monte carlo sampling methods using markov chains and their applications*, https://academic.oup.com/biomet/article-abstract/57/1/97/284580.

[56] J. Veitch and A. Vecchio, "Bayesian coherent analysis of in-spiral gravitational wave signals with a detector network," *Phys. Rev.*, vol. D81, p. 062 003, 2010. DOI: 10.1103/PhysRevD.81.062003. arXiv: 0911.3820 [astro-ph.CO].

[57] P. C. Peters and J. Mathews, "Gravitational radiation from point masses in a keplerian orbit," *Phys. Rev.*, vol. 131, pp. 435–440, 1 1963. DOI: 10.1103/PhysRev.131.435. [Online]. Available: https://link.aps.org/doi/10.1103/PhysRev.131.435.

[58] P. C. Peters, "Gravitational radiation and the motion of two point masses," *Phys. Rev.*, vol. 136, B1224–B1232, 4B 1964. DOI: 10.1103/PhysRev.136.B1224. [Online]. Available: https://link.aps.org/doi/10.1103/PhysRev.136.B1224.

[59] T. Dietrich, S. Bernuzzi, and W. Tichy, "Closed-form tidal approximants for binary neutron star gravitational waveforms constructed from high-resolution numerical relativity simulations," *Phys. Rev.*, vol. D96, no. 12, p. 121 501, 2017. DOI: 10.1103/PhysRevD.96.121501. arXiv: 1706.02969 [gr-qc].

[60] T. Dietrich *et al.*, "Matter imprints in waveform models for neutron star binaries: Tidal and self-spin effects," *Phys. Rev.*, vol. D99, no. 2, p. 024 029, 2019. DOI: 10.1103/PhysRevD.99.024029. arXiv: 1804.02235 [gr-qc].

[61] B. P. Abbott *et al.*, "Properties of the binary neutron star merger GW170817," *Phys. Rev.*, vol. X9, no. 1, p. 011 001, 2019. DOI: 10.1103/PhysRevX.9.011001. arXiv: 1805.11579 [gr-qc].

[62] M. Campanelli, C. O. Lousto, and Y. Zlochower, "Spinning-black-hole binaries: The orbital hang up," *Phys. Rev.*, vol. D74, p. 041 501, 2006. DOI: 10.1103/PhysRevD.74.041501. arXiv: gr-qc/0604012 [gr-qc].

[63] P. Schmidt, F. Ohme, and M. Hannam, "Towards models of gravitational waveforms from generic binaries II: Modelling precession effects with a single effective precession parameter," *Phys. Rev.*, vol. D91, no. 2, p. 024 043, 2015. DOI: 10.1103/PhysRevD.91.024043. arXiv: 1408.1810 [gr-qc].

[64] L. Blanchet, "Gravitational radiation from post-newtonian sources and inspiralling compact binaries," *Living Reviews in Relativity*, vol. 9, no. 1, p. 4, 2006, ISSN: 1433-8351. DOI: 10.12942/lrr-2006-4. [Online]. Available: https://doi.org/10.12942/lrr-2006-4.

[65] S. A. Teukolsky, "Rotating black holes - separable wave equations for gravitational and electromagnetic perturbations," *Phys. Rev. Lett.*, vol. 29, pp. 1114–1118, 1972. DOI: 10.1103/PhysRevLett.29.1114.

[66] H.-P. Nollert and R. H. Price, "Quantifying excitations of quasinormal mode systems," *J. Math. Phys.*, vol. 40, pp. 980–1010, 1999. DOI: 10.1063/1.532698. arXiv: gr-qc/9810074 [gr-qc].

[67] I. Kamaretsos, M. Hannam, S. Husa, *et al.*, "Black-hole hair loss: learning about binary progenitors from ringdown signals," *Phys. Rev.*, vol. D85, p. 024 018, 2012. DOI: 10.1103/PhysRevD.85.024018. arXiv: 1107.0854 [gr-qc].

[68] A. Buonanno, G. B. Cook, and F. Pretorius, "Inspiral, merger and ring-down of equal-mass black-hole binaries," *Phys. Rev.*, vol. D75, p. 124 018, 2007. DOI: 10.1103/PhysRevD.75.124018. arXiv: gr-qc/0610122 [gr-qc].

[69] S. Husa, S. Khan, M. Hannam, *et al.*, "Frequency-domain gravitational waves from non-precessing black-hole binaries. I. New numerical waveforms and anatomy of the signal," *arXiv Prepr. arXiv1508.07250*, pp. 1–17, 2015, ISSN: 2470-0010. DOI: 10.1103/PhysRevD.93.044006. arXiv: 1508.07250. [Online]. Available: http://arxiv.org/abs/1508.07250.

[70] A. Buonanno and T. Damour, "Effective one-body approach to general relativistic two-body dynamics," *Phys. Rev. D*, vol. 59, p. 084 006, 8 1999. DOI: 10.1103/PhysRevD.59.084006. [Online]. Available: https://link.aps.org/doi/10.1103/PhysRevD.59.084006.

[71] A. Buonanno and T. Damour, "Transition from inspiral to plunge in binary black hole coalescences," *Phys. Rev.*, vol. D62, p. 064 015, 2000. DOI: 10.1103/PhysRevD.62.064015. arXiv: gr-qc/0001013 [gr-qc].

[72] T. Damour, "Coalescence of two spinning black holes: an effective one-body approach," *Phys. Rev.*, vol. D64, p. 124 013, 2001. DOI: 10.1103/PhysRevD.64.124013. arXiv: gr-qc/0103018 [gr-qc].

[73] A. Buonanno, Y. Chen, and T. Damour, "Transition from inspiral to plunge in precessing binaries of spinning black holes," *Phys. Rev.*, vol. D74, p. 104 005, 2006. DOI: 10.1103/PhysRevD.74.104005. arXiv: gr-qc/0508067 [gr-qc].

[74] A. Taracchini, A. Buonanno, Y. Pan, *et al.*, "Effective-one-body model for black-hole binaries with generic mass ratios and spins," *Phys. Rev. D*, vol. 89, p. 061 502, 6 2014. DOI: 10.1103/PhysRevD.89.061502. [Online]. Available: https://link.aps.org/doi/10.1103/PhysRevD.89.061502.

[75] A. Bohé *et al.*, "Improved effective-one-body model of spinning, nonprecessing binary black holes for the era of gravitational-wave astrophysics with advanced detectors," *Phys. Rev.*, vol. D95, no. 4, p. 044 028, 2017. DOI: 10.1103/PhysRevD.95.044028. arXiv: 1611.03703 [gr-qc].

[76] P. Ajith, S. Babak, Y. Chen, *et al.*, "Template bank for gravitational waveforms from coalescing binary black holes: Nonspinning binaries," *Phys. Rev. D*, vol. 77, p. 104 017, 10 2008. DOI: 10.1103/PhysRevD.77.104017. [Online]. Available: https://link.aps.org/doi/10.1103/PhysRevD.77.104017.

[77] C. Cutler and E. E. Flanagan, "Gravitational waves from merging compact binaries: How accurately can one extract the binary's parameters from the inspiral wave form?" *Phys. Rev.*, vol. D49, pp. 2658–2697, 1994. DOI: 10.1103/PhysRevD.49.2658. arXiv: gr-qc/9402014 [gr-qc].

[78] L. Blanchet, A. Buonanno, and G. Faye, "Higher-order spin effects in the dynamics of compact binaries. II. Radiation field," *Phys. Rev.*, vol. D74, p. 104 034, 2006, [Erratum: Phys. Rev.D81,089901(2010)]. DOI: 10.1103/PhysRevD.81.089901, 10.1103/PhysRevD.74.104034, 10.1103/PhysRevD.75.049903. arXiv: gr-qc/0605140 [gr-qc].

[79] T. Damour, B. R. Iyer, and B. S. Sathyaprakash, "A Comparison of search templates for gravitational waves from binary inspiral," *Phys. Rev.*, vol. D63, p. 044 023, 2001, [Erratum: Phys. Rev.D72,029902(2005)]. DOI: 10.1103/PhysRevD.63.044023, 10.1103/PhysRevD.72.029902. arXiv: gr-qc/0010009 [gr-qc].

[80] A. Buonanno, B. Iyer, E. Ochsner, *et al.*, "Comparison of post-Newtonian templates for compact binary inspiral signals in gravitational-wave detectors," *Phys. Rev.*, vol. D80, p. 084 043, 2009. DOI: 10.1103/PhysRevD.80.084043. arXiv: 0907.0700 [gr-qc].

[81] M. Boyle, D. A. Brown, L. E. Kidder, *et al.*, "High-accuracy comparison of numerical relativity simulations with post-Newtonian expansions," *Phys. Rev.*, vol. D76, p. 124 038, 2007. DOI: 10.1103/PhysRevD.76.124038. arXiv: 0710.0158 [gr-qc].

[82] M. Hannam, S. Husa, J. A. Gonzalez, *et al.*, "Where post-Newtonian and numerical-relativity waveforms meet," *Phys. Rev.*, vol. D77, p. 044 020, 2008. DOI: 10.1103/PhysRevD.77.044020. arXiv: 0706.1305 [gr-qc].

[83] K. S. Thorne, "Multipole expansions of gravitational radiation," *Rev. Mod. Phys.*, vol. 52, pp. 299–339, 2 1980. DOI: 10.1103/RevModPhys.52.299. [Online]. Available: https://link.aps.org/doi/10.1103/RevModPhys.52.299.

[84] L. Blanchet, G. Faye, B. R. Iyer, *et al.*, "The Third post-Newtonian gravitational wave polarisations and associated spherical harmonic modes for inspiralling compact binaries in quasi-circular orbits," *Class. Quant. Grav.*, vol. 25, p. 165 003, 2008, [Erratum: Class. Quant. Grav.29,239501(2012)]. DOI: 10.1088/0264-9381/25/16/165003, 10.1088/0264-9381/29/23/239501. arXiv: 0802.1249 [gr-qc].

[85] L. E. Kidder, "Using full information when computing modes of post-Newtonian waveforms from inspiralling compact binaries in circular orbit," *Phys. Rev.*, vol. D77, p. 044 016, 2008. DOI: 10.1103/PhysRevD.77.044016. arXiv: 0710.0614 [gr-qc].

[86] B. Moore, M. Favata, K. G. Arun, *et al.*, "Gravitational-wave phasing for low-eccentricity inspiralling compact binaries to 3PN order," *Phys. Rev.*, vol. D93, no. 12, p. 124 061, 2016. DOI: 10.1103/PhysRevD.93.124061. arXiv: 1605.00304 [gr-qc].

[87] A. Klein, Y. Boetzel, A. Gopakumar, *et al.*, "Fourier domain gravitational waveforms for precessing eccentric binaries," *Phys. Rev.*, vol. D98, no. 10, p. 104 043, 2018. DOI: 10.1103/PhysRevD.98.104043. arXiv: 1801.08542 [gr-qc].

[88] L Blanchet and G Schafer, "Gravitational wave tails and binary star systems," *Classical and Quantum Gravity*, vol. 10, no. 12, pp. 2699–2721, 1993. DOI: 10.1088/0264-9381/10/12/026. [Online]. Available: https://doi.org/10.1088%2F0264-9381%2F10%2F12%2F026.

[89] L. Blanchet and T. Damour, "Hereditary effects in gravitational radiation," *Phys. Rev. D*, vol. 46, pp. 4304–4319, 10 1992. DOI: 10.1103/PhysRevD.46.4304. [Online]. Available: https://link.aps.org/doi/10.1103/PhysRevD.46.4304.

[90] D. Christodoulou, "Nonlinear nature of gravitation and gravitational wave experiments," *Phys. Rev. Lett.*, vol. 67, pp. 1486–1489, 1991. DOI: 10.1103/PhysRevLett.67.1486.

[91] M. Favata, "Nonlinear gravitational-wave memory from binary black hole mergers," *Astrophys. J.*, vol. 696, pp. L159–L162, 2009. DOI: 10.1088/0004-637X/696/2/L159. arXiv: 0902.3660 [astro-ph.SR].

[92] T. W. Baumgarte and S. L. Shapiro, *Numerical Relativity: Solving Einstein's Equations on the Computer*. Cambridge University Press, 2010. DOI: 10.1017/CBO9781139193344.

[93] R. L. Arnowitt, S. Deser, and C. W. Misner, "The Dynamics of general relativity," *Gen. Rel. Grav.*, vol. 40, pp. 1997–2027, 2008. DOI: 10.1007/s10714-008-0661-1. arXiv: gr-qc/0405109 [gr-qc].

[94] J. W. York Jr., "Kinematics and Dynamics of General Relativity," in *Proceedings, Sources of Gravitational Radiation: Seattle, WA, USA, July 24 - August 4, 1978*, pp. 83–126.

[95] T. W. Baumgarte and S. L. Shapiro, "Numerical integration of einstein's field equations," *Phys. Rev. D*, vol. 59, p. 024 007, 2 1998. DOI: 10.1103/PhysRevD.59.024007. [Online]. Available: https://link.aps.org/doi/10.1103/PhysRevD.59.024007.

[96] M. Shibata and T. Nakamura, "Evolution of three-dimensional gravitational waves: Harmonic slicing case," *Phys. Rev. D*, vol. 52, pp. 5428–5444, 10 1995. DOI: 10.1103/PhysRevD.52.5428. [Online]. Available: https://link.aps.org/doi/10.1103/PhysRevD.52.5428.

[97] J Thornburg, "Coordinates and boundary conditions for the general relativistic initial data problem," *Classical and Quantum Gravity*, vol. 4, no. 5, pp. 1119–1131, 1987. DOI: 10.1088/0264-9381/4/5/013. [Online]. Available: https://doi.org/10.1088%2F0264-9381%2F4%2F5%2F013.

[98] F. Pretorius, "Evolution of binary black-hole spacetimes," *Phys. Rev. Lett.*, vol. 95, p. 121 101, 12 2005. DOI: 10.1103/PhysRevLett.95.121101. [Online]. Available: https://link.aps.org/doi/10.1103/PhysRevLett.95.121101.

[99] D. A. Hemberger, M. A. Scheel, L. E. Kidder, *et al.*, "Dynamical Excision Boundaries in Spectral Evolutions of Binary Black Hole Spacetimes," *Class. Quant. Grav.*, vol. 30, p. 115 001, 2013. DOI: 10.1088/0264-9381/30/11/115001. arXiv: 1211.6079 [gr-qc].

[100] M. Campanelli, C. O. Lousto, P. Marronetti, *et al.*, "Accurate evolutions of orbiting black-hole binaries without excision," *Phys. Rev. Lett.*, vol. 96, p. 111 101, 11 2006. DOI: 10.1103/PhysRevLett.96.111101. [Online]. Available: https://link.aps.org/doi/10.1103/PhysRevLett.96.111101.

[101] J. G. Baker, J. Centrella, D.-I. Choi, *et al.*, "Gravitational-wave extraction from an inspiraling configuration of merging black holes," *Phys. Rev. Lett.*, vol. 96, p. 111 102, 11 2006. DOI: 10.1103/PhysRevLett.96.111102. [Online]. Available: https://link.aps.org/doi/10.1103/PhysRevLett.96.111102.

[102] D. R. Brill and R. W. Lindquist, "Interaction energy in geometrostatics," *Phys. Rev.*, vol. 131, pp. 471–476, 1 1963. DOI: 10.1103/PhysRev.131.471. [Online]. Available: https://link.aps.org/doi/10.1103/PhysRev.131.471.

[103] M. Hannam, S. Husa, F. Ohme, *et al.*, "Wormholes and trumpets: Schwarzschild spacetime for the moving-puncture generation," *Phys. Rev. D*, vol. 78, p. 064 020, 6 2008. DOI: 10.1103/PhysRevD.78.064020. [Online]. Available: https://link.aps.org/doi/10.1103/PhysRevD.78.064020.

[104] G. B. Cook, "Initial data for numerical relativity," *Living Rev. Rel.*, vol. 3, p. 5, 2000. DOI: 10.12942/lrr-2000-5. arXiv: gr-qc/0007085 [gr-qc].

[105] J. M. Bowen and J. W. York, "Time-asymmetric initial data for black holes and black-hole collisions," *Phys. Rev. D*, vol. 21, pp. 2047–2056, 8 1980. DOI: 10.1103/PhysRevD.21.2047. [Online]. Available: https://link.aps.org/doi/10.1103/PhysRevD.21.2047.

[106] M. Hannam, S. Husa, D. Pollney, *et al.*, "Geometry and regularity of moving punctures," *Phys. Rev. Lett.*, vol. 99, p. 241 102, 2007. DOI: 10.1103/PhysRevLett.99.241102. arXiv: gr-qc/0606099 [gr-qc].

[107] F. Estabrook, H. Wahlquist, S. Christensen, *et al.*, "Maximally slicing a black hole," *Phys. Rev. D*, vol. 7, pp. 2814–2817, 10 1973. DOI: 10.1103/PhysRevD.7.2814. [Online]. Available: https://link.aps.org/doi/10.1103/PhysRevD.7.2814.

[108] B. Brügmann, J. A. González, M. Hannam, *et al.*, "Calibration of moving puncture simulations," *Phys. Rev. D*, vol. 77, p. 024 027, 2 2008. DOI: 10.1103/PhysRevD.77.024027. [Online]. Available: https://link.aps.org/doi/10.1103/PhysRevD.77.024027.

[109] M. Alcubierre, B. Bruegmann, P. Diener, *et al.*, "Gauge conditions for long term numerical black hole evolutions without excision," *Phys. Rev.*, vol. D67, p. 084 023, 2003. DOI: 10.1103/PhysRevD.67.084023. arXiv: gr-qc/0206072 [gr-qc].

[110] B. Brügmann, W. Tichy, and N. Jansen, "Numerical simulation of orbiting black holes," *Phys. Rev. Lett.*, vol. 92, p. 211 101, 21 2004. DOI: 10.1103/PhysRevLett.92.211101. [Online]. Available: https://link.aps.org/doi/10.1103/PhysRevLett.92.211101.

[111] L. E. Kidder, M. A. Scheel, S. A. Teukolsky, *et al.*, "Black hole evolution by spectral methods," *Phys. Rev. D*, vol. 62, p. 084 032, 8 2000. DOI: 10.1103/PhysRevD.62.084032. [Online]. Available: https://link.aps.org/doi/10.1103/PhysRevD.62.084032.

[112] *Spectral einstein code*, https://www.black-holes.org/code/SpEC.html.

[113] F. Loffler *et al.*, "The Einstein Toolkit: A Community Computational Infrastructure for Relativistic Astrophysics," *Class. Quant. Grav.*, vol. 29, p. 115 001, 2012. DOI: 10.1088/0264-9381/29/11/115001. arXiv: 1111.3344 [gr-qc].

[114] I. Hinder *et al.*, "Error-analysis and comparison to analytical models of numerical waveforms produced by the NRAR Collaboration," *Class. Quant. Grav.*, vol. 31, p. 025 012, 2014. DOI: 10.1088/0264-9381/31/2/025012. arXiv: 1307.5307 [gr-qc].

[115] J. Healy, C. O. Lousto, Y. Zlochower, *et al.*, "The RIT binary black hole simulations catalog," *Class. Quant. Grav.*, vol. 34, no. 22, p. 224 001, 2017. DOI: 10.1088/1361-6382/aa91b1. arXiv: 1703.03423 [gr-qc].

[116] M. Boyle *et al.*, "The SXS Collaboration catalog of binary black hole simulations," 2019. arXiv: 1904.04831 [gr-qc].

[117] *Lvc nr waveforms repository*, https://git.ligo.org/waveforms/lvcnr-lfs.

[118] M. Ansorg, B. Brügmann, and W. Tichy, "Single-domain spectral method for black hole puncture data," *Phys. Rev. D*, vol. 70, p. 064 011, 6 2004. DOI: 10.1103/PhysRevD.70.064011. [Online]. Available: https://link.aps.org/doi/10.1103/PhysRevD.70.064011.

[119] S. Husa, J. A. González, M. Hannam, *et al.*, "Reducing phase error in long numerical binary black hole evolutions with sixth-order finite differencing," *Classical and Quantum Gravity*, vol. 25, no. 10, p. 105 006, 2008. DOI: 10.1088/0264-9381/25/10/105006. [Online]. Available: https://doi.org/10.1088%2F0264-9381%2F25%2F10%2F105006.

[120] M. J. Berger and J. Oliger, "Adaptive Mesh Refinement for Hyperbolic Partial Differential Equations," *Journal of Computational Physics*, vol. 53, pp. 484–512, Mar. 1984. DOI: 10.1016/0021-9991(84)90073-1.

[121] E. Newman and R. Penrose, "An Approach to gravitational radiation by a method of spin coefficients," *J. Math. Phys.*, vol. 3, pp. 566–578, 1962. DOI: 10.1063/1.1724257.

[122] J. Calderón Bustillo, A. Bohé, S. Husa, *et al.*, "Comparison of subdominant gravitational wave harmonics between post-Newtonian and numerical relativity calculations and construction of multi-mode hybrids," 2015. arXiv: 1501.00918 [gr-qc].

[123] I. MacDonald, S. Nissanke, H. P. Pfeiffer, *et al.*, "Suitability of post-Newtonian/numerical-relativity hybrid waveforms for gravitational wave detectors," *Class. Quant. Grav.*, vol. 28, p. 134 002, 2011. DOI: 10.1088/0264-9381/28/13/134002. arXiv: 1102.5128 [gr-qc].

[124] S. Ossokine, L. Kidder, H. Pfeiffer, *et al.*, "Transitional precession in binary black hole systems," in *APS Meeting Abstracts*, 2018, p. D14.004.

[125] P. Schmidt, M. Hannam, and S. Husa, "Towards models of gravitational waveforms from generic binaries: A simple approximate mapping between precessing and non-precessing inspiral signals," *Phys. Rev.*, vol. D86, p. 104 063, 2012. DOI: 10.1103/PhysRevD.86.104063. arXiv: 1207.3088 [gr-qc].

[126] T. A. Apostolatos, C. Cutler, G. J. Sussman, *et al.*, "Spin-induced orbital precession and its modulation of the gravitational waveforms from merging binaries," *Phys. Rev. D*, vol. 49, pp. 6274–6297, 12 1994. DOI: 10.1103/PhysRevD.49.6274. [Online]. Available: https://link.aps.org/doi/10.1103/PhysRevD.49.6274.

[127] K. G. Arun, A. Buonanno, G. Faye, *et al.*, "Higher-order spin effects in the amplitude and phase of gravitational waveforms emitted by inspiraling compact binaries: Ready-to-use gravitational waveforms," *Phys. Rev.*, vol. D79, p. 104 023, 2009, [Erratum: Phys. Rev.D84,049901(2011)]. DOI: 10.1103/PhysRevD.79.104023, 10.1103/PhysRevD.84.049901. arXiv: 0810.5336 [gr-qc].

[128] K. Chatziioannou, A. Klein, N. Yunes, *et al.*, "Constructing Gravitational Waves from Generic Spin-Precessing Compact Binary Inspirals," *Phys. Rev.*, vol. D95, no. 10, p. 104 004, 2017. DOI: 10.1103/PhysRevD.95.104004. arXiv: 1703.03967 [gr-qc].

[129] ——, "Gravitational Waveforms for Precessing, Quasicircular Compact Binaries with Multiple Scale Analysis: Small Spin Expansion," *Phys. Rev.*, vol. D88, no. 6, p. 063 011, 2013. DOI: 10.1103/PhysRevD.88.063011. arXiv: 1307.4418 [gr-qc].

[130] S. Khan, K. Chatziioannou, M. Hannam, *et al.*, "Phenomenological model for the gravitational-wave signal from precessing binary black holes with two-spin effects," 2018. arXiv: 1809.10113 [gr-qc].

[131] M. Boyle, L. E. Kidder, S. Ossokine, *et al.*, "Gravitational-wave modes from precessing black-hole binaries," 2014. arXiv: 1409.4431 [gr-qc].

[132] W. B. Bonnor, M. A. Rotenberg, and L. Rosenhead, "Transport of momentum by gravitational waves: The linear approximation," *Proceedings of the Royal Society of London. Series A. Mathematical and Physical Sciences*, vol. 265, no. 1320, pp. 109–116, 1961. DOI: 10.1098/rspa.1961.0226. eprint: https://royalsocietypublishing.org/doi/pdf/10.1098/rspa.1961.0226. [Online]. Available: https://royalsocietypublishing.org/doi/abs/10.1098/rspa.1961.0226.

[133] A. Peres, "Classical radiation recoil," *Phys. Rev.*, vol. 128, pp. 2471–2475, 5 1962. DOI: 10.1103/PhysRev.128.2471. [Online]. Available: https://link.aps.org/doi/10.1103/PhysRev.128.2471.

[134] J. Bekenstein, "Gravitational-Radiation Recoil and Runaway Black Holes," *Astrophysical Journal, Vol. 183*, vol. 183, pp. 657–664, Jul. 1973. DOI: 10.1086/152255.

[135] J. A. Gonzalez, U. Sperhake, B. Bruegmann, *et al.*, "Total recoil: The Maximum kick from nonspinning black-hole binary inspiral," *Phys. Rev. Lett.*, vol. 98, p. 091 101, 2007. DOI: 10.1103/PhysRevLett.98.091101. arXiv: gr-qc/0610154 [gr-qc].

[136] F. Herrmann, I. Hinder, D. Shoemaker, *et al.*, "Gravitational recoil from spinning binary black hole mergers," *Astrophys. J.*, vol. 661, pp. 430–436, 2007. DOI: 10.1086/513603. arXiv: gr-qc/0701143 [GR-QC].

[137] M. Koppitz, D. Pollney, C. Reisswig, *et al.*, "Recoil Velocities from Equal-Mass Binary-Black-Hole Mergers," *Phys. Rev. Lett.*, vol. 99, p. 041 102, 2007. DOI: 10.1103/PhysRevLett.99.041102. arXiv: gr-qc/0701163 [GR-QC].

[138] M. Campanelli, C. O. Lousto, Y. Zlochower, *et al.*, "Maximum gravitational recoil," *Phys. Rev. Lett.*, vol. 98, p. 231 102, 2007. DOI: 10.1103/PhysRevLett.98.231102. arXiv: gr-qc/0702133 [GR-QC].

[139] J. A. Gonzalez, M. D. Hannam, U. Sperhake, *et al.*, "Supermassive recoil velocities for binary black-hole mergers with antialigned spins," *Phys. Rev. Lett.*, vol. 98, p. 231 101, 2007. DOI: 10.1103/PhysRevLett.98.231101. arXiv: gr-qc/0702052 [GR-QC].

[140] B. Bruegmann, J. A. Gonzalez, M. Hannam, *et al.*, "Exploring black hole superkicks," *Phys. Rev.*, vol. D77, p. 124 047, 2008. DOI: 10.1103/PhysRevD.77.124047. arXiv: 0707.0135 [gr-qc].

[141] C. O. Lousto, M. Campanelli, Y. Zlochower, *et al.*, "Remnant Masses, Spins and Recoils from the Merger of Generic Black-Hole Binaries," *Class. Quant. Grav.*, vol. 27, p. 114 006, 2010. DOI: 10.1088/0264-9381/27/11/114006. arXiv: 0904.3541 [gr-qc].

[142] M. Chiaberge, J. C. Ely, E. T. Meyer, *et al.*, "The puzzling case of the radio-loud QSO 3C 186: a gravitational wave recoiling black hole in a young radio source?" *&A*, vol. 600, A57, A57, 2017. DOI: 10.1051/0004-6361/201629522. arXiv: 1611.05501 [astro-ph.GA].

[143] R. Cotesta, A. Buonanno, A. Bohé, *et al.*, "Enriching the Symphony of Gravitational Waves from Binary Black Holes by Tuning Higher Harmonics," *Phys. Rev.*, vol. D98, no. 8, p. 084 028, 2018. DOI: 10.1103/PhysRevD.98.084028. arXiv: 1803.10701 [gr-qc].

[144] Y. Pan, A. Buonanno, A. Taracchini, *et al.*, "Inspiral-merger-ringdown waveforms of spinning, precessing black-hole binaries in the effective-one-body formalism," *Phys. Rev.*, vol. D89, no. 8, p. 084 006, 2014. DOI: 10.1103/PhysRevD.89.084006. arXiv: 1307.6232 [gr-qc].

[145] S. Khan, S. Husa, M. Hannam, *et al.*, "Frequency-domain gravitational waves from nonprecessing black-hole binaries. II. A phenomenological model for the advanced detector era," *Phys. Rev.*, vol. D93, no. 4, p. 044 007, 2016. DOI: 10.1103/PhysRevD.93.044007. arXiv: 1508.07253 [gr-qc].

[146] L. London, S. Khan, E. Fauchon-Jones, *et al.*, "First higher-multipole model of gravitational waves from spinning and coalescing black-hole binaries," *Phys. Rev. Lett.*, vol. 120, no. 16, p. 161 102, 2018. DOI: 10.1103/PhysRevLett.120.161102. arXiv: 1708.00404 [gr-qc].

[147] M. Hannam, P. Schmidt, A. Bohé, *et al.*, "Simple Model of Complete Precessing Black-Hole-Binary Gravitational Waveforms," *Phys. Rev. Lett.*, vol. 113, no. 15, p. 151 101, 2014. DOI: 10.1103/PhysRevLett.113.151101. arXiv: 1308.3271 [gr-qc].

[148] P. Ajith, M. Hannam, S. Husa, *et al.*, "Inspiral-merger-ringdown waveforms for black-hole binaries with nonprecessing spins," *Phys. Rev. Lett.*, vol. 106, p. 241 101, 24 2011. DOI: 10.1103/PhysRevLett.106.241101. [Online]. Available: https://link.aps.org/doi/10.1103/PhysRevLett.106.241101.

[149] L. Santamaria *et al.*, "Matching post-Newtonian and numerical relativity waveforms: systematic errors and a new phenomenological model for non-precessing black hole binaries," *Phys. Rev.*, vol. D82, p. 064 016, 2010. DOI: 10.1103/PhysRevD.82.064016. arXiv: 1005.3306 [gr-qc].

[150] K. G. Arun, B. R. Iyer, B. S. Sathyaprakash, *et al.*, "Parameter estimation of inspiralling compact binaries using 3.5 post-Newtonian gravitational wave phasing: The Non-spinning case," *Phys. Rev.*, vol. D71, p. 084 008, 2005, [Erratum: Phys. Rev.D72,069903(2005)]. DOI: 10.1103/PhysRevD.71.084008,10.1103/PhysRevD.72.069903. arXiv: gr-qc/0411146 [gr-qc].

[151] F. Ohme, A. B. Nielsen, D. Keppel, *et al.*, "Statistical and systematic errors for gravitational-wave inspiral signals: A principal component analysis," *Phys. Rev.*, vol. D88, no. 4, p. 042 002, 2013. DOI: 10.1103/PhysRevD.88.042002. arXiv: 1304.7017 [gr-qc].

[152] P. Ajith, "Addressing the spin question in gravitational-wave searches: Waveform templates for inspiralling compact binaries with nonprecessing spins," *Phys. Rev.*, vol. D84, p. 084 037, 2011. DOI: 10.1103/PhysRevD.84.084037. arXiv: 1107.1267 [gr-qc].

[153] E. Poisson and C. M. Will, "Gravitational waves from inspiraling compact binaries: Parameter estimation using second postNewtonian wave forms," *Phys. Rev.*, vol. D52, pp. 848–855, 1995. DOI: 10.1103/PhysRevD.52.848. arXiv: gr-qc/9502040 [gr-qc].

[154] P. Kumar, T. Chu, H. Fong, *et al.*, "Accuracy of binary black hole waveform models for aligned-spin binaries," *Phys. Rev.*, vol. D93, no. 10, p. 104 050, 2016. DOI: 10.1103/PhysRevD.93.104050. arXiv: 1601.05396 [gr-qc].

[155] M. Boyle, R. Owen, and H. P. Pfeiffer, "A geometric approach to the precession of compact binaries," *Phys. Rev.*, vol. D84, p. 124 011, 2011. DOI: 10.1103/PhysRevD.84.124011. arXiv: 1110.2965 [gr-qc].

[156] R. O'Shaughnessy, B. Vaishnav, J. Healy, *et al.*, "Efficient asymptotic frame selection for binary black hole spacetimes using asymptotic radiation," *Phys. Rev.*, vol. D84, p. 124 002, 2011. DOI: 10.1103/PhysRevD.84.124002. arXiv: 1109.5224 [gr-qc].

[157] M. Boyle, R. Owen, and H. P. Pfeiffer, "Geometric approach to the precession of compact binaries," *Phys. Rev. D*, vol. 84, p. 124 011, 12 2011. DOI: 10.1103/PhysRevD.84.124011. [Online]. Available: https://link.aps.org/doi/10.1103/PhysRevD.84.124011.

[158] D. Martin, "E. p. wigner, group theory and its application to the quantum mechanics of atomic spectra, (academic press inc., new york, 1959), j. j. griffin, ix 372 pp.,80s.," *Proceedings of the Edinburgh Mathematical Society*, vol. 12, no. 1, 67–67, 1960. DOI: 10.1017/S0013091500025220.

[159] J. N. Goldberg, A. J. Macfarlane, E. T. Newman, *et al.*, "Spins spherical harmonics," *Journal of Mathematical Physics*, vol. 8, no. 11, pp. 2155–2161, 1967. DOI: 10.1063/1.1705135. eprint: https://doi.org/10.1063/1.1705135. [Online]. Available: https://doi.org/10.1063/1.1705135.

[160] C. K. Mishra, A. Kela, K. G. Arun, *et al.*, "Ready-to-use post-Newtonian gravitational waveforms for binary black holes with nonprecessing spins: An update," *Phys. Rev.*, vol. D93, no. 8, p. 084 054, 2016. DOI: 10.1103/PhysRevD.93.084054. arXiv: 1601.05588 [gr-qc].

[161] K. Chatziioannou, A. Klein, N. Cornish, *et al.*, "Analytic Gravitational Waveforms for Generic Precessing Binary Inspirals," *Phys. Rev. Lett.*, vol. 118, no. 5, p. 051 101, 2017. DOI: 10.1103/PhysRevLett.118.051101. arXiv: 1606.03117 [gr-qc].

[162] Y. Pan, A. Buonanno, M. Boyle, *et al.*, "Inspiral-merger-ringdown multipolar waveforms of nonspinning black-hole binaries using the effective-one-body formalism," *Phys. Rev.*, vol. D84, p. 124 052, 2011. DOI: 10.1103/PhysRevD.84.124052. arXiv: 1106.1021 [gr-qc].

[163] V. Varma, P. Ajith, S. Husa, *et al.*, "Gravitational-wave observations of binary black holes: Effect of nonquadrupole modes," *Phys. Rev.*, vol. D90, no. 12, p. 124 004, 2014. DOI: 10.1103/PhysRevD.90.124004. arXiv: 1409.2349 [gr-qc].

[164] J. Calderón Bustillo, F. Salemi, T. Dal Canton, *et al.*, "Sensitivity of gravitational wave searches to the full signal of intermediate-mass black hole binaries during the first observing run of advanced ligo," *Phys. Rev. D*, vol. 97, p. 024 016, 2 2018. DOI: 10.1103/PhysRevD.97.024016. [Online]. Available: https://link.aps.org/doi/10.1103/PhysRevD.97.024016.

[165] I. Harry, J. C. Bustillo, and A. Nitz, "Searching for the full symphony of black hole binary mergers," *Phys. Rev. D*, vol. 97, p. 023 004, 2 2018. DOI: 10.1103/PhysRevD.97.023004. [Online]. Available: https://link.aps.org/doi/10.1103/PhysRevD.97.023004.

[166] V. Varma and P. Ajith, "Effects of nonquadrupole modes in the detection and parameter estimation of black hole binaries with nonprecessing spins," *Phys. Rev. D*, vol. 96, p. 124 024, 12 2017. DOI: 10.1103/PhysRevD.96.124024. [Online]. Available: https://link.aps.org/doi/10.1103/PhysRevD.96.124024.

[167] J. Calderón Bustillo, S. Husa, A. M. Sintes, *et al.*, "Impact of gravitational radiation higher order modes on single aligned-spin gravitational wave searches for binary black holes," *Phys. Rev. D*, vol. 93, p. 084 019, 8 2016. DOI: 10.1103/PhysRevD.93.084019. [Online]. Available: https://link.aps.org/doi/10.1103/PhysRevD.93.084019.

[168] J. Calderón Bustillo, P. Laguna, and D. Shoemaker, "Detectability of gravitational waves from binary black holes: Impact of precession and higher modes," *Phys. Rev.*, vol. D95, no. 10, p. 104 038, 2017. DOI: 10.1103/PhysRevD.95.104038. arXiv: 1612.02340 [gr-qc].

[169] C. Capano, Y. Pan, and A. Buonanno, "Impact of higher harmonics in searching for gravitational waves from nonspinning binary black holes," *Phys. Rev. D*, vol. 89, p. 102 003, 10 2014. DOI: 10.1103/PhysRevD.89.102003. [Online]. Available: https://link.aps.org/doi/10.1103/PhysRevD.89.102003.

[170] B. P. Abbott, R. Abbott, T. D. Abbott, *et al.*, "Properties of the Binary Black Hole Merger GW150914," *Phys. Rev. Lett.*, vol. 116, no. 24, p. 241 102, 2016. DOI: 10.1103/PhysRevLett.116.241102. arXiv: 1602.03840 [gr-qc].

[171] B. P. Abbott, R. Abbott, T. D. Abbott, *et al.*, "Improved analysis of gw150914 using a fully spin-precessing waveform model," *Phys. Rev. X*, vol. 6, p. 041 014, 4 2016. DOI: 10.1103/PhysRevX.6.041014. [Online]. Available: https://link.aps.org/doi/10.1103/PhysRevX.6.041014.

[172] C. Pankow, P. Brady, E. Ochsner, *et al.*, "Novel scheme for rapid parallel parameter estimation of gravitational waves from compact binary coalescences," *Phys. Rev. D*, vol. 92, p. 023 002, 2 2015. DOI: 10.1103/PhysRevD.92.023002. [Online]. Available: https://link.aps.org/doi/10.1103/PhysRevD.92.023002.

[173] J. Lange, R. O'Shaughnessy, and M. Rizzo, "Rapid and accurate parameter inference for coalescing, precessing compact binaries," 2018. arXiv: 1805.10457 [gr-qc].

[174] B. P. Abbott *et al.*, "Directly comparing GW150914 with numerical solutions of Einstein's equations for binary black hole coalescence," *Phys. Rev.*, vol. D94, no. 6, p. 064 035, 2016. DOI: 10.1103/PhysRevD.94.064035. arXiv: 1606.01262 [gr-qc].

[175] J. Lange *et al.*, "Parameter estimation method that directly compares gravitational wave observations to numerical relativity," *Phys. Rev.*, vol. D96, no. 10, p. 104 041, 2017. DOI: 10.1103/PhysRevD.96.104041. arXiv: 1705.09833 [gr-qc].

[176] T. Damour, B. R. Iyer, and B. S. Sathyaprakash, "Frequency-domain p-approximant filters for time-truncated inspiral gravitational wave signals from compact binaries," *Phys. Rev. D*, vol. 62, p. 084 036, 8 2000. DOI: 10.1103/PhysRevD.62.084036. [Online]. Available: https://link.aps.org/doi/10.1103/PhysRevD.62.084036.

[177] S. Husa, M. Hannam, J. A. González, *et al.*, "Reducing eccentricity in black-hole binary evolutions with initial parameters from post-newtonian inspiral," *Phys. Rev. D*, vol. 77, p. 044 037, 4 2008. DOI: 10.1103/PhysRevD.77.044037. [Online]. Available: https://link.aps.org/doi/10.1103/PhysRevD.77.044037.

[178] M. Hannam, S. Husa, F. Ohme, *et al.*, "Simulations of black-hole binaries with unequal masses or nonprecessing spins: Accuracy, physical properties, and comparison with post-Newtonian results," *Phys. Rev.*, vol. D82, p. 124 008, 2010. DOI: 10.1103/PhysRevD.82.124008. arXiv: 1007.4789 [gr-qc].

[179] E. E. Flanagan and S. A. Hughes, "Measuring gravitational waves from binary black hole coalescences: 2. The Waves' information and its extraction, with and without templates," *Phys. Rev.*, vol. D57, pp. 4566–4587, 1998. DOI: 10.1103/PhysRevD.57.4566. arXiv: gr-qc/9710129 [gr-qc].

[180] L. Lindblom, B. J. Owen, and D. A. Brown, "Model Waveform Accuracy Standards for Gravitational Wave Data Analysis," *Phys. Rev.*, vol. D78, p. 124 020, 2008. DOI: 10.1103/PhysRevD.78.124020. arXiv: 0809.3844 [gr-qc].

[181] E. Baird, S. Fairhurst, M. Hannam, *et al.*, "Degeneracy between mass and spin in black-hole-binary waveforms," *Phys. Rev.*, vol. D87, no. 2, p. 024 035, 2013. DOI: 10.1103/PhysRevD.87.024035. arXiv: 1211.0546 [gr-qc].

[182] P. Ajith *et al.*, "The NINJA-2 catalog of hybrid post-Newtonian/numerical-relativity waveforms for non-precessing black-hole binaries," *Class. Quant. Grav.*, vol. 29, p. 124 001, 2012, [Erratum: Class. Quant. Grav.30,199401(2013)]. DOI: 10.1088/0264-9381/30/19/199401, 10.1088/0264-9381/29/12/124001. arXiv: 1201.5319 [gr-qc].

[183] J. Aasi *et al.*, "The NINJA-2 project: Detecting and characterizing gravitational waveforms modelled using numerical binary black hole simulations," *Class. Quant. Grav.*, vol. 31, p. 115 004, 2014. DOI: 10.1088/0264-9381/31/11/115004. arXiv: 1401.0939 [gr-qc].

[184] M. Ansorg, B. Bruegmann, and W. Tichy, "A Single-domain spectral method for black hole puncture data," *Phys. Rev.*, vol. D70, p. 064 011, 2004. DOI: 10.1103/PhysRevD.70.064011. arXiv: gr-qc/0404056 [gr-qc].

[185] P. Schmidt, I. W. Harry, and H. P. Pfeiffer, "Numerical Relativity Injection Infrastructure," 2017. arXiv: 1703.01076 [gr-qc].

[186] *Arcca webpage*, https://www.cardiff.ac.uk/advanced-research-computing.

[187] T. B. Littenberg, J. G. Baker, A. Buonanno, *et al.*, "Systematic biases in parameter estimation of binary black-hole mergers," pp. 1–16, 2011. DOI: 10.1103/PhysRevD.87.104003. arXiv: arXiv:1210.0893v1. [Online]. Available: https://arxiv.org/abs/1210.0893.

[188] *Publicly available o1 posterior data*, https://dcc.ligo.org/LIGO-T1800235/public.

[189] E. Hamilton and M. Hannam, "Inferring black-hole orbital dynamics from numerical-relativity gravitational waveforms," *Phys. Rev.*, vol. D98, no. 8, p. 084 018, 2018. DOI: 10.1103/PhysRevD.98.084018. arXiv: 1807.06331 [gr-qc].

[190] L. Pekowsky, R. O'Shaughnessy, J. Healy, *et al.*, "Comparing gravitational waves from nonprecessing and precessing black hole binaries in the corotating frame," *Phys. Rev.*, vol. D88, no. 2, p. 024 040, 2013. DOI: 10.1103/PhysRevD.88.024040. arXiv: 1304.3176 [gr-qc].

[191] *Phenompv2 – technical notes for the lal implementation*, https://dcc.ligo.org/LIGO-T1500602.

[192] A. Buonanno, L. E. Kidder, A. H. Mroue, *et al.*, "Reducing orbital eccentricity of precessing black-hole binaries," *Phys. Rev.*, vol. D83, p. 104 034, 2011. DOI: 10.1103/PhysRevD.83.104034. arXiv: 1012.1549 [gr-qc].

[193] A. Ramos-Buades, S. Husa, and G. Pratten, "Simple procedures to reduce eccentricity of binary black hole simulations," *Phys. Rev.*, vol. D99, no. 2, p. 023 003, 2019. DOI: 10.1103/PhysRevD.99.023003. arXiv: 1810.00036 [gr-qc].

[194] E. Fauchon-Jones, C. Kalaghatgi, E. Hamilton, *et al.*, "Bam catalogue of binary black hole simulations," 2019, In preparation.

[195] A. Buonanno, Y.-b. Chen, and M. Vallisneri, "Detecting gravitational waves from precessing binaries of spinning compact objects: Adiabatic limit," *Phys. Rev.*, vol. D67, p. 104 025, 2003, [Erratum: Phys. Rev.D74,029904(2006)]. DOI: 10.1103/PhysRevD.67.104025,10.1103/PhysRevD.74.029904. arXiv: gr-qc/0211087 [gr-qc].

[196] V. Varma, S. E. Field, M. A. Scheel, *et al.*, "Surrogate models for precessing binary black hole simulations with unequal masses," 2019. arXiv: 1905.09300 [gr-qc].

[197] J. Blackman, S. E. Field, M. A. Scheel, *et al.*, "Numerical relativity waveform surrogate model for generically precessing binary black hole mergers," *Phys. Rev.*, vol. D96, no. 2, p. 024 058, 2017. DOI: 10.1103/PhysRevD.96.024058. arXiv: 1705.07089 [gr-qc].

[198] K. Chatziioannou *et al.*, "On the properties of the massive binary black hole merger GW170729," 2019. arXiv: 1903.06742 [gr-qc].

[199] B. P. Abbott *et al.*, "Binary Black Hole Population Properties Inferred from the First and Second Observing Runs of Advanced LIGO and Advanced Virgo," 2018. arXiv: 1811.12940 [astro-ph.HE].

[200] B. P. Abbott, R. Abbott, T. D. Abbott, *et al.*, "Binary Black Hole Mergers in the first Advanced LIGO Observing Run," *Phys. Rev.*, vol. X6, no. 4, p. 041 015, 2016, [erratum: Phys. Rev.X8,no.3,039903(2018)]. DOI: 10.1103/PhysRevX.6.041015,10.1103/PhysRevX.8.039903. arXiv: 1606.04856 [gr-qc].

[201] P. B. Graff, A. Buonanno, and B. S. Sathyaprakash, "Missing Link: Bayesian detection and measurement of intermediate-mass black-hole binaries," *Phys. Rev.*, vol. D92, no. 2, p. 022 002, 2015. DOI: 10.1103/PhysRevD.92.022002. arXiv: 1504.04766 [gr-qc].

[202] T. Damour and A. Nagar, "New effective-one-body description of coalescing nonprecessing spinning black-hole binaries," *Phys. Rev. D*, vol. 90, p. 044 018, 4 2014. DOI: 10.1103/PhysRevD.90.044018. [Online]. Available: https://link.aps.org/doi/10.1103/PhysRevD.90.044018.

[203] A. Nagar, T. Damour, C. Reisswig, *et al.*, "Energetics and phasing of nonprecessing spinning coalescing black hole binaries," *Phys. Rev. D*, vol. 93, p. 044 046, 4 2016. DOI: 10.1103/PhysRevD.93.044046. [Online]. Available: https://link.aps.org/doi/10.1103/PhysRevD.93.044046.

[204] A. Nitz, I. Harry, D. Brown, *et al.*, "Gwastro/pycbc: 1.12.3 release," 2018. DOI: 10.5281/zenodo.1410598.

[205] *Creating median on-source psd with bayeswave*, https://www.lsc-group.phys.uwm.edu/ligovirgo/cbcnote/ParameterEstimationModelSelection/O2_PE/BayesWaveMedianPSD.

[206] V. Tiwari, S. Fairhurst, and M. Hannam, "Constraining black-hole spins with gravitational wave observations," *Astrophys. J.*, vol. 868, no. 2, p. 140, 2018. DOI: 10.3847/1538-4357/aae8df. arXiv: 1809.01401 [gr-qc].

[207] S. Fairhurst, "Source localization with an advanced gravitational wave detector network," *Class. Quant. Grav.*, vol. 28, p. 105 021, 2011. DOI: 10.1088/0264-9381/28/10/105021. arXiv: 1010.6192 [gr-qc].

[208] B. P. Abbott *et al.*, "Prospects for Observing and Localizing Gravitational-Wave Transients with Advanced LIGO, Advanced Virgo and KAGRA," *Living Rev. Rel.*, vol. 21, no. 1, p. 3, 2018. DOI: 10.1007/s41114-018-0012-9, 10.1007/lrr-2016-1. arXiv: 1304.0670 [gr-qc].